Spring 5-15-2017

Sub 2 nm Particle Characterization in Systems with Aerosol Formation and Growth

Yang Wang
Washington University in St. Louis

WASHINGTON UNIVERSITY IN ST. LOUIS
School of Engineering and Applied Science
Department of Energy, Environmental and Chemical Engineering

Dissertation Examination Committee:
Pratim Biswas, Chair
Michel Attoui
Richard Axelbaum
Rajan Chakrabarty
Jingkun Jiang
Brent Williams

Sub 2 nm Particle Characterization in Systems with Aerosol Formation and Growth

by

Yang Wang

A dissertation presented to
The Graduate School
of Washington University in
partial fulfillment of the
requirements for the degree
of Doctor of Philosophy

May 2017
St. Louis, Missouri

Table of Contents

List of Figures

List of Tables

Acknowledgments

I would like to express my deepest and most sincere gratitude to Professor Pratim Biswas, my PhD advisor, for his wise guidance and continuous support of my scientific research. He introduced me to the marvelous world of aerosol science, and shared with me his excitement and knowledge of this field. I am sure that my entire life will benefit greatly from his guidance in both research and life.

I thank Professors Richard Axelbaum, Rajan Chakrabarty, Brent Williams, Michel Attoui, and Jingkun Jiang for serving on my dissertation committee, and providing valuable suggestions to improve this dissertation and my career plan. They are, and will always be, my career role models.

I also thank the colleagues in the Aerosol & Air Quality Research Laboratory for providing their help and assistance. We are a big family with a glorious history and bright future, and we are all working hard to make AAQRL "the world's best aerosol group". Especially, I want to thank Profs. Wei-Ning Wang and Yanjie Hu for their valuable help and guidance on my research; Dr. Jiaxi Fang for fruitful discussions, hands-on instrumentation, and programming; and Dr. He Jing, Dr. Yi Jiang, Jiayu, Zhichao, Girish, and Sukrant for their collaboration on our projects. I also want to thank Pai, Ted, and many other rotation/undergraduate/visiting students who helped me in conducting experiments. Many thanks also go to my friends and the staff in the EECE department and the engineering school. I thank Mr. Ballard from the Engineering Communication Center for helping me with my manuscript and dissertation editing.

I really appreciated and enjoyed the two-week visiting experience at the University of Helsinki in 2015. This couldn't have been possible without support from Profs. Pratim Biswas, Michel

Attoui, Markku Kulmala, and Tuukka Petäjä. Many thanks go to Drs. Juha Kangasluoma, Heikki Junninen, and Joonas Vanhanen, who introduced their “friends” (Herrmann DMA, APi-TOF, and PSM-bCPC) to me, and collaborated with me on many projects.

I want to thank the funding agency, the Solar Energy Research Institute for India and the United States (SERIIUS), and the Otis, Dorothy and Bryce Sproul Family Fellowship for supporting my study and research at Washington University.

Finally, I do want to express my special gratitude to my lovely wife and lab mate, Jiayu Li. Many thanks also go to my parents and parents-in-law, Hongbin Wang, Xiuxia Ma, Dacun Li, and Yuxia Sun for their tremendous support and encouragement for my PhD studies.

Yang Wang

Washington University in St. Louis

May 2017

Abstract of The Dissertation

Sub 2 nm Particle Characterization in Systems with Aerosol Formation and Growth

by

Yang Wang

Doctor of Philosophy in Energy, Environmental and Chemical Engineering

School of Engineering and Applied Science

Washington University in St. Louis, 2017

Professor Pratim Biswas, Chair

Aerosol science and technology enable continual advances in material synthesis and atmospheric pollutant control. Among these advances, one important frontier is characterizing the initial stages of particle formation by real time measurement of particles below 2 nm in size. Sub 2 nm particles play important roles by acting as seeds for particle growth, ultimately determining the final properties of the generated particles. Tailoring nanoparticle properties requires a thorough understanding and precise control of the particle formation processes, which in turn requires characterizing nanoparticle formation from the initial stages. The knowledge on particle formation in early stages can also be applied in quantum dot synthesis and material doping. This dissertation pursued two approaches in investigating incipient particle characterization in systems with aerosol formation and growth: (1) using a high-resolution differential mobility analyzer (DMA) to measure the size distributions of sub 2 nm particles generated from high-temperature aerosol reactors, and (2) analyzing the physical and chemical pathways of aerosol formation during combustion.

Part. 1. Particle size distributions reveal important information about particle formation dynamics. DMAs are widely utilized to measure particle size distributions. However, our knowledge of the initial stages of particle formation is incomplete, due to the Brownian broadening effects in conventional DMAs. The first part of this dissertation studied the applicability of high-resolution DMAs in characterizing sub 2 nm particles generated from high-temperature aerosol reactors, including a flame aerosol reactor (FLAR) and a furnace aerosol reactor (FUAR). Comparison against a conventional DMA (Nano DMA, Model 3085, TSI Inc.) demonstrated that the increased sheath flow rates and shortened residence time indeed greatly suppressed the diffusion broadening effect in a high-resolution DMA (half mini type). The incipient particle size distributions were discrete, suggesting the formation of stable clusters that may be intermediate phases between initial chemical reactions and downstream particle growth. The evolution of incipient cluster size distributions further provided information on the gaseous precursor reaction kinetics, which matched well with the data obtained through other techniques.

Part 2. The size distributions and their evolution measured by the DMAs help explain the physical pathways of aerosol formation. The chemical analysis of the incipient particles is an important counterpart to the existing characterization method. The chemical compositions of charged species were measured online with an atmospheric pressure interface time-of-flight mass spectrometer (APi-TOF). The tandem arrangement of the high-resolution DMA and the APi-TOF realized the simultaneous measurement of the mobility and the mass of combustion-generated natively charged particles, which enabled their chemical and physical formation pathways to be derived. The results showed that the initial stages of particle formation were strongly influenced by chemically ionized species during combustion, and that incipient particles composed of pure oxides did not exist. The effective densities of the incipient particles were much lower than those of bulk materials, due to their amorphous structures and different chemical compositions. Measuring incipient particles with high-resolution DMAs is limited because a DMA classifies charged particles only, while the charging characteristics of sub 2 nm particles are not well understood. The charge fraction of combustion-generated incipient particles was measured by coupling a charged particle remover and a condensation particle counter. A high charge fraction was observed, confirming the strong interaction among chemically ionized species and formed particles. The combustion system was modeled by using a unimodal aerosol dynamics model combined with Fuchs' charging theory, and showed that the charging process indeed affected particle formation dynamics during combustion.

<u>Chapter 1: Introduction</u>

The results of this chapter have been compiled in Wang, Y., Attoui, M., Biswas, P. (2017). Sub-2 nm Particle Measurement in High-temperature Aerosol Reactors: a Review. J. Aerosol Sci. In preparation.

1.1 Background and Motivation

The monumental agreement at the 21st Conference of the Parties (COP-21) in Paris demonstrates that all countries, regardless of their development status, are committed to deep cuts in greenhouse gas emissions. To accomplish this, there is a need to make rapid progress in developing new fossil fuel combustion technologies and in manufacturing advanced materials for sustainable energy utilization. Aerosol science and technology play a central role in both areas. The combustion of fossil fuels is accompanied with the generation of ultrafine particles, from both primary (Wang et al. 2013) and secondary sources (Guo et al. 2014). Through their existence in atmospheric and aquatic systems, these particles create negative effects on the environment and human health (Biswas and Wu 2005). Control of airborne particulate matter (PM) is becoming a critical issue in developing countries, and is a complicated task to manage since a large proportion of PM is composed of secondary aerosols formed from vapor precursor reactions and particle growth at nanometer scales. On the other hand, aerosols synthesized in the gas phase have received tremendous attention during the past few decades. Their particular mechanical, thermal, acoustic, electrical, and optical characteristics arise from their large specific surface area and from quantum effects. The annual production of functional nanoparticles, including silica, titania, and carbon black, is in the millions of tons, valued at over $15 billion/year (Li et al. 2016). They have been widely applied in areas including catalysis (Nie et al. 2016), solar energy utilization (Hu et al. 2016), paint production, sensor technology (Haddad et al. 2016), and the rubber industry. Other ambitious uses of nanoparticles are also being projected, including water treatment using functional carbon based nanoparticles (Jiang et al. 2015) and drug delivery using polymeric or metal nanoparticles (Karakoçak et al. 2016).

In order to control the aerosol emission from fossil fuel combustion and tailor the properties of synthesized aerosols, a thorough understanding of aerosol formation and growth dynamics is needed. Classical theories of aerosol dynamics predict that most nanoparticles develop in a "bottom-up" approach, starting with precursor reactions and moving sequentially through supersaturated vapor nucleation, vapor condensation, coagulation, and sintering, as shown in Figure 1.1. Among these processes, incipient particle formation and growth, especially in the size range near or below 2 nm, still remain mostly mysterious due to the limitations of instrumentation.

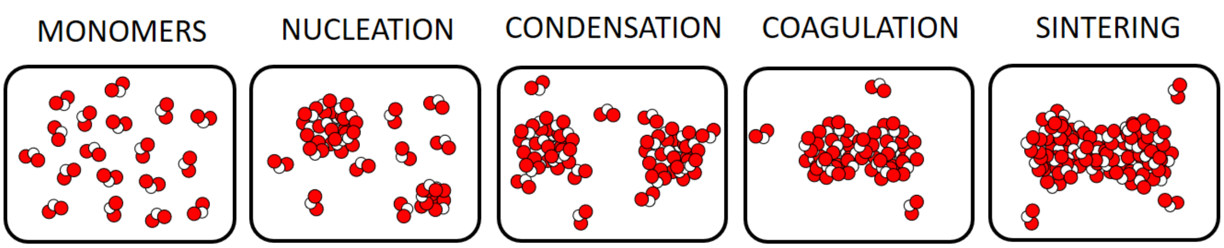

Figure 1.1 The "bottom-up" approach in aerosol formation and growth dynamics.

Conventional aerosol instruments start to face difficulties in characterizing particles as small as 2 nm (or in some other work, 3 nm). For example, the latest generation of condensation particle counters (e.g., Model 3776, TSI Inc.) cannot detect particles smaller than 2.5 nm, so the starting stages of particle formation, such as nucleation and condensation, cannot be observed. Although operating the condensation particle counters (CPCs) with different types of working fluid and operating conditions can slightly lower the detectable size limit, it is still strongly dependent on the chemical composition of the particles (Iida et al. 2009; Kangasluoma et al. 2014; Kuang et al. 2012). The high diffusivity of sub 2 nm particles also causes diffusion broadening of the instrument's transfer function, causing inaccurate the measurement (Jiang et al. 2011a;

Stolzenburg 1988; Wang et al. 2014). Furthermore, conventional aerosol measurement techniques heavily rely on aerosol charging, which is realized via the physical collision between ions and particles (Fuchs 1963; Hoppel and Frick 1986). But for sub 2 nm particles, their chemical properties, such as electron and proton affinities, start to play crucial roles during the charging process. Hence the process cannot be fully characterized by particle physics any more (Kangasluoma et al. 2016). These challenges directly lead to the design and manufacture of advanced aerosol instruments that will help us uncover the secrets of the initial stages of aerosol formation, in both the atmospheric environment and laboratory studies.

1.1.1 Instruments for measuring sub 2 nm particles

Aerosols can be characterized by many aspects, among which size, concentration, and chemical composition are most important. Various aerosol properties, such as visibility, toxicity, and reactivity, are derived from or closely related to these three properties. In order to characterize sub 2 nm particles, conventional aerosol instruments need to be modified and upgraded.

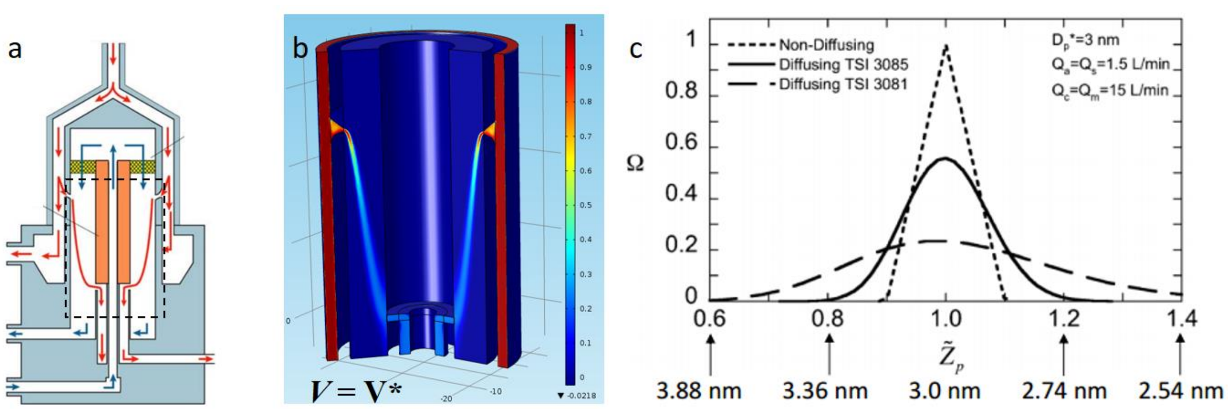

Figure 1.2 a) Schematic diagram of a TSI "Nano" DMA (Taken from the TSI SMPS Model 3080 manual); b) the trajectory of particles classified by the DMA; c) transfer functions of a DMA under the non-diffusing condition, a TSI "Nano" DMA, and a TSI "Long" DMA, when classifying 3 nm particles (Taken from Jiang et al. 2011a).

Differential mobility analyzers

Differential mobility analyzers (DMAs) are widely used for the online measurement of particle mobility sizes. They act as an electric filter, allowing only particles with certain electrical mobilities, i.e., mobility sizes, to pass through and be further monitored by particle counters (Figure 1.2). The mobility size of the classified particles is dependent on the voltage applied on the DMA, the DMA flow condition, and the DMA geometry. Theoretical analysis of flow and electric fields using stream functions shows that, when particle diffusion is neglected, the resolution of size classification (the ratio of the transfer function peak mobility to the full width at half maximum of the transfer function) equals the ratio of sheath flow rate to aerosol flow rate (Knutson and Whitby 1975). Accordingly, the idea of the "transfer function" was developed, which describes the probability of particles with an arbitrary mobility being classified at the voltage corresponding to a specific mobility (Figure 1.2c). The shape of the transfer function is triangular under the non-diffusing condition, whereas it becomes broadened when particles are diffusive. This broadening is due to particle Brownian motion, which cause them to deviate from the theoretical trajectories. The diffusion broadening of the DMA transfer function is a significant issue when we measure sub 2 nm particles, since the diffusion coefficient is inversely proportional to the square of particle diameter in the free molecular regime (Friedlander 2000). As shown in Figure 1.2c, when a "Long" DMA (Model 3081, TSI Inc.) and a "Nano" DMA (Model 3085, TSI Inc.) were used to classify 3 nm particles, the transfer functions become broadened in different degrees. Owing to the longer residence time of particles in the "Long" DMA, the transfer function is severely broadened, meaning that particles with sizes between 2.54 and 3.88 nm can all pass through the classification zone of the DMA.

There are two methods for reducing the broadening effect of DMA transfer functions. One remedy is to increase the sheath-to-aerosol flow ratio to inherently enhance the measurement resolution. The other is to reduce the residence time of particles in the DMA. Based on these concepts, much effort has been made to develop DMAs that are optimized for sub 2 nm particle measurement (Brunelli et al. 2009; de la Mora and Kozlowski 2013; Rosser and de la Mora 2005; Santos et al. 2009; Steiner et al. 2010). The Herrmann DMA (Herrmann et al. 2000) and half-mini DMA (de la Mora and Kozlowski 2013) are two representative designs of high-resolution DMAs. Both DMAs can accommodate sheath flow rates higher than 800 lpm without developing turbulent flow, and the length of the classification zone is significantly reduced in order to decrease the particle residence time. When calculating the mobility size of classified particles using conventional DMAs, one needs to know the sheath flow rate of the DMA, together with DMA geometry and voltage settings. This is highly problematic in high-resolution DMAs, whose extremely high sheath flow rate cannot be measured accurately. Hence, high-resolution DMAs are typically calibrated with ion standards of known mobilities, based on which the mobilities of other classified particles can be measured (Ude and de la Mora 2005).

Particle counters

Particle concentration is a critical parameter for evaluating the impact of aerosols. By coupling concentration measurement with size classification, the size distribution of aerosols is also obtained. Particle concentrations are normally measured with a condensation particle counter (CPC) or an electrometer. An aerosol electrometer measures the current created by the collection of charged aerosols on a metal filter. It is ideal for the measurement of sub 2 nm charged particles, since these particles normally carry one charge only, and the metal filter can reach almost 100% efficiency in collecting these charged particles. However, the usage of electrometers has two drawbacks. One disadvantage is that an electrometer measures charged particles only, while the charging of sub 2 nm particles is highly dependent on the chemical composition of the particles (Kangasluoma et al. 2016). Thus, the electrometer may capture only a glimpse of the entire aerosol ensemble, which may lead to considerably biased conclusions. The detection limit of an electrometer is another disadvantage. Presently, the lowest detection limit of an electrometer is in the range of fA (femtoampere, 10^{-15} A). For aerosols with a concentration of 1 #/cc, in order to create a response above this detection limit, the flow rate of aerosol going through the electrometer should be at least 600 lpm, but current designs of electrometers cannot handle such a high flow rate (the maximum flow rate is 10 lpm for the TSI Electrometer, Model 3068B). CPCs, on the other hand, have a very low detection limit (down to 0.1 #/cc) and measure particle concentration regardless of the charging state. A CPC grows a sampled particle, by condensing the vapor of a working fluid on the surface of the particle, until it has an optically detectable size (~ 1 μm) (Stolzenburg 1988). The smallest particle that can be condensationally grown (or activated) is determined by the Kelvin equation, which considers the effect of the saturation ratio, surface tension, temperature, and molecular volume of the working fluid (Friedlander 2000). The Kelvin equation dictates that the commonly used butanol-based CPCs have a smallest detectable size of 2.5 nm. Although changing the CPC's working condition could further lower the detectable size, the improvement is not significant (Kuang et al. 2012). A detailed calculation using the Kelvin equation and the data of more than 800 organic compounds suggests that diethylene glycol (DEG) is the best candidate working fluid for activating the condensational growth of sub 2 nm particles (Iida et al. 2012). However, because the condensational growth rate is another complex function of the above parameters, the grown particles are not large enough to be detected by the optical components in the CPC directly.

Hence, a two-stage CPC was developed, where the first stage uses DEG to grow particles to a moderate size, and the second stage uses butanol to measure the concentration of the grown particles (Figure 1.3) (Jiang et al. 2011b). This design directly led to the manufacture of the two newest types of CPC first stages, the particle size magnifier (PSM, Model A11 CNC-system, Airmodus Oy) and the Nano Enhancer (Model 3777, TSI Inc.). Although the activation of sub 2 nm particles is still strongly dependent on the chemical composition of the sampled particles (Kangasluoma et al. 2014), a careful calibration of the system with the tested particle composition can effectively extend the detectable size to 1 nm. These modifications greatly facilitate the observation of particle formation and growth in the initial stages.

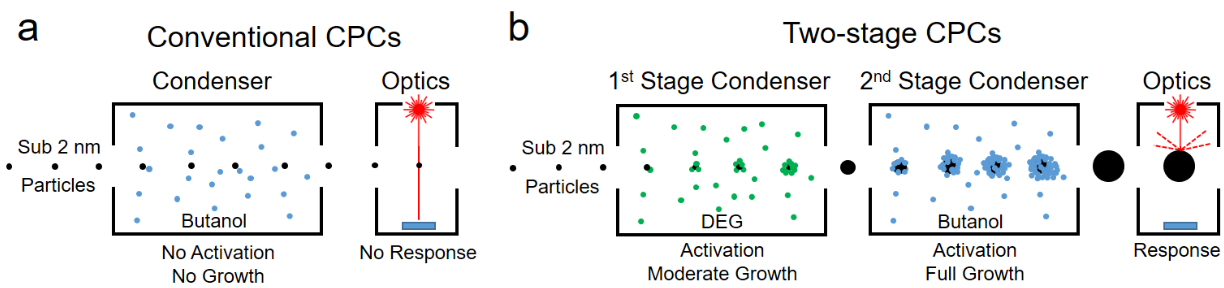

Figure 1.3 The working principles of a single stage and a two-stage CPC.

Mass spectrometers

In order to comprehensively evaluate the impact of aerosols, their chemical properties need to be characterized. The aerosol mass spectrometer (AMS, Aerodyne Inc.) is well established for measuring the chemical compositions of aerosols with sizes above 40 nm. However, to resolve the participating compounds during particle formation in the initial stages, the chemical composition measurements of atmospheric ions/clusters must be improved. The newly developed Atmospheric Pressure Interface Time-of-Flight Mass Spectrometer (APi-TOF, Tofwerk AG) can detect and measure ambient ions in the mass/charge range up to 2000 Th (Junninen et al. 2010). It has a mass accuracy higher than 0.002% and a mass resolving power of 3000 Th/Th. The Api-TOF provides a nearly universal interface for atmospheric pressure sampling, and this key feature is widely utilized in laboratory and field studies of sub 2 nm particle formation.

1.1.2 Measuring sub 2 nm particles generated from aerosol reactors

The combination of the three mentioned enhanced particle detectors (high resolution DMA coupled with an electrometer, PSM-bCPC, and APi-TOF) has served as a powerful tool in understanding atmospheric particle formation below 2 nm and the role of ions in atmospheric nucleation (Almeida et al. 2013; Ehn et al. 2014; Kirkby et al. 2011; Kulmala et al. 2013; Schobesberger et al. 2013). The usage of these instruments in atmospheric studies was reviewed by Zhang et al. (2011). On the other hand, few studies have reported the measurement of sub 2 nm particles with these instruments in aerosol reactors. Because aerosol reactors generate particles through intense chemical reactions, the mechanism of particle formation and the resulting observations are largely different from atmospheric studies. Existing measurements of sub 2 nm particles generated from aerosol reactors are briefly reviewed as follows.

Flame aerosol reactor

Combustion is a major source of PM formation. The precise control of aerosol formation during combustion crucially affects both the applications of flame-generated particles and their environmental implications. However, a detailed understanding of the particle dynamics in flames is lacking due to the fast reaction rate of combustion, making it difficult to control particle formation and growth processes. Up until now, most of progress in measuring sub 2 nm particles from flame aerosol reactors has been made in the study of soot particles. Hence, the major focus of this dissertation was the characterization of flame-generated incipient particles during the combustion synthesis of functional nanomaterials (Fang et al. 2014; Wang et al. 2014; Wang et al. 2015; Wang et al. 2016; Wang et al. 2017a; 2017b). Soot formation is an important branch of combustion study, since these particles are a major byproduct of fossil fuel combustion and have great environmental and energy impacts. In order to clarify the mechanism of soot formation from the gas to particle phase, many studies have reported the measurement of ultrafine (d_p < 100 nm) particle size distributions using DMAs (Camacho et al. 2013; Zhao et al. 2003). The first measurements of sub 2 nm soot particles were conducted by Sgro et al. (2007, 2009, 2010, and 2011) through a series of experiments using high-resolution DMAs to unveil the charging characteristics of nascent soot particles. Incipient particle size distributions (>1 nm) were measured under a series of equivalence ratios, and showed that the first particles observed in flames have a size of 2 nm, consistent with previous measurements using other techniques. The charge distribution of the nascent soot particles was very close to the Boltzmann charge distribution due to the high temperature in flames (Sgro et al. 2010; Sgro et al. 2011). Recent measurements of nascent soot in flames using a half-mini DMA shed light on the challenges and potential artifacts affecting studies on soot inception by DMA techniques (Carbone et al. 2016). The sampling of the nascent soot particles was shown to be challenging, since the quenching of chemical reactions and particle dynamics was very difficult for sub 2 nm particles. With an appropriate sampling system, the high-resolution DMA-measured particle size distributions matched well with those obtained by atomic force microscopy of thermophoretically sampled soot particles (Carbone et al. 2017a; b).

Furnace aerosol reactor

Furnace aerosol reactors (FUARs) are widely used in the synthesis of functional nanomaterials, because the controllable furnace temperatures help create tunable environments for particle formation and growth (Messing et al. 1993). The relatively lower reaction rates compared to those in flame aerosol reactors also assist in analyzing the particle formation and growth mechanisms (Cho and Biswas 2006; Cho et al. 2011). Particles generated from FUARs played important roles in the 1990s, when researchers attempted to measure the charge distributions of sub-micrometer particles (Wiedensohler 1988; Wiedensohler and Fissan 1991). FUARs can generate sub 2 nm particles by heating a material (such as a metal and a salt) while rapidly quenching the particle growth by introducing clean diluting gas at high flow rates. Recent measurements of these sub 2 nm particles with the enhanced particle detectors showed that most of these particles were clustered with unidentified organic molecules (Kangasluoma et al. 2013). Therefore, there is still room for improving the purity of furnace generated incipient particles.

Glowing wire generator

The glowing wire generator (GWG), where material is evaporated from the surface of a heated wire and subsequently quenched by a gas stream, was introduced by Schmidt-Ott et al. (1980) and has been applied for the production of metallic particles for research since then (Nasibulin et al. 2005; Peineke et al. 2006; Peineke and Schmidt-Ott 2008). The generated particles are typically in the range of a few angstroms to a few nanometers, where unexpected behaviors of the nanoparticles may be found (Peineke et al. 2009). The invention of instruments for measuring sub 2 nm particles made it feasible to accurately measure the size and concentration of these particles (Peineke et al. 2009). Clusters with characteristic mobility sizes were observed, and the mechanisms of metal evaporation and ion attachment were further elucidated (Maisser et al. 2015; Peineke et al. 2009).

The study of the GWGs, in return, directly accelerated the development of instruments for detecting incipient particles. The GWG is a convenient source of sub 2 nm particles, since it produces self-charged particles with a single charge (most particles are attached with OH^-) and repeatable mass spectrums (Kangasluoma et al. 2013). Sub 2 nm particles generated from GWGs have been used to calibrate the transfer function and transmission efficiencies of high-resolution DMAs and characterize the detection efficiency of sub 2 nm particles when using two-stage CPCs under various conditions (Kangasluoma et al. 2015; Kangasluoma et al. 2013; Kangasluoma et al. 2014).

1.2 Dissertation Outline

This dissertation has two main objectives:

1) To evaluate the performance of high-resolution DMAs in measuring the incipient particles generated from flame and furnace aerosol reactors

2) To investigate the detailed formation pathways of nascent particles during combustion synthesis of functional nanomaterials

The two objectives are studied and described in the five chapters of the dissertation. Each chapter is self-contained, with an introduction, experimental section, results, discussion, and conclusions. Chapters 2 and 3 describe systematic studies using high-resolution DMAs in a flame and a furnace aerosol reactor, respectively. These studies characterized the performance of high-resolution DMAs, and offered new methods for data analysis using the incipient particle size distributions. With the assistance of mass spectrometry and enhanced particle counters, the particle formation and growth pathways in a flame aerosol reactor were examined based on the existing measurement of incipient particle size distributions. This work shows the importance of chemical ionization in the initial stages of particle formation during combustion, and is developed further in Chapters 4 and 5. In addition, Chapter 6 numerically investigates the influence of charging on particle coagulation at different temperatures, aiming to obtain a comprehensive picture of particle formation and growth in flames.

1.3 References

Almeida, J., Schobesberger, S., Kürten, A., Ortega, I. K., Kupiainen-Määttä, O., Praplan, A. P., Adamov, A., Amorim, A., Bianchi, F., Breitenlechner, M. (2013). Molecular understanding of sulphuric acid-amine particle nucleation in the atmosphere. Nature 502:359-363.

Biswas, P. and Wu, C.-Y. (2005). Nanoparticles and the environment. J. Air Waste Manag. Assoc. 55:708-746.

Brunelli, N., Flagan, R., Giapis, K. (2009). Radial differential mobility analyzer for one nanometer particle classification. Aerosol Sci. Technol. 43:53-59.

Camacho, J., Lieb, S., Wang, H. (2013). Evolution of size distribution of nascent soot in n-and i-butanol flames. Proc. Combust. Inst. 34:1853-1860.

Carbone, F., Attoui, M., Gomez, A. (2016). Challenges of measuring nascent soot in flames as evidenced by high-resolution differential mobility analysis. Aerosol Sci. Technol. 50:740-757.

Carbone, F., Moslih, S., Gomez, A. (2017a). Probing Gas-to-Particle Transition in a Moderately Sooting Atmospheric Pressure Ethylene/Air Laminar Premixed Flame. Part I: Gas Phase and Soot Ensemble Characterization. Combust. Flame just accepted.

Carbone, F., Moslih, S., Gomez, A. (2017b). Probing Gas-to-Particle Transition in a Moderately Sooting Atmospheric Pressure Ethylene/Air Laminar Premixed Flame. Part II: Molecular clusters and nascent soot particle size distributions. Combust. Flame just accepted.

Cho, K. and Biswas, P. (2006). Sintering rates for pristine and doped titanium dioxide determined using a tandem differential mobility analyzer system. Aerosol Sci. Technol. 40:309-319.

Cho, K., Chung, K.-S., Biswas, P. (2011). Coagulation coefficient of agglomerates with different fractal dimensions. Aerosol Sci. Technol 45:740-743.

de la Mora, J. F. and Kozlowski, J. (2013). Hand-held differential mobility analyzers of high resolution for 1-30nm particles: Design and fabrication considerations. J. Aerosol Sci. 57:45-53.

Ehn, M., Thornton, J. A., Kleist, E., Sipilä, M., Junninen, H., Pullinen, I., Springer, M., Rubach, F., Tillmann, R., Lee, B. (2014). A large source of low-volatility secondary organic aerosol. Nature 506:476-479.

Fang, J., Wang, Y., Attoui, M., Chadha, T. S., Ray, J. R., Wang, W.-N., Jun, Y.-S., Biswas, P. (2014). Measurement of sub-2 nm clusters of pristine and composite metal oxides during nanomaterial synthesis in flame aerosol reactors. Anal. Chem. 86:7523-7529.

Friedlander, S. K. (2000). Smoke, dust, and haze: fundamentals of aerosol behavior. Oxford University Press New York, USA.

Fuchs, N. (1963). On the stationary charge distribution on aerosol particles in a bipolar ionic atmosphere. Geofisica pura e applicata 56:185-193.

Guo, S., Hu, M., Zamora, M. L., Peng, J., Shang, D., Zheng, J., Du, Z., Wu, Z., Shao, M., Zeng, L. (2014). Elucidating severe urban haze formation in China. PNAS 111:17373-17378.

Haddad, K., Abokifa, A., Kavadiya, S., Chadha, T., Shetty, P., Wang, Y., Fortner, J., Biswas, P. (2016). Growth of single crystal, oriented SnO 2 nanocolumn arrays by aerosol chemical vapour deposition. CrystEngComm 18:7544-7553.

Herrmann, W., Eichler, T., Bernardo, N., Fernández de la Mora, J. (2000). Turbulent transition arises at reynolds number 35,000 in a short vienna type DMA with a large laminarization inlet, in Abstract AAAR Conference, 15B5.

Hoppel, W. A. and Frick, G. M. (1986). Ion-aerosol attachment coefficients and the steady-state charge distribution on aerosols in a bipolar ion environment. Aerosol Sci. Technol. 5:1-21.

Hu, Y., Jiang, H., Li, Y., Wang, B., Zhang, L., Li, C., Wang, Y., Cohen, T., Jiang, Y., Biswas, P. (2016). Engineering the outermost layers of TiO2 nanoparticles using in situ Mg doping in a flame aerosol reactor. AIChE J.

Iida, K., Stolzenburg, M. R., McMurry, P. H. (2009). Effect of working fluid on sub-2 nm particle detection with a laminar flow ultrafine condensation particle counter. Aerosol Sci. Technol. 43:81-96.

Jiang, J., Attoui, M., Heim, M., Brunelli, N. A., McMurry, P. H., Kasper, G., Flagan, R. C., Giapis, K., Mouret, G. (2011a). Transfer functions and penetrations of five differential mobility analyzers for sub-2 nm particle classification. Aerosol Sci. Technol. 45:480-492.

Jiang, J., Zhao, J., Chen, M., Eisele, F. L., Scheckman, J., Williams, B. J., Kuang, C., McMurry, P. H. (2011b). First measurements of neutral atmospheric cluster and 1–2 nm particle number size distributions during nucleation events. Aerosol Science and Technology 45:ii-v.

Jiang, Y., Wang, W.-N., Liu, D., Nie, Y., Li, W., Wu, J., Zhang, F., Biswas, P., Fortner, J. D. (2015). Engineered crumpled graphene oxide nanocomposite membrane assemblies for advanced water treatment processes. Environ. Sci. Technol. 49:6846-6854.

Junninen, H., Ehn, M., Petäjä, T., Luosujärvi, L., Kotiaho, T., Kostiainen, R., Rohner, U., Gonin, M., Fuhrer, K., Kulmala, M. (2010). A high-resolution mass spectrometer to measure atmospheric ion composition. Atmos. Meas. Tech. 3:1039-1053.

Kangasluoma, J., Attoui, M., Junninen, H., Lehtipalo, K., Samodurov, A., Korhonen, F., Sarnela, N., Schmidt-Ott, A., Worsnop, D., Kulmala, M. (2015). Sizing of neutral sub 3nm tungsten oxide clusters using Airmodus Particle Size Magnifier. J. Aerosol Sci. 87:53-62.

Kangasluoma, J., Junninen, H., Lehtipalo, K., Mikkilä, J., Vanhanen, J., Attoui, M., Sipilä, M., Worsnop, D., Kulmala, M., Petäjä, T. (2013). Remarks on ion generation for CPC detection efficiency studies in sub-3-nm size range. Aerosol Sci. Technol. 47:556-563.

Kangasluoma, J., Kuang, C., Wimmer, D., Rissanen, M. P., Lehtipalo, K., Ehn, M., Worsnop, D. R., Wang, J., Kulmala, M., Petäjä, T. (2014). Sub-3 nm particle size and composition dependent response of a nano-CPC battery. Atmos. Meas. Tech. 7:689-700.

Kangasluoma, J., Samodurov, A., Attoui, M., Franchin, A., Junninen, H., Korhonen, F., Kurtén, T., Vehkamäki, H., Sipilä, M., Lehtipalo, K. (2016). Heterogeneous Nucleation onto Ions and Neutralized Ions: Insights into Sign-Preference. J. Phys. Chem. C 120:7444-7450.

Karakoçak, B. B., Raliya, R., Davis, J. T., Chavalmane, S., Wang, W.-N., Ravi, N., Biswas, P. (2016). Biocompatibility of gold nanoparticles in retinal pigment epithelial cell line. Toxicol. In Vitro 37:61-69.

Kirkby, J., Curtius, J., Almeida, J., Dunne, E., Duplissy, J., Ehrhart, S., Franchin, A., Gagné, S., Ickes, L., Kürten, A. (2011). Role of sulphuric acid, ammonia and galactic cosmic rays in atmospheric aerosol nucleation. Nature 476:429-433.

Knutson, E. O. and Whitby, K. T. (1975). Aerosol classification by electric mobility: apparatus, theory, and applications. J. Aerosol Sci. 6:443-451.

Kuang, C., Chen, M., McMurry, P. H., Wang, J. (2012). Modification of laminar flow ultrafine condensation particle counters for the enhanced detection of 1 nm condensation nuclei. Aerosol Sci. Technol. 46:309-315.

Kulmala, M., Kontkanen, J., Junninen, H., Lehtipalo, K., Manninen, H. E., Nieminen, T., Petäjä, T., Sipilä, M., Schobesberger, S., Rantala, P. (2013). Direct observations of atmospheric aerosol nucleation. Science 339:943-946.

Li, S., Ren, Y., Biswas, P., Stephen, D. T. (2016). Flame aerosol synthesis of nanostructured materials and functional devices: Processing, modeling, and diagnostics. Prog. Energy Combust. Sci. 55:1-59.

Maisser, A., Barmpounis, K., Attoui, M., Biskos, G., Schmidt-Ott, A. (2015). Atomic Cluster Generation with an Atmospheric Pressure Spark Discharge Generator. Aerosol Sci. Technol. 49:886-894.

Messing, G. L., Zhang, S. C., Jayanthi, G. V. (1993). Ceramic powder synthesis by spray pyrolysis. J. Am. Ceram. Soc. 76:2707-2726.

Nasibulin, A. G., Moisala, A., Brown, D. P., Jiang, H., Kauppinen, E. I. (2005). A novel aerosol method for single walled carbon nanotube synthesis. Chem. Phys. Lett. 402:227-232.

Nie, Y., Wang, W.-N., Jiang, Y., Fortner, J., Biswas, P. (2016). Crumpled reduced graphene oxide–amine–titanium dioxide nanocomposites for simultaneous carbon dioxide adsorption and photoreduction. Catal. Sci. Technol. 6:6187-6196.

Peineke, C., Attoui, M., Robles, R., Reber, A., Khanna, S., Schmidt-Ott, A. (2009). Production of equal sized atomic clusters by a hot wire. J. Aerosol Sci. 40:423-430.

Peineke, C., Attoui, M., Schmidt-Ott, A. (2006). Using a glowing wire generator for production of charged, uniformly sized nanoparticles at high concentrations. J. Aerosol Sci. 37:1651-1661.

Peineke, C. and Schmidt-Ott, A. (2008). Explanation of charged nanoparticle production from hot surfaces. J. Aerosol Sci. 39:244-252.

Rosser, S. and de la Mora, J. F. (2005). Vienna-type DMA of high resolution and high flow rate. Aerosol Sci. Technol 39:1191-1200.

Santos, J., Hontanón, E., Ramiro, E., Alonso, M. (2009). Performance evaluation of a high-resolution parallel-plate differential mobility analyzer. Atmos. Chem. Phys 9:2419-2429.

Schmidt-Ott, A., Schurtenberger, P., Siegmann, H. (1980). Enormous yield of photoelectrons from small particles. Phy. Rev. Lett. 45:1284.

Schobesberger, S., Junninen, H., Bianchi, F., Lönn, G., Ehn, M., Lehtipalo, K., Dommen, J., Ehrhart, S., Ortega, I. K., Franchin, A. (2013). Molecular understanding of atmospheric particle formation from sulfuric acid and large oxidized organic molecules. PNAS 110:17223-17228.

Sgro, L., Barone, A., Commodo, M., D'Alessio, A., De Filippo, A., Lanzuolo, G., Minutolo, P. (2009). Measurement of nanoparticles of organic carbon in non-sooting flame conditions. Proc. Combust. Inst. 32:689-696.

Sgro, L. A., D'Anna, A., Minutolo, P. (2010). Charge distribution of incipient flame-generated particles. Aerosol Sci. Technol. 44:651-662.

Sgro, L. A., D'Anna, A., Minutolo, P. (2011). Charge fraction distribution of nucleation mode particles: New insight on the particle formation mechanism. Combust. Flame 158:1418-1425.

Sgro, L. A., De Filippo, A., Lanzuolo, G., D'Alessio, A. (2007). Characterization of nanoparticles of organic carbon (NOC) produced in rich premixed flames by differential mobility analysis. Proc. Combust. Inst. 31:631-638.

Steiner, G., Attoui, M., Wimmer, D., Reischl, G. (2010). A medium flow, high-resolution Vienna DMA running in recirculating mode. Aerosol Sci. Technol. 44:308-315.

Stolzenburg, M. R. (1988). An ultrafine aerosol size distribution measuring system. na.

Ude, S. and de la Mora, J. F. (2005). Molecular monodisperse mobility and mass standards from electrosprays of tetra-alkyl ammonium halides. J. Aerosol Sci. 36:1224-1237.

Wang, X., Williams, B., Wang, X., Tang, Y., Huang, Y., Kong, L., Yang, X., Biswas, P. (2013). Characterization of organic aerosol produced during pulverized coal combustion in a drop tube furnace. Atmos. Chem. Phys 13:10919-10932.

Wang, Y., Fang, J., Attoui, M., Chadha, T. S., Wang, W.-N., Biswas, P. (2014). Application of Half Mini DMA for sub 2 nm particle size distribution measurement in an electrospray and a flame aerosol reactor. J. Aerosol Sci. 71:52-64.

Wang, Y., Kangasluoma, J., Attoui, M., Fang, J., Junninen, H., Kulmala, M., Petäjä, T., Biswas, P. (2017a). Observation of incipient particle formation during flame synthesis by tandem differential mobility analysis-mass spectrometry (DMA-MS). Proc. Combust. Inst. 36: 745-752.

Wang, Y., Kangasluoma, J., Attoui, M., Fang, J., Junninen, H., Kulmala, M., Petäjä, T., Biswas, P. (2017b). The high charge fraction of flame-generated particles in the size range below 3 nm measured by enhanced particle detectors. Combust. Flame 176:72-80.

Wang, Y., Liu, P., Fang, J., Wang, W.-N., Biswas, P. (2015). Kinetics of sub-2 nm TiO2 particle formation in an aerosol reactor during thermal decomposition of titanium tetraisopropoxide. J. Nanopart. Res. 17:1-13.

Wang, Y., Sharma, G., Koh, C., Kumar, V., Chakrabarty, R. K., Biswas, P. (2016). Influence of flame-generated ions on the simultaneous charging and coagulation of nanoparticles during combustion. Aerosol Sci. Technol. *Under review*.

Wiedensohler, A. (1988). An approximation of the bipolar charge distribution for particles in the submicron size range. J. Aerosol Sci. 19:387-389.

Wiedensohler, A. and Fissan, H. (1991). Bipolar charge distributions of aerosol particles in high-purity argon and nitrogen. Aerosol Sci. Technol. 14:358-364.

Zhang, R., Khalizov, A., Wang, L., Hu, M., Xu, W. (2011). Nucleation and growth of nanoparticles in the atmosphere. Chem. Rev. 112:1957-2011.

Zhao, B., Yang, Z., Wang, J., Johnston, M. V., Wang, H. (2003). Analysis of soot nanoparticles in a laminar premixed ethylene flame by scanning mobility particle sizer. Aerosol Sci. Technol. 37:611-620.

Chapter 2: Application of Half Mini DMA for sub 2 nm Particle Size Distribution Measurement in an Electrospray and a Flame Aerosol Reactor

The results of this chapter have been published in Wang, Y., Fang, J., Attoui, M., Chadha, T. S., Wang, W.-N., Biswas, P. (2014). Application of Half Mini DMA for sub 2 nm particle size distribution measurement in an electrospray and a flame aerosol reactor. J. Aerosol Sci. 71:52-64.

Abstract

Conventional Differential Mobility Analyzers (DMA) have had limited success in classifying sub 2 nm particles with high resolution, primarily due to diffusion broadening. High flow DMAs have been able to overcome this limitation and achieve high-resolution classification of sub 2 nm particles, by maintaining laminar flow at high Reynolds numbers. A Half Mini DMA was compared with a Nano DMA (TSI model 3085) for sub 2 nm size distribution measurements of organic ions generated by electrospray of tetra-heptyl ammonium bromide (THAB) solution and aerosols generated by a premixed flat flame reactor. Obscurities in ion peak measurements with the Nano DMA indicated a higher diffusion effect. Calculations of the diffusing transfer functions indicated that the Half Mini DMA deviated significantly from ideal conditions, possibly due to the higher demands for a more precise electrode placement and a smaller surface roughness, since it is operated at a high sheath flow rate.

The Half Mini DMA was then applied to study the formation of flame-generated aerosols in the sub 2 nm range. This is the first reported measurement of these clusters in an aerosol reactor. The effects of the flame synthesis precursor (titanium (IV) isopropoxide), the Kr-85 radioactive neutralizer, and the tubing materials on the flame aerosol size distribution measurements were investigated. After the introduction of titanium (IV) isopropoxide, several discrete peaks were detected, suggesting discrete cluster formation during the initial stages of TiO_2 particle synthesis. The addition of a radioactive neutralizer balanced the size distribution of flame aerosols by changing the charging mechanisms. Compared with copper tubing, silicone conductive tubing generated extremely high positive ion contamination after neutralization.

2.1 Introduction

Particle nucleation and growth below 2 nm has significant implications for many practical applications, such as nanomaterial synthesis and atmospheric pollutant control. Size distribution measurements are a common method of characterizing particle formation and can provide fundamental information on primary particle distribution. In addition, the size distribution can be further analyzed to establish particle formation mechanisms. Differential Mobility Analyzers (DMA) are widely used for real-time aerosol size distribution measurements. A DMA classifies the particles as a function of electrical mobility, from which the particle size can be obtained. By connecting a DMA to a particle counting device, the particle concentration can also be obtained. The final size distribution function is determined using a standardized data inversion method, by taking the neutralizer charging efficiency, DMA transfer function, and particle counter detection efficiency into consideration (Stolzenburg & McMurry, 2008).

As particle size decreases below 10 nm, the effect of Brownian diffusion becomes significant and compromises the accuracy of DMAs (Stolzenburg, 1988). Efforts have been made through redesigned DMAs to address the issues of Brownian broadening of the transfer functions. Different structures of DMAs for the classification of nanometer-sized aerosols were reviewed by Intra and Tippayawong (2008). Among these, the Nano DMA was designed with a shortened aerosol transport passage and optimized based on experimental and numerical results (Chen *et al.* 1996, 1998). Significant improvements were observed when compared with previous DMA designs.

Since then, the field of aerosol research has seen a push in studying particle formation mechanisms below 2 nm, an important size range for atmospheric nucleation, vapor deposition, and ion interactions. These smaller particle sizes bring new challenges to existing designs of DMAs since diffusion cannot be further suppressed by simply increasing the sheath flow rates. Current DMA designs may demonstrate flow instability inside the instrument at higher sheath flow rates (Seto *et al.* 1997; Aalto *et al.* 2001). Recently, de la Mora and Kozlowski (2013) developed a high flow DMA (Half Mini DMA, Nanoengineering Corp.) able to achieve transonic sheath flow rates. Laminar flow is maintained at these high sheath flow rates (100~700 lpm) by incorporating flow straighteners upstream of the classification zone, along with a diffuser downstream (Kulkarni *et al.* 2011). The design possesses two major advantages. First, the residence time for ultrafine particles in the instrument is decreased by orders of magnitude, resulting in a substantial suppression of diffusion losses. Second, because the theoretical resolution of DMAs can be represented as the ratio of the sheath flow rate over the aerosol flow rate (Knutson & Whitby, 1975), increasing the sheath flow rate can also considerably enhance the resolution for measurement of nanosized particles despite Brownian broadening. Many groups have already taken advantages of high flow DMAs to study various systems: the gas phase protein ion density determination (Maißer *et al.* 2011), the generation of 1-3.5 nm monomobile particle size standards (Attoui *et al.* 2013), the ion composition determination in a corona charger (Manninen *et al.* 2011) and a radioactive charger (Steiner *et al.* 2013), and the observation of heterogeneous nucleation (Winkler *et al.* 2008). However, until now, high flow DMAs have not been used for measurements in aerosol reactors.

The accurate mobility measurement of sub 2 nm particles with a high flow DMA depends on mobility standards for calibration (Ude & de la Mora, 2005). In a cylindrical DMA, the product of the DMA voltage (V) and classified particle electrical mobility (Z) is a constant, if flow rates are kept the same. Once the DMA voltage corresponding to the mobility standard is known, the electrical mobility of particles classified under other DMA voltages can be calculated. Currently, the electrospray of large organic ions, such as tetra-methyl ammonium, tetra-propyl ammonium, and tetra-heptyl ammonium ions, is a commonly used method to generate mobility standards with large concentrations. In addition, these ions are insensitive to fluctuations in humidity and can be further applied to calibrate and determine the transfer function of DMAs (Jiang *et al.* 2011; Ude & de la Mora, 2005).

Flame aerosol reactors (FLAR) are important methods for synthesizing nanoparticles with high production rates and scale up capabilities. Functional materials, including metal oxides (Thimsen *et al.* 2008; Zhang *et al.* 2012), fullerenes (Goel *et al.* 2002), nanotubes (Height *et al.* 2004), and nanowires (Rao & Zheng, 2009), have been produced with this method. Aerosols are formed primarily through nucleation, condensation, coagulation, and aggregation, and have high concentrations below 6 nm (Thimsen, 2009). Numerous studies have been conducted on combustion chemistry at the molecular level (Qin *et al.* 2000; Law *et al.* 2003) and particle growth in the size range above 2 nm (Thimsen & Biswas, 2007; Tiwari *et al.* 2008). However, particle formation and growth in the size range between the molecular level (~0.1 nm) and 2 nm, have not been studied in flame aerosol reactors due to limitations in instrumentation (Jiang *et al.* 2007a; Kasper *et al.* 1997; Zhao *et al.* 2003; McMurry *et al.* 2011). The *in situ* high flow DMA characterization of the aerosols generated from a flame reactor can provide detailed information bridging the knowledge gap between combustion chemistry and particle synthesis.

In order to classify sub 2 nm aerosols based on electrical mobility, the particle charge distribution must be known before they enter the DMA. Radioactive neutralization is the most common method for charge conditioning of aerosols. A steady state charge distribution is obtained through the collision of free ions with sample aerosols (Fuchs, 1963; Mohnen, 1977;

Reischl *et al.* 1996). However, for ultrafine size distribution measurements, the presence of free ions may interfere, potentially causing errors in data inversion (Sgro *et al.* 2010; Manninen, *et al.* 2011; McMurry, *et al.* 2011). The transport of aerosols through various tubing materials can also generate particle contaminants influencing size distribution measurements. While previous studies were focused on pure ion mobility characterization of these contaminants (Steiner & Reischl, 2012), the interaction between ion contaminants and sample aerosols has not been thoroughly investigated. Research is needed to find the best operation condition to avoid contamination in sub 2 nm particle measurements.

With diverse DMA designs available for the measurement of ultrafine particle size distributions, a comparison of these designs would allow researchers to properly select the appropriate instrument. In particular, the Half Mini DMA and Nano DMA have not been evaluated for size distribution measurements below 2 nm. By comparing such results, we can assess how increasing the sheath flow rates can significantly suppress the effects of diffusion. In this study, the accuracies of a Half Mini DMA and a Nano DMA were compared for aerosols generated by electrospraying tetra-heptyl ammonium bromide (THAB) and from a premixed methane-air flat flame reactor, focusing on sub 2 nm particles. In addition, size distribution measurements during nanoparticle flame synthesis were conducted with a Half Mini DMA. In order to shed light on the charging mechanisms in the flame qualitatively, size distributions were measured with and without neutralizers. The dependence of ion contamination on the tubing material was demonstrated. Issues in data inversion for sub 2 nm particle measurements were also discussed.

2.2 Methods

The experimental setup for particle generation and measurement (Figure 2.1), methods for data inversion, and the experimental plan are described as follows.

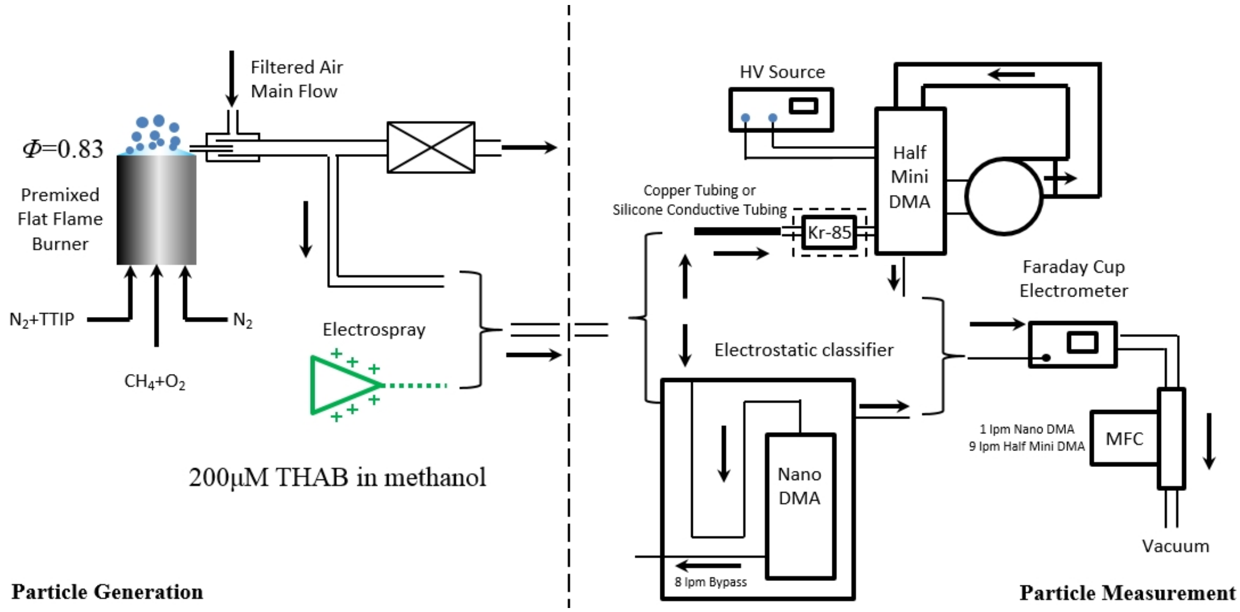

Figure 2.1 Schematic diagram of the experimental setup. During the comparison of the Half Mini DMA and Nano DMA, the Kr-85 neutralizer was not used.

2.2.1 Experimental setup

THAB (99%, Sigma Aldrich) ions were generated by electrospray for the calibration and comparison of the two DMAs. An electrospray source designed by Ude and de la Mora (2005) was used. A 200 μM electrospray solution was prepared by diluting THAB into methanol (99.9%, Sigma Aldrich). Ion peaks detected from the electrospray source are displayed in Figure 2.2a; and they matched well with existing studies (Ude & de la Mora, 2005; Jiang *et al.* 2011).

Ions generated from a methane-air premixed flat flame reactor were also measured. The burner body was a 2.54 cm (O.D.) stainless tubing containing 3.18mm stainless steel beads on a mesh support, and capped by a stainless steel honeycomb mesh. A more detailed description of the system can be found elsewhere (Thimsen, 2009; Fang *et al.* 2014). Fuel and air flow rates were maintained by mass flow controllers (MKS Inc.) at 0.81 lpm of CH_4, 1.95 lpm of O_2 and 6.60 lpm of N_2. During TiO_2 synthesis, a bypass N_2 flow of 0.66 lpm was first introduced into a bubbler containing a titanium (IV) isopropoxide precursor (TTIP, Sigma-Aldrich, 97%) and then mixed with the main flow. This arrangement produced a molar feed rate of 0.22 mmol/h of TTIP, which was determined by the saturation vapor pressure (Siefering & Griffin, 1990).

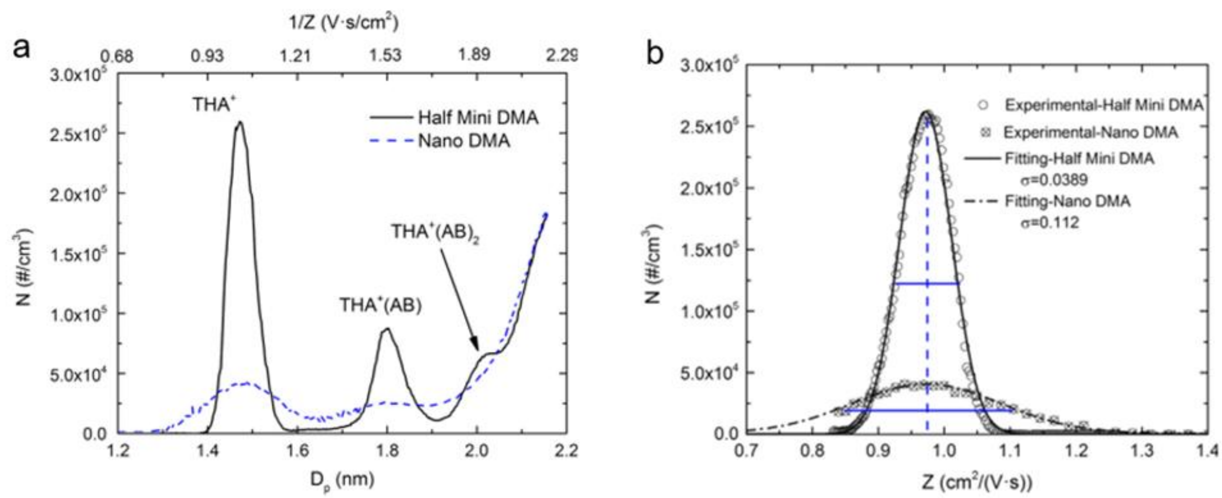

Figure 2.2 (a) Size distributions of the THAB ions measured by the Half Mini DMA and Nano DMA at a 15:1 sheath-to-aerosol flow ratio. Half Mini DMA; Nano DMA. (b) Mobility spectrums of the THA^+ monomer peak measured with the Half Mini DMA and Nano DMA at a sheath-to-aerosol flow ratio of 15:1 and curve fitting with Gaussian distributions. Half Mini DMA measured results; Nano DMA measured results; Gaussian curve fitting of the Half Mini DMA results; Gaussian curve fitting of the Nano DMA results.

Aerosols in the flame were sampled using a dilution nozzle in order to quench possible chemical reactions and coagulation in the sampling lines (Ahn *et al.* 2001; Sgro *et al.* 2009; Zhao, *et al.* 2003). In this work, the sampling system described in Ahn *et al.* (2001) was used. The inlet of the sample nozzle was placed 0.64 cm above the flame sheet. The flame temperature of 1300K was measured using a type R thermocouple (Pt-Rh:Pt 2-mm bead). The temperature after dilution was 310K. The sampling and dilution flow rates were 1.50 lpm and 42.4 lpm respectively. This yielded a dilution ratio of 120, defined as $R = (T_{aerosol} \cdot Q_{dilution})/(T_{dilution} \cdot Q_{aerosol})$, considering the effect of volume expansion in a flame (Zhao, *et al*. 2003).

A sheath-to-aerosol flow ratio of 15:1 was maintained during the comparisons of the two DMAs. The sheath and aerosol flow rates were 15.0 lpm and 1.0 lpm respectively for the Nano DMA, and 136.0 lpm and 9.0 lpm respectively for the Half Mini DMA. The sheath flow rate of the Half Mini DMA was calculated based on the calibration with THAB ions and the data inversion method described in Section 2.2.2. The transfer function is defined as the probability of a particle of a given mobility successfully traversing the classifier when a given voltage is applied to the center-electrode (Knutson & Whitby, 1975). Maintaining the same sheath-to-aerosol flow ratio would result in an identical non-diffusing transfer function shape. However, due to diffusion effects, the transfer function becomes broader and lower (Stolzenburg & McMurry, 2008). By comparing normalized full-width at half-maximum (NFWHM) or the resolution of the size distribution, the diffusion effect of the two DMAs were evaluated.

Both the Nano DMA and Half Mini DMA were operated in a closed loop configuration to balance the aerosol inlet and outlet flow rates. In order to minimize diffusion losses in the transport line, the Nano DMA was operated with a bypass flow of 8.0 lpm to ensure that both the Half Mini DMA and Nano DMA were taking 9.0 lpm of aerosol flow from the aerosol sources.

For the Nano DMA system, since the measurements focused on sub 2 nm particles, the corresponding applied voltage scan ranged from 0 V to ±10 V with a 15 lpm sheath flow. The applied voltage was provided by a bipolar analog output channel using a data acquisition board

(NI 9264, National Instruments). The sheath and bypass flow rates of the Nano DMA were controlled by adjustable blowers in an Electrostatic Classifier (EC 3080, TSI Inc.).

The voltage across the Half Mini DMA was generated using a high voltage source (Prodisc 20DC). In order to remove unclassified particles and maintain the system temperature at around 25 ℃, an inline HEPA filter and a homemade heat radiator were applied in the Half Mini DMA system. A controllable sheath flow ranging from 100 lpm to 700 lpm was provided by a pump driven by a brushless motor (DOMEL Incorporation).

In both systems, the DMA voltages and data acquisition were controlled by a Labview program; the step voltages for the Nano DMA and the Half Mini DMA were 0.01V and 4V, respectively. Classified particles were counted with a custom-built Faraday cup electrometer (FCE). The sample aerosol flow rate was controlled by a mass flow controller (MKS Inc.) downstream of the FCE.

While examining the effects of the precursor, the radioactive neutralizer, and the tubing materials on size distribution measurements with the Half Mini DMA, the resolution was increased by changing the sheath-to-aerosol flow ratio to 24:1. This was done by increasing the sheath flow to 218.0 lpm while maintaining a sampling flow rate of 9.0 lpm.

A Krypton-85 neutralizer (Model 3077; 74 MBq; TSI Inc.; half life 10.76 years; produced in July, 2005) was applied to study the effect of charge conditioning on sub 2 nm particle measurements. Copper tubing and silicone conductive tubing were used to study the influence of the contaminants released from tubing materials. Both tubings are widely used in aerosol sampling and measurement. In this study, a 20 cm section in the sampling line was left for connection with either copper tubing or silicone conductive tubing (Figure 2.1), while copper tubing was used in the rest of the system. Each tubing had an inner diameter of 4.76 mm and both were purged with ultra-purified nitrogen (>99.99%, Air Gas Inc.) for more than 24 hours before the start of all experiments.

2.2.2 Data inversion

Stolzenburg and McMurry (2008) presented a detailed data inversion process for a cylindrical DMA to convert the applied DMA voltage to particle size (D_p), and the particle number concentration to the size distribution function ($dN / d\ln D_p$).

In a closed loop cylindrical DMA, the electrical mobility (Z) of a particle is directly dependent on the voltage applied to the DMA (V); geometric parameters, such as the bullet length (L), bullet inner radius (R_1), bullet outer radius (R_2); and the flow rates, including sheath flow rate (Q_c) and aerosol flow rate (Q_s) (Knutson & Whitby, 1975). Z is given by

$$Z = \frac{(Q_c + Q_m)}{4\pi LV}\ln\left(\frac{R_2}{R_1}\right). \tag{2.1}$$

As THAB ions are used for calibration, the sheath flow rate for the Half Mini DMA was calculated using Eq. (2.1).

By definition, Z is also a function of the number of elementary charges carried by a particle (n), a single electron charge (e), the particle diameter (D_p), and the air viscosity (μ)

$$Z = \frac{Cne}{3\pi\mu D_p}, \tag{2.2}$$

where the slip correction factor (C) provided by Allen *et al.* (1985) is used in this study. By equating both sides of Eqs. (2.1) and (2.2), the correlation between voltage and particle diameter can be derived as

$$V = \frac{3\mu D_p}{Cne} \frac{(Q_c + Q_m)}{4L} \ln(\frac{R_2}{R_1}). \quad (2.3)$$

For small cluster measurements, the inverse mobility, 1/Z, is also frequently used as an indicator of particle size, since it is directly proportional to the applied DMA voltage as shown in Eq. (2.1) (Attoui *et al.* 2013; Ude & de la Mora, 2005). In the following graphs, the inverse mobility corresponding to the particle diameter is plotted as the upper x-axis.

For the conversion of raw data $N(V)$ (measured total concentration downstream of the DMA set at voltage V) to the size distribution function ($dN / d\ln D_p$), if the particle is assumed to carry one unit charge, the relationship between the particle number concentration and the size distribution function can be written as

$$\frac{dN}{d\ln D_p} = \frac{\alpha N(V)}{\frac{Q_a}{Q_s}\eta_{DET}(D_p) f_c(D_p)\beta(1+\delta)}, \quad (2.4)$$

where β and δ are dimensionless flow parameters. The constant α can be derived from the relationship between Z and D_p. Detailed expressions can be found elsewhere (Stolzenburg & McMurry, 2008). $\eta_{DET}(D_p)$ is the detection efficiency of the particle counter, and $f_c(D_p)$ is the charging efficiency of the neutralizer.

In this study, the detection efficiency of the electrometer is assumed to be 100% for convenience of data inversion, despite the possible issue of diffusion loss. A prediction of particle losses in the system would require a detailed analysis of the flow fields in the instruments and transport lines. When data inversion was executed using Eqs. (2.3) and (2.4), the only unknown parameter was the charging efficiency. There are few studies on the charging efficiency of sub 2 nm particles in radioactive neutralizers or for flame-generated aerosols (Gopalakrishnan *et al.* 2013), since it is dependent on whether the cluster is natively charged or neutral. According to Fuchs' theory (1963) and existing experimental results (Wiedensohler & Fissan, 1991; Reischl *et al.* 1996), the neutralization efficiency of sub 2 nm particles is very low, due to the low collision frequency between neutralizer ions and sampled aerosol. Natively charged particles most likely retain their charges, while a very small fraction of neutral particles become charged after neutralization. Studies have also shown that radioactive neutralization generates a large number of sub 2 nm ions or charged clusters that may interfere with sample aerosols (Kallinger, *et al.* 2012). Moreover, below 2 nm, the chemical composition of particles takes on a more important role in determining the particles' properties (McMurry, *et al.* 2011). The uniformity of the sample aerosol assumed in Fuchs' theory can no longer be valid. These issues increase the difficulty of correctly executing the data inversion process. In the results Section 2.3.3, two different charging mechanisms were used, assuming the sample aerosol was either natively charged or neutral. The dependence on chemical composition is neglected in this work.

2.2.3 Experimental Plan

Twelve sets of experiments were designed, focusing on the comparison of the two types of DMAs along with the factors influencing sub 2 nm particle measurements in flames (Table 2.1). Cases 1 through 4 targeted DMA comparisons in measurements on electrospray and flame ions.

The influences of the precursor and the neutralizer were investigated by cases 5 to 8. In cases 7 through 12, measurements on both unburned gas mixture and flame aerosols were conducted to study the influence of tubing materials.

Table 2.1 Experimental Plan

Case Number	DMA Type	Particle Source	Precursor (TTIP)	Neutralizer	Tubing Material	Sheath to Aerosol ratio
1	Nano	THAB	/	×	Copper	15:1
2	Nano	Flame	×	×	Copper	15:1
3	Half Mini	THAB	/	×	Copper	15:1
4	Half Mini	Flame	×	×	Copper	15:1
5	Half Mini	Flame	×	×	Copper	24:1
6	Half Mini	Flame	√	×	Copper	24:1
7	Half Mini	Flame	×	√	Copper	24:1
8	Half Mini	Flame	√	√	Copper	24:1
9	Half Mini	Flame	×	√	Silicone Conductive	24:1
10	Half Mini	Flame	√	√	Silicone Conductive	24:1
11	Half Mini	Unburned gas mixture	/	√	Copper	24:1
12	Half Mini	Unburned gas mixture	/	√	Silicone Conductive	24:1

2.3 Results and Discussion

2.3.1 Comparison between the Half Mini DMA and Nano DMA

Measurement on THAB ions generated by electrospray

The Half Mini DMA and Nano DMA were first compared using THAB ions generated by electrospray. Theoretically, three distinct ion peaks with inverse mobility values of 1.03 Vs/cm^2, 1.52 Vs/cm^2, and 1.85 Vs/cm^2 can be detected (Ude & de la Mora, 2005). Figure 2.2a shows the ion peaks measured by both the Half Mini DMA and Nano DMA. A higher resolving power was indeed observed in the Half Mini DMA measurements. By comparing the approximate total number concentrations of the first and the second peak, it was concluded that the diffusion loss inside the Nano DMA was significant.

Because THAB ions have been established as monodisperse size standards, information on the DMA transfer function could be obtained. The mobility spectrum of the first peak, THA$^+$, was used for the comparison of the two DMA transfer functions (Figure 2.2b). For the Nano DMA, only the higher mobility part of the THA$^+$ peak was analyzed, since the diffusion broadening of the THA$^+$(AB) peak caused an overlap with the THA$^+$ peak, as shown in Figure 2.2a. The NFWHMs for the Nano DMA and Half Mini DMA were calculated to be 0.26 and 0.10, respectively. The resolution of a DMA, on the other hand, can be defined as the inverse of the NFWHM, i.e., $R = Z^* / \Delta Z_{FWHM} = 1/NFWHM$ (Flagan, 1999). Therefore, the resolutions of the Half Mini DMA and Nano DMA were 10 and 3.8, respectively. This result demonstrates that in the Half Mini DMA, the effects of diffusion broadening are much smaller than in the Nano DMA. The resolution of a DMA without diffusion effects depends on the ratio of the sheath to aerosol flow rates, i.e., 15 in this case (Knutson & Whitby, 1975). Hence it should be noted that the Half Mini DMA is still far from conditions where diffusion is eliminated.

To evaluate the effect of diffusion broadening on the transfer functions quantitatively, diffusing transfer function theory (Stolzenburg, 1988) was applied. The calculated standard deviation values of the transfer function were compared with the experimental results. According to Stolzenburg's theory (1988), the standard deviation of the DMA diffusing transfer function can be represented as the product of the theoretical standard deviation and a multiplicative factor: $\sigma = \sigma_{theo} \cdot f_{\sigma}$, where f_{σ} is dependent on the instrument's non-ideality, electrode imperfections and misalignments, and other factors that may influence the flow or electric fields. σ_{theo} is determined by the geometry of the DMA and the dimensionless diffusion coefficient of the classified particles: $\sigma_{theo} = G_{DMA} \cdot \tilde{D}$, where G_{DMA} is dependent on the DMA classification zone length (L), inner diameter (R_1), outer diameter (R_2). Detailed expressions of the parameters can be found elsewhere (Stolzenburg, 1988; Flagan, 1999; Stolzenburg & McMurry, 2008; Jiang *et al.* 2011).

Table 2.2 Geometric parameters, theoretical and experimental standard deviations, and multiplicative factors of the Half Mini DMA and Nano DMA.

	L (mm)	R_1 (mm)	R_2 (mm)	σ_{theo}	σ	f_{σ}
Half Mini DMA	4.00	4.00	6.00	0.0144	0.0389	2.70
Nano DMA	49.9	9.37	19.1	0.111	0.112	1.01

The standard deviation, σ, on the other hand, can be derived via curve fitting of the experimental results, as shown in Figure 2.2b. Therefore, the multiplicative factor indicating the deviation from the theoretically predicted diffusion condition was calculated. Geometric parameters, standard deviations, and calculated multiplicative factors are listed in Table 2.2. It can be seen that the multiplicative factor for the Half Mini DMA is much higher than 1, indicating a large deviation from the theoretically predicted working condition. The result is reasonable for a high flow DMA, since the classification zone, which is within several millimeters, becomes sensitive to misplacement of the electrode and surface roughness.

On the other hand, the diffusing transfer function theory predicts the Nano DMA experimental transfer function very well, signifying the robustness of the Nano DMA design. Similar results were also observed by Jiang *et al*. (2011).

Measurement of the flame ions generated from a premixed flat flame reactor

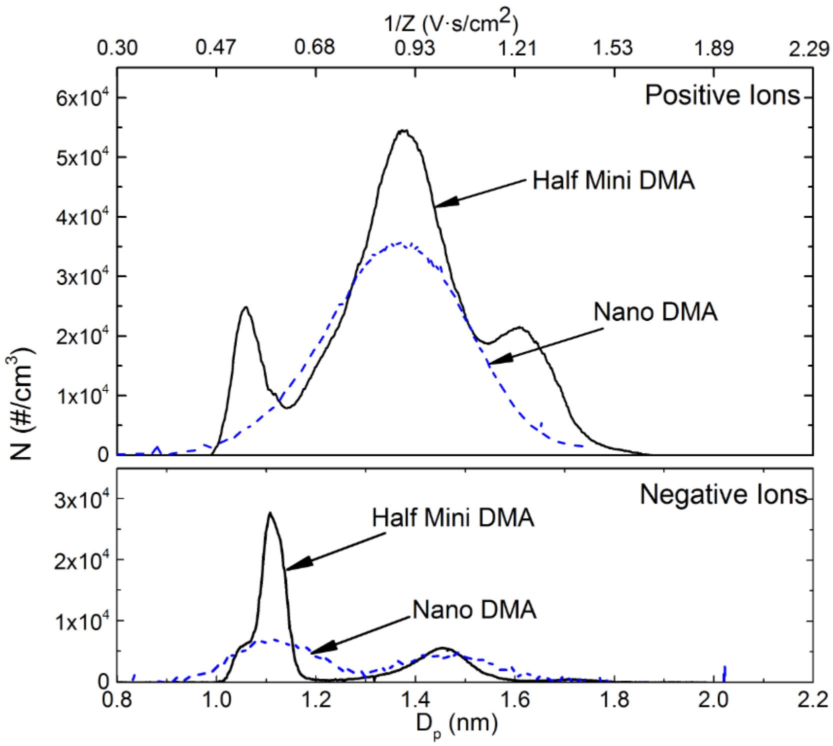

Figure 2.3 Size distributions of positive and negative ions generated in a blank premixed flat flame, as measured by the Half Mini DMA and Nano DMA. ——— Half Mini DMA; - - - Nano DMA.

In experimental case 2 and case 4, the Half Mini DMA and Nano DMA were also compared for the measurement of flame ions generated from a premixed flat flame reactor. Results are shown in Figure 2.3. In the case of a blank flame, i.e., a flame without the addition of precursors, characteristic ion peaks below 2 nm were detected. The Half Mini DMA demonstrated a smaller diffusion broadening effect, similar to that for THAB ions. These results indicated that the Half

Mini DMA could clearly distinguish characteristic ion clusters below 2 nm with high resolution. Such measurements can further help examine the initial stage of particle formation.

The detection of characteristic ion peaks in a blank flame raises intriguing questions on the origin of these ions and the role they play in particle formation. There may be several reasons for the presence of these ions. First, we suspect that these ions may be organic radicals produced during the combustion of methane. The combustion process includes complicated pathways with the production of multiple free radicals (Turns, 1996). These ions may be stable radicals generated during the combustion process. Second, it is also possible that these ions are generated from thermionic charging. Existing studies (Jiang *et al.* 2007b; Sahu *et al.* 2012) have shown that at high temperatures, positive particles can be generated by electron ejection. This mechanism also predicts a higher total positive ion concentration which is consistent with the trends of the experimental results. Although fuel-lean combustion conditions were used, soot precursors or organic carbon may still form (Sgro, *et al.* 2007, 2009). These particles may lose electrons and become charged. The possibility that these particles were generated by the hot burner or dilution probe surface through thermoemission or surface ionization cannot be neglected either (Peineke & Schmidt-Ott, 2008).

Nevertheless, further work with mass spectrometry is needed to investigate the exact chemical species of the ions and how these ions interact during the flame synthesis of nanoparticles. Existing studies have highlighted the advantages of ionic physical and chemical analysis using a tandem arrangement of a high flow DMA and a mass spectrometer (Steiner, *et al.* 2013; Manninen, *et al.* 2011). Due to the existence of these ions, ion-induced nucleation may take place during nanoparticle flame synthesis (Vishnyakov *et al.* 2011). The difference between positive and negative ion concentrations may also cause a biased charge distribution of the nanoparticles generated in a flame.

2.3.2 Factors influencing size distribution measurements of flame aerosols

Effect of the flame synthesis precursor (TTIP) on size distribution measurement

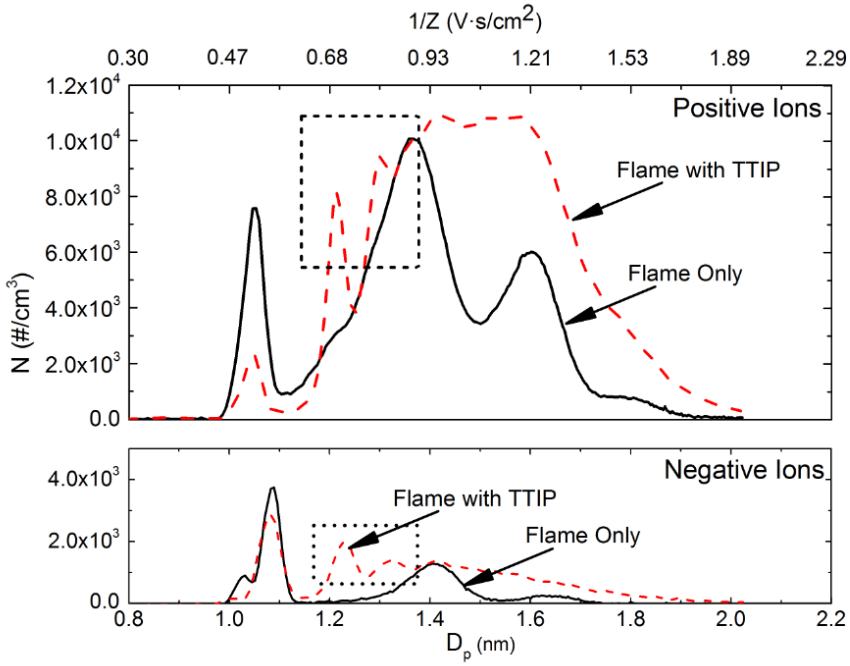

Figure 2.4 Size distributions of positive and negative ions and charged particles generated in a premixed flat flame reactor. ——— flame only; – – – flame with TTIP addition; dashed boxes highlight the discrete ion peaks

The performance of a Half Mini DMA for measuring size distributions during the flame synthesis of TiO_2 was investigated (cases 5 and 6), with the results plotted in Figure 2.4. This was done by adding TTIP as a vapor precursor to the premixed flat flame.

When compared with the blank flame condition, new ion peaks in both polarities below 1.45 nm and a broader distribution after 1.45 nm were observed. This is the first study that provides measured data of discrete clusters during synthesis of particles in a flame reactor, which can be further used in discrete-sectional modeling of particle formation and growth (Wu & Flagan, 1988; Biswas *et al.* 1997).

In the presence of TTIP, the signal strength for the blank flame-generated ion peaks decreased, most notably for the positive ion peak at around 1 nm. TiO_2 cluster formation may consume more positive ions than negative ions. The consumption of flame ions may come from either particle charging or ion induced nucleation. According to Fuchs' theory (1963), the relatively small mobility of the positive ions measured in experimental case 5 (Figure 2.3) may result in a higher consumption than for negative ions (Reischl *et al.* 1996). It should also be noticed that the difference between the mobility of the positive and negative ion peaks around 1 nm is not significant. The higher consumption of positive ions is more likely driven by the polarity dependence of the ion-cluster reaction, rather than by diffusion charging. In a study of heterogeneous nucleation, negative ions showed a stronger effect on inducing nucleation (Winkler, *et al.* 2008); however, there have not been detailed studies in flame systems. During the flame synthesis of TiO_2 in a methane-air flat flame, the total positive ion concentration was still higher than the total negative ion concentration, as shown in Figure 2.4. This can also be explained by thermionic charging and the intrusion of positive radicals, as discussed in Section 2.3.1.

The resolution of the Half Mini DMA at a higher sheath-to-aerosol flow ratio of 24:1 was examined. By comparing Figure 2.3 and Figure 2.4 for the Half Mini DMA measurement of the first positive peak in a flame only condition, a higher resolved shape can be observed at a sheath-to-aerosol flow ratio of 24:1. If the first positive peak is regarded as monodisperse, the resolutions are calculated to be 7.3 and 11 for sheath-to-aerosol flow ratios of 15:1 and 24:1. When compared with the THAB measurements with a 15:1 sheath-to-aerosol ratio (Figure 2.2b), the resolution decreased from 10 to 7.3, since the decreased size (from 1.47 nm to 1.02 nm) resulted in a stronger diffusion broadening effect.

Effect of radioactive neutralizer on size distribution measurement

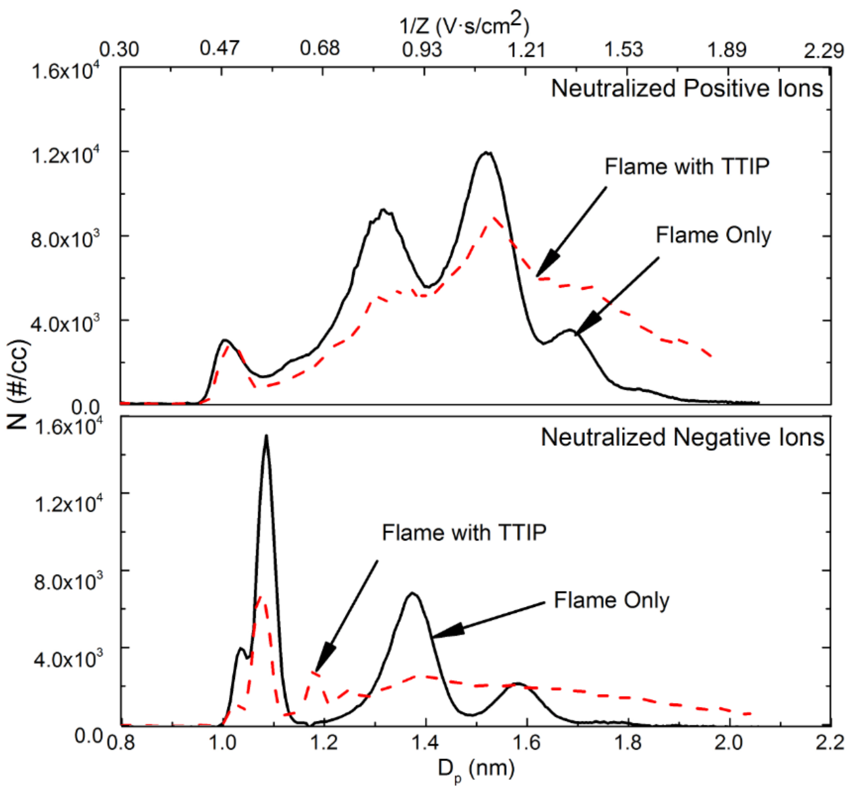

Figure 2.5 Size distributions of radioactively neutralized positive and negative ions and charged particles generated in a premixed flat flame reactor. ——— flame only; - - - flame with TTIP addition.

The effect of a bipolar radioactive neutralizer (Kr-85) on size distribution measurements was studied (cases 5 through 8). Figure 2.5 displays the size distributions measured with a neutralizer in a blank flame condition and during TiO_2 synthesis. After charge conditioning, two main effects were found. First, flame ions were neutralized differently, based on ion polarity. The major positive ion peak at around 1 nm was significantly suppressed, while the negative ion signal increased, resulting in a more balanced charge distribution. However, a near-symmetric charge distribution predicted by Fuchs' theory is not observed. The shape of the size distribution curve is substantially different for positive and negative ions. As explained previously, the measured particles can be seen as a mixture of neutralizer ions, natively charged particles without neutralization, and neutralized particles. The distinct mobilities of each species may result in different final size distributions.

Second, for negative ions, no new ion peaks were observed in comparison to the case without a neutralizer, while the signal strengths increased (comparing with Figure 2.4). This phenomenon indicates that the negative ions generated in the neutralizer were identical to those generated in the flame. Hydrated ions, $X^-(H_2O)_n$ (X = NO_3^-, NO_2^- etc.) were believed to be the predominant ions generated in neutralizers (Cabane & Playe, 1980), which may depend on the humidity. A recent study with a tandem DMA-mass spectrometer system further shows that by passing clean air through a radioactive neutralizer, the ion peak at around 1 nm is mainly composed of NO_3^- and $HNO_3 \cdot NO_3^-$ (Steiner, *et al.* 2013). In the flame, due to the presence of organic and inorganic radicals and high concentration of water vapor, it is also possible that similar ions were formed.

With the addition of TTIP for the flame synthesis of TiO_2, charge conditioning with a neutralizer resulted in a different size distribution (Figure 2.4 and Figure 2.5). This alternation may be caused by differences in charging mechanisms in the flame and neutralizer. Both thermionic charging and diffusion charging determine the charge distribution of aerosols in a flame; while in a radioactive neutralizer, diffusion charging is the only mechanism that determines the aerosol charge distribution (Jiang, *et al.* 2007b).

Effect of tubing material on size distribution measurement

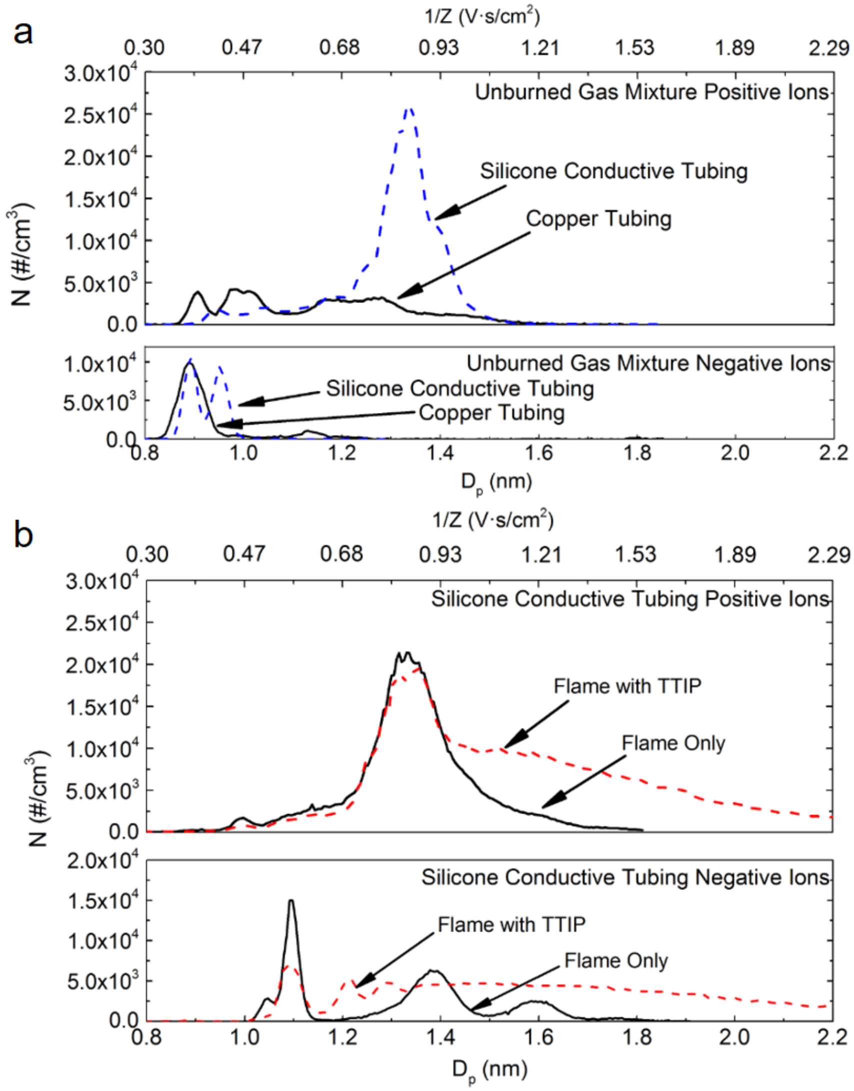

Figure 2.6 (a) Size distributions of positive and negative ions produced in the Kr-85 neutralizer when copper or silicone conductive tubing was used to transport the unburned gas mixture to the Half Mini DMA. ——— copper tubing; - - - silicone conductive tubing. (b) Size distributions of neutralized positive and negative ions generated in a blank flame and flame with TTIP precursor when silicone conductive tubing was used to transport the sample aerosols to the Half Mini DMA. ——— flame only; - - - TTIP flame.

The effect of tubing material on the size distribution measurement of both the unburned gas mixture and flame ions were investigated. From Figure 2.6a, it can be seen that at normal temperatures, for unburned gas mixtures with clean copper tubing, ions were still detected. These ions may originate from the neutralizer (Kallinger, *et al.* 2012). However, when silicone conductive tubing was used in the system, extremely high amounts of positive ion contamination at around 1.37 nm were observed. For negative ions, an additional ion peak appeared in the silicone conductive tubing measurement results.

During the sampling of flame aerosols, the interference of ion peaks from silicone tubing continued to dominate in positive ion measurements, as seen when comparing the TTIP measurement results in Figure 2.4 and Figure 2.6b. This result demonstrated that for measurement of sub 2 nm particles, copper tubing may be a better choice for transporting sample aerosols. On the other hand, for negative ions, the contamination from conductive tubing was not as strong as that of positive ions, which might be caused by the fact that the organic molecules released from the conductive tubing were positively charged.

2.3.3 Data Inversion Results

In Figure 2.7, the size distribution functions of the neutralized TiO_2 particles (case 8, negative ions) were plotted with the assumption of two different charging efficiencies. By assuming that measured negative clusters were natively neutral and became singly charged due to collisions with ions in the neutralizer, the Wiedensohler (1986) charge distribution function can be used

$$f(-1) = 10^k, \qquad (2.5)$$

where

$$k = \sum_{i=0}^{5} a_i(N)(\log\frac{D_p}{nm})^i \ . \qquad (2.6)$$

Here, $f(-1)$ is the fraction of singly negatively charged particles in the total population of particle having a size of D_p. k can be calculated by several constants listed elsewhere

(Wiedensohler, *et al.* 1986). On the other hand, if we assume that measured clusters were natively charged before neutralization, and the charge state did not change due to the low collision efficiency with the neutralizer ions, a 100% charging efficiency $f_c(D_p)$ can be used in Eq. (2.4). Hence a different size distribution function of the negative ions can be derived.

It is seen in Figure 2.7 that different charge distribution assumptions not only resulted in a large difference in particle concentrations, but also caused an alternation of the normalized shape of the size distribution function.

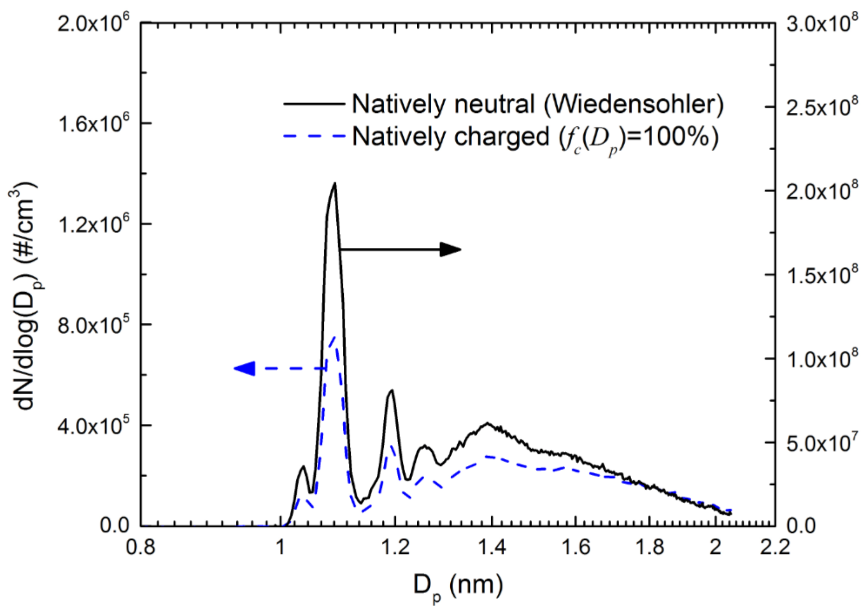

Figure 2.7 Size distribution functions of neutralized flame-generated particles (Case 8, negative) calculated from data inversion. ——— assuming particles were natively neutral (using Wiedensohler charging efficiency); – – – assuming particles were natively charged (using 100% charging efficiency).

It should also be noted that Fuchs' theory predicts a near-symmetric charge distribution after neutralization, while in our experiments, such symmetry was not observed. Hence, using the Wiedensohler charge distribution (1986) is not the most appropriate approach for deriving the size distribution. However, this issue reveals both the complexity and the uniqueness of charging mechanisms in the sub 2 nm range. Further research is needed to determine the actual charging mechanisms and charge distribution for sub 2 nm particles in both neutralizers and flames.

2.4 Conclusions

This work compared the accuracy of the Half Mini DMA and Nano DMA in measurements of sub 2 nm ions and charged particles generated by electrospray and by a premixed flat flame reactor. For both measurements, a lower diffusion effect was observed in the Half Mini DMA.

The Half Mini DMA was used to investigate the formation of TiO_2 clusters during flame synthesis, the impact of use of radioactive neutralizers and tubing materials on size distribution measurements. When TTIP was introduced into the flame reactor, discrete TiO_2 ion peaks were observed, indicating a discrete size distribution at initial stages of particle formation. Use of a radioactive neutralizer resulted in a balanced distribution of the positive and negative particles. The alteration in the size distribution when compared with the cases without a neutralizer indicated different charging mechanisms in a flame and neutralizer. During the transport of the sample aerosols, the silicone conductive tubing generated very large quantities of positive contaminant ions with mobility diameters of approximately 1.37 nm. This effect remained when measuring flame-generated nanoparticles. These results suggest that copper tubing is a more appropriate choice than silicone conductive tubing when measuring size distributions under 2 nm.

The size distribution measurements of flame aerosols in the sub 2 nm range can provide fundamental information on particle formation processes. Future work on flame aerosol measurements with the Half Mini DMA is needed, which will greatly broaden our vision of nanoparticle synthesis and pollutant control.

2.5 References

Aalto, P., Hämeri, K., Becker, E., Weber, R., Salm, J., Mäkelä, J.M., Hoell, C., O'dowd, C.D., Karlsson, H., & Hansson, H.C. (2001). Physical characterization of aerosol particles during nucleation events. *Tellus B*, 53, 344-358.

Ahn, K., Sohn, S., Jung, C., & Choi, M. (2001). In situ measurement of nano particle size distribution and charge characteristics in H_2/O_2/TEOS diffusion flame. *Scripta materialia*, 44, 1889-1892.

Allen, M.D., & Raabe, O.G. (1985). Slip correction measurements of spherical solid aerosol particles in an improved Millikan apparatus. *Aerosol Sci Tech*, 4, 269-286.

Attoui, M., Paragano, M., Cuevas, J., & Fernandez de la Mora, J. (2013). Tandem DMA Generation of Strictly Monomobile 1–3.5 nm Particle Standards. *Aerosol Sci Tech*, 47, 499-511.

Biswas, P., Wu, C.Y., Zachariah, M.R., & McMillin, B. (1997). Characterization of iron oxide-silica nanocomposites in flames: Part II. Comparison of discrete-sectional model predictions to experimental data. *J Mater Res*, 12, 714-723.

Cabane, M., & Playe, P. (1980). Mass spectra of negative ions in air-like gas mixtures at atmospheric pressure. *J Aerosol Sci*, 11, 475-482.

Chen, D.-R., Pui, D.Y., Hummes, D., Fissan, H., Quant, F., & Sem, G. (1998). Design and evaluation of a nanometer aerosol differential mobility analyzer (Nano-DMA). *J Aerosol Sci*, 29, 497-509.

Chen, D., Pui, D.Y., Hummes, D., Fissan, H., Quant, F., & Sem, G. (1996). Nanometer differential mobility analyzer (Nano-DMA): design and numerical modeling. *J Aerosol Sci*, 27, 137-138.

Fang, J., Leavey, A., & Biswas, P. (2014). Controlled studies on aerosol formation during biomass pyrolysis in a flat flame reactor. *Fuel*, 116, 350-357.

Fernández de la Mora, J., & Kozlowski, J. (2013). Hand-held differential mobility analyzers of high resolution for 1–30 nm particles: Design and fabrication considerations. *J Aerosol Sci*, 57, 45-53.

Flagan, R.C. (1999). On differential mobility analyzer resolution. *Aerosol Science & Technology*, 30, 556-570.

Fuchs, N. (1963). On the stationary charge distribution on aerosol particles in a bipolar ionic atmosphere. *Geofisica pura e applicata*, 56, 185-193.

Goel, A., Hebgen, P., Vander Sande, J.B., & Howard, J.B. (2002). Combustion synthesis of fullerenes and fullerenic nanostructures. *Carbon*, 40, 177-182.

Gopalakrishnan, R., Meredith, M.J., Larriba-Andaluz, C., & Hogan Jr, C.J. (2013). Brownian Dynamics Determination of the Bipolar Steady State Charge Distribution on Spheres and Non-spheres in the Transition Regime. *J Aerosol Sci*, 63, 126-145.

Height, M.J., Howard, J.B., Tester, J.W., & Vander Sande, J.B. (2004). Flame synthesis of single-walled carbon nanotubes. *Carbon*, 42, 2295-2307.

Intra, P., & Tippayawong, N. (2008). An overview of differential mobility analyzers for size classification of nanometer-sized aerosol particles. *Songklanakarin Journal of Science and Technology*, 30, 243-256.

Jiang, J., Attoui, M., Heim, M., Brunelli, N.A., McMurry, P.H., Kasper, G., Flagan, R.C., Giapis, K., & Mouret, G. (2011). Transfer functions and penetrations of five differential mobility analyzers for sub-2 nm particle classification. *Aerosol Sci Tech*, 45, 480-492.

Jiang, J., Chen, D.-R., & Biswas, P. (2007a). Synthesis of nanoparticles in a flame aerosol reactor with independent and strict control of their size, crystal phase and morphology. *Nanotechnology*, 18, 285603.

Jiang, J., Lee, M.-H., & Biswas, P. (2007b). Model for nanoparticle charging by diffusion, direct photoionization, and thermionization mechanisms. *J Electrostat*, 65, 209-220.

Kallinger, P., Steiner, G., & Szymanski, W.W. (2012). Characterization of four different bipolar charging devices for nanoparticle charge conditioning. *J Nanopart Res*, 14, 1-8.

Kasper, M., Siegmann, K., & Sattler, K. (1997). Evaluation of an in situ sampling probe for its accuracy in determining particle size distributions from flames. *J Aerosol Sci*, 28, 1569-1578.

Knutson, E., & Whitby, K. (1975). Aerosol classification by electric mobility: apparatus, theory, and applications. *J Aerosol Sci*, 6, 443-451.

Kulkarni, P., Baron, P.A., & Willeke, K. (2011). *Aerosol measurement: principles, techniques, and applications*. Wiley, (Chapter 32).

Law, C.K., Sung, C.J., Wang, H., & Lu, T. (2003). Development of comprehensive detailed and reduced reaction mechanisms for combustion modeling. *AIAA journal*, 41, 1629-1646.

Maißer, A., Premnath, V., Ghosh, A., Nguyen, T.A., Attoui, M., & Hogan, C.J. (2011). Determination of gas phase protein ion densities via ion mobility analysis with charge reduction. *Physical Chemistry Chemical Physics*, 13, 21630-21641.

Manninen, H., Franchin, A., Schobesberger, S., Hirsikko, A., Hakala, J., Skromulis, A., Kangasluoma, J., Ehn, M., Junninen, H., & Mirme, A. (2011). Characterisation of corona-generated ions used in a Neutral cluster and Air Ion Spectrometer (NAIS). *Atmospheric Measurement Techniques Discussions,* 4, 2099-2125.

McMurry, P.H., Kulmala, M., & Worsnop, D.R. (2011). Special Issue on Aerosol Measurements in the 1 nm Range. *Aerosol Sci Tech*, 45, i-i.

Mohnen, V. (1977). Formation, nature, and mobility of ions of atmospheric importance. *In Electrical processes in atmospheres Electrical processes in atmospheres* (pp. 1-17). Springer, City.

Peineke, C., & Schmidt-Ott, A. (2008). Explanation of charged nanoparticle production from hot surfaces. *J Aerosol Sci*, 39, 244-252.

Qin, Z., Lissianski, V.V., Yang, H., Gardiner, W.C., Davis, S.G., & Wang, H. (2000). Combustion chemistry of propane: a case study of detailed reaction mechanism optimization. *P Combust Inst*, 28, 1663-1669.

Rao, P.M., & Zheng, X. (2009). Rapid catalyst-free flame synthesis of dense, aligned α-Fe2O3 nanoflake and CuO nanoneedle arrays. *Nano letters,* 9, 3001-3006.

Reischl, G., Mäkelä, J., Karch, R., & Necid, J. (1996). Bipolar charging of ultrafine particles in the size range below 10 nm. *J Aerosol Sci*, 27, 931-949.

Sahu, M., Park, J., & Biswas, P. (2012). In Situ Charge Characterization of TiO2 and Cu–TiO2 Nanoparticles in a Flame Aerosol Reactor. *J Nanopart Res*, 14, 1-11.

Seto, T., Nakamoto, T., Okuyama, K., Adachi, M., Kuga, Y., & Takeuchi, K. (1997). Size distribution measurement of nanometer-sized aerosol particles using DMA under low-pressure conditions. *J Aerosol Sci*, 28, 193-206.

Sgro, L., Barone, A., Commodo, M., D'Alessio, A., De Filippo, A., Lanzuolo, G., & Minutolo, P. (2009). Measurement of nanoparticles of organic carbon in non-sooting flame conditions. *P Combust Inst*, 32, 689-696.

Sgro, L., De Filippo, A., Lanzuolo, G., & D'Alessio, A. (2007). Characterization of nanoparticles of organic carbon (NOC) produced in rich premixed flames by differential mobility analysis. *P Combust Inst*, 31, 631-638.

Sgro, L.A., D'Anna, A., & Minutolo, P. (2010). Charge distribution of incipient flame-generated particles. *Aerosol Sci Tech*, 44, 651-662.

Siefering, K., & Griffin, G. (1990). Growth kinetics of CVD TiO2: influence of carrier gas. *J Electrochem Soc*, 137, 1206-1208.

Steiner, G., & Reischl, G.P. (2012). The effect of carrier gas contaminants on the charging probability of aerosols under bipolar charging conditions. *J Aerosol Sci*, 54, 21-31.

Steiner, G., Jokinen, T., Junninen, H., Sipilä, M., Petäjä, T., Worsnop, D., Reischl, G.P., & Kulmala, M. (2013). High-Resolution Mobility and Mass Spectrometry of Negative Ions Produced in a 241Am Aerosol Charger. *Aerosol Sci Tech*, 48, 260-269.

Stolzenburg, M.R. (1988). *An ultrafine aerosol size distribution measuring system.* University of Minnesota.

Stolzenburg, M.R., & McMurry, P.H. (2008). Equations governing single and tandem DMA configurations and a new lognormal approximation to the transfer function. *Aerosol Sci Tech*, 42, 421-432.

Tiwari, V., Jiang, J., Sethi, V., & Biswas, P. (2008). One-step synthesis of noble metal–titanium dioxide nanocomposites in a flame aerosol reactor. *Applied Catalysis A: General,* 345, 241-246.

Thimsen, E., & Biswas, P. (2007). Nanostructured photoactive films synthesized by a flame aerosol reactor. *Aiche J,* 53, 1727-1735.

Thimsen, E., Rastgar, N., & Biswas, P. (2008). Nanostructured TiO2 films with controlled morphology synthesized in a single step process: Performance of dye-sensitized solar cells and photo watersplitting. *The Journal of Physical Chemistry C,* 112, 4134-4140.

Thimsen, E.J. (2009). *Metal oxide semiconductors for solar energy harvesting*. Washington University in St. Louis.

Turns, S.R. (1996). *An introduction to combustion* (Vol. 499). McGraw-Hill New York, (Chapter 5).

Ude, S., & de la Mora, J.F. (2005). Molecular monodisperse mobility and mass standards from electrosprays of tetra-alkyl ammonium halides. *J Aerosol Sci*, 36, 1224-1237.

Vishnyakov, V., Kiro, S., & Ennan, A. (2011). Heterogeneous ion-induced nucleation in thermal dusty plasmas. *Journal of Physics D: Applied Physics*, 44, 215201.

Wiedensohler, A., Lütkemeier, E., Feldpausch, M., & Helsper, C. (1986). Investigation of the bipolar charge distribution at various gas conditions. *J Aerosol Sci*, 17, 413-416.

Wiedensohler, A., & Fissan, H. (1991). Bipolar charge distributions of aerosol particles in high-purity argon and nitrogen. *Aerosol Sci Tech*, 14, 358-364.

Winkler, P.M., Steiner, G., Vrtala, A., Vehkamäki, H., Noppel, M., Lehtinen, K.E., Reischl, G.P., Wagner, P.E., & Kulmala, M. (2008). Heterogeneous nucleation experiments bridging the scale from molecular ion clusters to nanoparticles. *Science*, 319, 1374-1377.

Wu, J.J., & Flagan, R.C. (1988). A discrete-sectional solution to the aerosol dynamic equation. *J Colloid Interf Sci*, 123, 339-352.

Zhao, B., Yang, Z., Wang, J., Johnston, M.V., & Wang, H. (2003). Analysis of soot nanoparticles in a laminar premixed ethylene flame by scanning mobility particle sizer. *Aerosol Sci Tech*, 37, 611-620.

Zhang, Y., Shuiqing, L., Deng, S., Yao, Q., & Tse, S.D. (2012). Direct synthesis of nanostructured TiO_2 films with controlled morphologies by stagnation swirl flames. *J Aerosol Sci*, 44, 71-82.

Chapter 3: Kinetics of Sub 2 nm TiO_2 Particle Formation in an Aerosol Reactor during Thermal Decomposition of Titanium Tetraisopropoxide

The results of this chapter have been published in Wang, Y., Liu, P., Fang, J., Wang, W.-N., Biswas, P. (2015). Kinetics of sub-2 nm TiO_2 particle formation in an aerosol reactor during thermal decomposition of titanium tetraisopropoxide. J. Nanopart. Res. 17:1-13.

Abstract

Particle size distribution measurements from differential mobility analyzers (DMAs) can be utilized to study particle formation mechanisms. However, knowledge on the initial stages of particle formation is incomplete, since in conventional DMAs, the Brownian broadening effect limits their ability to measure sub 2 nm sized particles. Previous studies have demonstrated the capability of high flow DMAs, such as the Half Mini DMAs, to measure sub 2 nm particles with significantly higher resolutions than conventional DMAs.

A Half Mini DMA was applied to study the kinetics of sub 2 nm TiO_2 nanoparticle formation in a furnace aerosol reactor, through the thermal decomposition of titanium tetraisopropoxide (TTIP). The influence of parameters such as reaction temperature, residence time, precursor concentration, and the introduction of bipolar charges on sub 2 nm particle size distributions were studied. A first order reaction rate derived from the dependence of size distributions on reaction temperature matched well with existing literature data. The change in precursor residence time and precursor concentration altered the size distributions correspondingly, indicating the occurrence of TTIP thermal decomposition. The introduction of bipolar charges in aerosol reactors enhanced the consumption of reactants, possibly due to ion-induced nucleation and induced dipole effects.

3.1 Introduction

A tremendous growth in demand for nanoparticles has been witnessed in recent years. Unlike bulk materials, nanoparticles exhibit distinctive physical, thermal, acoustic, electric, and optical properties that lead to a wide array of applications. Pristine metal oxide nanoparticles, such as TiO_2, ZnO, and CuO, and their composites have received extensive attention due to their wide usage in pigments, additives, catalysts (Freund et al. 2008; Jiang et al. 2014), photovoltaic device components (O'Regan and Grätzel 1991; Thimsen et al. 2008; Wang et al. 2012), and battery materials (Zhang et al. 2011; Chadha et al. 2014).

In industry, gas-phase routes are a major methodology for synthesizing metal oxide nanoparticles, with an annual yield of over 2 million tons and a revenue of over 4 billion USD (Wegner and Pratsinis 2003). In this process, nanoparticles are formed via a bottom-up method involving cluster formation and consumption. The pathway of the formation of metal oxides can be described as follows. First, metallic precursors react through thermal decomposition or oxidation to form metal oxide vapors; then supersaturated vapor molecules nucleate homogeneously or heterogeneously to form stable molecular clusters. Next, metal oxide vapors condense on existing nuclei; and finally, metal oxide particles coagulate and sinter to form particles with desired sizes, crystal phases, or other characteristics. In order to tailor nanoparticle properties, a thorough understanding and precise control of the particle formation processes are needed, both of which require the characterization of nanoparticle formation.

Size characterization is one of the most common methods for measuring nanoparticles, since size distributions and their evolution under different synthesis conditions will facilitate the understanding of particle formation mechanisms. Real time size distribution measurements of particles are usually conducted with differential mobility analyzers (DMAs) (Knutson and Whitby 1975; Wang and Flagan 1990). A DMA, acting as an electric mobility classifier, allows only particles with certain electrical mobilities (mobility sizes) to pass through the instrument and to be further monitored by particle counters. Utilizing this instrument, various studies on particle formation and growth have been conducted, including particle generation in flame aerosol reactors (Jiang et al. 2007; Sgro et al. 2007; Fang et al. 2014a), particle sintering mechanisms (Cho and Biswas 2006; Cho et al. 2007; Mädler et al. 2002; Eggersdofer et al. 2012), and particle charging mechanisms (Sahu and Biswas 2011; Kim et al. 2005; Maricq 2004; Maricq 2008; Hogan et al. 2009). A detailed review of these studies indicates that particle dynamics were investigated only in the size range above 2 nm. Information on particle nucleation and growth at initial stages is missing, forming a knowledge gap between chemical reactions, which typically happen on the molecular scale, and particle growth above 2 nm. The lack of information on incipient nanoparticles is due to Brownian diffusion effects in conventional DMAs, which adds uncertainty to particle movements in DMAs and causes broadening of measured particle size distributions, compromising the accuracy of the size distribution measurements (Stolzenburg 1988; Stolzenburg and McMurry 2008). In order to counteract the effects of diffusion, DMAs with high sheath flow rates, typically over 100 lpm, were designed; so that the particle diffusing time in the classification zone is reduced, and the accuracy and resolution of the measurement is enhanced (Fernandez de la Mora 2011; Fernández de la Mora and Kozlowski 2013; Hontañón et al. 2013; Wang et al. 2014). DMAs with high sheath flow rates have previously been used in studies including the calculation of ion mobility-volume relationship (Larriba et al. 2011), the generation of monomobile particle size standards (Attoui et al. 2013), the determination of ion composition (Junninen et al. 2010; Manninen et al.

2011; Steiner et al. 2013), and the observation of heterogeneous nucleation (Winkler et al. 2008). Recently, few studies by our group (Fang et al. 2014b; Wang et al. 2014) have focused on sub 2 nm cluster formation in flame reactors. These measurements by a hand-held DMA with high sheath flow rates (Half Mini DMA) implied that collisional growth is likely to take place in the sub 2 nm range (Fang et al. 2014b).

Our previous work on sub 2 nm particle measurements showed that flame aerosol reactors generate a large amount of background ions, some of which may overlap with the newly formed particles in mobility spectrums (Fang et al. 2014b). Furnace aerosol reactors have been widely chosen to study particle formation mechanisms due to the less interference of background species, and the simplicity and uniformity of the flow and temperature fields, which enable them to provide direct evidence of particle formation and growth (Moravec et al. 2001). Previous studies on TiO_2 nanoparticle formation through the thermal decomposition of titanium tetraisopropoxide (TTIP) were carried out in furnace aerosol reactors, and Arrhenius first order reaction rates were determined (Nakaso et al. 2003). Discrete sectional models were used to simulate these systems, yielding results that qualitatively predicted the experimental results (Okuyama et al. 1989, 1990). Nonetheless, due to the limitation of the instrumentation, none of these studies investigated initial stage particle dynamics on the sub 2 nm scale. In furnace aerosol reactors, particles are generally formed with little charge interaction (Adachi et al. 2003). The addition of bipolar charges may enhance the coagulation efficiency of particles due to induced dipole effects (Zhang et al. 2011). There is also evidence that charges may alter the size, shape, and concentration of the synthesized particles in aerosol reactors due to ion-induced nucleation effects (Adachi et al. 2004). Hence, it would be interesting to see the role of the addition of bipolar charges on particle formation and growth in the sub 2 nm range.

In this study, a Half Mini DMA was utilized to determine the kinetics of TiO_2 particle formation and growth during the thermal decomposition of TTIP in a furnace aerosol reactor. Sub 2 nm particle size distributions as a function of furnace temperatures were obtained and analyzed. Arrhenius first order reaction rates were determined from the evolution of measured size distributions. The effects of precursor residence time, precursor concentration, and the addition of bipolar charges on the evolution of sub 2 nm particle size distributions were also studied.

3.2 Materials and Methods

3.2.1 Experimental Setup

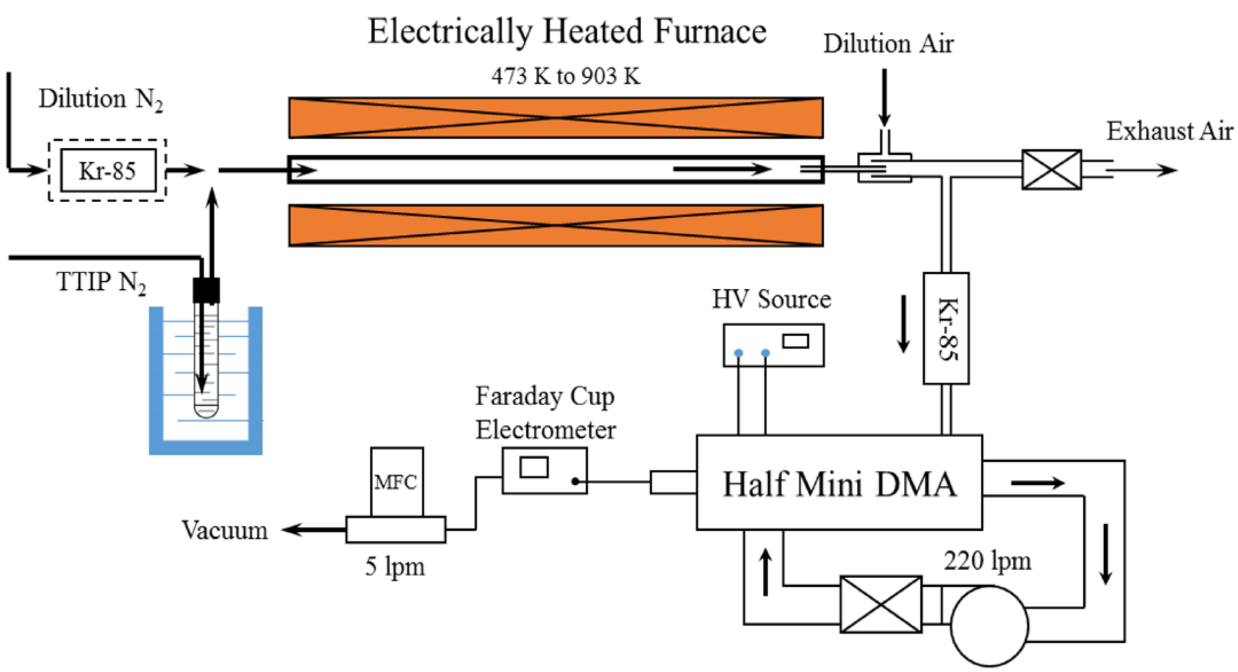

Figure 3.1 Schematic diagram of the experimental setup. The Kr-85 neutralizer upstream of the furnace was used for studying the influence of bipolar ionic charge introduction on particle formation.

The experimental setup for this work consisted of four sections: a precursor feeder, an electrically heated furnace, a dilution sampler, and a Half Mini DMA system. A schematic diagram of the experimental setup is shown in Figure 3.1. The TiO_2 nanoparticles were synthesized by the thermal decomposition of titanium tetraisopropoxide (TTIP, Sigma-Aldrich Inc., >97%). TTIP was introduced into the furnace by bubbling clean and dry N_2 (Airgas, NI 300) through TTIP liquid. The TTIP bubbler (MDC Vacuum Products) was placed in a water bath maintained at 25°C. The concentration of TTIP was calculated according to the saturation vapor pressure data presented by Siefering and Griffin (1990). Before entering the furnace, the TTIP carrier gas mixed with another stream of N_2 (dilution N_2), so that the precursor concentration and the precursor residence time could be varied by altering the flow rates of the two streams with mass flow controllers (MKS Inc.). To study the influence of ionic charges on particle formation, the dilution N_2 was first passed through a Krypton-85 radioactive charger (TSI 3077A), so that bipolar ions can be generated (Zeleny, 1931; Bradbury, 1932; Kallinger et al. 2012).

The thermal decomposition of TTIP was accomplished by sending the gas mixture through the electrically heated furnace (Fisher Scientific Inc.). A quartz tube with a size of 16 × 356 mm (ID × L) was used as the tubular reactor. The stainless steel tubes connecting the bubbler and the quartz tube were also maintained at a temperature of 25°C to prevent TTIP from condensing on the tube walls. To study the effect of temperature on particle synthesis, the furnace was operated at various temperatures. Figure 3.2 shows a temperature profile as a function of the distance from the furnace inlet, when the furnace was set to 723 K. To account for the temperature variation along the reactor, an “effective reaction zone” (ER zone) was defined, assuming TTIP decomposed only in the ER zone, where the furnace temperature was equal to the set temperature (Nakaso et al. 2003). The precursor residence time is further calculated by dividing the volume of the ER zone by the corrected flow rate considering the effect of thermal expansion.

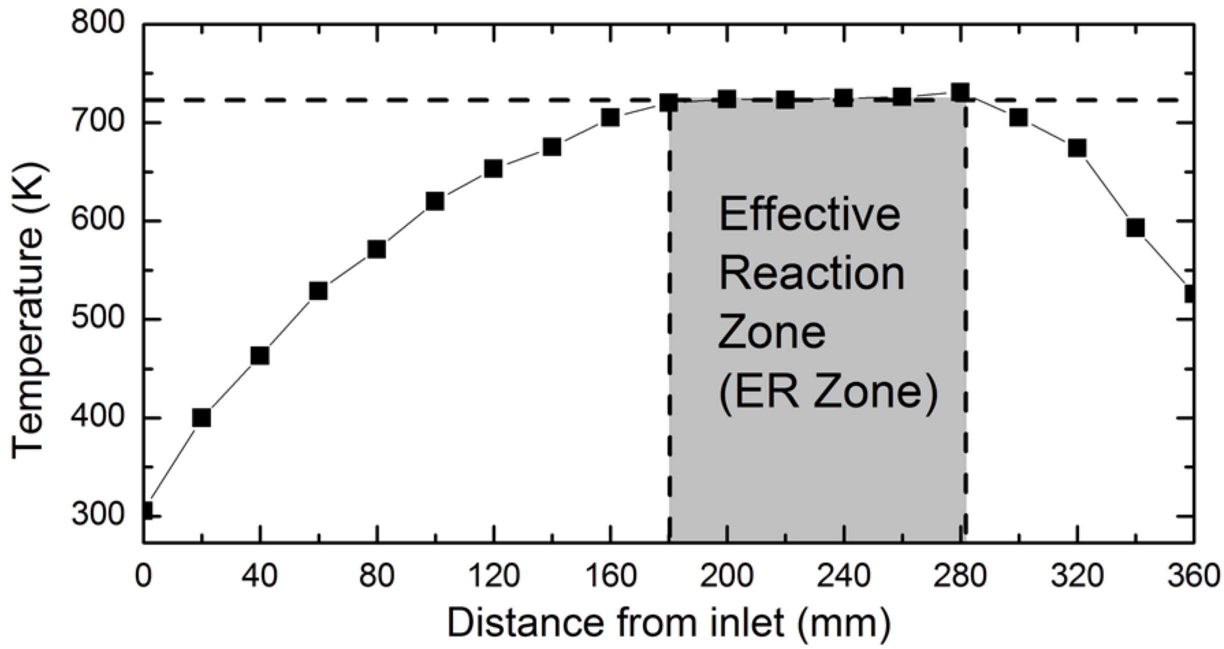

Figure 3.2 Temperature distribution in the reactor as a function of the distance from the reactor inlet when the furnace was set to 723 K. Shaded area is the effective reaction zone (ER zone).

At the outlet of the quartz tube, a dilution sampling probe was used to sample particles while quenching further reactions and particle growth. The design of the sampling tube was similar to the one presented by Ahn et al. (2001). Aerosols were sampled with a flow rate of 1.20 lpm, determined with a bubble flow meter (Gilibrator, Sensidyne Inc.). The flow rate ratio of the dilution air and the sampled aerosol was measured to be 29.0. Considering the thermal expansion effect at high temperatures, the actual dilution ratio (R_D) was calculated using $R_D = T_{sample} \cdot Q_{dilution} / T_{dilution} \cdot Q_{sample} = 29.0 \cdot T_{sample} / T_{dilution}$, where T_{sample} was the temperature at the outlet of the furnace, and $T_{dilution}$ was the temperature of the dilution air (Zhao et al. 2003).

Prior to entering the DMA for size classification, sampled aerosols were charged with a radioactive charger (Kr-85, Model 3077A, TSI Inc.), since the thermal decomposition of TTIP does not involve much ion interaction, and most of the particles remain uncharged, as observed in this and previous studies (Adachi et al. 2003). The Half Mini DMA was operated in a closed loop, where the sheath flow was filtered, cooled, and recirculated by an inline HEPA filter (Ideal Vacuum Products, LLC), a homemade radiator, and a brushless blower (DOMEL Inc.), respectively (Wang et al. 2014). The sheath flow rate was calculated to be 220 lpm, according to the calibration method mentioned elsewhere (Ude and de la Mora 2005; Wang et al. 2014). The aerosol inlet and outlet flow rates were balanced due to the closed loop configuration. Both of the flow rates were maintained at 5 lpm by a mass flow controller (MKS Inc.) downstream of the DMA.

A high voltage source (Prodisc 20DC) was used to control the applied voltage on the DMA using a Labview program with a voltage step of 5 V. At the outlet of the DMA, a home-built Faraday cup electrometer (FCE) recorded the classified particle number concentration (Heim et al. 2010). By switching the polarity of the high voltage applied on the DMA, the number concentrations of both positively and negatively charged particles could be measured. Charged particle size distributions were then obtained by relating the particle mobility size, calculated from the applied voltage, with the particle concentration monitored by the FCE (Wang et al. 2014). In this work, the mobility sizes calculated from Stokes-Millikan law were reported, representing the drag force on particles. According to existing studies, the mobility sizes are approximately 0.3 nm larger than the volume sizes for particles below 2 nm (Larriba et al. 2011). Also note that the actual particle size distribution function ($dN/d\log D_p$) was not calculated, due to the complexity of the charging mechanisms of sub 2 nm particles (Gopalakrishnan et al. 2013; Wang et al. 2014). The transmission efficiency of the half mini DMA was assumed to be the same for particles with a same size. Hence, the electrometer-measured cluster concentration was assumed to be proportional to the cluster concentration before size-classification.

3.2.2 Experimental Plan

Table 3.1 Experimental plan for the thermal decomposition studies of TTIP

	Temperature (T [K])	**Residence time in ER zone (t [s])**	**Precursor Concentration (C [mmol/m^3])**	**Introduction of Bipolar charges**
Group 1	473 to 903	0.132 to 0.252	2.4	–
Group 2	723	0.101 to 0.303	2.4	–
Group 3	723	0.152	0.72 to 4.8	–
Group 4	723	0.152	2.4	√

The experiments were conducted to systematically investigate the effects of parameters relating to the kinetics of particle formation, including reaction temperatures, precursor residence times, and precursor concentrations. Furthermore, the effect of bipolar ionic charge introduction on particle formation was studied by examining the influence of using a radioactive neutralizer as the source of ions. A brief summary of the experimental plan is shown in Table 3.1. To study the effect of reaction temperature (Group 1), furnace temperatures were varied from 473 K to 903 K. A precursor concentration of 2.4 mmol/m^3 was maintained by controlling the flow rate ratio of the precursor carrier N_2 (Q_C) to the dilution N_2 (Q_D) to be 1:2, and the total N_2 flow to be 3 lpm. The change of reaction temperatures also affected the precursor residence time in the ER zone, and the actual residence time is calculated with the ideal gas law. Group 2 experiments examined the influence of precursor residence time. A furnace temperature of 723K and a precursor concentration of 2.4 mmol/m^3 were maintained, while total flows of N_2 ranging from 1.5 lpm to 4.5 lpm were used, corresponding to a residence time ranging from 0.101 s to 0.303 s. To investigate the effect of precursor concentration on the kinetics of particle formation (Group 3), the furnace was maintained at 723 K and the total flow of N_2 was kept at 3 lpm. $Q_C : Q_D$ was altered from 1:9 to 2:1, resulting in precursor concentrations ranging from 0.72 mmol/m^3 to 4.8 mmol/m^3. The influence of charge addition on particle formation and growth was investigated by experiments listed in Group 4. The ER zone temperature, precursor residence time, and precursor concentration were maintained at 723 K, 0.152 s, and 2.4 mmol/m^3, respectively.

3.3 Results and Discussion

This section discusses the effects of reaction temperature, precursor residence time, precursor concentration, and the introduction of bipolar charges on reaction kinetics and particle formation and growth.

3.3.1 Effect of Reaction Temperature

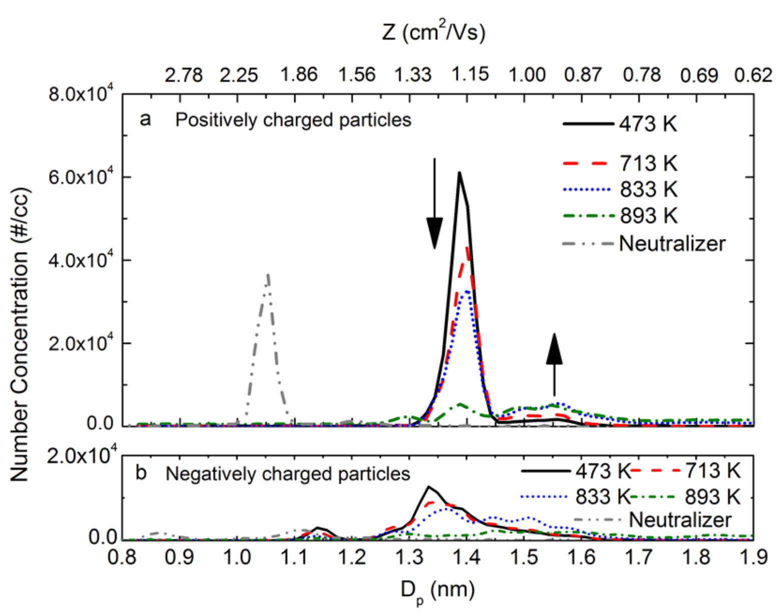

Figure 3.3 Particle size distributions as a function of reaction temperatures at a precursor concentration of 2.4 mmol/m^3. (a) positively charged particles, (b) negatively charged particles. Size distributions of neutralizer generated ions are also displayed.

Size distributions of both positively and negatively charged particles measured with the Half Mini DMA at different furnace temperatures are illustrated in Figures 3.3 and 3.4, with notable ion peaks identified in Figure 3.4 by dashed lines (note different scales of y-axis). Low furnace temperature (473 K) experiments detected positively charged ions at 1.4 nm (peak #1 in Figure 3.4a) and negatively charged ions at 1.15 nm and 1.35 nm (peaks #1 and 2 in Figure 3.4b). These ion peaks were possibly generated by the ionization of TTIP and intermediate molecules in the Kr-85 radioactive neutralizer, since the temperature was not high enough to trigger extensive thermal decomposition of TTIP (Moravec et al. 2001; Eiceman et al. 2013). Figure 3.3 also displays the size distributions of the neutralizer ions without the addition of TTIP, which are significantly different from the ones detected with TTIP addition.

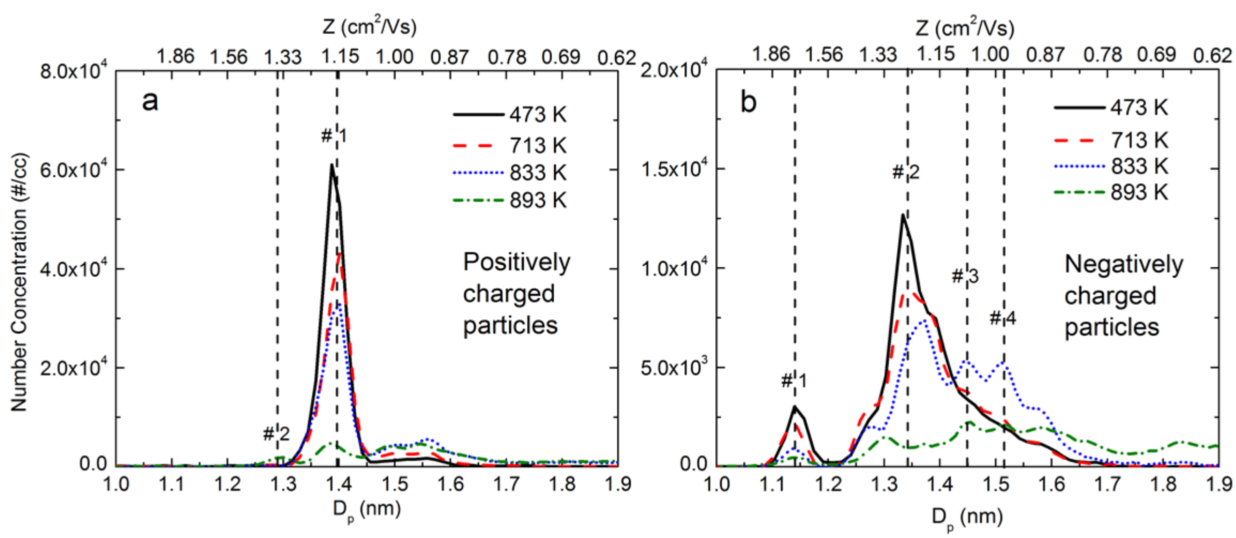

Figure 3.4 Particle size distributions as a function of reaction temperatures at a precursor concentration of 2.4 mmol/m^3. Note different y-axis ranges compared to Figure 3.3. (a) positively charged particles, (b) negatively charged particles. Distinguishable peaks are marked with dashed lines in both positively charged particle size distributions (#1 to 2) and negatively charged particle size distributions (#1 to 4).

As the furnace temperature increased, a decrease in the signals from positively charged particles (peak #1 in Figure 3.4a) was observed, indicating the occurrence of the consumption of TTIP molecules. At the same time, the concentration of positively charged particles with sizes between 1.45 to 1.6 nm increased. At 833 K, newly formed negatively charged particles with sizes of 1.45 nm and 1.53 nm appeared (peaks #3 and 4 in Figure 3.4b). The concentrations of both peaks decreased as temperature further increased, indicating the consumption of these particles through further reaction or particle growth. When the furnace temperature was increased to 893 K, the signals of the originally detected particles in both polarities were significantly reduced due to higher rates of reaction and particle growth into larger sizes. Continuous particle size distributions above 1.6 nm were observed in both polarities, indicating the formation and growth of TiO_2 particles.

An asymmetry of the positively and negatively charged particle size distributions was observed. As shown in Figures 3.3 and 3.4, the total concentration of positively charged particles was much higher than that of negatively charged particles. This is likely due to the fact that organic molecules are prone to carry positive charges. Similar phenomena were also found on the organic contaminants released by tube materials (Steiner and Reischl 2012; Wang et al. 2014). According to charge neutrality, the remaining negatively charged particles might be electrons, which cannot be detected by the DMA since they have extraordinarily high electrical mobilities of over 1000 cm^2/Vs (Romay and Pui 1992). As for the number of species of ions detected, it was also found that negatively charged particles were more diverse than positively charged particles. According to Fuchs' charging theory, the charging process due to collision with ions results in similar size distributions in both polarities (Fuchs 1963; Wiedensohler and Fissan 1991). The difference in the number of ion peaks in both polarities as shown in the results indicated that the charging mechanism of nanoparticles in the sub 2 nm range was not likely to be dominated by collision charging.

It was further observed that the clusters detected from the furnace aerosol reactor were comparatively larger than those detected in flame aerosol reactors (Wang et al. 2014, Fang et al. 2014b). This was likely to be caused by the different particle formation mechanisms at different reaction temperatures. Since the furnace aerosol reactor was operated at relatively lower temperatures (below 1000 K), the precursor molecules might grow to larger clusters before reacting to form TiO_2 clusters. In flame aerosol reactors, the high temperatures encountered (around 1700 K) cause a rapid reaction of precursors resulting in the formation of smaller clusters.

3.3.2 Determination of Chemical Reaction Rates

The decrease of the cluster signal strength as a function of reaction temperature indicated the consumption of precursor molecules due to thermal decomposition. Measured results can therefore be used to obtain reaction rates. By converting the particle mobility to mass with an empirical relationship, $Z = \exp(-0.0347\ln^2(m) - 0.0374\ln(m) + 1.4662)$, where Z is the electrical mobility of the ion in $cm^2/V \cdot s$ and *m* is the mass of ion in Da (Kilpatrick, 1971; Mäkelä et al. 1996), it was found that the calculated mass of the major peak in positively charged particle size distributions (peak #1 of Figure 3.4a, calculated atomic mass with 289 Da) matched well with protonated TTIP molecules (actual atomic mass with 285.2 amu). The existence of the protonated TTIP molecules also agrees with the ionization mechanisms of molecules under the effect of β radiation (Kim et al. 1978; Eiceman et al. 2013). To be noted is that the Kilpatrick's mass-mobility relationship is a curve fitted correlation, and the effect of chemical composition is not taken into consideration. These problems compromise the accuracy in predicting the chemical composition of the detected clusters from mobility values. The accurate determination of the cluster mass depends on the measurement with mass spectrometers. Combined quantum mechanics and molecular dynamics simulation were used by others (Larriba et al. 2011; Larriba and Hogan 2013; Ouyang et al. 2013) to accurately predict the cluster mass amd mobility relationship. A deviation from Kilpatrick's relationship (Kilpatrick, 1971; Mäkelä et al. 1996) below the cluster mass of 200 Da was reported (Steiner et al. 2013). Future work will incorporate both experimental and computational methods to investigate the mobility and mass relationship of clusters genereated during the particle formation process.

A first order reaction rate was estimated by utilizing the signal strength of peak # 1 (Figure 3.4a) in the positively charged particle size distributions, following the routine shown below. The overall chemical reaction for thermal decomposition of TTIP is

$$TTIP \rightarrow TiO_2 + 4C_3H_6 + 2H_2O\,. \tag{3.1}$$

Therefore, the first order reaction rate (R) is

$$R = -k_d C_{TTIP}\,,$$

where C_{TTIP} is the concentration of TTIP, and k_d is the first order reaction rate constant, which has the form of

$$k_d = k_0 \exp(-E_a / R_g T)\,. \tag{3.2}$$

E_a is the activation energy, R_g is the gas constant, and k_0 is a pre-exponential factor.

Assuming plug flow in the tubular reactor (Nakaso et al. 2003), the concentration of TTIP decreases following the differential equation

$$dC_{TTIP} / dt = -R = -k_d C_{TTIP}, \tag{3.3}$$

yielding

$$\ln(C_{TTIP} / C_{TTIP,0}) = -k_d t, \tag{3.4}$$

where $C_{TTIP,0}$ is the concentration of TTIP without reaction, and t is the precursor residence time in the ER zone.

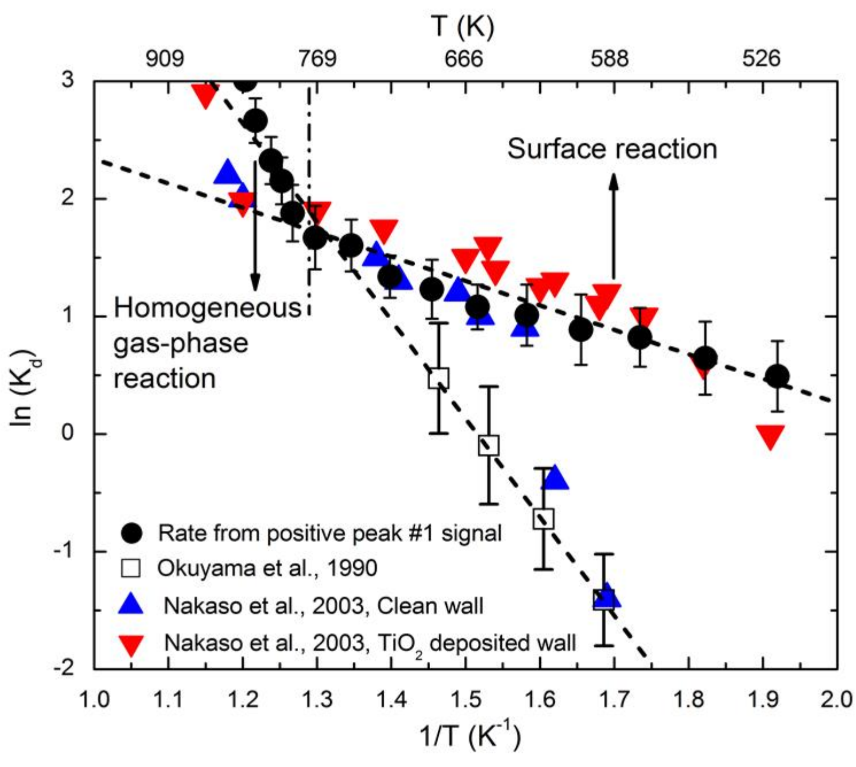

Figure 3.5 First order reaction rate constants of TTIP thermal decomposition as a function of inverse reaction temperatures.

Ideally, the actual concentration of TTIP is proportional to the area under the peak in Figure 3.4a. In this work, the signal strength of the peak (height) was used to represent the TTIP concentration since the peaks were approximately triangular. $C_{TTIP,0}$ was chosen as the signal strength at 473 K, where minimal reaction took place. By extrapolating the signal strengths of the TTIP peaks at different temperatures, the reaction rate constant k_d was calculated using Eq. (3.4). The calculated results (Figure 3.5) quantitatively match existing results derived with Fourier transform infrared spectroscopy (FTIR) (Nakaso et al. 2003). However, as mentioned by Nakaso *et al.* (2003), the FTIR method may have issues of signal overlap due to the similarity of bond structures among different species, introducing uncertainties into measurement results. The size classification method avoids the similarity of chemical properties and hence can serve as an alternative methodology for determining reaction rates.

Results from Figure 3.5 also demonstrated that below 800 K, the reaction rates measured in this work matched only with those measured when TiO_2 deposited on the wall (Nakaso et al. 2003). In the experiments, particle deposition onto the reactor wall could not be well controlled, and repeatable size distributions could be obtained only once the reactor wall was completely coated. The quick transition from the clean wall reaction regime to the TiO_2 deposited wall reaction regime observed by Nakaso et al. (2003) (Figure 3.5) also demonstrate this difficulty in controlling the reaction conditions. Compared to the gas-phase homogeneous reaction rate constant of TTIP thermal decomposition (Okuyama et al. 1990),

$$k_g = 3.96\times10^5[s^{-1}]\exp(-70.5[kJ/mol]/R_gT) \ , \tag{3.5}$$

calculated reaction rate constant below 803 K in this work had a form of

$$k_d = 99.5[s^{-1}]\exp(-16.4[kJ/mol]/R_gT), \tag{3.6}$$

indicating the significance of wall surface reaction on lowering the activation energy for TTIP reaction.

A notable increase of the reaction rate constant was observed at higher reaction temperatures (Figure 3.5). Similar results were also observed by Nakaso et al. (2003), although limited data points were presented. After plotting the size distributions obtained under temperatures higher than 803 K, it was seen that particles with continuous size distributions larger than 1.8 nm were formed (Figure 3.6). The enhanced reaction rates might be caused by the dominance of faster gas-phase reaction of TTIP at higher temperatures. This explanation could be confirmed by the fact that reaction rates obtained at higher temperatures followed the trendline of gas-phase reaction rates presented by Okuyama et al. (1990) (Figure 3.5). Due to the formation of particles with larger sizes, surface reactions on existing TiO_2 particles in gas phase might also start to play a role in TTIP consumption.

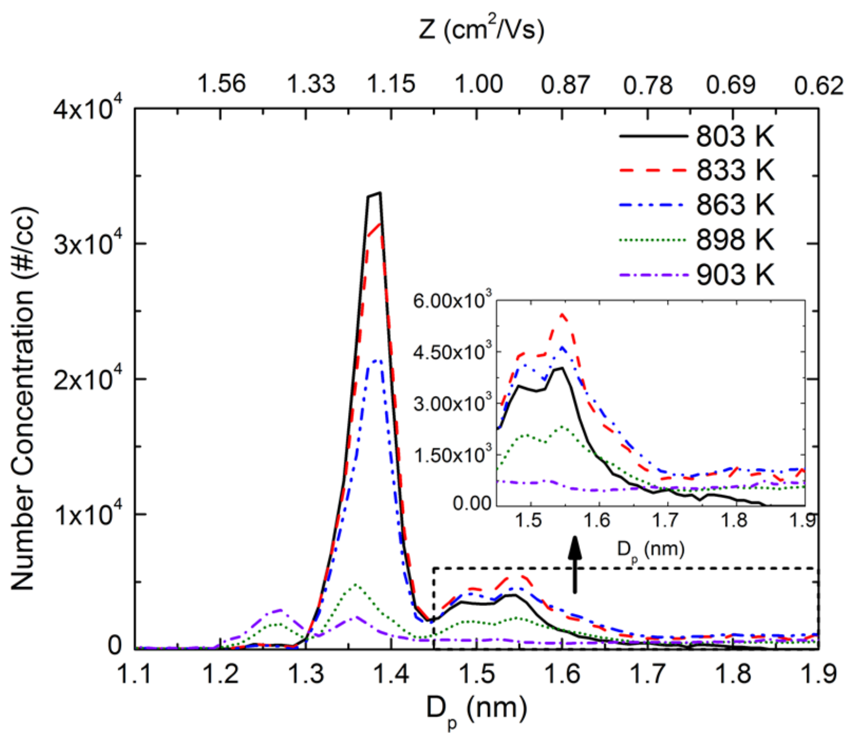

Figure 3.6 Positively charged particle size distributions at temperatures greater than 803 K. Precursor concentration was 2.4 mmol/m^3. Formation of particles with continuous sizes larger than 1.8 nm was observed under high temperature conditions.

Hence, a mechanism of TTIP thermal decomposition, including two reaction regimes, could be proposed, demonstrating the competition between homogeneous gas-phase reaction and heterogeneous surface reaction. Under low reaction temperatures (below ~800 K), due to the lower activation energy, heterogeneous surface reaction dominated the reaction regime. Under higher temperatures (above ~800 K), the reaction rate was promoted by the homogeneous gas-phase reaction of TTIP.

3.3.3 Role of Precursor Residence Time and Precursor Concentrations

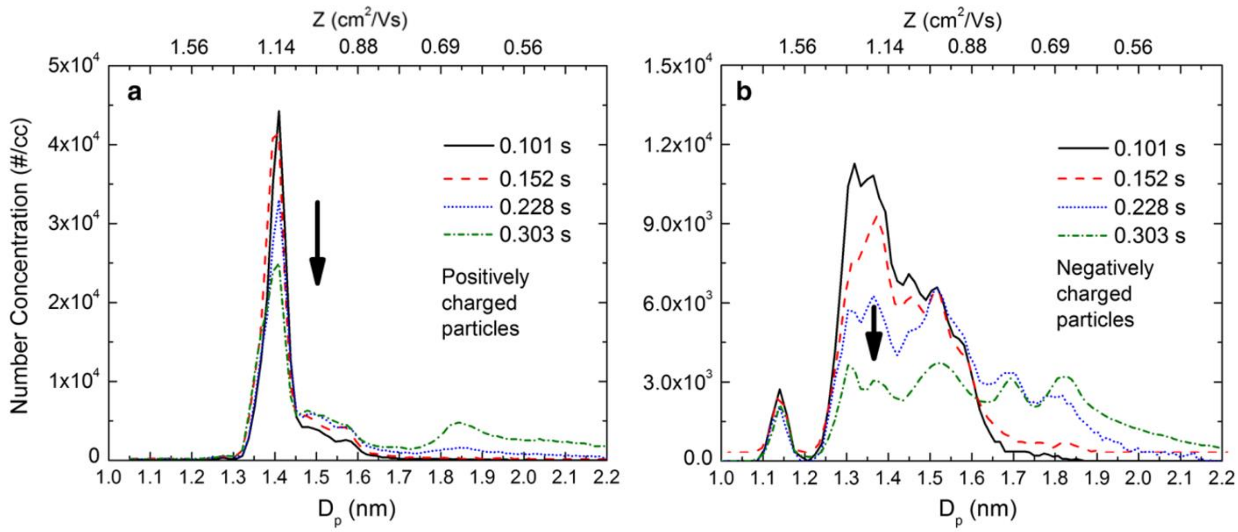

Figure 3.7 Charged particle size distributions as a function of precursor residence times in the furnace. Reaction temperature and precursor concentration were 723 K and 2.4 mmol/m^3 respectively. (a) positively charged particles, (b) negatively charged particles. Note different y-axis ranges.

Figures 3.7 and 3.8 show the influences of precursor residence time and precursor concentration on the evolution of charged particle size distributions. As the residence time increased, the major peaks of positively and negatively charged particles decreased and discrete ion peaks appeared (Figure 3.7), similar to the influence of increasing the reaction temperatures. In the case of higher residence time (0.303 s), continuous size distributions appeared, indicating the consumption of the precursor and the formation of larger particles. The increase in precursor concentration mainly resulted in an increase of detected signals, as shown in Figure 3.8a. It should be noticed that the measured TTIP signal strength was not strictly proportional to the initial precursor concentration, which did not follow the first-order reaction assumptions. This result suggested that there might be higher order reactions during the thermal decomposition of TTIP, which was also observed by Takahashi et al. (1985). Similarly, with higher precursor concentrations, more discrete ion peaks were detected in negatively charged particle size distributions, indicating a higher consumption rate of TTIP molecules.

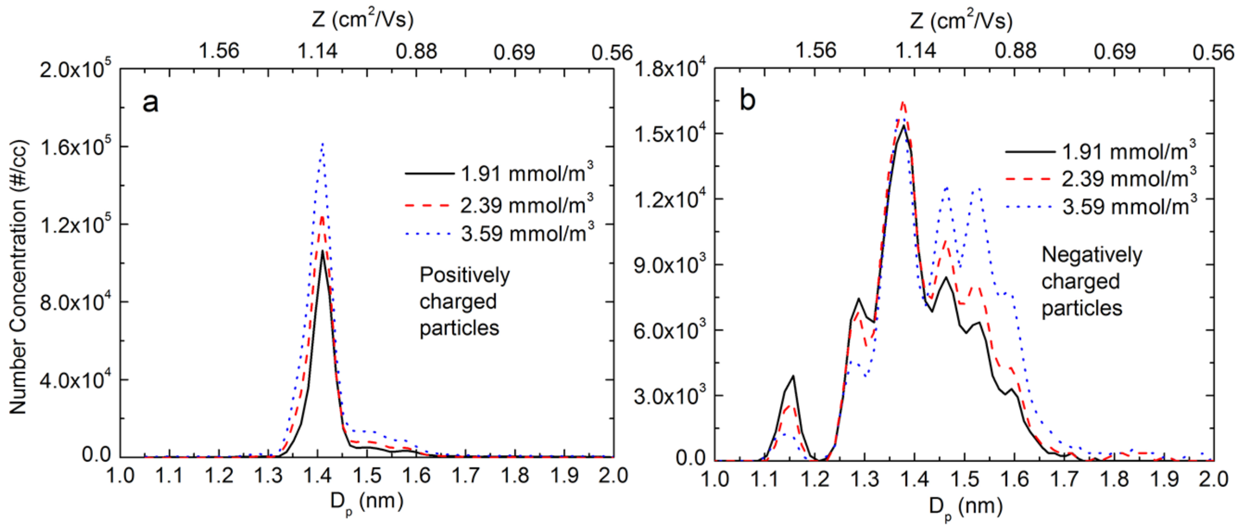

Figure 3.8 Charged particle size distributions as a function of precursor concentrations. Reaction temperature and precursor residence time were 723 K and 0.152 s respectively. (a) positively charged particles, (b) negatively charged particles. Note different y-axis ranges.

3.3.4 Influence of Bipolar Ionic Charges

Figure 3.9 displays the influence of the addition of bipolar ionic charges during the thermal decomposition of TTIP. After bipolar ions were introduced into the reactor, TTIP consumption was enhanced, as indicated by the decrease of the major positive peak concentration and the formation of larger particles. For negatively charged particles, size distributions did not alter much, demonstrating the difference in chemical properties between positively and negatively charged particles.

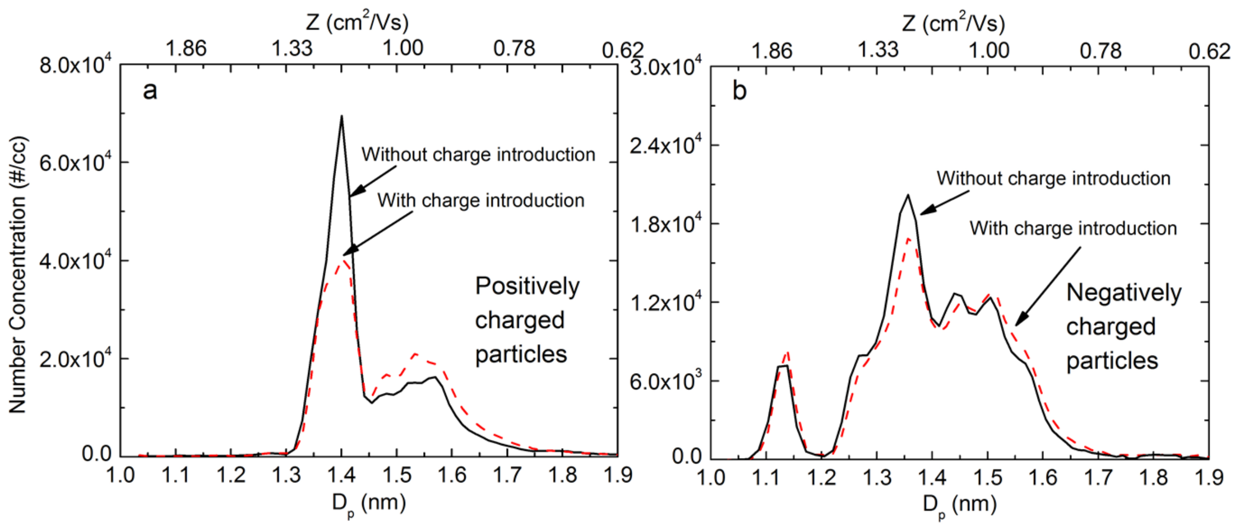

Figure 3.9 Charged particle size distributions measured with and without bipolar charge introduction into the furnace reactor. Reaction temperature, precursor residence time, and precursor concentration were 723 K, 0.152 s, and 2.4 mmol/m^3, respectively. (a) positively charged particles, (b) negatively charged particles. Note different y-axis ranges.

Depending on the species of the carrier gases, different types of bipolar charges are generated, including nitrate ions, hydrate ions, and organic contaminants (Steiner et al. 2012). A recent study conducted by Steiner et al (2013) indicated that nitrate ion (NO_3^-) may be the dominant ions for charging larger particles with negative polarity when using air or nitrogen as the carrier gases. The addition of bipolar charges may enhance particle formation and growth in two different ways. First, ion-induced nucleation might take place and increase the consumption of reactants (Adachi et al. 2004). Ion-induced nucleation has been intensively studied in atmospheric research since it accounts for a significant number of nucleation events (Enghoff and Svensmark 2008). By acting as nucleation centers, bipolar charges increase the heterogeneity of the system and decrease the barrier energy needed for forming stable clusters (Vishnyakov et al. 2011). Second, the introduction of ions might enhance the induced dipole effect and result in higher coagulation efficiencies between the nascent clusters (Zhang et al. 2011). In this way, particles with larger sizes are formed, and the consumption of reactants is enhanced.

3.4 Conclusions

The kinetics of TiO_2 particle formation and growth at initial stages during the thermal decomposition of TTIP were studied with a Half Mini DMA. Clusters below 2 nm were detected for the first time during the thermal decomposition of TTIP. Four factors affecting the reaction kinetics and particle formation and growth were studied: reaction temperature, precursor residence time, precursor concentration, and the introduction of bipolar ionic charges. As reaction temperature increased, a higher consumption of TTIP molecules was observed, while larger particles with characteristic sizes were detected, signifying the formation and growth of particles. The asymmetry of the positively and negatively charged particle size distributions implied that the collision charging is unlikely to be the major charging mechanism below 2 nm. The first order reaction rate derived from the decay of the TTIP signal as a function of the reaction temperature yielded a quantitative match with existing studies, indicating size measurement can serve as a new method for monitoring reaction rates. Wall reaction dominated the reaction mechanisms of TTIP below ~800 K, while under higher temperatures, homogeneous gas-phase reaction promoted the consumption of TTIP. As precursor residence time and precursor concentration increased, the change of the particle size distributions confirmed the formation and growth of TiO_2 particles by the thermal decomposition of TTIP. The addition of bipolar charges enhanced the consumption of TTIP molecules, possibly due to ion-induced nucleation effects and induced dipole effects. Knowledge on incipient particle formation and growth can bridge the gap between chemical reactions in molecular scale and particle further growth beyond nanometer scale, instructing applications such as nanomaterial production and atmospheric pollutant control.

3.5 References

Adachi M, Kusumi M, Tsukui S (2004) Ion-induced nucleation in nanoparticle synthesis by ionization chemical vapor deposition. Aerosol Sci Technol 38(5):496-505

Adachi M, Tsukui S, Okuyama K (2003) Nanoparticle formation mechanism in CVD reactor with ionization of source vapor. J Nanopart Res 5(1-2):31-37

Ahn K, Sohn S, Jung C, Choi M (2001) *In situ* measurement of nano particle size distribution and charge characteristics in H_2/O_2/TEOS diffusion flame. Scripta Mater 44(8):1889-1892

Attoui M, Paragano M, Cuevas J, Fernandez de la Mora J (2013) Tandem DMA generation of strictly monomobile 1–3.5 nm particle standards. Aerosol Sci Technol 47(5):499-511

Bradbury N. E. (1932) The absolute values of the mobility of gaseous ions in pure gases. Phys Rev 40(4):508

Chadha TS, Tripathi AM, Sagar M, Biswas P (2014) One-Dimensional, Additive-Free, Single-Crystal TiO2 Nanostructured Anodes Synthesized by a Single-Step Aerosol Process for High-Rate Lithium-Ion Batteries. Energy Technology (just accepted)

Cho K, Biswas P (2006) Sintering rates for pristine and doped titanium dioxide determined using a tandem differential mobility analyzer system. Aerosol Sci Technol 40(5):309-319

Cho K, Hogan Jr CJ, Biswas P (2007) Study of the mobility, surface area, and sintering behavior of agglomerates in the transition regime by tandem differential mobility analysis. J Nanopart Res 9(6):1003-1012

Eggersdofer ML, Gröhn AJ, Sorensen CM, McMurry PH, Pratsinis SE (2012) Mass-mobility characterization of flame-made ZrO_2 aerosols: Primary particle diameter and extent of aggregation. J Colloid Interface Sci 387(1): 12-23

Eiceman GA, Karpas Z, Hill Jr HH (2013) Ion mobility spectrometry. CRC press

Enghoff M, Svensmark H (2008) The role of atmospheric ions in aerosol nucleation–a review. Atmos Chem Phys 8(16):4911-4923

Fang J, Leavey A, Biswas P (2014a) Controlled studies on aerosol formation during biomass pyrolysis in a flat flame reactor. Fuel 116:350-357

Fang J, Wang Y, Attoui M, Chadha TS, Ray J, Wang WN, Jun YS, Biswas, P (2014b) Measurement of Sub 2 nm Clusters of Pristine and Composite Metal Oxides During Nanomaterials Synthesis in Flame Aerosol Reactors. Anal Chem 86(15):7523-7529

Fernandez de la Mora J (2011) Electrical Classification and Condensation Detection of Sub-3-nm Aerosols. Aerosol Measurement: Principles, Techniques, and Applications, Third Edition:697-721

Fernández de la Mora J, Kozlowski J (2013) Hand-held differential mobility analyzers of high resolution for 1–30nm particles: Design and fabrication considerations. J Aerosol Sci 57:45-53

Freund H, Pacchioni G (2008) Oxide ultra-thin films on metals: new materials for the design of supported metal catalysts. Chem Soc Rev 37(10): 2224-2242

Fuchs N (1963) On the stationary charge distribution on aerosol particles in a bipolar ionic atmosphere. Geofisica Pura Appl 56(1):185-193

Gopalakrishnan R, Meredith MJ, Larriba-Andaluz C, Hogan Jr CJ (2013) Brownian dynamics determination of the bipolar steady state charge distribution on spheres and non-spheres in the transition regime. J Aerosol Sci 63:126-145

Heim M, Attoui M, Kasper G (2010) The efficiency of diffusional particle collection onto wire grids in the mobility equivalent size range of 1.2–8nm. J Aerosol Sci 41(2): 207-222

Hogan Jr CJ, Biswas P, Chen DR (2009) Charged droplet dynamics in the submicrometer size range. J Phys Chem B 113(4):970-976

Hontañón E, Rouenhoff M, Azabal A, Ramiro E, Kruis FE (2013) Assessment of a Cylindrical and a Rectangular Plate Differential Mobility Analyzer for Size Fractionation of Nanoparticles at High Aerosol Flow Rates. Aerosol Sci Technol 48(3):333-339

Jiang J, Chen DR, Biswas P (2007) Synthesis of nanoparticles in a flame aerosol reactor with independent and strict control of their size, crystal phase and morphology. Nanotechnology 18(28):285603

Jiang Y, Wang WN., Biswas P, Fortner J (2014) Facile Aerosol Synthesis and Characterization of Ternary Crumpled Graphene-TiO2-Magnetite Nanocomposites for Advanced Water Treatment. ACS Appl Mater Inter 6(14) 11766-11774

Junninen H, et al. (2010) A high-resolution mass spectrometer to measure atmospheric ion composition. Atmos Meas Tech 3(4):1039-1053

Kallinger P, Setiner G, Szymanski W (2012) Characterization of four different bipolar charging devices for nanoparticle charge conditioning. J Nanopart Res 14(6):1-8

Kilpatrick W (1971) An experimental mass-mobility relation for ions in air at atmospheric pressure In: Proc Annu Conf Mass Spectrosc vol 19. p 320-325

Kim S, Betty K, Karasek F (1978) Mobility behavior and composition of hydrated positive reactant ions in plasma chromatography with nitrogen carrier gas. Anal Chem 50(14):2006-2012

Kim S, Woo K, Liu B, Zachariah M (2005) Method of measuring charge distribution of nanosized aerosols. J Colloid Interface Sci 282(1):46-57

Knutson E, Whitby K (1975) Aerosol classification by electric mobility: apparatus, theory, and applications. J Aerosol Sci 6(6):443-451

Larriba C, Hogan Jr CJ, Attoui M, Borrajo R, Garcia JF, de la Mora JF (2011) The mobility–volume relationship below 3.0 nm examined by tandem mobility–mass measurement. Aerosol Sci Technol 45(4):453-467

Larriba C, Hogan Jr CJ (2013) Ion mobilities in diatomic gases: measurement versus prediction with non-specular scattering models. J Phys Chem A 117(19):3887-3901

Mädler L, Stark WJ, Pratsinis SE (2002) Flame-made ceria nanoparticles. J Mater Res 17(06):1356-1362

Mäkelä JM, Jokinen V, Mattila T, Ukkonen A, Keskinen J (1996) Mobility distribution of acetone cluster ions. J Aerosol Sci 27(2):175-190

Manninen H, et al. (2011) Characterisation of corona-generated ions used in a Neutral cluster and Air Ion Spectrometer (NAIS). Atmos Meas Tech Discuss 4(2):2099-2125

Maricq M (2004) Size and charge of soot particles in rich premixed ethylene flames. Combust Flame 137(3):340-350

Maricq MM (2008) Bipolar diffusion charging of soot aggregates. Aerosol Sci Technol 42(4):247-254

Moravec P, Smolík J, Levdansky V (2001) Preparation of TiO_2 fine particles by thermal decomposition of titanium tetraisopropoxide vapor. J Mater Sci Lett 20(22):2033-2037

Nakaso K, Okuyama K, Shimada M, Pratsinis SE (2003) Effect of reaction temperature on CVD-made TiO_2 primary particle diameter. Chem Eng Sci 58(15):3327-3335

O'Regan B, Grätzel M (1991) A low-cost, high-efficiency solar cell based on dye-sensitized. Nature 353:737-740

Okuyama K, Jeung J-T, Kousaka Y, Nguyen HV, Wu JJ, Flagan RC (1989) Experimental control of ultrafine TiO_2 particle generation from thermal decomposition of titanium tetraisopropoxide vapor. Chem Eng Sci 44(6):1369-1375

Okuyama K, Ushio R, Kousaka Y, Flagan RC, Seinfeld JH (1990) Particle generation in a chemical vapor deposition process with seed particles. AIChE J 36(3):409-419

Ouyang H, Larriba C, Oberreit D, Hogan Jr CJ (2013) The Collision Cross Sections of Iodide Salt Cluster Ions in Air via Differential Mobility Analysis-Mass Spectrometry. J Am Soc Mass Spectrom 24(12):1833-1847

Romay FJ, Pui DY (1992) Free electron charging of ultrafine aerosol particles. J Aerosol Sci 23(7):679-692

Sahu M, Biswas P (2011) Single-step processing of copper-doped titania nanomaterials in a flame aerosol reactor. Nanoscale Res Lett 6(1):1-14

Sgro L, De Filippo A, Lanzuolo G, D'Alessio A (2007) Characterization of nanoparticles of organic carbon (NOC) produced in rich premixed flames by differential mobility analysis. P Combust Inst 31(1):631-638

Siefering K, Griffin G (1990) Growth kinetics of CVD TiO2: influence of carrier gas. J Electrochem Soc 137(4):1206-1208

Steiner G, Jokinen T, Junninen H, Sipilä M, Petäjä T, Worsnop D, Reischl G, Kulmala M (2013) High Resolution Mobility and Mass Spectrometry of Negative Ions Produced in an 241Am Aerosol Charger. Aerosol Sci Technol 48(3):261-270

Steiner G, Reischl GP (2012) The effect of carrier gas contaminants on the charging probability of aerosols under bipolar charging conditions. J Aerosol Sci 54:21-31

Stolzenburg MR (1988) An ultrafine aerosol size distribution measuring system. University of Minnesota

Stolzenburg MR, McMurry PH (2008) Equations governing single and tandem DMA configurations and a new lognormal approximation to the transfer function. Aerosol Sci Technol 42(6):421-432

Takahashi Y, Suzuki H, Nasu M (1985) Rutile growth at the surface of TiO2 films deposited by vapour-phase decomposition of isopropyl titanate. J. Chem. Soc., Faraday Trans. 1 81(12):3117-3125

Thimsen E, Rastgar N, Biswas P (2008) Nanostructured TiO_2 films with controlled morphology synthesized in a single step process: Performance of dye-sensitized solar cells and photo watersplitting. J Phys Chem C 112(11):4134-4140

Ude S, De la Mora JF (2005) Molecular monodisperse mobility and mass standards from electrosprays of tetra-alkyl ammonium halides. J Aerosol Sci 36(10):1224-1237

Vishnyakov V, Kiro S, Ennan A (2011) Heterogeneous ion-induced nucleation in thermal dusty plasmas. J Phys D: Appl Phys 44(21):215201

Wang SC, Flagan RC (1990) Scanning electrical mobility spectrometer. Aerosol Sci Technol 13(2):230-240

Wang WN, An WJ, Ramalingam B, Mukherjee S, Niedzwiedzki DM, Gangopadhyay S, and Biswas P (2012) Size and Structure Matter: Enhanced CO_2 Photoreduction Efficiency by Size-resolved Ultrafine Pt Nanoparticles on TiO_2 Single Crystals. J Am Chem Soc 134(27): 11276-11281

Wang Y, Fang J, Attoui M, Chadha TS, Wang W-N, Biswas P (2014) Application of Half Mini DMA for sub 2 nm particle size distribution measurement in an electrospray and a flame aerosol reactor. J Aerosol Sci 71(0):52-64

Wegner K, Pratsinis SE (2003) Scale-up of nanoparticle synthesis in diffusion flame reactors. Chem Eng Sci 58(20):4581-4589

Wiedensohler A, Fissan H (1991) Bipolar charge distributions of aerosol particles in high-purity argon and nitrogen. Aerosol Sci Technol 14(3):358-364

Winkler PM, Steiner G, Vrtala A, Vehkamäki H, Noppel M, Lehtinen K, Reischl G, Wagner P, Kulmala M (2008) Heterogeneous nucleation experiments bridging the scale from molecular ion clusters to nanoparticles. Science 319(5868):1374-1377

Zeleny J. (1931) The aging of ions in air and nitrogen. Phys Rev. 38(5):969

Zhang X, Zheng H, Battaglia V, Axelbaum RL (2011) Electrochemical performance of spinel $LiMn_2O_4$ cathode materials made by flame-assisted spray technology. J Power Sources 196(7):3640-3645

Zhang Y, Li S, Yan W, Yao Q, Stephen DT (2011) Role of dipole–dipole interaction on enhancing Brownian coagulation of charge-neutral nanoparticles in the free molecular regime. J Chem Phys 134(8):084501

Zhao B, Yang Z, Wang J, Johnston MV, Wang H (2003) Analysis of soot nanoparticles in a laminar premixed ethylene flame by scanning mobility particle sizer. Aerosol Sci Technol 37(8):611-620

Chapter 4: Observation of Incipient Particle Formation during Flame Synthesis by Tandem Differential Mobility Analysis-Mass Spectrometry (DMA-MS)

The results of this chapter have been published in Wang, Y., Kangasluoma, J., Attoui, M., Fang, J., Junninen, H., Kulmala, M., Petäjä, T., Biswas, P. (2017). Observation of incipient particle formation during flame synthesis by tandem differential mobility analysis-mass spectrometry (DMA-MS). Proc. Combust. Inst. 36: 745-752.

Abstract

While flame aerosol reactor (FLAR) synthesis of nanoparticles is widely used to produce a range of nanomaterials, incipient particle formation by nucleation and vapor condensation is not well understood. This gap in our knowledge of incipient particle formation is caused by limitations in instruments, where, during measurements, the high diffusivity of sub 3 nm particles significantly affects resolution and transport loss. This work used a high resolution Differential Mobility Analyzer (DMA) and an Atmospheric Pressure Interface-Mass Spectrometer (APi-TOF) to observe incipient particle formation during flame synthesis. By tandemly applying these two instruments, Differential Mobility Analysis-Mass Spectrometry (DMA-MS) measured the size and mass of the incipient particles simultaneously, and the effective density of the sub 3 nm particles was estimated. The APi-TOF further provided the chemical compositions of the detected particles based on highly accurate masses and isotope distributions. This study investigated the incipient particle formation in flames with and without the addition of synthesis precursors. Results from FLAR using two types of precursors including tetraethyl orthosilicate (TEOS) and titanium isopropoxide (TTIP) are presented. The effect of the precursor feed rates on incipient particle growth was also investigated.

4.1 Introduction

Flame synthesis is a gas-phase approach for producing nanomaterials on an industrial scale, due to its high reaction temperature and fast reaction rates [1]. Flame-synthesized products, such as metal oxides and carbon-based materials, have been widely applied in catalysis [2], solar energy utilization [3], sensor technology [4], the rubber industry [5], and so on. During flame synthesis, the pyrolysis and oxidation of synthesis precursors, the clustering of vapor molecules, particle nucleation, and particle growth through coagulation, vapor condensation, and sintering, all take place in a single-step manner, resulting in a high yield of nanoparticles [6, 7]. The high temperature and fast reaction rate in flames, on the other hand, make it difficult to analyze detailed particle formation pathways. As the starting of the entire particle formation process, especially below 3 nm, significantly affect the characteristics of the final products, such as size, morphology, crystallinity, and chemical composition. However, research on the early stages of particle formation mechanisms is limited by the performance of existing instruments [8, 9]. The *in situ* measurement of particle size distributions in aerosol reactors commonly rely on Differential Mobility Analyzers (DMAs), which can classify a steady and narrowly monomobile stream of charged particles from particles with a continuous spectrum of electrical mobilities [10]. However, the high diffusivity of the sub 3 nm particles greatly decreases the resolution of conventional DMAs and increases the diffusion loss of the measured particles [11]. Molecular Beam Mass Spectrometry (MBMS) is typically used to analyze the composition of flame-generated particles, but the required low-pressure and fuel-rich environment often deviates from the actual operating conditions of flame synthesis [12]. These limitations pose difficulties in measuring incipient particles during flame synthesis, hindering a comprehensive understanding of the particle formation mechanisms.

With the development of a new set of instruments for investigating atmospheric particle nucleation [13] and for analyzing protein properties [14] in the past decade, measuring sub 3 nm particle size and mass at atmospheric conditions has become feasible. DMAs with sheath flow rates of over 100 lpm are used to significantly reduce the residence time and the Brownian diffusion of particles in the instruments, increasing the resolution by orders of magnitude when measuring sub 3 nm particles [15]. The recently developed Atmospheric Pressure Interface Time-Of-Flight Mass Spectrometer (APi-TOF) is able to detect and analyze the chemical composition of atmospheric ions and charged clusters with high transmission and resolution [16]. Selected groups of molecular species were identified as playing an important role in atmospheric particle nucleation and growth [17]. Tandem Differential Mobility Analysis-Mass Spectrometry (DMA-MS) can simultaneously measure particle size and mass, and critical information on particle structure, charging characteristics, and formation mechanisms is obtained [18-20].

In this study, the incipient particle formation and growth below 3 nm in a premixed flat flame was investigated with the DMA-MS technique, where a high resolution DMA and an APi-TOF were used to counteract the particle Brownian diffusion and loss in the system. Direct measurement with the high resolution DMA coupled with an aerosol electrometer was conducted to provide the size distributions of particles generated during flame synthesis. The APi-TOF was used to determine the compositions of important intermediate particles during the synthesis of SiO_2 and TiO_2. The structure of the incipient flame-synthesized particles was further analyzed with the size and mass data measured by the DMA-MS.

4.2 Methods

4.2.1 Experimental Setup

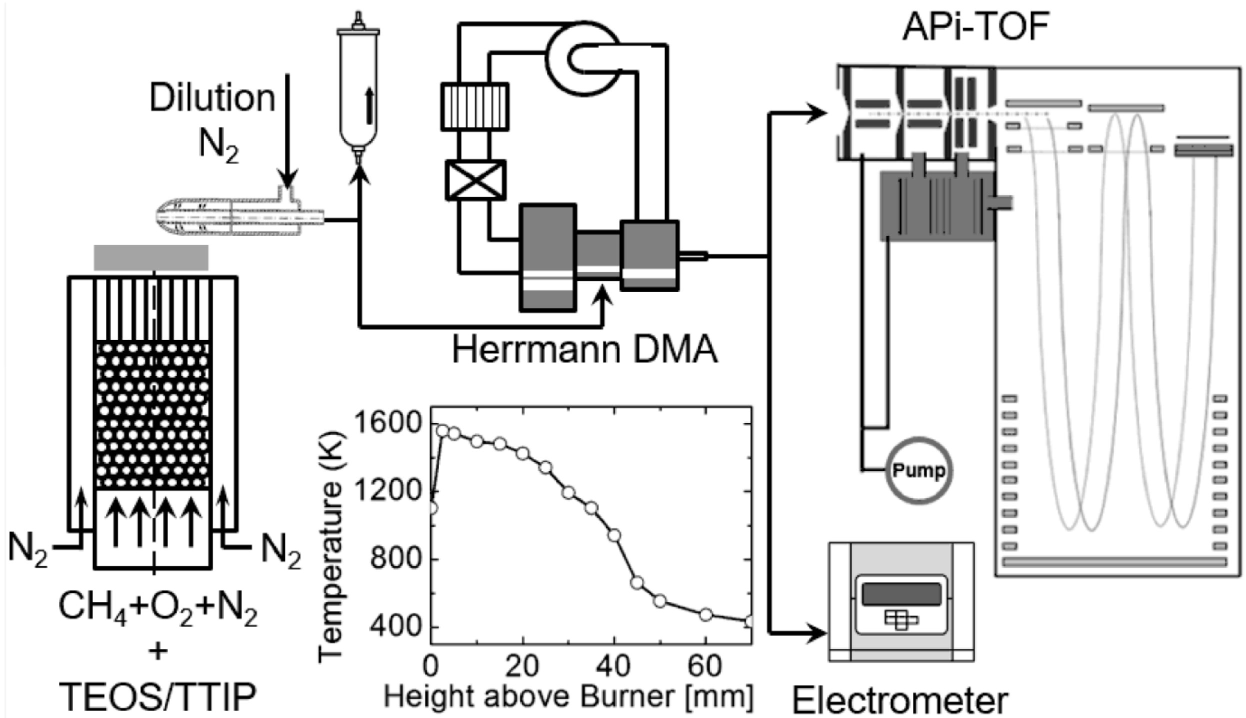

Figure 4.1 Schematic diagram of the experimental setup for measuring the incipient particles generated during flame synthesis. The Herrmann DMA classified particles with the same electrical mobility. The APi-TOF and the electrometer provided the mass spectrum and the concentration of the classified particles. The inset figure shows the temperature profile along the centerline above the burner.

Figure 4.1 shows the schematic diagram of the experimental setup. The system consisted a premixed flat flame burner, a dilution sampling probe, a high resolution DMA (Herrmann-type [21]), an APi-TOF (TOFWERK AG), and an aerosol electrometer (Model 3068B, TSI Inc.). A premixed flat flame was used in this study due to its uniformity and stability [22]. The stainless steel burner consisted of two concentric tubes with diameters of 0.75 inch and 1 inch, respectively, leaving a gap for passing a stream of N_2 (>99.95%, Linde AG) to protect the flame from the environment. In order to achieve a uniform velocity profile, the head of the burner was capped with a stainless steel honeycomb featuring a mesh size of 0.5 mm. Below the honeycomb cap, the inner tube was filled with 2 mm stainless steel beads for laminarizing the premixed flow streams. The gas mixture was composed of CH_4 (> 99.5%, Linde AG), O_2 (> 99.95%, Linde AG), and N_2, maintained at total flow rates of 1 lpm, 2.85 lpm, and 8 lpm respectively, with the help of mass flow controllers (MKS Inc.). The flame equivalence ratio (ϕ) was calculated to be 0.7. Organometallic precursors for synthesizing nanoparticles were introduced into the flame by bubbling a clean stream of N_2 though liquid precursors of tetraethyl orthosilicate (TEOS, > 98 %, Sigma-Aldrich Inc.) or titanium isopropoxide (TTIP, > 97 %, Sigma-Aldrich Inc.), at a temperature of 20 ^{o}C. At high temperatures in flames, these synthesis precursors reacted through thermal decomposition and oxidation to generate SiO_2 or TiO_2 nanoparticles, and previous studies demonstrated that a large amount of sub 3 nm particle were formed during these processes [8, 9, 11]. The feed rates of synthesis precursors were calculated according to the materials' saturation pressure data presented by Jang [23] for TEOS and Siefering and Griffin [24] for TTIP. Flame temperature was measured with a type R thermocouple, and the temperature profile is shown as the inset in Figure 4.1. Due to the low concentration of the synthesis precursors (as shown in Table 4.1), the effect of adding precursors on flame equivalence ratio and flame temperature were minimal. 5 mm above the head of the burner, a dilution sampling probe was used to introduce the flame-generated particles to downstream instruments while quenching further reactions and particle growth. By considering the thermal expansion of the sampled flow, a dilution ratio of 200 was attained [9]. Note that ionization sources were not applied in the system, implying that the downstream instruments measured the natively charged flame synthesized particles only. Due to a series of reported chemical ionization reactions, the flame acted as a neutral plasma that generated high concentrations of ions, which were sufficient to charge the incipient particles in the flame at various equivalence ratios [12]. It should be also noticed that not all of the flame-generated particles were charged, and the fraction of charged particles was a function of sampling height and flame conditions. To study the properties of neutral particles, well-characterized chemical ionization sources are needed to provide the neutral particles with known charges so that they can be detected by the instruments [25].

A Herrmann-type DMA was used to classify sub 3 nm particles with high resolution. The DMA was operated in a closed loop to maintain the same flow rate of the aerosol inlet and outlet flows. An inline blower (DOMEL Inc.) provided the recirculating sheath flow (> 500 lpm), and an inline filter and heat exchanger removed the remaining particles and released the heat generated by the blower, respectively. The DMA classifies particles according to the relationship between the drag force and the electrostatic force. When a voltage (V) is applied across the electrodes of the DMA, the classified particles have a uniform mobility (Z) [10], which is further related to the size of a particle by $Z = Cne/3\pi\mu D_p$, where C is the Cunningham slip correction factor, n is the number of charges on the particle, e is the electronic charge, μ is the air viscosity, and D_p is the particle mobility size. For sub 3 nm particles, it is safe to assume that classified particles carry a single charge [26], which was also observed by the mass spectrometer during the experiments, since the isotope peaks that differ by mass units other than 1 were not detected. The potential across the DMA was applied by a high voltage source (Spellman Inc.) controlled by a Labview program. During the measurements, a step voltage of 3 V, a step time of 1 s, and a voltage scanning range of 100 to 1000 V were used to classify particles with size from 0.5 to 2 nm. It should be noted that the mobility size does not necessarily represent the particle physical size, especially for sub 3 nm particles whose chemical composition may significantly determine the structure of the cluster, while the size of non-spherical particles is poorly defined. Existing studies show that the particle mobility size subtracted by 0.3 nm agrees well with the volume size of the sub 3 nm clusters [18]. However, for simplicity, this study used particle mobility size as the indicator of particle physical size. At the same time, the inverse mobility values are marked in the graphs for reference. Before measuring the flame-generated particles, the DMA was first calibrated with the particles generated by electro-spraying a 0.2 mM tetraheptylammonium bromide-methanol solution [15]. The mobility of particles classified at an arbitrary DMA voltage can be accurately determined. We should also note that, although the DMA sheath flow is significantly increased, the high diffusivity of the sub 3 nm particles can still play a role in lowering the resolution of the DMA measurements, which is discussed in more detail in our previous work [11].

Downstream of the DMA, an aerosol electrometer (EM) collected the classified monomobile particles at a flow rate of 10 lpm. The recorded current was directly proportional to the charged particle concentration if particles carried one unit charge. In the following, the particle size distributions were qualitatively shown with the EM current as a function of particle size, since the data inversion of sub 3 nm particle size distributions was difficult to conduct due to the chemistry-dependent charging process [11]. The APi-TOF measured the mass-to-charge ratio (m/z) of the DMA-classified sub 3 nm particles. It can achieve a mass resolving power of 3000 Th/Th and a mass accuracy of 0.002%. The chemical composition of the measured particles was further analyzed by tofTools (a Matlab based set of programs [16, 27]), with the help of the highly accurate atomic mass and isotope distributions. Before measurements, the APi-TOF was calibrated with nitrate ions produced by a chemical ionization source. The DMA-MS technique simultaneously measures the particle size and the mass spectrum of the DMA-classified particles. The mass-size relationship further reveals the structure and effective density of the detected particles. This study investigated the mass-size relationship of the negatively charged particles only, since the positively charged particles were found to be unstable when they were transported from the DMA to the APi-TOF [20, 25, 28]. The obtained data are conveniently represented as contour plots, with the x-axis being the particle size or electrical mobility, and y-axis being m/z. The color of the data point denotes the relative abundance of the signal (black stands for the most intense signal, and white stands for the least intense signal).

4.2.2 Experimental Plan

Five sets of experiments were conducted in this study and tabulated in Table 4.1. Test 1 studied the properties of charged particles generated from blank flames without the addition of the precursors. Tests 2 and 3 were conducted with the addition of different types of precursors to investigate the formation pathways of different types of nanoparticles. Tests 4 and 5, together with Test 2, further examined the influence of synthesis precursor feed rates on the incipient particle formation during flame synthesis.

Table 4.1 Experimental plan.

Test	Precursor Type	Feed rates [mmol/hr]
1	N/A	N/A
2	TEOS	0.118
3	TTIP	0.157
4	TEOS	0.235
5	TEOS	0.353

4.3 Results and Discussion

4.3.1 Particle formation in blank flames

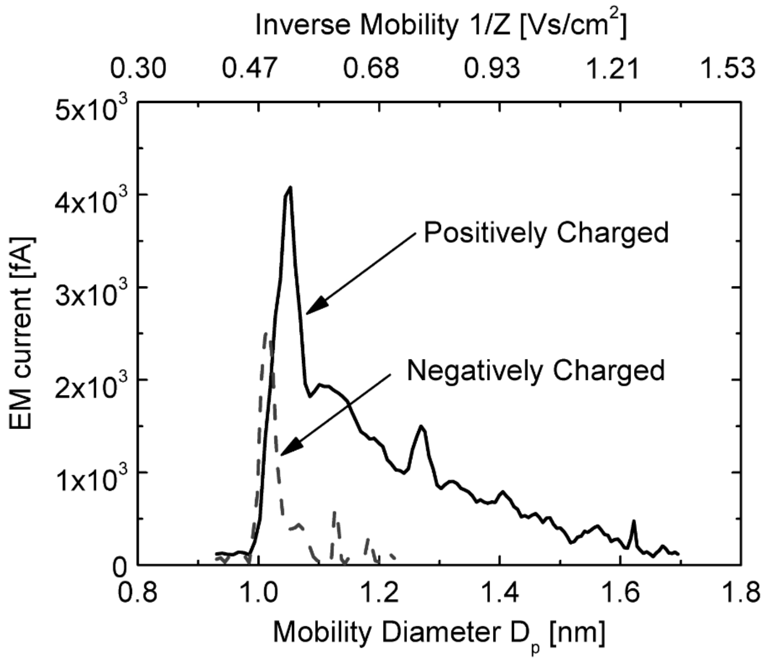

Figure 4.2 Size distributions of sub 3 nm charged particles generated from the blank flame.

Figure 4.2 shows the DMA-measured size distributions of the natively charged particles generated from the blank flame without the addition of the precursors. Charged particles below 1.8 nm in both polarities were observed in large quantities. The chemical ionization reactions in the flame are major sources of these charged particles [12]. The positively charged particles had a larger and broader distribution of sizes, yielding a relatively smaller electrical mobility compared to negatively charged particles. Similar results were observed in commonly used ionization sources such as radioactive neutralizers [20, 29] and corona dischargers [28]. The explanation for this phenomenon may be that, during the ionization process, the relatively large organic molecules act as positive charge carriers, while negative charge carriers are dominated by electrons. The electrons further combine with other molecules to form relatively smaller negatively charged particles with low proton affinities. Based on charge neutrality, the concentration difference between the positively and the negatively charged particles (Figure 4.2) also indicated that the remaining negative charge carriers were electrons, whose electrical mobility is too high (> 1000 cm^2/Vs [12]) to be measured by the DMA. These charged particles may actively collide with nanoparticles during flame synthesis conditions. According to Fuchs charging theory [25], this difference in the averaged electrical mobility will cause a higher fraction of particles carrying negative charges, which has been observed in previous studies [30, 31].

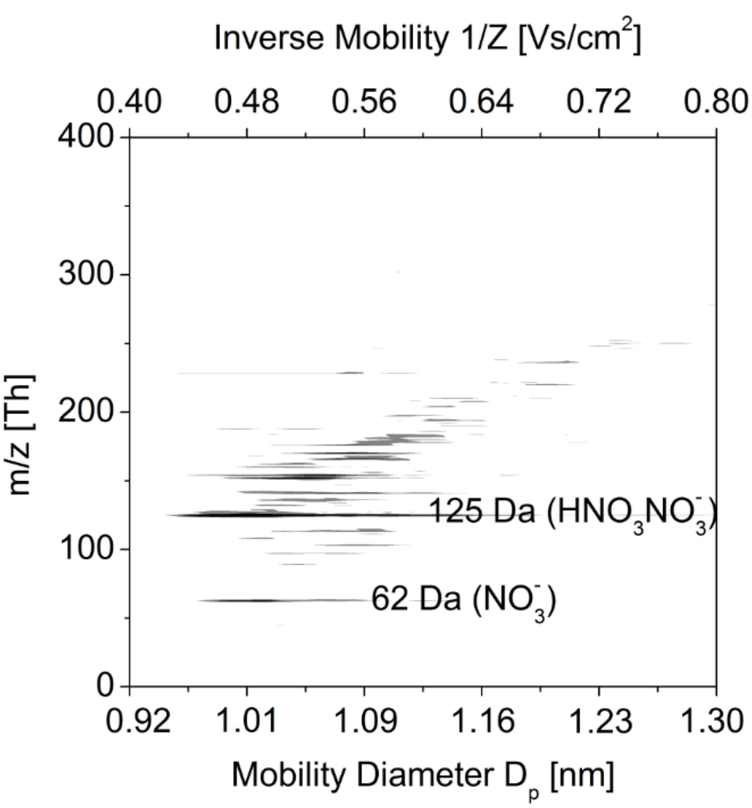

Figure 4.3 Contour plot showing the abundance of the blank flame-generated negatively charged particles as a function of size and m/z.

Figure 4.3 displays the mass-size relationship of the negatively charged particles generated from the blank flame. At the inverse mobility of 0.48 Vs/cm^2 (mobility size of 1.01 nm) where the EM detected the highest particle concentration (Figure 4.2), the mass spectrum indicated that these particles were mainly composed of nitrate ions (NO_3^- at m/z of 62 Th, and $HNO_3 \cdot NO_3^-$ at m/z of 125 Th). The formation of these nitrate ions might be caused by the active NO_x production in the blank flame, especially when the combustible mixture was premixed and the flame was operated in a fuel-lean condition [32]. The NO_x species may further react with water vapor to form nitrate ions. Due to their low proton affinities, these nitrate ions became the dominant negative charge carriers, which was also observed in other types of ionization sources [20, 28, 33]. The existence of two different masses (62 Da and 125 Da) corresponding to a same mobility size (1.01 nm) suggested that the ions might be fragmented when they transported from the DMA to the APi-TOF. Aside from the nitrate ions, negatively charged particles with sizes and masses larger than 1.01 nm and 125 Da respectively were also detected. They were probably generated during the collision between electrons with relatively larger organic molecules. The detection of a spectrum of ions implied the complexity of chemical ionization reactions and the following particle charging process in flames.

4.3.2 Addition of flame synthesis precursors

The sub 3 nm particle size distributions obtained under different synthesis conditions are shown in Figure 4.4. When synthesis precursors were added to the flame, the DMA measurements detected particles larger than flame-generated particles, as a result of particle formation and growth. The sizes of these particles were also found to be discrete instead of continuous, which implied that certain stable species might act as important intermediates during particle formation. The average size and concentration of the positively charged particles was still greater than those of the negatively charged particles, where the existence of relatively small charge carriers might play an important role, as explained above.

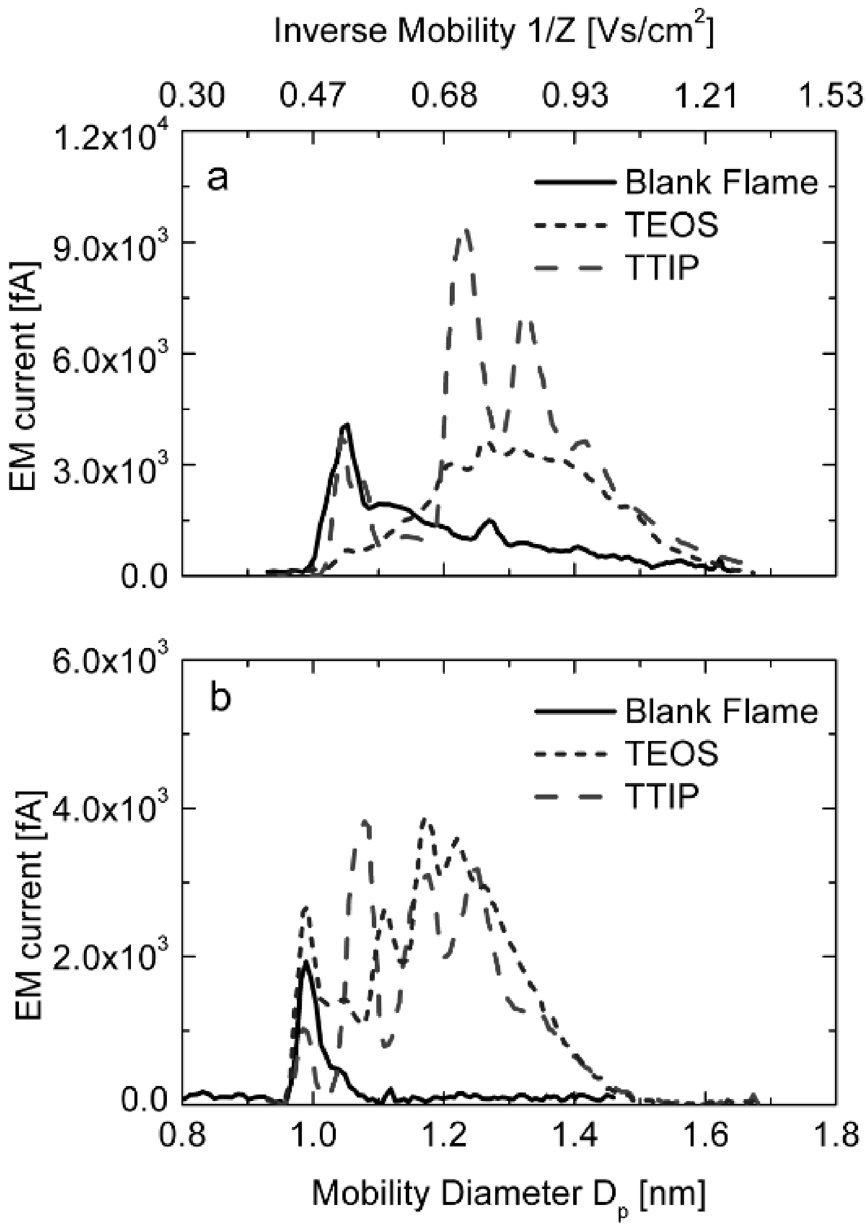

Figure 4.4 Size distributions of sub 3 nm charged particles under different synthesis conditions. a) positively charged particles; b) negatively charged particles. Note different scales of y-axes.

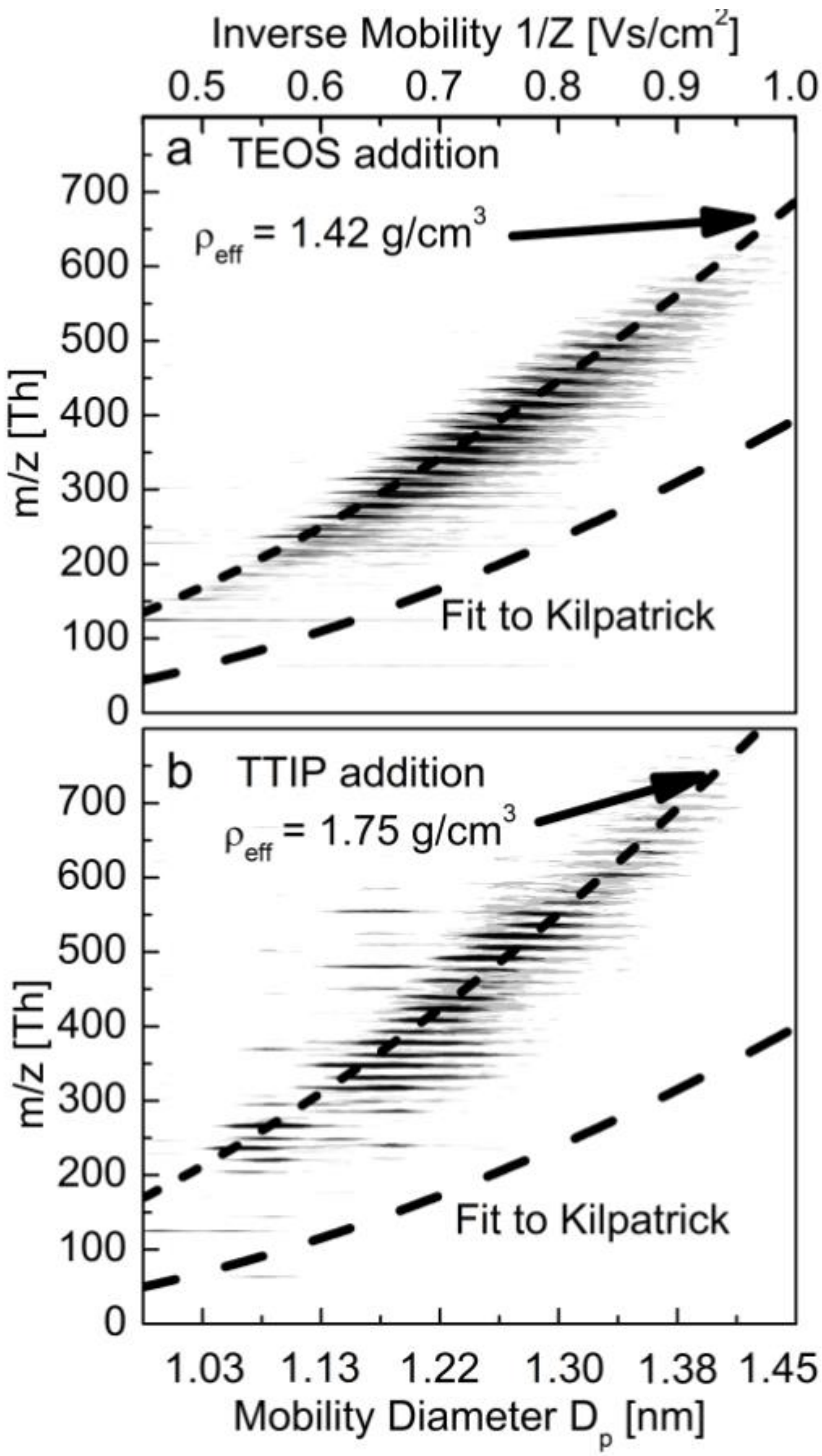

Figure 4.5 Contour plots showing the abundance of negatively charged particles during flame synthesis conditions as a function of size and m/z. a) using TEOS as synthesis precursor; b) using TTIP as synthesis precursor. The mass-size relationships assuming that particles were spherical are displayed as short-dashed lines. The fit to Kilpatrick's mass-mobility relationship is displayed as long-dashed lines.

Table 4.2 Chemical compositions of major negatively charged particles detected by the APi-TOF under different flame conditions.

Blank flame		**TEOS addition**		**TTIP addition**	
Chemical formula	**m/z**	**Chemical formula**	**m/z**	**Chemical formula**	**m/z**
NO_3^-	61.9878	NO_3^-	61.9878	NO_3^-	61.9878
$HNO_3 \cdot NO_3^-$	124.9835	$Si_2H_6NO_{10}^-$	235.9530	$TiN_2O_{10}^-$	235.9032
		$Si_3H_6NO_{12}^-$	295.9198	$TiN_3O_{11}^-$	265.9012
		$Si_3H_8NO_{13}^-$	313.9303	$Ti_2NO_{11}^-$	285.8437
		$Si_4H_{10}NO_{16}^-$	319.9077	$Ti_2N_2O_{14}^-$	347.8308

The mass-size relationships of the flame-generated sub 3 nm particles during synthesis conditions are shown in Figure 4.5. Major negatively charged species, such as $Si_2O_4(H_2O)_3NO_3^-$ (236 Th), $Si_3O_6(H_2O)_3NO_3^-$ (296 Th), $TiO_2(NO_3)_3^-$ (266 Th), and $Ti_2O_8(NO_3)_2^-$ (348 Th) were detected by the APi-TOF. Table 4.2 lists the incipient particles with identified compositions and atomic masses. The existence of nitrate ions in the silicon and titanium-containing particles implied a strong interaction between the flame-generated ions and the synthesized particles. Since flame synthesis is conducted with N_2 as the diluting gas on many occasions, these detected ions may act as contaminants for particle growth and crystallization. Hence, further studies investigating the incipient particle formation mechanisms without N_2 participation are needed. Figure 4.5 also shows that the detected particles fell into different bands with strong signal intensities. A lot of these bands were separated by the atomic masses of N (14 Da), O (18 Da), or H_2O (18 Da), instead of by the atomic mass of SiO_2 (60 Da) or TiO_2 (80 Da).

This result suggested the high involvement of blank flame-generated species in particle synthesis. To confirm that the measured charged particles represent the characteristics of those generated in the flame, further experiments using an enhanced condensation particle counter and a charged particle remover was conducted. Results show that under the tested conditions, the charging fraction of sub 3 nm particles is extremely high, where more than 90% of the flame-generated sub 3 nm particles were charged [34]. The high charge fraction also contradicts the classical charging theories, suggesting that further studies on the charging mechanisms of particles in flames are needed.

Depending on the type of nanoparticles synthesized, the mass-size relationships show different trends in Figure 4.5. At a same mobility size of 1.30 nm, the particles generated from TTIP reactions (~ 550 Da) were heavier than the particles generated from TEOS reactions (~ 420 Da), which was possibly caused by the higher atomic mass of titanium. Based on the mass and mobility size values, an effective density (ρ_{eff}) could be calculated for these incipient particles following the method introduced below. By assuming that the detected particles were spherical, the effective density satisfied the relationship of $m = \pi D_p^3 \rho_{eff} / 6$, where m is the particle mass and D_p is the particle size. The value of the effective density should guarantee that most of the data points in the contour plot fall on the curve representing the spherical particle mass-size relationship. Further calculation indicated that using particle volume size (mobility size subtracted by 0.3 nm [18]) as D_p provided a better fit when calculating ρ_{eff}, since the mobility size of a particle overestimates the physical size below 3 nm, due to the enhanced interaction between the charged cluster and the dipole it induced in the gas molecules [18]. The particles generated from flames with the addition of TEOS and TTIP had effective densities of 1.42 g/cm^3

and 1.75 g/cm^3, respectively. These incipient particles were less dense than the SiO_2 and TiO_2 bulk crystals (2.65 g/cm^3 and 4.23 g/cm^3), possibly because these particles were in an amorphous state, where the atoms were not tightly packed. The attachment of the species other than oxides, such as nitrate and organic molecules, on these incipient particles might also lower the density of the detected particles.

The simultaneously measured mobility and mass of the flame-generated incipient particles could be compared with the data calculated from empirically determined mass-mobility relationships. The most widely used mass-mobility relationship was presented by Kilpatrick [35] and was further fitted with a function of

$$Z = \exp[-0.0347\ln^2(m) - 0.0376\ln(m) + 1.4662], \tag{4.1}$$

where Z and m represent the particle electrical mobility (unit: cm^2/Vs) and atomic mass (unit: Da), respectively [36]. The fitted functions of Kilpatrick's mass-mobility relationship are also displayed in Figure 4.5, showing that, at a same electrical mobility, the actual particle mass is higher than the mass predicted by the empirical relationship. This discrepancy can be explained by the fact that the electrical mobility is largely determined by the structure of particles, while particles with similar structures can have different chemical compositions and atomic masses. Due to the existence of relatively heavy species such as silicon and titanium, the flame-generated incipient particles had higher masses. Since researchers often rely on Kilpatrick's relationship to convert the measured mobility to the mass of particles in order to decipher the particle composition, this measured result proves that the existing mass-mobility relationships will be dependent on the type of chemical species. Directly using these relationships may therefore cause errors. To better predict the mass-mobility relationships, numerical methods were used by researchers to consider the physical collision and potential interaction between the molecular clusters and particles, where a desirable agreement was observed between the calculated and the experimentally measured mass and mobility data [37].

4.3.3 Effect of the synthesis precursor feed rates

Figure 4.6 shows the effect of TEOS feed rates on the DMA-MS measured incipient particle size and mass distributions. The concentration of the particles with larger sizes and masses increased as more precursors were fed to the flame, indicating a stronger particle growth process by vapor condensation and coagulation. The concentration of the smaller charged particles with low mass and size decreased due to coagulation and the scavenging effect caused by the existing larger particles. The calculated effective density remained the same (Figure 4.6), demonstrating that the particle formation pathway did not change as a function of precursor feed rates.

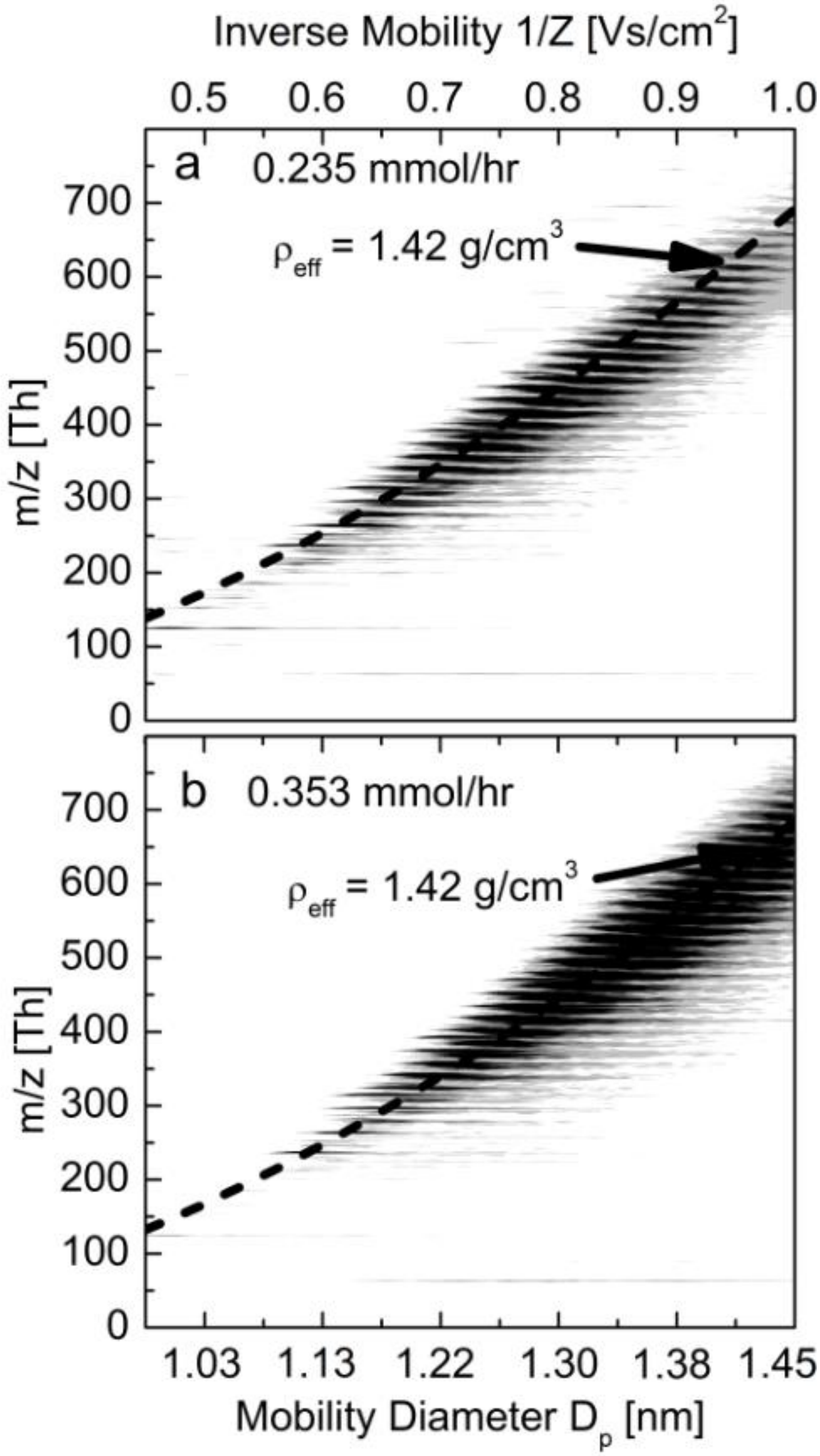

Figure 4.6 Contour plots showing the abundance of negatively charged particles generated at different TEOS feed rates as a function of size and m/z. a) TEOS feed rate of 0.235 mmol/hr; b) TEOS feed rate of 0.353 mmol/hr. The mass-size relationships assuming that particles were spherical are displayed as short-dashed lines.

4.4 Conclusions

The incipient particle formation during flame synthesis was investigated for the first time using the tandem DMA-MS technique. A high resolution DMA and an APi-TOF were used to measure the size and mass of the sub 3 nm particles simultaneously in the flames without the addition of synthesis precursors and with the addition of TEOS or TTIP.

Measurements in a blank flame detected a large number of sub 3 nm particles generated from chemical ionization reactions, and determined that nitrate ions dominated in the negative ions. The formation of nitrate ions may be related with the NO_x formation in flames. Measurements conducted with the addition of synthesis precursors found particles with discrete size distributions, indicating the existence of stable particles as important intermediates during flame synthesis. The blank flame-generated ions played an important role during particle synthesis, since the APi-TOF observed the appearance of nitrate ions in particles containing silicon or titanium. Future work on flame synthesis while manipulating the ion properties, may bring new perspectives on manufacturing functional nanomaterials at high temperatures. The effective densities of the incipient particles were calculated by assuming that the particles were spheres. These particles had lower densities than the bulk materials of SiO_2 and TiO_2, possibly because of the impurities in the particles and their amorphous structures. The commonly used Kilpatrick's mass-mobility relationship was also evaluated in this study, and the difference between the measured data and the Kilpatrick's relationship suggested that particle compositions largely determined particle mass and mobility. As precursor feed rate increased, particles with larger mass and sizes were formed due to enhanced coagulation and vapor condensation. The unchanged particle effective density implied that the particle formation pathway in flames was not a function of precursor feed rates.

4.5 References

[1] P. Roth, Proc. Combust. Inst. 31 (2007) 1773-1788.

[2] F. Niu, S. Li, Y. Zong, Q. Yao, J. Phys. Chem. C, 118 (2014) 19165-19171.

[3] E. Thimsen, N. Rastgar, P. Biswas, J. Phys. Chem. C 112 (2008) 4134-4140.

[4] S. Bakrania, C. Perez, M. Wooldridge, Proc. Combust. Inst. 31 (2007) 1797-1804.

[5] P.T. Spicer, C. Artelt, S. Sanders, S.E. Pratsinis, J. Aerosol Sci. 29 (1998) 647-659.

[6] J. Jiang, D.-R. Chen, P. Biswas, Nanotechnology, 18 (2007) 285603.

[7] Y. Zhang, L. Shuiqing, S. Deng, Q. Yao, S.D. Tse, J. Aerosol Sci. 44 (2012) 71-82.

[8] J. Fang, Y. Wang, M. Attoui, T.S. Chadha, J.R. Ray, W.-N. Wang, Y.-S. Jun, P. Biswas, Anal. Chem. 86 (2014) 7523-7529.

[9] Y. Wang, P. Liu, J. Fang, W.-N. Wang, P. Biswas, J. Nanopart. Res. 17 (2015) 1-13.

[10] E. Knutson, K. Whitby, J. Aerosol Sci. 6 (1975) 443-451.

[11] Y. Wang, J. Fang, M. Attoui, T.S. Chadha, W.-N. Wang, P. Biswas, J. Aerosol Sci. 71 (2014) 52-64.

[12] A.B. Fialkov, Prog. Energy Combust. Sci. 23 (1997) 399-528.

[13] M. Kulmala, J. Kontkanen, H. Junninen, K. Lehtipalo, H.E. Manninen, T. Nieminen, T. Petäjä, M. Sipilä, S. Schobesberger, P. Rantala, Science 339 (2013) 943-946.

[14] C.J. Hogan Jr, J.F. de la Mora, J. Am. Soc. Mass. Spectrom. 22 (2011) 158-172.

[15] J. Fernandez de la Mora, Aerosol Measurement: Principles, Techniques, and Applications, John Wiley & Sons, Inc., Hoboken, New Jersey, U.S., 2011, p. 697.

[16] H. Junninen, M. Ehn, T. Petäjä, L. Luosujärvi, T. Kotiaho, R. Kostiainen, U. Rohner, M. Gonin, K. Fuhrer, M. Kulmala, Atmos. Meas. Tech. 3 (2010) 1039-1053.

[17] M. Ehn, J.A. Thornton, E. Kleist, M. Sipilä, H. Junninen, I. Pullinen, M. Springer, F. Rubach, R. Tillmann, B. Lee, Nature 506 (2014) 476-479.

[18] C. Larriba, C.J. Hogan Jr, M. Attoui, R. Borrajo, J.F. Garcia, J.F. de la Mora, Aerosol Sci. Technol. 45 (2011) 453-467.

[19] A. Maißer, V. Premnath, A. Ghosh, T.A. Nguyen, M. Attoui, C.J. Hogan, PCCP 13 (2011) 21630-21641.

[20] A. Maißer, J.M. Thomas, C. Larriba-Andaluz, S. He, C.J. Hogan, J. Aerosol Sci. 90 (2015) 36-50.

[21] W. Herrmann, T. Eichler, N. Bernardo, J. Fernández de la Mora, Annual Conference of the American Association for Aerosol Research, St. Louis, MO, U.S., 2000.

[22] X. Wang, E. Cotter, K.N. Iyer, J. Fang, B.J. Williams, P. Biswas, Proc. Combust. Inst. 35 (2015) 2347-2354.

[23] H.D. Jang, Aerosol Sci. Technol. 30 (1999) 477-488.

[24] K. Siefering, G. Griffin, J. Electrochem. Soc. 137 (1990) 1206-1208.

[25] J. Kangasluoma, M. Attoui, H. Junninen, K. Lehtipalo, A. Samodurov, F. Korhonen, N. Sarnela, A. Schmidt-Ott, D. Worsnop, M. Kulmala, J. Aerosol Sci. 87 (2015) 53-62.

[26] N. Fuchs, Geofis. pura appl. 56 (1963) 185-193.

[27] H. Junninen, *Data Cycle in Atmospheric Physics: from Detected Millivolts to Understanding the Atmosphere*, PhD thesis, University of Helsinki, Helsinki, Finland, 2014.

[28] H. Manninen, A. Franchin, S. Schobesberger, A. Hirsikko, J. Hakala, A. Skromulis, J. Kangasluoma, M. Ehn, H. Junninen, A. Mirme, Atmos. Meas. Tech. Discuss. 4 (2011) 2099-2125.

[29] P. Kallinger, G. Steiner, W.W. Szymanski, J. Nanopart. Res. 14 (2012) 1-8.

[30] M.M. Maricq, Aerosol Sci. Tech. 42 (2008) 247-254.

[31] M. Sahu, J. Park, P. Biswas, J. Nanopart. Res. 14 (2012) 1-11.

[32] S.R. Turns, An introduction to combustion, McGraw-Hill, New York, U.S., 1996.

[33] G. Steiner, T. Jokinen, H. Junninen, M. Sipilä, T. Petäjä, D. Worsnop, G.P. Reischl, M. Kulmala, Aerosol Sci. Technol. 48 (2014) 261-270.

[35] Y. Wang, J. Kangasluoma, M. Attoui, H. Junninen, M. Kulmala, T. Petäjä, P. Biswas, Combust. Flame. 176 (2017) 72-80.

[35] W. Kilpatrick, in: Proc. Annu. Conf. Mass Spectrosc, 1971, pp. 320-325.

[36] J.M. Mäkelä, V. Jokinen, T. Mattila, A. Ukkonen, J. Keskinen, J. Aerosol Sci. 27 (1996) 175-190.

[37] C. Larriba, C.J. Hogan Jr, J. Phys. Chem. A, 117 (2013) 3887-3901.

Chapter 5: The High Charge Fraction of Flame-generated Particles in the Size Range below 3 nm Measured by Enhanced Particle Detectors

The results of this chapter have been published in Wang, Y., Kangasluoma, J., Attoui, M., Fang, J., Junninen, H., Kulmala, M., Petäjä, T., Biswas, P. (2017). The high charge fraction of flame-generated particles in the size range below 3 nm measured by enhanced particle detectors. Combust. Flame 176:72-80.

Supplementary figures and tables are available in Appendix I

Abstract

Charging in flames significantly affects the properties of the resultant particles produced because of its influence in almost all stages of particle formation. The charging characteristics of flame-generated sub-3 nm particles were investigated with three enhanced particle detectors including a high resolution differential mobility analyzer (DMA) coupled with an electrometer, a particle size magnifier coupled with a butanol-based condensation particle counter (PSM-bCPC), and an atmospheric pressure interface time-of-flight mass spectrometer (APi-TOF). Up to 95% of the flame-generated sub-3 nm particles were charged at a sampling height of 5 mm above the burner, indicating the existence of a strong ionization process in the investigated flame. This high fraction of charged particles contradicts the classical charging theories, which predict < 1% charge fraction for particles below 3 nm. Positively and negatively charged sub-3 nm particles generated from a blank flame were dominated by organic ions and nitrate ions respectively. The flame-generated ions play an important role during titanium dioxide (TiO_2) nanoparticle synthesis, as shown by the attachment of nitrate species on Ti-containing particles observed by the APi-TOF. The effects of the sampling height and precursor feed rate were also investigated.

5.1 Introduction

In recent years, the demand for precise control of functional flame-synthesized nanoparticle properties, such as their size, morphology, and crystal phase, has led to a growing interest in studying particle formation mechanisms in high temperature systems. While synthesizing nanoparticles, the flame generates a large amount of ions and charged particles due to the chemical ionization and thermal ionization reactions [1-4]. The existence of these ions makes the flame a quasi-neutral plasma that significantly impacts particle formation and growth processes that eventually determine the properties of the synthesized nanomaterials. The highly concentrated ions and charged species actively collide with the synthesized nanoparticles, affecting the final product due to enhanced coagulation effects [5, 6]. More importantly, the particle nucleation and growth at initial stages are strongly chemistry-dependent [7, 8], and therefore the flame-generated ions and particles may selectively combine with the synthesis precursors and nucleated nanoparticles, producing nanomaterials with undesired or in some instances, tailored contamination. Therefore, the study of particle charging characteristics needs to focus on how the flame-generated ions affect the particle synthesis and what can be done to control these processes.

Much work has been conducted on measuring the charging characteristics of flame-generated nanoparticles. Langmuir probes are often used to determine the total concentration of the charged species in the flames due to their simple design, although the theory can be complex [1, 9, 10]. Condensation particle counters (CPCs) measure total particle concentrations regardless of charging states, and by coupling the CPCs with a charged particle remover (CPR), studies have determined the neutral fractions of flame synthesized particles [11]. Size-resolved particle charge fractions, or charge distributions, are typically determined by using the tandem differential mobility analyzer (TDMA) method. It utilizes two differential mobility analyzers (DMAs), which classify particles according to their electrical mobility equivalent size, based on the balance between the electrostatic force and drag force [12, 13]. In a TDMA setup, by passing the monomobile particles classified by the first DMA into a charge conditioner and then into a second DMA for mobility scanning, the fractions of particles carrying a specific number of charges can be determined [14, 15]. Theoretical analysis of the particle charging characteristics rely on the Fuchs' charging theory [16] or Boltzmann's charging theory [17], which assumes that particle charging is in a steady state or in equilibrium. Brownian dynamic simulation has been conducted to calculate the steady state-charge distribution on particles with arbitrary shapes [18]. Experimentally measured charge distributions matched quantitatively with the theoretically predicted results in the particle size range between 10 nm and 1000 nm [11, 19].

It should be noted, however, that most of the charging studies, mentioned above, focused on particles larger than 3 nm. Also, the charging of particles in the size ranges of initial stages of formation and growth have not been studied in sufficient detail. This has been partly because of the limitation in available instruments and methods. For example, DMAs suffer from low resolution due to the high diffusivity of the sub-3 nm particles [20], while the activation of sub-3 nm particles in CPCs has always been a difficult problem [21]. Moreover, as the particle size drops below 3 nm, which is comparable to the size of the ions, the particle charging process changes from physical collisions between ions and particles to chemical reactions between the charged and uncharged molecular clusters. Due to the differences in the chemical properties and proton affinities, neutral species can be charged at different efficiencies, which cannot be predicted by the classical charging theories. These limitations hinder a comprehensive understanding of the particle charging mechanisms, forming a knowledge gap in the formation of particles.

A series of enhanced particle detectors created in recent decades can be valuable tools to study the charging characteristics of sub-3 nm particles. In order to counteract the diffusion broadening of the DMA transfer functions, high resolution DMAs with new configurations or with sheath flow rates over 100 liters per minute (lpm) were designed [22, 23], so that the residence time and diffusional loss of classified particles were significantly reduced. By applying an electrometer downstream of the high resolution DMA, the concentration of the classified sub-3 nm particles can be readily measured [3, 24-29]. Conventional CPCs have been modified in many aspects, which include their working fluid [30], working temperature [31], flow rates [31], and flow pattern [32, 33], to effectively activate the condensational growth of particles below 3 nm. Using diethylene glycol (DEG) as the working fluid, a particle size magnifier (PSM) can grow particles from as small as 1 nm [33] to a size that can be detected by subsequent, conventional butanol CPCs (bCPCs). By scanning the saturation ratio, particles with different sizes are activated and counted, so that the size distributions of the sub-3 nm particles are obtained [34, 35]. Molecular Beam Mass Spectrometry (MBMS) has often been used in studying ion generation in flames, these studies were typically conducted in low pressure and fuel-rich conditions due to the strict requirements of the setup [1]. Limited studies have been conducted in atmospheric pressure $CH_4/O_2/Ar$ flames wherein important chemical ionization reactions have been identified [36-38]. Particle mass spectrometry [39] and transmission electron microscopy of particles collected by molecular beam sampling [40] have also been used for investigating the charging characteristics, growth dynamics, and shapes of incipient soot nanoparticles. The recently developed atmospheric pressure interface time-of-flight mass spectrometer [41] (APi-TOF, Tofwerk AG) greatly helps determine the chemical composition of the sub-3 nm charged particles in accessible conditions [42]. The combination of the three mentioned enhanced particle detectors (high resolution DMA coupled with an electrometer, PSM-bCPC, and APi-TOF) has served as a powerful tool in understanding the atmospheric particle formation below 3 nm and the role of ions in the atmospheric nucleation [43, 44]. Table 5.1 is a brief summary of the instruments discussed above for incipient particle measurement including their acronyms and functions.

Table 5.1 A list of instruments commonly for incipient particle measurement.

Instrument	**Acronym**	**Function**
Differential Mobility Analyzer	DMA	Classify particles as a function of mobility size
Tandem Differential Mobility Analyzer	TDMA	Determine particle charge fraction as a function of particle mobility size
Condensation Particle Counter	CPC	Measure particle number concentrations
Butanol CPC	bCPC	Measure particle number concentrations with butanol as the working fluid
Particle Size Magnifier	PSM	Grow particles as small as 1 nm to a detectable size using diethylene glycol as the working fluid
Molecular Beam Mass Spectrometer	MBMS	Detect the chemical composition of ions through the well-designed compact skimmer inlet system
Atmospheric Pressure Interface Time-of-Flight Mass Spectrometer	APi-TOF MS	Detect the composition of ambient ions with a mass accuracy higher than 0.002% and a resolving power of 3000 Th/Th
Charged Particle Remover	CPR	Remove charged ions and particles

In this work, three enhanced particle detectors were applied in studying the particle charging characteristics of flame-generated sub-3 nm particles. The total and neutral particle size distributions were measured by the PSM-bCPC, and were compared with the high resolution DMA-measured particle mobility size distributions. The APi-TOF further identified the chemical compositions of the flame-generated sub-3 nm charged particles. This study also investigated the effects of the sampling height, the addition of a synthesis precursor, and the precursor feed rates on the chemical compositions, size distributions, and charging characteristics of the flame-generated sub-3 nm particles.

5.2 Experimental setups and methods

5.2.1 Premixed flat flame aerosol reactor

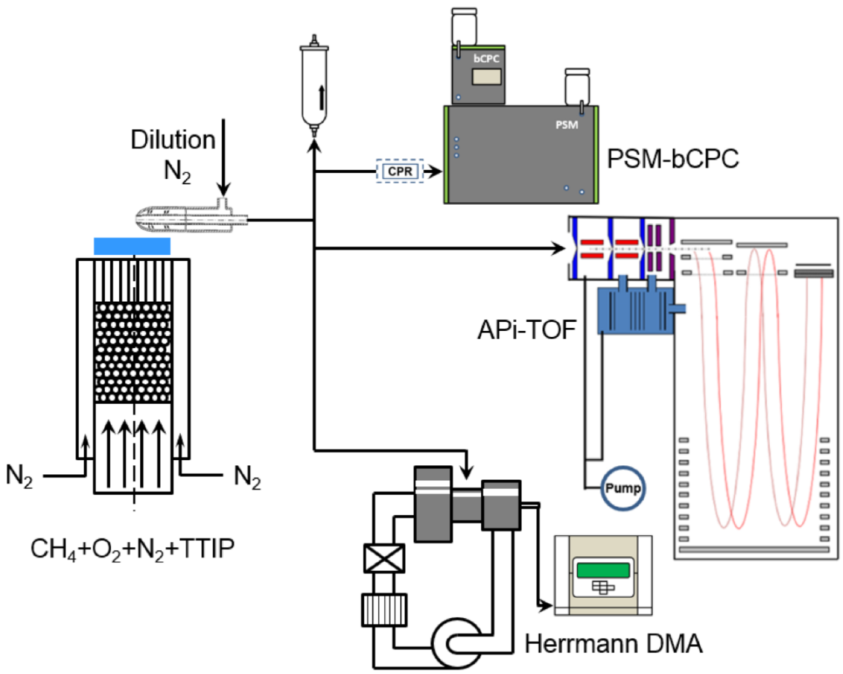

Figure 5.1 A schematic diagram of the experimental setup.

Figure 5.1 shows a schematic diagram of the experimental setup. A premixed flat flame was used in this study for generating sub-3 nm particles, due to its high stability, one-dimensionality, and broad usage. The combustion mixture consisted of methane (CH_4, > 99.5%, Linde AG) and oxygen (O_2, >99.95%, Linde AG). Nitrogen (N_2, >99.95%, Linde AG) was used to dilute the system and control the flame temperature. A set of mass flow controllers (MKS Inc.) maintained the total flow rates of CH_4, O_2, and N_2 at 1.00 lpm, 2.85 lpm, and 6.00 lpm, respectively, keeping the flame equivalence ratio at 0.70 (fuel-lean). The stainless steel burner was made of two concentric cylinders with inner and outer diameters of 19 and 25 mm, respectively, forming a gap to provide an extra stream of N_2 with a flow rate of 3 lpm for shielding the flame. The inner cylinder was capped by a honeycomb with a mesh size of 0.5 mm, and was further filled with 2 mm stainless steel beads to maintain laminar flow with a uniform velocity profile at the head of the burner. To study the effects of the addition of a synthesis precursor and precursor feed rates, a bypass flow of N_2 was passed through a bubbler containing titanium isopropoxide (TTIP, Sigma-Aldrich Inc., >97%) at a stable temperature of around 20 ^{o}C and subsequently fed into the flame. The effect of adding precursors on flame equivalence ratio and flame temperature were minimal because of the low feed rates of the precursors (Table 5.2). Due to the imperfect design of the burner, the flame does not look entirely flat. The vertical distance from the highest point of the flame to the lowest point of the flame was approximately 3 mm, and the flame height (the distance between the lower side of the flame sheet and the upper side of the burner) was approximately 1 mm. Inside the flame, thermal decomposition, hydrolysis, and combustion of TTIP resulted in the production of titanium dioxide (TiO_2). Previous measurements conducted with a high-resolution DMA have shown that a large quantity of sub-3 nm particles is formed during these processes [3, 20, 45], and the existence of these particles were confirmed by atomic force microscopy (AFM) images of particles collected by thermophoretic sampling [3]. The DMA-measured and AFM-determined particle size distributions matched considerably well in the studied particle size range, indicating the accuracy of the DMA measurement. In order to quench further reactions and particle growth, the sub-3 nm particles were sampled by a radially positioned dilution probe with an inlet diameter of 0.5 mm at a dilution N_2 flow rate of 24 lpm. The outer diameter of the dilution probe was 8 mm. A dilution ratio of around 200 was reached considering the thermal expansion of the sampled flow. Detailed descriptions of the dilution probe can be found in Wang et al. [45] The sampled sub-3 nm particles were then introduced to the enhanced particle detectors.

Table 5.2 Experimental plan.

Test #	Probe height (H_{AB}) [mm]	*TTIP* feed rate [mmol/h]
1	5	0
2	10	0
3	15	0
4	20	0
5	5	0.043
6	5	0.085
7	5	0.128
8	5	0.170
9	5	0.213
10	10	0.213
11	20	0.213

5.2.2 Enhanced particle detectors

This study used a Herrmann-type high resolution DMA (Herrmann DMA) [46, 47], a PSM-bCPC [33], and an APi-TOF [41] to detect the concentration and chemical composition of the sub-3 nm particles.

The Herrmann DMA was operated in a closed loop so that the inlet and outlet sheath flows were balanced. The rate-controllable sheath flow was provided by a brushless blower (DOMEL Inc.), and was further cleaned and cooled by an inline filter and heat radiator. The voltage across the two electrodes of the DMA was applied by a high voltage power supply (Spellman Inc.) controlled by LabVIEW. The DMA measurement used a step voltage of 3 V and a step time of 1 s, which were found to be sufficient for obtaining stable signals. After being classified by the Herrmann DMA, the charged sub-3 nm particles were introduced to an aerosol electrometer (3068B, TSI Inc.) operated at a flow rate of 10 lpm. By assuming that the measured particles carried a single charge, the particle concentration was directly proportional to the current measured by the electrometer (EM). The EM current data were collected by the LabVIEW through RS-232 communication. In the results section, the DMA-measured particle size distributions are represented qualitatively by the EM current as a function of particle size, since the data inversion of the sub-3 nm particles was found to be highly chemistry-dependent [20]. In order to obtain the mobility of the classified particles at each DMA voltage, the Herrmann DMA was calibrated by the mobility standards generated from the electrosprays of tetra-heptyl ammonium bromide methanol solution (THABr, 99%, Sigma-Aldrich) before the measurements [48]. The measurement accuracy of the Herrmann DMA has been thoroughly characterized in a recent study [47]. The size of the classified particles was further calculated based on the Stokes-Millikan equation and the definition of electrical mobility [17],

$$Z = \frac{eC}{3\pi\mu d_p}, \tag{5.1}$$

where Z is the particle electrical mobility, e is the electronic charge, C is the slip correction factor, μ is the air viscosity, and d_p is the mobility diameter of the particle. Existing studies suggest that the volumetric diameter (d_v) of a sub-3 nm particle can be approximated by subtracting d_p by 0.3 nm, which is the gas molecule's effective diameter [49]. Further calculation is also needed to derive the exact value of the particle mobility diameter, since the influence of the ion-induced dipole potential on the particle mobility is not evaluated in the Stokes-Millikan equation for sub-3 nm particles [49, 50]. However, for simplicity, the mobility diameter of the particle calculated by Eq. (5.1) was used to evaluate the particle size distributions.

The PSM-bCPC measured the sub-3 nm particle size distributions based on the size-dependent particle activation. Sub-3 nm particles were first grown by the PSM in an environment of supersaturated DEG vapors, and then introduced to a bCPC for further growth and optical detection. Details about the theory and operation can be found elsewhere [33, 35]. The PSM detection efficiency was calibrated using the positively charged particles generated in the flame. Conditions of the blank flame and with TTIP addition were calibrated separately to obtain different calibration curves. These curves were then used separately for interpreting the PSM data. Due to the fact that different species of particles were observed in positively charged, negatively charged, and neutral particles, uncertainty exists in the PSM-obtained particle number concentrations and charge fractions. Furthermore, existing studies suggested that neutral particles are less easy to activate due to the missing of ion-induced dipole effects [5, 6, 49, 50].However, a recent study has revealed that heterogeneous nucleation does not clearly favor particles with certain charging states, while the chemical composition of the sub-3 nm particles plays a more important role [51]. In this study, the PSM-bCPC (Model A11, Airmodus Oy) was used to determine the charge distributions of the sub-3 nm particles. Teflon tubing is widely found to significantly remove ions and charged particles due to the electric field built at the inner surface of the tube, and this property makes it a convenient and efficient charged particle remover (CPR). This charge-removing effect can be achieved with a very short section of the tube (a few centimeters), since the mean surface electric field for the Teflon tubing can be in the range of 50-200 V/cm [52]. This charge-removing effect is significantly suppressed by using conductive tubing for aerosol sampling. A 6.0 mm-wide, 10 cm-long Teflon tubing or conductive silicone tubing was initiated before the PSM-bCPC, so that both the neutral and total particle size distributions can be measured. The same length of tubes could guarantee the same amount of diffusion loss in the tubes. The charge distribution of the flame-generated sub-3 nm particles were then calculated by comparing the size distributions obtained with different tubes.

The chemical composition of the flame-generated charged particles was obtained by directly feeding the sample aerosols to the APi-TOF. The APi-TOF could achieve a mass resolving power of 3000 Th/Th and a mass accuracy of 0.002%. The spectra were further analyzed with tofTools (a MATLAB®-based set of programs) [53], where the accurate mass and isotope distributions determined the exact species of the charged particles. To better analyze incipient clusters with similar chemical compositions, a mass defect plot was created which uses measured ion mass plotted on the x-axis and mass defect against nominal mass (integer mass) on the y-axis [41]. For example, since carbon has an atomic mass of 12.0000 (nominal mass of 12) and hydrogen has an atomic mass of 1.0078 (nominal mass of 1), C_nH_n clusters will have a mass defect of +0.0078n. By plotting C_nH_n clusters in a mass defect plot, one can get a straight line with a slope of +0.0078/(12+1.0078). In a mass defect plot, each section of straight lines represents species spaced by a same molecular composition. The mass defect plot can further help in understanding the conversion and reaction of the species. The “Kendrick mass defect spectrum” is based on this idea where both the x-axis and y-axis are scaled to assist the analysis of grouped hydrocarbons [54].

The particle residence times in the sampling lines were approximately 12 ms, 52 ms, 9 ms, and 30 ms, for the sections from the dilution sampler inlet to the DMA inlet, from the dilution sampler inlet to the PSM-bCPC inlet, from the dilution sampler inlet to the APi-TOF inlet, and from the DMA outlet to the EM inlet, respectively. However, the particle loss in the system took place dominantly in the instruments. For example, the transmission efficiencies of particles in the APi-TOF and the DMA were estimated to be 0.1 to 0.5% and 1 to 22%, respectively, depending on the setting of the instruments [41, 47]. Due to the difficulty for calibrating the particle transmission efficiencies, the particle loss was not evaluated. It should be noted that sampling in a flame with a probe will inevitably alter a sample. Although it has been carefully calibrated, the dilution sampler used in this study may not be sufficient to quench all reactions and particle dynamics. A recent study by Carbone et al. [24] shows that measuring sub 3 nm soot particles with dilution samplers is very challenging, since the critical conditions for suppressing particle coagulation and charge distribution were not achieved even at a dilution ratio of 6.2×10^{3}. Existing studies also suggested that an adequate dilution ratio larger than 10^4 is typically required so that the obtained particle size distributions are “asymptotic” [55]. Furthermore, the rapid cooling of the sample may also impact the complex state of vapor-cluster balance in the flame, and cause alteration of the incipient particle measurement [38, 56, 57]. Hence, there is a small chance that the observed incipient particles might not have been formed in the flame and are not reflective accurately of flame species.

5.2.3 Experimental plan

Eleven sets of experiments (Table 5.2) were designed to study the effects of the sampling height, addition of synthesis precursor (TTIP), and precursor feed rates on the charging characteristics of flame-generated sub-3 nm particles. Tests 1 to 4 were conducted without TTIP addition to study the effect of sampling height on the particles generated from blank flames. Tests 5 to 11 investigated the effect of TTIP feed rates and sampling height during TiO_2 synthesis. The sampling height (H_{AB}) was the vertical distance from the head of the burner to the inlet of the dilution sampler. The TTIP feed rate was calculated based on the saturation vapor pressure of TTIP in N_2 presented by Siefering and Griffin [58].

5.3 Results and discussion

5.3.1 Sub-3 nm particles generated from a blank flame

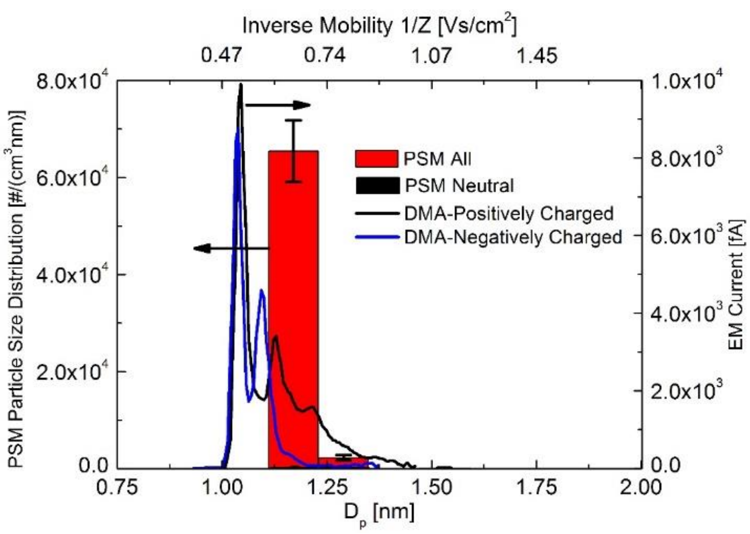

Figure 5.2 PSM and DMA-measured size distributions of blank flame-generated sub-3 nm particles at H_{AB} = 5 mm.

Figure 5.2 shows the PSM-measured size distribution of particles generated from the blank flame at a sampling height of 5 mm. The neutral particle size distribution was also measured, which is not distinguishable in the graph, indicating a minimal formation of neutral particles in this condition. This result also explained the qualitative match between the shapes of the PSM and DMA-measured size distributions below 3 nm, because the DMA classified charged particles only. A large amount of charged clusters below 1.5 nm were generated from the blank flame, which was also observed in previous studies [3, 20]. These charged particles were generally believed to come from the intensive chemical ionization and thermal ionization during combustion [1]. During CH_4 combustion, the chemically produced positively and negatively charged species mainly come from the reactions

$$CH + O \rightarrow CHO^{+} + e^{-}, \text{ and} \tag{5.2}$$

$$CH^{*} + C_2H_2 \rightarrow C_3H_3^{+} + e^{-}, \tag{5.3}$$

where the formed ions and electrons may collide with other molecules to form more stable charged species [59]. According to recent work by Jones and Hayhurst [38], reaction shown in Eq. (5.2) dominates more oxygen-rich flames of methane (C/O $\leq$ 0.4). A pool of positive ions is then formed rapidly, mainly through proton transfer from CHO^{+} to other intermediates and final products of combustion. Previous measurements with Langmuir probes and MBMS determined that the concentration of ions produced by chemical ionization in flames can be as high as 10^{11}#/cm^3 [19, 38, 60]. An estimation of ion concentration in this investigated flame was also conducted, and the ion concentration was approximately 10^{10}#/cm^3 (supplementary content). This value is close to the those obtained in the work of Jones and Hayhurst [38]. The effect of thermal ionization can be briefly evaluated by Saha's equation, where the equilibrium concentrations of thermally ionized charged species can be calculated by

$$K = \frac{n_+ \cdot n_e}{n} = G(\frac{2\pi m_e kT}{h^2}) \exp(-\frac{A_I}{kT}), \qquad (5.4)$$

where K is the equilibrium constant, n_+, n_e, and n are the concentrations of the positively charged species, electrons, and neutral particles. G is defined as $g_+ \cdot g_e / g$, where g_+, g_e, and g are the statistical weights of an ion, electron, and neutral particle, respectively. m_e is the electron mass, k is Boltzmann's constant, T is temperature (a value of 2200 K is used), and h is Plank's constant. A_I is the ionization potential of the species, which is typically larger than 10 eV in a fuel-lean flame [61]. The calculated value of K was below 10^{-12} #/m^3, indicating a minimal effect of thermal ionization in this studied flame. Hence, we could conclude that most of these ions were coming from the chemical ionization in the flame.

The DMA-measured size distributions (Figure 5.2) demonstrates that positively charged particles had larger averaged mobility sizes (lower electrical mobilities) than negatively charged particles, which is common in ionization sources [62]. The inverse mobilities are labeled in the upper x-axis of Figure 5.2 as a reference. A possible explanation for the difference in the average mobilities between the polarities is that chemical ionization reactions produce relatively large organic particles as positive charge carriers, while electrons are the dominant negative charge carrier. These free electrons can further attach on other species with smaller mobility sizes to generate negative ions at atmospheric pressure [38, 63, 64] through

$HX + e^- \rightarrow H + X^-.$

(5.5) Through this reaction, major negative ions, such as C_2H^- and OH^-, or halogen ions, can be generated [38, 64]. According to Fuchs theory, the difference in the electrical mobility may cause a higher fraction of particles to carry negative charges, since the more mobile negatively charged clusters may collide with neutral particles more frequently. It should also be noted that the measured ion mobilities were higher than those obtained in sooting flames (~ 1 cm^2/Vs), where larger clusters of unsaturated carbon clusters were formed [1].

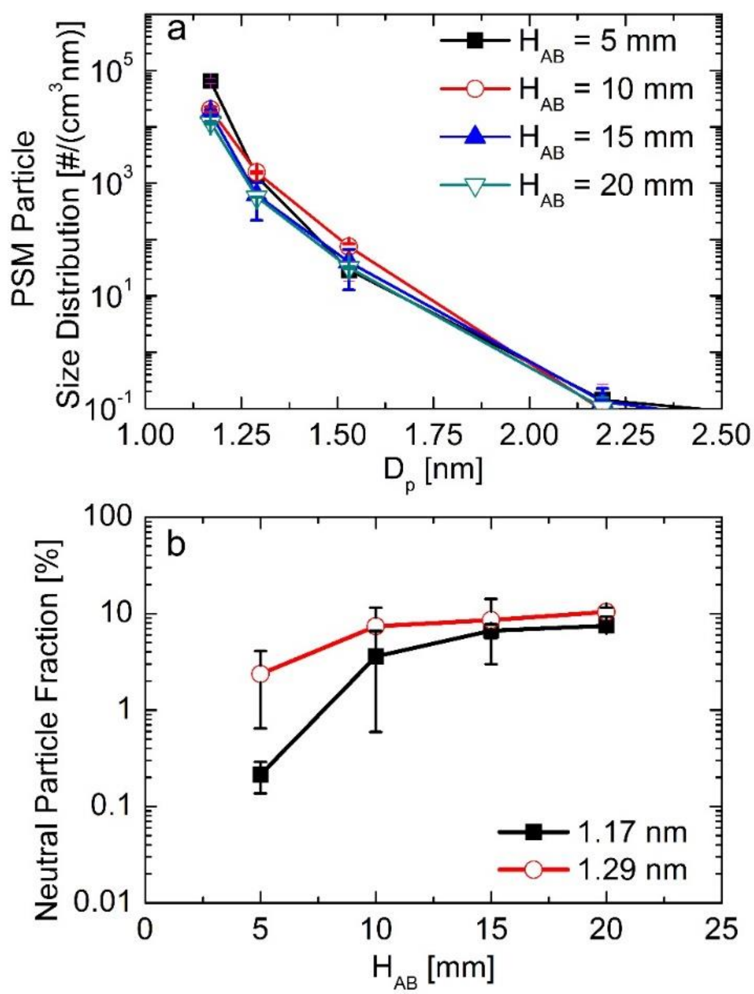

Figure 5.3 Effect of sampling height on: (a) PSM-measured size distributions and (b) neutral fractions of blank flame-generated sub-3 nm particles.

Figure 5.3 displays the effect of sampling height on the PSM-measured particle size distributions and neutral particle fractions. As the probe height (H_{AB}) increased, a minor decrease in the particle concentration was observed (Figure 5.3a), which could be explained by the formation of neutral particles by ion recombination above the flame sheet. One should notice that the concentration of sub-3 nm particles at different H_{AB} were still in similar orders of magnitude, implying a relatively long age (>10 ms) of the generated particles. The neutral fraction of sub-3 nm particles was very low (< 10%, Figure 5.3b), and as the residence time increased (higher H_{AB}), the recombination of ions did not have a significant effect on the neutral fractions. The neutral particle fraction was far from the theory-predicted values of around 100% for particles below 10 nm, indicating that a large fraction of particles were charged in this size range during combustion. Furthermore, the neutral fraction of 1.29 nm particles was always higher than that of 1.17 nm particles (Figure 5.3b), contradicting the classical charging theories which predict a lower charging probability of particles with smaller sizes. This large discrepancy may be caused by the chemical ionization which produces positive ions with different sizes as stated earlier, and may also be a result of the unsteady charging process, which is not considered in classical charging theories. This feature requires additional experimental work.

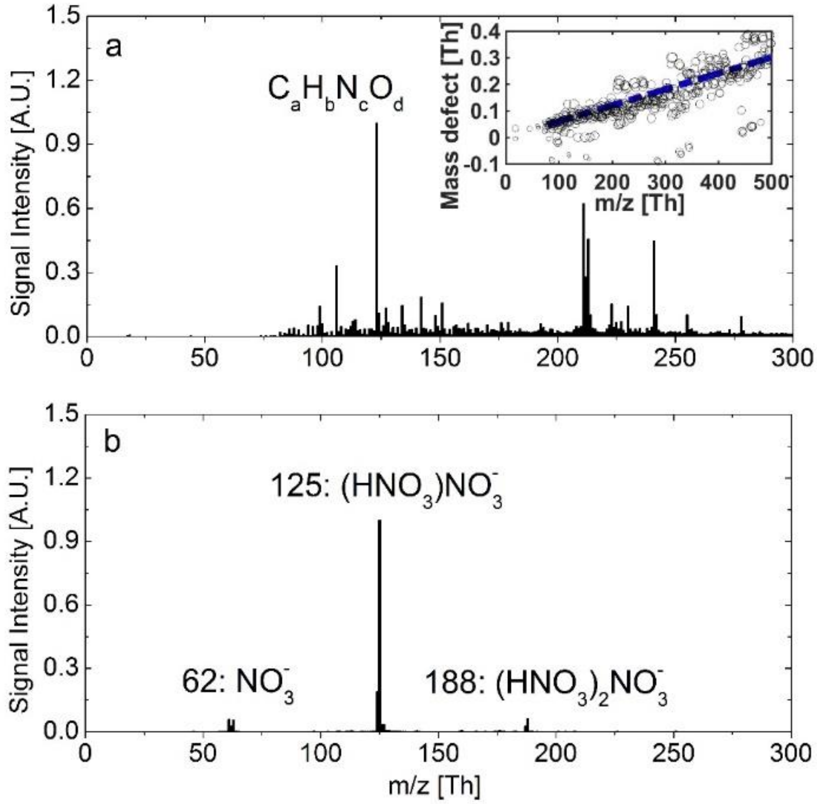

Figure 5.4 Mass spectrum of blank flame-generated ions measured by the APi-TOF. a) mass spectrum of positive ions; inset plot: mass defect plot of the positive ions (size of the circle indicates the relative abundance of the species); the blue line shows the mass defects of C_nH_n clusters and b) mass spectrum of negative ions.

The mass spectra of the positively and negatively charged sub-3 nm particles are shown in Figure 5.4. The spectra of the positive particles contained a lot of hydrocarbons peaks, which complicated the identification of the ion species (Figure 5.4a). Possible compositions of the major peaks were $C_4H_{11}O_3^+$ (107.0708 Da), $CH_{16}O_6^+$ (120.0634 Da), $C_{14}H_{30}N^+$ (212.2378 Da), and $C_{15}H_{32}ON^+$ (242.2487 Da). Unfortunately, the chemical structure of these charged clusters cannot be deciphered. Future work will be attempted to analyze the chemical structures and locate functional groups of these clusters, so that more information can be derived for incipient particle formation. The inset figure shows the mass defect plot of the positively charged particles, with the fitted line displaying the mass defects of particles with a chemical formula of C_nH_n. The match between most of the data points and the fitted line indicates that the formed positively charged sub-3 nm particles were mainly composed of unsaturated hydrocarbons. It is also possible that the formation of polycyclic aromatic hydrocarbons (PAH) took place during the combustion of methane [65, 66]. These detected species are important intermediates during particle formation due to their high abundance. Furthermore, they can provide the surface area for particle condensation and coagulation growth. It is interesting that the detected major species (such as $C_4H_{11}O_3^+$ and $CH_{16}O_6^+$) did not fall on the fitted mass defect line, which requires more effort to explain this phenomenon. The negatively charged clusters were mostly composed of nitrate ions. Major peaks of NO_3^- (61.9878 Da), $HNO_3NO_3^-$ (124.9835 Da), and $(HNO_3)_2NO_3^-$ (187.9791 Da) were detected and confirmed by the highly resolved atomic masses and isotope distributions. The existence of nitrogen-containing species might be a result of NO_x formation, especially when the flame was operated in a fuel-lean condition which favors NO_x production. Further, the electrons and water produced by combustion might react with NO_x to generate nitrate ions, which were also found to be the dominant ions in other types of ionization sources such as radioactive neutralizers [62, 67] and corona dischargers [68]. Due to its high concentration, the nitrate ions were very likely to participate in the charging of sub-3 nm particles during particle synthesis, as discussed in the following section.

5.3.2 Sub-3 nm particles generated during flame synthesis of TiO_2

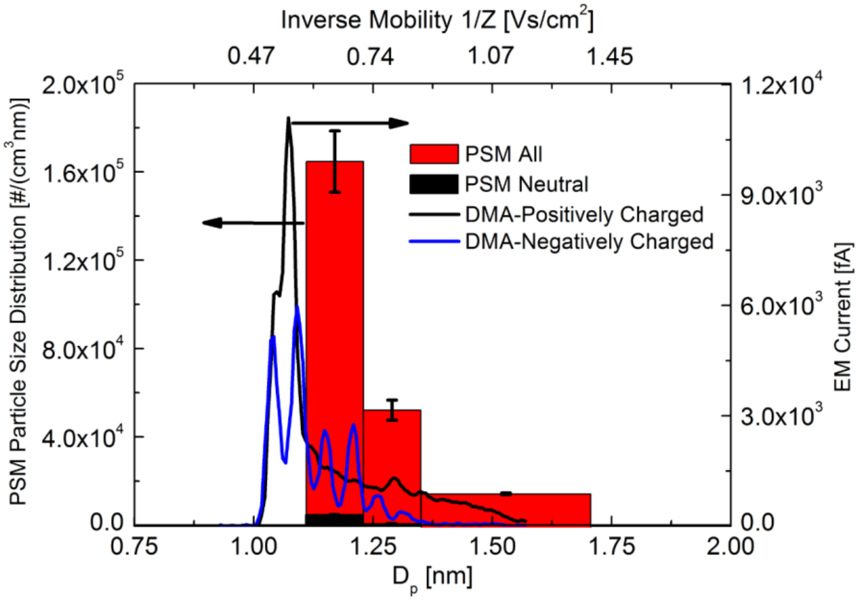

Figure 5.5 PSM and DMA-measured size distributions of flame-generated sub-3 nm particles during the flame synthesis of *TiO_2*. The sampling probe height was 5 mm and *TTIP* feed rate was 0.170 mmol/hr.

After TTIP was introduced to the flame, particles with mobility sizes larger than 1.5 nm were detected by both the PSM-bCPC and DMA (Figure 5.5). This increase in size was a result of particle nucleation and growth at the initial stages. The neutral particle concentrations also increased compared to the blank flame conditions, although the neutral fraction was still low (~ 5% at H_{AB} = 5 mm). Due to the large fraction of the charged particles, DMA-measured particle size distributions again matched well with the PSM-measured total particle size distributions. Separate peaks between 1 nm and 1.25 nm were detected in the DMA-measured particle size distributions, indicating the formation of some stable particles during the synthesis of TiO_2 [3]. These stable particles may act as important intermediates during the formation of TiO_2. Again, positively charged particles had larger averaged mobility sizes than the negatively charged particles.

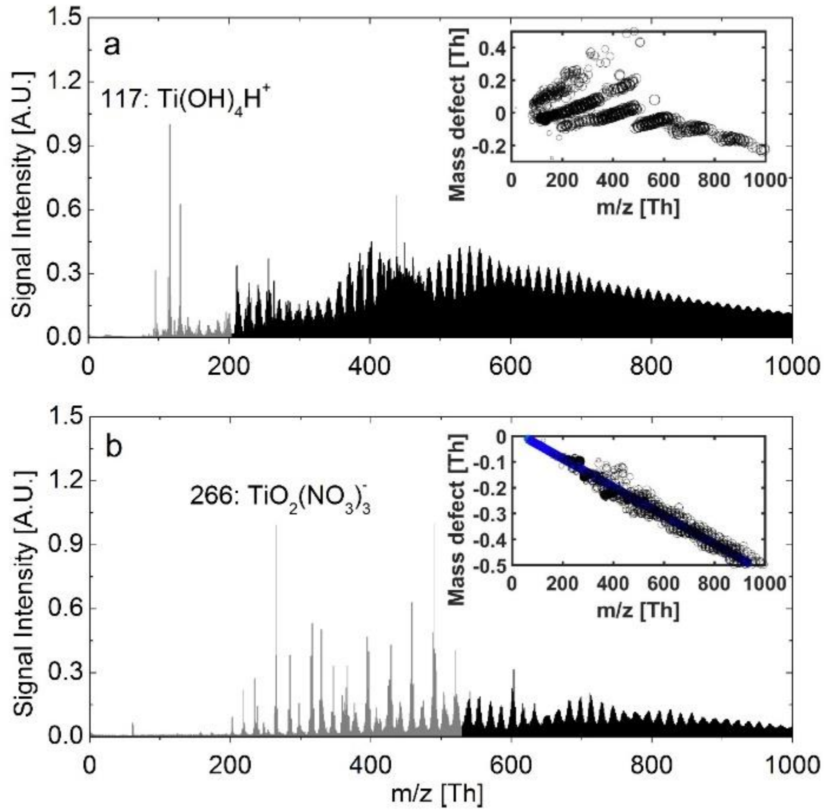

Figure 5.6 Mass spectrum of flame-generated sub-3 nm particles measured by the APi-TOF during the synthesis of TiO_2. The identified peaks are shown in gray color: a) shows positively charged particles; inset plot: mass defect plot of the positive ions (size of the circle indicates the relative abundance of the species) and b) shows negatively charged particles; inset plot: mass defect plot of the negative ions (size of the circle indicates the relative abundance of the species); the blue line shows the mass defect of clusters with NO_3 as the core and TiO_2NO_3 as the additional group.

The chemical compositions of the sub-3 nm charged particles were analyzed with the APi-TOF, and the mass spectra are displayed in Figure 5.6. A significant number of peaks was detected in both polarities. The existence of titanium elements in the particles was confirmed with the high-accuracy mass and the titanium isotope distribution (^{48}Ti: 73.7%; ^{46}Ti: 8.3%; ^{47}Ti: 7.4%; ^{49}Ti: 5.4%; ^{50}Ti: 5.2%). The identified peaks are represented in Figure 5.6 and listed in Table 5.3. Classical nucleation theories [22] predicted that a TiO_2 single molecule could serve as a stable monomer due to its low saturation vapor pressure; however, pure TiO_2 particles were not detected by the mass spectrometer. A major peak of $Ti(OH)_4H^+$ was found in the positively charged particles, which agreed with the TTIP reaction pathways in a $H_2/O_2/Ar$ premixed flame proposed by Shmakov et al. [69] Similar species were also observed in a fuel-rich C_2H_2/O_2 premixed flame with the addition of atomized droplets of $TiCl_4$ aqueous solution [70]. Other identified positively charged species typically contained unreacted hydrocarbons from TTIP propanol groups, indicating the necessity for future controlled experiments studying ion generation from propanol flames. As for negatively charged species, the nitrate ions played an important role in the formation of sub-3 nm particles. The APi-TOF detected a series of titanium and nitrate-containing particles, for example, $TiO_4(NO_3)_2^-$ at m/z of 235.9032 Th, $TiO_2(NO_3)_3^-$ at m/z of 265.9012 Th, and $Ti_2O_8(NO_3)_2^-$ at m/z of 347.8308 Th, etc. The detected compositions indicate that, in molecular clusters, titanium has preferable oxidation states other than +4. This may demonstrate a strong interaction between the flame-generated ions and the synthesized materials, where the flame-generated ions were actively consumed during the particle formation at initial stages. This scavenging effect also explains the increase of neutral particle fraction observed in Figure 5.5. It is also possible that the precursor molecule, TTIP may become readily ionized in the flame, serving as the seed for further particle growth. It should be noted that the flame-generated ions in the sub-3 nm particles might serve as contaminants for the further growth of particles and may affect crystallization. Therefore, it would be worthwhile to conduct similar measurements in systems without the presence of hydrocarbon and nitrate species, such as in $H_2/O_2/Ar$ flames, in order to study the effect of organic and nitric ions on particle formation and growth. A recent study has shown that pure tungsten oxide clusters can be detected through the measurement with molecular beam mass spectrometry in an $H_2/O_2/Ar$ flame at low pressures. However, since flame synthesis is mainly conducted with the participation of N_2, and due to safety considerations and cost-effectiveness, hydrocarbons are commonly used as fuels, further work investigating the role of nitrate and hydrocarbon species in the particle growth and crystallization processes is still needed.

Table 5.3 List of some major positive and negative compounds within the ion spectra measured by the APi-TOF.

Identified positive ions		**Identified negative ions**	
Integer m/z	**Chemical formula**	**Integer m/z**	**Chemical formula**
97	$HC_4O_3^+$	62	NO_3^-
117	$TiH_5O_4^+$	204	$TiN_2O_8^-$
132	$TiH_4O_5^+$	220	$TiN_2O_9^-$
143	$TiC_2H_7O_4^+$	236	$TiN_2O_{10}^-$
146	$TiCH_6O_5^+$	266	$TiN_3O_{11}^-$
159	$TiC_2H_7O_5^+$	286	$Ti_2NO_{11}^-$
173	$TiC_3H_9O_5^+$	348	$Ti_2N_2O_{14}^-$
187	$TiC_4H_{11}O_5^+$	396	$Ti_3N_2O_{14}^-$
229	$TiC_6H_{13}O_6^+$	460	$Ti_2N_2O_{18}^-$

The mass defect plots of the positively and negatively charged particles are displayed as insets in Figure 5.6. Most of the negatively charged particles fell on the straight line representing the mass defects of particles containing NO_3 as the core and TiO_2NO_3 as the additional group. The mass defect plot of the positively charged particles shows some interesting properties. Detected particles had a major trend of decreasing mass defects as the atomic mass increased because of the addition of titanium and oxygen, which have negative mass defects, i.e., exact atomic mass of 47.9479 and 15.9949, respectively. However, the whole mass defect plot was composed of separate segments where the mass defect was increasing with atomic mass, possibly contributed by the existing hydrocarbons, since hydrogen has a positive mass defect (exact mass of 1.0078). These segments indicate the presence of dehydrogenation and dehydration during the precursor reaction. The different patterns of the mass defect plot clearly suggest the presence of different reaction regimes during the formation of TiO_2 particles. Apart from the cluster mobility and mass spectrum, the mass and mobility information of specific molecular cluster is also of great interest, since it can reveal critical information on the structure of these molecular clusters, such as collision cross section area, atom arrangement, etc [29]. However, in order to obtain the particle mobility and mass simultaneously, a tandem arrangement of the DMA and mass spectrometer, and more complex data analysis are required, which can be found in a recent study of the same group [4].

5.3.3 Effect of precursor feed rate and sampling height

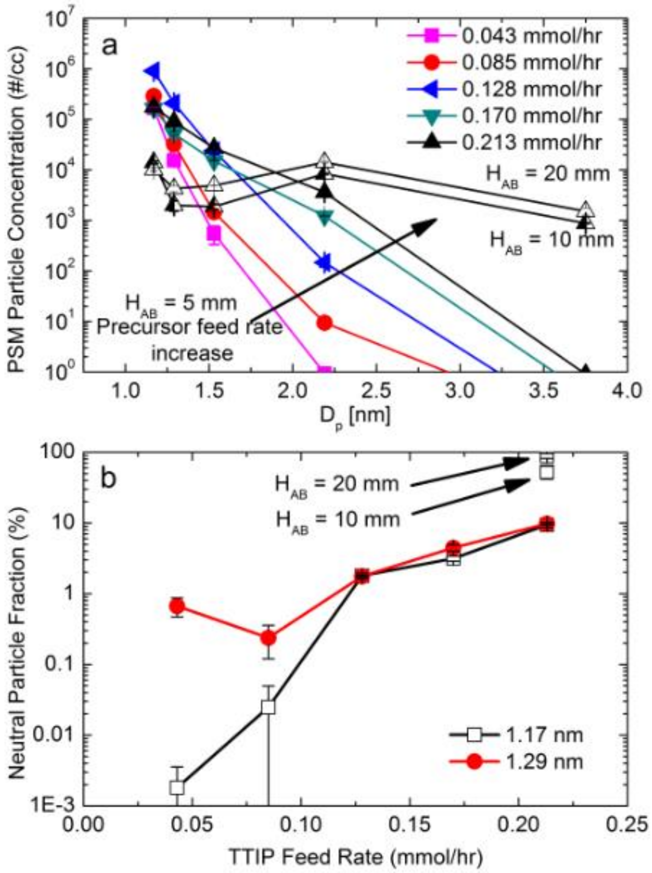

Figure 5.7 Effect of the precursor feed rate and sampling height on: (a) PSM-measured size distributions and (b) neutral fractions of flame-generated sub-3 nm particles. Figure 5.7a displays the size distributions of sub-3 nm particles synthesized at a feed rate of 0.213 mmol/hr at H_{AB} = 10 and 20 mm. (a). Figure 5.7b shows the neutral fractions of 1.17 nm particles generated with a *TTIP* feed rate of 0.213 mmol/hr at H_{AB} = 10 and 20 mm.

Due to the scavenging of flame-generated ions by the synthesized materials, one would expect a positive correlation between the neutral particle fraction and the precursor feed rate. Figure 5.7 shows the PSM-measured size distributions and neutral particle fractions as a function of the precursor feed rate. It was observed that when H_{AB} = 5 mm, particles larger than 1.5 nm were formed, while smaller particles at around 1.1 nm were first generated and then consumed, due to the enhanced coagulation and continue particle growth (Figure 5.7a). The neutral particle fraction indeed increased with the TTIP feed rate, reaching around 10% with a precursor feed rate of 0.213 mmol/hr where H_{AB} = 5 mm, confirming the strong interaction between the flame-generated ions and the synthesized particles.

Unlike the case for the blank flame-generated ions (Figure 5.4), sampling height significantly changed the size distribution and neutral fraction of particles formed from the flame with precursor addition. At a precursor feed rate of 0.213 mmol/hr, the particle size distribution shifted from 1.1 nm to 2.25 nm as sampling height increased (Figure 5.7a). The neutral fraction also greatly increased, approaching around 90% when the sampling height was 20 mm. The neutral fractions of 1.17 nm and 1.29 nm particles were 53.8±11.2 % and 56.8±13.4 % at H_{AB}=10 mm, and 88.9±7.1 % and 82.3±18.3 % at H_{AB}=20 mm. This large difference in the charge fraction is attributed to the existence of particles with larger sizes. The ions produced by the chemical ionization in the flame randomly collided with and attach onto particles formed from *TTIP* reaction. Particles with larger sizes possessed larger cross-sectional areas (and coagulation sink [71]), facilitating the recombination and neutralization of the system. This effect might have also been maximized, due to the small size scale of this charging process. Still, the neutral particle fractions were far from the theoretically predicted values, indicating a need for analytically studying the time-dependent charging mechanisms in the flame [2].

5.4 Conclusions

With the help of three enhanced particle detectors, the charging characteristics of sub-3 nm flame-generated particles were studied for the first time (to the best of our knowledge). The PSM-bCPC and high resolution DMA matched qualitatively well in measuring the sub-3 nm particle size distributions. Coupled with a CPR, the PSM-bCPC measured the neutral particle size distributions during combustion, and the neutral particle fraction in the flame was found to be significantly lower than predicted by classical theory. The APi-TOF provided the chemical compositions of the sub-3 nm charged species. Under blank flame conditions, the positively charged particles were mainly composed of hydrocarbons, while nitrate ions dominated the negatively charged particles. NO_x formation was considered to be the major reason for generating nitrate species. A strong interaction between the flame-generated ions and synthesized materials was observed, which was indicated by the existence of nitrate species in the Ti-containing particles. The appearance of these ion species might further affect the quality of the final synthesized product. The formation of particles during combustion consumed the flame-generated ions, which further increased the neutral particle fraction in the flame. Flame-generated ions play an important role during the particle formation at the initial stages. New perspectives on synthesizing functional nanomaterials through combustion may be obtained through changing the ion characteristics in flame environments.

5.5 References

[1] A.B. Fialkov, Investigations on ions in flames, Prog. Energy Combust. Sci. 23 (1997) 399-528.

[2] J. Jiang, M.-H. Lee, P. Biswas, Model for nanoparticle charging by diffusion, direct photoionization, and thermionization mechanisms, J. Electrostat. 65 (2007) 209-220.

[3] J. Fang, Y. Wang, M. Attoui, T.S. Chadha, J.R. Ray, W.-N. Wang, Y.-S. Jun, P. Biswas, Measurement of sub-2 nm clusters of pristine and composite metal oxides during nanomaterial synthesis in flame aerosol reactors, Anal. Chem. 86 (2014) 7523-7529.

[4] Y. Wang, J. Kangasluoma, M. Attoui, J. Fang, H. Junninen, M. Kulmala, T. Petäjä, P. Biswas, Observation of incipient particle formation during flame synthesis by tandem differential mobility analysis-mass spectrometry (DMA-MS), Proc. Combust. Inst. (2016). http://dx.doi.org/10.1016/j.proci.2016.07.005.

[5] M. Adachi, M. Kusumi, S. Tsukui, Ion-induced nucleation in nanoparticle synthesis by ionization chemical vapor deposition, Aerosol Sci. Technol. 38 (2004) 496-505.

[6] Y. Zhang, S. Li, W. Yan, Q. Yao, D.T. Stephen, Role of dipole–dipole interaction on enhancing Brownian coagulation of charge-neutral nanoparticles in the free molecular regime, The Journal of chemical physics 134 (2011) 084501.

[7] J. Kangasluoma, C. Kuang, D. Wimmer, M. Rissanen, K. Lehtipalo, M. Ehn, D. Worsnop, J. Wang, M. Kulmala, T. Petäjä, Sub-3 nm particle size and composition dependent response of a nano-CPC battery, Atmos. Meas. Tech. 7 (2014) 689-700.

[8] J. Kirkby, J. Curtius, J. Almeida, E. Dunne, J. Duplissy, S. Ehrhart, A. Franchin, S. Gagné, L. Ickes, A. Kürten, Role of sulphuric acid, ammonia and galactic cosmic rays in atmospheric aerosol nucleation, Nature 476 (2011) 429-433.

[9] J. Guo, J.M. Goodings, A.N. Hayhurst, S.G. Taylor, A simple method for measuring positive ion concentrations in flames and the calibration of a nebulizer/atomizer, Combust. Flame 133 (2003) 335-343.

[10] I. Langmuir, H. Mott-Smith, Langmuir probe technique, Gen. Elec. Rev 27 (1924) 449.

[11] M. Sahu, J. Park, P. Biswas, In Situ Charge Characterization of TiO_2 and Cu-TiO_2 Nanoparticles in a Flame Aerosol Reactor, J. Nanopart. Res. 14 (2012) 1-11.

[12] E. Knutson, K. Whitby, Aerosol classification by electric mobility: apparatus, theory, and applications, J. Aerosol Sci. 6 (1975) 443-451.

[13] X. Ma, C. Zangmeister, M. Zachariah, Soot oxidation kinetics: a comparison study of two tandem ion-mobility methods, J. Phys. Chem. C 117 (2013) 10723-10729.

[14] M. Attoui, M. Paragano, J. Cuevas, J. Fernandez de la Mora, Tandem DMA generation of strictly monomobile 1–3.5 nm particle standards, Aerosol Sci. Technol. 47 (2013) 499-511.

[15] M. Maricq, Size and charge of soot particles in rich premixed ethylene flames, Combust. Flame 137 (2004) 340-350.

[16] N. Fuchs, On the stationary charge distribution on aerosol particles in a bipolar ionic atmosphere, Geofisica pura e applicata 56 (1963) 185-193.

[17] S.K. Friedlander, Smoke, dust, and haze: fundamentals of aerosol behavior, Oxford University Press New York, USA, 2000.

[18] R. Gopalakrishnan, M.J. Meredith, C. Larriba-Andaluz, C.J. Hogan Jr, Brownian dynamics determination of the bipolar steady state charge distribution on spheres and non-spheres in the transition regime, J. Aerosol Sci. 63 (2013) 126-145.

[19] S. Kim, K. Woo, B. Liu, M. Zachariah, Method of measuring charge distribution of nanosized aerosols, J. Colloid Interface Sci. 282 (2005) 46-57.

[20] Y. Wang, J. Fang, M. Attoui, T.S. Chadha, W.-N. Wang, P. Biswas, Application of Half Mini DMA for sub 2 nm particle size distribution measurement in an electrospray and a flame aerosol reactor, J. Aerosol Sci. 71 (2014) 52-64.

[21] K. Iida, M.R. Stolzenburg, P.H. McMurry, Effect of working fluid on sub-2 nm particle detection with a laminar flow ultrafine condensation particle counter, Aerosol Sci. Technol. 43 (2009) 81-96.

[22] J. Fernández de la Mora, J. Kozlowski, Hand-held differential mobility analyzers of high resolution for 1-30nm particles: Design and fabrication considerations, J. Aerosol Sci. 57 (2013) 45-53.

[23] J. Fernandez de la Mora, High-Resolution Mobility Analysis of Charge-Reduced Electrosprayed Protein Ions, Anal. Chem. 87 (2015) 3729-3735.

[24] F. Carbone, M. Attoui, A. Gomez, Challenges of measuring nascent soot in flames as evidenced by high resolution differential mobility analysis, Aerosol Science and Technology 50 (2016) 740-757.

[25] L.A. Sgro, A. D’Anna, P. Minutolo, Charge fraction distribution of nucleation mode particles: New insight on the particle formation mechanism, Combust. Flame 158 (2011) 1418-1425.

[26] L. Sgro, A. Barone, M. Commodo, A. D’Alessio, A. De Filippo, G. Lanzuolo, P. Minutolo, Measurement of nanoparticles of organic carbon in non-sooting flame conditions, Proc. Combust. Inst. 32 (2009) 689-696.

[27] L. Sgro, A. De Filippo, G. Lanzuolo, A. D’Alessio, Characterization of nanoparticles of organic carbon (NOC) produced in rich premixed flames by differential mobility analysis, Proc. Combust. Inst. 31 (2007) 631-638.

[28] L.A. Sgro, A. D'Anna, P. Minutolo, Charge distribution of incipient flame-generated particles, Aerosol Sci. Technol. 44 (2010) 651-662.

[29] H. Ouyang, S. He, C. Larriba-Andaluz, C.J. Hogan Jr, IMS-MS and IMS-IMS Investigation of the Structure and Stability of Dimethylamine-Sulfuric Acid Nanoclusters, J. Phys. Chem. A 119 (2015) 2026-2036.

[30] D. Wimmer, K. Lehtipalo, A. Franchin, J. Kangasluoma, F. Kreissl, A. Kürten, A. Kupc, A. Metzger, J. Mikkilä, T. Petäjä, Performance of diethylene glycol based particle counters in the sub 3 nm size range, Atmos. Meas. Tech 6 (2013) 1793-1804.

[31] C. Kuang, M. Chen, P.H. McMurry, J. Wang, Modification of laminar flow ultrafine condensation particle counters for the enhanced detection of 1 nm condensation nuclei, Aerosol Sci. Technol. 46 (2012) 309-315.

[32] L.A. Sgro, J. Fernández de la Mora, A simple turbulent mixing CNC for charged particle detection down to 1.2 nm, Aerosol Sci. Technol. 38 (2004) 1-11.

[33] J. Vanhanen, J. Mikkilä, K. Lehtipalo, M. Sipilä, H. Manninen, E. Siivola, T. Petäjä, M. Kulmala, Particle size magnifier for nano-CN detection, Aerosol Sci. Technol. 45 (2011) 533-542.

[34] K. Lehtipalo, J. Leppä, J. Kontkanen, J. Kangasluoma, A. Franchin, D. Wimmer, S. Schobesberger, H. Junninen, T. Petäjä, M. Sipilä, Methods for determining particle size distribution and growth rates between 1 and 3 nm using the Particle Size Magnifier, Boreal Environ. Res. 19 (2014) 215-236.

[35] J. Kangasluoma, M. Attoui, H. Junninen, K. Lehtipalo, A. Samodurov, F. Korhonen, N. Sarnela, A. Schmidt-Ott, D. Worsnop, M. Kulmala, Sizing of neutral sub 3nm tungsten oxide clusters using Airmodus Particle Size Magnifier, J. Aerosol Sci. 87 (2015) 53-62.

[36] J. Goodings, D. Bohme, C.-W. Ng, Detailed ion chemistry in methane-oxygen flames. I. Positive ions, Combust. Flame 36 (1979) 27-43.

[37] J. Goodings, D. Bohme, C.-W. Ng, Detailed ion chemistry in methane-oxygen flames. II. Negative ions, Combust. Flame 36 (1979) 45-62.

[38] H.R. Jones, A.N. Hayhurst, Measurements of the concentrations of positive and negative ions along premixed fuel-rich flames of methane and oxygen, Combust. Flame 166 (2016) 86-97.

[39] H. Mätzing, W. Baumann, H. Bockhorn, H.-R. Paur, H. Seifert, Detection of electrically charged soot particles in laminar premixed flames, Combust. Flame 159 (2012) 1082-1089.

[40] A. Fialkov, A. Hayhurst, S. Taylor, S. Newcomb, Shapes of soot particles, both charged and uncharged, after molecular beam sampling a premixed oxyacetylene flame, burning at atmospheric pressure, Combust. Sci. Technol. 185 (2013) 1762-1776.

[41] H. Junninen, M. Ehn, T. Petäjä, L. Luosujärvi, T. Kotiaho, R. Kostiainen, U. Rohner, M. Gonin, K. Fuhrer, M. Kulmala, A high-resolution mass spectrometer to measure atmospheric ion composition, Atmos. Meas. Tech. 3 (2010) 1039-1053.

[42] M. Kulmala, J. Kontkanen, H. Junninen, K. Lehtipalo, H.E. Manninen, T. Nieminen, T. Petäjä, M. Sipilä, S. Schobesberger, P. Rantala, Direct observations of atmospheric aerosol nucleation, Science 339 (2013) 943-946.

[43] S. Schobesberger, H. Junninen, F. Bianchi, G. Lönn, M. Ehn, K. Lehtipalo, J. Dommen, S. Ehrhart, I.K. Ortega, A. Franchin, Molecular understanding of atmospheric particle formation from sulfuric acid and large oxidized organic molecules, PNAS 110 (2013) 17223-17228.

[44] J. Almeida, S. Schobesberger, A. Kürten, I.K. Ortega, O. Kupiainen-Määttä, A.P. Praplan, A. Adamov, A. Amorim, F. Bianchi, M. Breitenlechner, Molecular understanding of sulphuric acid-amine particle nucleation in the atmosphere, Nature 502 (2013) 359-363.

[45] Y. Wang, P. Liu, J. Fang, W.-N. Wang, P. Biswas, Kinetics of sub-2 nm TiO_2 particle formation in an aerosol reactor during thermal decomposition of titanium tetraisopropoxide, J. Nanopart. Res. 17 (2015) 1-13.

[46] W. Herrmann, T. Eichler, N. Bernardo, J. Fernández de la Mora, Turbulent transition arises at Re 35000 in a short Vienna type DMA with a large laminarizing inlet, Annual Conference of the AAAR, St. Louis, MO, 2000, pp. 6-10.

[47] J. Kangasluoma, M. Attoui, F. Korhonen, L. Ahonen, E. Siivola, T. Petäjä, Characterization of a Herrmann type high resolution differential mobility analyzer, Aerosol Sci. Technol. 50 (2016) 222-229.

[48] S. Ude, J.F. De la Mora, Molecular monodisperse mobility and mass standards from electrosprays of tetra-alkyl ammonium halides, J. Aerosol Sci. 36 (2005) 1224-1237.

[49] C. Larriba, C.J. Hogan Jr, M. Attoui, R. Borrajo, J.F. Garcia, J.F. de la Mora, The mobility-volume relationship below 3.0 nm examined by tandem mobility-mass measurement, Aerosol Sci. Technol. 45 (2011) 453-467.

[50] B.K. Ku, J.F. de la Mora, Relation between electrical mobility, mass, and size for nanodrops 1-6.5 nm in diameter in air, Aerosol Science and Technology 43 (2009) 241-249.

[51] J. Kangasluoma, A. Samodurov, M. Attoui, A. Franchin, H. Junninen, F. Korhonen, T. Kurtén, H. Vehkamäki, M. Sipilä, K. Lehtipalo, Heterogeneous Nucleation onto Ions and Neutralized Ions: Insights into Sign-Preference, J. Phys. Chem. C 120 (2016) 7444-7450.

[52] B. Liu, D. Pui, K. Rubow, W. Szymanski, Electrostatic effects in aerosol sampling and filtration, Ann. Occup. Hyg. 29 (1985) 251-269.

[53] H. Junninen, Data cycle in atmospheric physics: From detected millivolts to understanding the atmosphere, Department of Physical Sciences, University of Helsinki, Helsinki, 2014.

[54] C.A. Hughey, C.L. Hendrickson, R.P. Rodgers, A.G. Marshall, K. Qian, Kendrick mass defect spectrum: a compact visual analysis for ultrahigh-resolution broadband mass spectra, Anal. Chem. 73 (2001) 4676-4681.

[55] B. Zhao, Z. Yang, J. Wang, M.V. Johnston, H. Wang, Analysis of soot nanoparticles in a laminar premixed ethylene flame by scanning mobility particle sizer, Aerosol Sci. Technol. 37 (2003) 611-620.

[56] N.A. Burdett, A.N. Hayhurst, Hydration of gas-phase ions and the measurement of boundary-layer cooling during flame sampling into a mass spectrometer, J. Chem. Soc., Faraday Trans. 78 (1982) 2997-3007.

[57] A. Hayhurst, Mass spectrometric sampling of a flame, Combust. Explos. Shock Waves 48 (2012) 516-525.

[58] K. Siefering, G. Griffin, Growth kinetics of CVD TiO_2: influence of carrier gas, J. Electrochem. Soc. 137 (1990) 1206-1208.

[59] H. Calcote, 8th International Symposium on Combustion, Williams and Wilkins, Baltimore, (1962) 184.

[60] J.M. Goodings, J. Guo, A.N. Hayhurst, S.G. Taylor, Current-voltage characteristics in a flame plasma: analysis for positive and negative ions, with applications, Int. J. Mass Spectrom. 206 (2001) 137-151.

[61] H. Calcote, Mechanisms for the formation of ions in flames, Combust. Flame 1 (1957) 385-403.

[62] A. Maißer, J.M. Thomas, C. Larriba-Andaluz, S. He, C.J. Hogan, The mass-mobility distributions of ions produced by a Po-210 source in air, J. Aerosol Sci. 90 (2015) 36-50.

[63] A. Hayhurst, D. Kittelson, The positive and negative ions in oxy-acetylene flames, Combust. Flame 31 (1978) 37-51.

[64] S. Axford, A. Hayhurst. Mass spectrometric sampling of negative ions from flames of hydrogen and oxygen: the kinetics of electron attachment and Detachment in Hot Mixtures of

H_2O, O_2, OH and HO_2. In: editor^editors. Proceedings of the Royal Society of London A: Mathematical, Physical and Engineering Sciences; 1996: The Royal Society. p. 1007-1033.

[65] C.K. Law, Combustion physics, Cambridge University Press2006.

[66] S.R. Turns, An introduction to combustion, McGraw-Hill New York1996.

[67] G. Steiner, T. Jokinen, H. Junninen, M. Sipilä, T. Petäjä, D. Worsnop, G.P. Reischl, M. Kulmala, High-Resolution Mobility and Mass Spectrometry of Negative Ions Produced in a 241Am Aerosol Charger, Aerosol Sci. Technol. 48 (2014) 261-270.

[68] H. Manninen, A. Franchin, S. Schobesberger, A. Hirsikko, J. Hakala, A. Skromulis, J. Kangasluoma, M. Ehn, H. Junninen, A. Mirme, Characterisation of corona-generated ions used in a Neutral cluster and Air Ion Spectrometer (NAIS), Atmos. Meas. Tech. 4 (2011) 2767-2776.

[69] A. Shmakov, O. Korobeinichev, D. Knyazkov, A. Paletsky, R. Maksutov, I. Gerasimov, T. Bolshova, V. Kiselev, N. Gritsan, Combustion chemistry of Ti (OC3H7)4 in premixed flat burner-stabilized H2/O2/Ar flame at 1atm, Proc. Combust. Inst. 34 (2013) 1143-1149.

[70] J.M. Goodings, Q. Tran, N.S. Karellas, Ion chemistry of transition metals in hydrocarbon flames. II. Cations of Sc, Ti, V, Cr, and Mn, Can. J. Chem. 66 (1988) 2219-2228.

[71] M. Kulmala, M. Maso, J. Mäkelä, L. Pirjola, M. Väkevä, P. Aalto, P. Miikkulainen, K. Hämeri, C. O'dowd, On the formation, growth and composition of nucleation mode particles, Tellus B 53 (2001) 479-490.

Chapter 6: Influence of Flame-generated Ions on the Simultaneous Charging and Coagulation of Nanoparticles during Combustion

The results of this chapter have been published in Wang, Y., Sharma, G., Koh, C., Kumar, V., Chakrabarty, R. K., Biswas, P. (2017). Influence of flame-generated ions on the simultaneous charging and coagulation of nanoparticles during combustion. Aerosol Sci. Technol. doi:10.1080/02786826.2017.1304635.

Supplementary figures and tables are available in Appendix II

Abstract

Flames generate a large amount of chemically and thermally ionized species, which are involved in the growth dynamics of particles formed in flames. However, existing models predicting particle formation and growth do not consider particle charging, which may lead to bias in the calculated size distribution of particles. In this study, Fuchs' charging theory was coupled with a monodisperse particle growth model to study the simultaneous charging and coagulation of nanoparticles during combustion. In order to quantify the charging characteristics of nanoparticles, a high-resolution DMA was used to measure the mobilities of ions generated from a premixed flat flame operated at various conditions. The effect of temperature on ion-particle and particle-particle combination coefficients was further examined. The proposed model showed that the influence of charging on particle growth dynamics was more prominent when the ion concentration was comparable to or higher than the particle concentrations, a condition which may be encountered in flame synthesis and solid fuel-burning. Simulated results also showed that unipolar ion environments strongly suppressed the coagulation of particles. In the end, a simplified analysis of the relative importance of particle charging and coagulation was proposed by comparing the characteristic time scales of these two mechanisms.

6.1 Introduction

Combustion is a major source of particulate matter (PM) generation (Biswas and Wu 2005). The precise control of aerosol formation during combustion is equally crucial for both the applications of flame-generated particles (Hu et al. 2016; Li et al. 2016b; Liu et al. 2015) and their environmental implications (Li et al. 2016a; Wang et al. 2013). However, a detailed understanding of the particle dynamics in flames is lacking due to the fast reaction rate of combustion, making it difficult to control the particle formation and growth processes. Due to the limitations of instruments, the particle nucleation and growth at initial stages during combustion, especially below 3 nm, still remain to be a knowledge gap (Wang et al. 2014). At the same time, because of chemical ionization and thermal ionization mechanisms (Fialkov 1997), flames generate large numbers of ions and charged clusters with concentrations as high as 10^{10} /cm^3. A recent study conducted with a series of enhanced particle detectors showed that the fraction of charged species can be high in a premixed flame (Wang et al. 2017). The presence of these ions makes the flame a quasi-neutral plasma that may notably affect the property of the produced particles. The highly concentrated ions and charged clusters actively collide with the formed nanoparticles, adding electrostatic potentials to the system, and further altering the properties of the generated particles, such as their size, shape, and crystallinity (Jiang et al. 2007a; Zhang et al. 2012). This effect is significantly enhanced when manipulated ion environments (such as unipolar-ion environments and concentrated ion environments) are imposed (Vemury and Pratsinis 1995; 1996; Vemury et al. 1997; Xiong et al. 2016; Zhang et al. 2012; Zhang et al. 2011; Karnani et al. 2015; Weinberg et al. 2013).

According to Fuchs' charging theory, the particle charging probability is determined by the mass and mobility of the surrounding ions (Fuchs 1963). Although it neglects the effect of particle morphology and absolute ion concentrations, Fuchs' charging theory provides a quantitative match with the experimentally measured charging probabilities of particles between 3 nm to 1 μm (Gopalakrishnan et al. 2015; Hoppel and Frick 1986; Jiang et al. 2007a; Reischl et al. 1996). Therefore, direct measurement of ion mass and mobility can shed light upon particle charging probabilities in flames. Previously, this type of measurement was difficult due to the low resolution of instruments determining the mobility of highly diffusive ions below 3 nm. With the development of differential mobility analyzers (DMAs) with high sheath flow rates, the residence time for particle diffusion in the instrument is greatly reduced, enhancing the resolution of ion mobility measurements (Fang et al. 2014; Kangasluoma et al. 2016a; Wang et al. 2014; Wang et al. 2015; Carbone et al. 2016). The coupling of a high-resolution DMA with an atmospheric pressure-inlet mass spectrometer (MS), i.e., tandem DMA-MS, enables the simultaneous measurement of ion mobility and mass, through which the accurate calculation of the interaction between ions and particles becomes achievable (Gopalakrishnan et al. 2015; Maißer et al. 2015). Apart from creating the ion-particle interactions, the presence of ions in particle systems also modifies the charge distributions of particles, changing the electrostatic potentials among the flame-generated particles and altering the coagulation growth of flame-generated nanoparticles. In existing models predicting particle formation in flames, the influence of particle charging is not evaluated, although the attractive or repulsive forces among particles can vary the coagulation coefficients greatly (Friedlander 2000).

In order to study how ions affect particle formation in flames, one needs to solve the particle general dynamic equation by coupling particle charging and coagulation (Jiang et al. 2007b). Existing studies have attempted to solve these two mechanisms separately. By assuming particle size distributions remain constant, kinetic equations tracking the concentrations of ions and particles with different charging states were solved based on the ion-particle combination coefficients (Fuchs 1963; Jean et al. 2015; Reischl et al. 1996; López-Yglesias and Flagan, 2013). There is a plethora of modeling methods predicting particle formation dynamics where particle charging is not considered, including the unimodal model, bimodal model, method of moments, and discrete-sectional model (Wu and Flagan 1988; Landgrebe and Pratsinis 1990; Tsantilis et al. 2002). These models are applicable when there is a large difference between the characteristic times for particle charging and coagulation. However, when the two time scales are similar to each other, such assumptions ignoring certain mechanisms cannot be made, especially in flame systems, where the particle coagulation time may have a broad range depending on the particle concentrations in different scenarios. Few studies to date have investigated simultaneous charging and coagulation during particle formation and growth. Alonso et al. (199) studied the transient charging and coagulation of nanoparticles in an aerosol charger with constant ion concentration, in order to examine the effect of mean aerosol residence time on the output concentration of charged particles. Fujimoto et al. (2003) calculated the unipolar ion charging and particle coagulation during aerosol formation from titanium isopropoxide thermal decomposition at temperatures below 500 ^{o}C, and predicted that the particles' average size, standard deviation, and concentration were affected greatly. Recently, Kim et al. (2016) simulated the charging and coagulation of radioactive and non-radioactive particles in the atmosphere and found that the mutual effects of the two mechanisms indeed alter the particle size distribution. These studies demonstrate that simultaneous particle charging and coagulation may be different from particle dynamics predicted by commonly used models.

In this paper, the simultaneous charging and coagulation of flame-generated particles by coupling Fuchs' charging theory with a monodisperse model predicting particle growth dynamics was simulated. In order to quantify the particle charging mechanism, a high-resolution DMA was used to measure the mobility distributions of ions generated from a premixed flat flame. Different operating conditions of the flame were applied to study their influence on ion generation. The obtained ion mobilities were used as inputs to the proposed model for calculating particle growth dynamics in the presence of charging, where the effects of initial particle concentration and the polarity of the ions were specifically investigated.

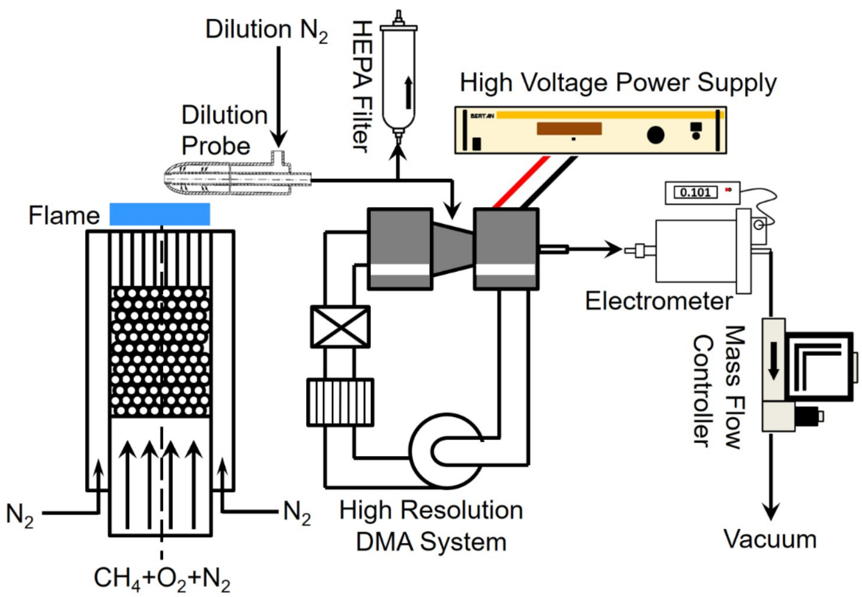

Figure 6.1 Schematic diagram of the experimental setup, including a premixed flat flame and a high-resolution DMA system.

6.2 Methods

6.2.1 Experimental setup

Figure 6.1 shows a schematic diagram of the experimental setup. A premixed flat flame was used in this study to measure ion mobility distributions, due to its high stability, uniformity, and broad usage. A detailed description of the setup can be found elsewhere (Wang et al. 2016). The combustion mixture was composed of methane (CH_4, Airgas Inc.), oxygen (O_2, Airgas Inc.), and nitrogen (N_2, Airgas Inc.) whose flow rates were controlled by mass flow controllers (MKS Inc.). Before their mobility distributions were examined, the flame-generated ions were sampled with a dilution probe operated at a dilution ratio of 180, with N_2 (Airgas Inc.) as the dilution gas. A high-resolution DMA (half mini-type (Fernández de la Mora and Kozlowski 2013)) was used to measure the mobility of the flame-generated ions. Details of the DMA setting and calibration method (Ude and de la Mora 2005) can be found in the supplemental information. The ion mobility distributions in both polarities can be obtained by scanning the DMA voltage from 0 to ±5 kV. The mobility size of the ions (d_{ion}) was then calculated by

$$Z = Cne / 3\pi\mu d_{ion} \tag{6.1}$$

where C is the Cunningham slip correction factor, n is the number of charges on the particle, e is the electronic charge, μ is the air viscosity, and d_{ion} is the ion mobility size. It should be noted that the d_{ion} value calculated with this equation is larger than its actual value (volumetric size) due to the ion-induced dipole created on the surrounding gas molecules (Larriba et al. 2011). However, since size information is not needed in calculating the charging characteristics of flame-generated particles, Eq. (6.1) is still used to qualitatively show the size of the ions. In this study, it was assumed that all the flame-generated ions carry one charge only, which is typical in combustion systems (Fialkov 1997). The concentration of charged clusters was calculated based on the current recorded by the electrometer, as introduced in the supplemental information.

Table 6.1 Experimental plan showing the combination of flow rates, adiabatic flame temperatures, and sampling heights.

Test #	Flow rates (lpm)			ϕ	T_A (K)	H_{AB} (mm)
	CH_4	O_2	N_2			
1	0.85	2.85	7.33	0.60	2015	5
2	1.20	2.85	8.10	0.85	2401	5
3	1.42	2.85	9.09	1.00	2529	5
4	1.57	2.85	8.09	1.10	2416	5
5	1.20	2.85	8.10	0.85	2401	5 – 20

A series of flow rates in the flat flame was used to study the effects of the flame equivalence ratio on flame-generated ions. Additional measurements at different heights above the burner (H_{AB}) were conducted to elucidate the ion properties as a function of residence time after their formation. The detailed flow rates, flame equivalence ratio (ϕ), and H_{AB} combinations are listed in Table 6.1. The flow rate settings achieved ϕ values of 0.60, 0.85, 1.00, and 1.10 in Tests 1 through 4. Since changing ϕ can result in different flame speeds and flame positions, N_2 flow was adjusted accordingly to maintain a constant height of the flame sheet. Table 6.1 also lists the adiabatic flame temperatures under different flow rate settings calculated using the major-minor species model (Turns, 1996). Note that due to temperature and dilution effects, the sampling at the same H_{AB} does not imply equal residence time in different flames. The ion mobility distributions were measured in a broad range of H_{AB} (5 – 20 mm), where different characteristics of positive and negative ions were observed. The effect of sampling height on ion size and mobility distribution is discussed in the supplemental information due to the page limit.

6.2.2 Simulation method

Ion-particle and particle-particle combination coefficients

In order to track simultaneous particle charging and coagulation, combination rates among the ions and particles, which are determined by the ion-particle and particle-particle combination coefficients were calculated.

According to Fuchs' charging theory (1963), the only unknown parameters in calculating the ion-particle combination coefficient are the positive and negative ion mobilities and masses. Ideally, the mobility and mass of an ion should be measured with a tandem DMA-MS setup, where these values are obtained at the same time (Maißer et al. 2015; Wang et al. 2016). Due to the instrument limitation, ion mobility was the only parameter measured in this study. Approximate mass values of 140 amu and 70 amu for positive and negative ions were used, which are in the range of existing measurement results obtained with mass spectrometers (Fialkov 1997). These atomic mass values also agree with a recent study on the measurement of premixed flat flame-generated ions with an atmospheric pressure-inlet time-of-flight mass spectrometer, where the dominant positive charge carriers were hydrocarbons (100-250 amu) and dominant negative charge carriers were nitrate-related ions (62 amu and 125 amu) (Wang et al. 2017). As pointed out by the study of the sensitivity analysis in Fuchs' charging model, the main influential variable is the difference between the positive and negative ion mobilities, which were measured accurately in this study (Tigges et al. 2015). Because the DMA-measured flame-generated ions had distributed mobilities, the number-weighted mean mobilities of the positive and negative ions was calculated. Furthermore, since the mobility values were measured at 298 K, which was the sheath flow temperature of the DMA, one needs to convert the measured mobility values to those at other temperatures. Here, a mobility-temperature dependence of

$Z \propto T^{0.5}$ was used (Larriba et al. 2011). The influence of other mobility-temperature dependences on calculating the ion-particle combination coefficient was discovered to be small (Figure A2.1). The ion-particle combination coefficient $\eta_i^{\pm}$ of positive (+) and negative (–) ions with a particle carrying *i* elementary units of charge can be derived as

$$\eta_i^{\pm} = \frac{\beta_i^{\pm} \exp[-\phi_i(\delta^{\pm})/kT]}{1+\exp[-\phi_i(\delta^{\pm})/kT][\beta_i^{\pm}/4\pi D^{\pm}]\int_0^1 \exp[\phi_i(\delta^{\pm}/x)/kT]dx} \tag{6.2}$$

The particle-particle combination coefficient for the Brownian collision of spherical particles in the free molecular and continuum regime (Seinfeld and Pandis 2012) is given by

$$\beta_{brownian}(d_i, d_j) = 2\pi(d_i + d_j)(D_i + D_j)\left\{\frac{d_i + d_j}{d_i + d_j + 2(g_i^2 + g_j^2)^{1/2}} + \frac{8(D_i + D_j)}{(d_i + d_j)(c_i^2 + c_j^2)^{1/2}}\right\}^{-1} \tag{6.3}$$

In the presence of electrostatic interaction between charged particles, the combination coefficient is modified by a correction factor (W) (Friedlander 2000) which is given by

$$\beta_{coag}^{i,j}(d_i, d_j) = \frac{\beta_{brownian}(d_i, d_j)}{W(z_i, z_j)} \tag{6.4}$$

Detailed explanations and calculation results of Eqs. (6.2) to (6.4) are included in the supplemental information.

Calculation of simultaneous particle charging and coagulation

Using the ion-particle and particle-particle combination coefficients, the detailed equations describing the concentrations of ions and particles with different charging states can be written.

The following differential equations track the ion number concentration ($n_{\pm}$), particle number concentration ($N_{p,k}$), and total particle volume concentration ($V_{p,k}$) at any time:

$$\frac{dn_{\pm}}{dt} = q_{\pm} - \alpha n_{\pm} n_{\mp} - n_{\pm} \sum_{k=-m}^{k=m} \eta_k^{\pm} N_{p,k} \tag{6.5}$$

In this equation, *k* is the number of charges carried by each particle, $q_{\pm}$ is the generation rate of ions, α is the ion recombination coefficient, and $\eta_k^{\pm}$ is the ion-particle combination coefficient calculated in Eq. (6.2). The three terms on the right hand side (RHS) of Eq. (6.5) correspond to the rate of ion generation, the loss of ions due to recombination, and the loss of the ions due to collision with particles, respectively. When solving Eq. (6.5), for simplicity, the rate of ion generation was set to 0 due to the thinness of the reaction zone (flat flame sheet) in combustion, and the initial concentration of ions was set to be 10^{10} /cm^3, based on a summary of existing measurements of ion concentrations in flames (Fialkov, 1997; Kim et al. 2005; Alquaity et al. 2016). As illustrated in previous studies, the change of fuel type and combustion equivalence ratio will affect the ion concentrations, however, the influence was not strong, where the ion concentrations were in the range of 10^9 to 10^{11} /cm^3. It reveals that the ion concentrations in the flame may be an intrinsic value, which may not be very sensitive to flame conditions due to combustion chemistries. Regarding the ion recombination, theoretically, since the masses and mobilities of electrons and negatively charged clusters were significantly different from each other, a complete model should consider this difference in recombination coefficients. However, due to the difficulty in retrieving the data on recombination coefficients between positive ions and elections, in this model, the recombination was considered to take place between positively and negatively charged clusters only, and a constant value of 1×10^{-7} cm^3/s obtained in various combustion studies was used (Fialkov, 1997). α increases as temperature decreases, since the attractive electrostatic potential start to dominate over kinetic movement of ions with opposite polarities. In this study, the influence of using larger α values at lower temperatures was determined to be minimal. The number concentration and total volume of particles carrying *k* charges are described by

$$\begin{aligned}\frac{dN_{p,k}}{dt} &= n_+ N_{p,k-1}\eta_{k-1}^+ + n\_N_{p,k+1}\eta_{k+1}^+ - n_+ N_{p,k}\eta_k^+ - n\_N_{p,k}\eta_k^- + \frac{1}{2}\sum_{i=-m}^{i=+m}\sum_{j=-m}^{j=+m}{}^{\forall i+j=k}\beta_{coag}^{i,j}N_{p,i}N_{p,j} \\ &\quad - N_{p,k}\sum_{j=-m}^{j=+m}\beta_{coag}^{k,j}N_{p,j} - 4\pi Z^k e^2 k N_k \sum_{j=-m}^{j=+m} jN_{p,j}\end{aligned} \tag{6.6}$$

$$\begin{aligned}\frac{dV_{p,k}}{dt} &= n_+ V_{p,k-1}\eta_{k-1}^+ + n\_V_{p,k+1}\eta_{k+1}^+ - n_+ V_{p,k}\eta_k^+ - n\_V_{p,k}\eta_k^- + \frac{1}{2}\sum_{i=-m}^{i=+m}\sum_{j=-m}^{j=+m}{}^{\forall i+j=k}\beta_{coag}^{i,j}N_{p,i}N_{p,j}(v_i + v_j) \\ &\quad - N_{p,k}v_k\sum_{j=-p}^{j=+p}\beta_{coag}^{k,j}N_{p,j} - 4\pi Z^k e^2 k V_{p,k} \sum_{j=-m}^{j=+m} jN_{p,j}\end{aligned} \tag{6.7}$$

$$v_k = \frac{V_{p,k}}{N_{p,k}} \tag{6.8}$$

In these equations, v_k is the volume of each particle with charge k, $\beta_{coag}^{i,j}$ is the particle-particle combination coefficient calculated with Eqs. (6.2) and (6.4), and Z^k is the mobility of particles with k charges. In both equations, the first and second terms on the RHS together account for the gain of particles by ion-particle collision. The third and fourth terms together account for loss of particles by ion-particle collision. The fifth term represents the gain of particles through the coagulation of charged particles. The sixth term accounts for the loss of particles through coagulation, and the seventh term accounts for the loss of particles due to electrostatic dispersion. Note that *m*, the highest charging state of particles, is assumed to take values between -4 and +4 in this study.

The simulation assumes a constant temperature environment (300, 600, 1200, or 2400 K) synthesizing TiO_2 nanoparticles, and records the particle size and the concentrations of ions and particles as a function of time. It should be noted that in flame systems, the flow field and temperature field are not uniform, so the assumption of a constant temperature may not be valid. However, in premixed flat flames, the one-dimensionality and uniformity of the flame makes it similar to a plug flow reactor, where investigating particle charging and coagulation at specific temperatures is meaningful.

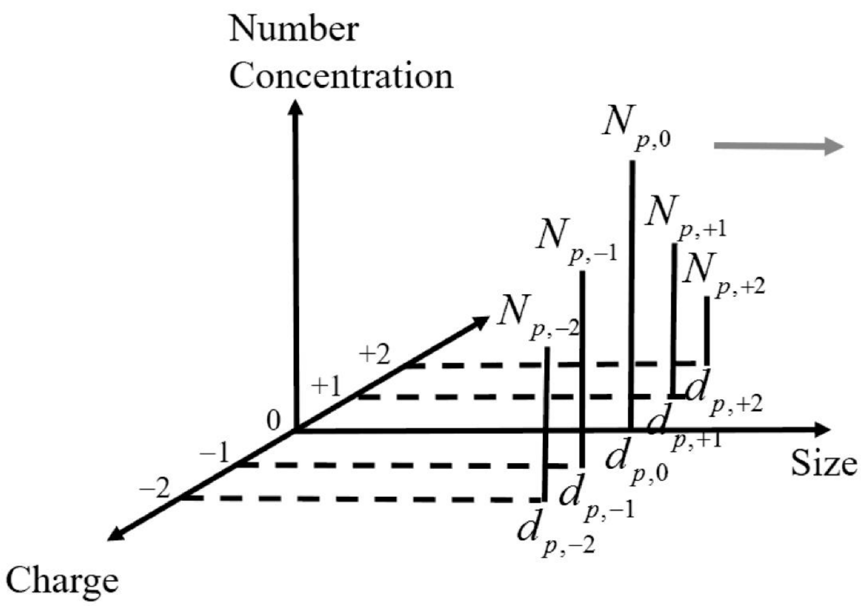

Figure 6.2 Schematic diagram of the monodisperse model for charge (k) from −2 to +2. For each charge there is one mode represented by $N_{p,k}$ and $d_{p,k}$. The arrow pointing towards right indicates that as time goes by coagulation leads to increase in size for all the modes. Note that the size ($d_{p,k}$) may be different for different values of k .

Eqs. (6.5) to (6.8) together represent a population balance on the ion concentration, particle number concentration and particle volume concentration, respectively. This system of coupled ordinary differential equations is non-dimensionalized and solved using the VODE solver in Python with backward differentiation formulas (BDF). At any time t, this monodisperse model assumes one size mode for each charge, v_k, calculated by Eq. (6.8), instead of a particle size distribution (Vemury et al. 1997). The schematic of the model is shown in Figure 6.2. This model is found to be in good agreement with the predictions of highly accurate aerosol dynamics model. The slight error which is contributed by the overestimation of mean particle diameter and underestimation of the particle number concentration is inconsequential (Landgrebe and Pratsinis 1990). Both bipolar and unipolar ion environments were simulated, since flame synthesis under these conditions can be achieved (Vemury and Pratsinis 1995; 1996; Vemury et al. 1997). A baseline group that calculates particle dynamics with coagulation only was also conducted for comparing the results. A total simulated time of 1 s was used, since in flame systems, the residence time of particles in a specific temperature zone is less than 1 s. For the simulations performed, the total number concentration of particles at any time t, $N_p(t)$ is the sum of all the positively charged, negatively charged and neutral particles.

$$N_p(t) = \sum_{k=-m}^{k=+m} N_{p,k}(t) \tag{6.9}$$

The average diameter of particles at any time t, $d_{p,avg}(t)$ is defined as:

$$d_{p,avg}(t) = \frac{\sum_{k=-m}^{k=+m} N_{p,k}(t) d_{p,k}(t)}{N_p(t)} \tag{6.10}$$

The average charge on the particles at any time t, $q_{p,avg}(t)$ is calculated as:

$$q_{p,avg}(t) = \frac{\sum_{k=-m}^{k=+m} N_{p,k}(t) q_{p,k}(t)}{N_p(t)} \tag{6.11}$$

Table 6.2 lists the parameters and their values used in the simulation. Different initial particle concentrations were used to study influence of initial particle-to-ion concentration ratio on particle growth, since in real situations, the initial particle concentration in a flame can be easily changed by adjusting the precursor concentration. The initial particle size was assumed to be 0.4 nm, which is the diameter of a TiO_2 molecule (Tsantilis et al. 2002). Furthermore, particles were set to be neutral at the initial time.

Table 6.2 Parameters used in the simulation of particle simultaneous charging and coagulation.

Parameters	**Values**
Initial Positive Ion Concentration ($N_{i,t=0}$)	10^{10} /cm^3
Initial Negative Ion Concentration ($N_{i,t=0}$)	10^{10} /cm^3 (bipolar)/ 0 /cm^3 (unipolar)
Positive Ion Mobility and Mass	1.54 cm^2/Vs and 140 amu
Negative Ion Mobility and Mass	1.97 cm^2/Vs and 70 amu
Initial Particle Concentration (all neutral) ($N_{p,t=0}$)	10^8 / 10^{10} / 10^{12} / 10^{13} /cm^3
Initial Particle Diameter	0.4 nm
Temperature (T) Ion Recombination Coefficient (α)	300 / 600 / 1200 / 2400 K 10^{-7} cm^3/s

6.3 Results and Discussion

6.3.1 Size and mobility distribution of flame-generated ions

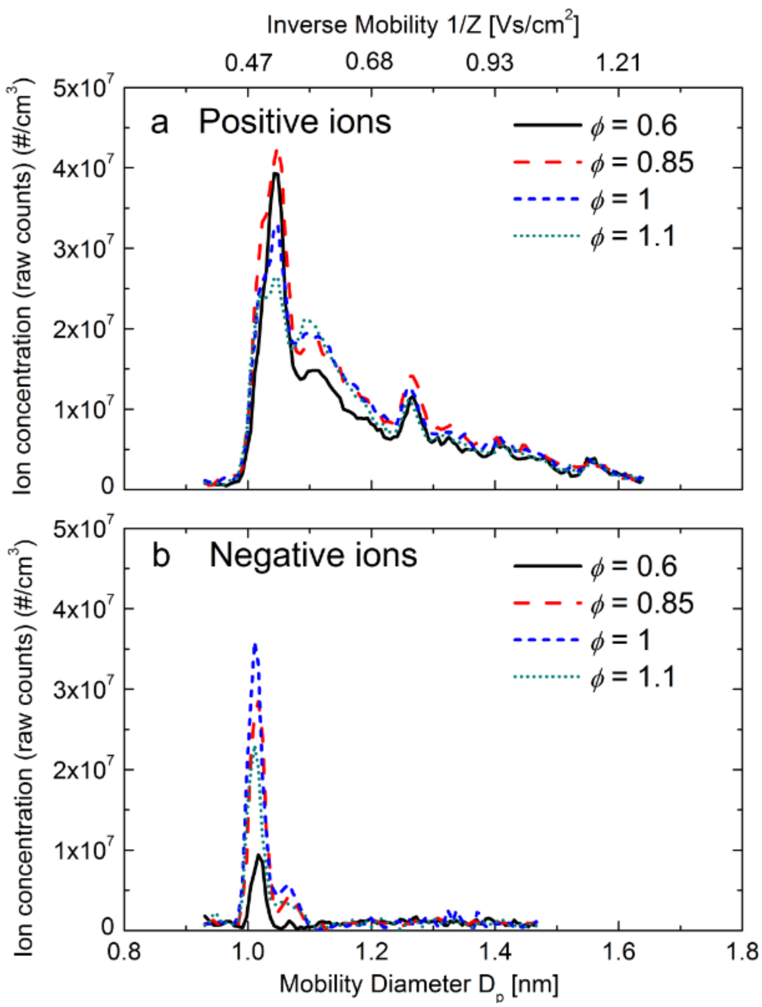

Figure 6.3 Positive and negative ion size distributions as a function of flame equivalence ratio (ϕ). Sampling height H_{AB} = 5 mm. The corresponding ion inverse mobility is labeled in the upper x-axis. Note that the y-axis is the raw counts monitored by the electrometer.

Figure 6.3 displays the size and mobility distributions of positive and negative ions generated from flames operated at different equivalence ratios (ϕ). The high-resolution DMA detected characteristic peaks at 1.04, 1.10, and 1.27 nm in positive ions and at 1.01 and 1.06 nm in negative ions. These charged particles were believed to come from the intensive chemical ionization in the studied flames, where the temperatures were not high enough to generate charged species through thermal ionization (Fialkov 1997; Jiang et al. 2007b; Wang et al. 2017). One can also notice that the measured ion sizes are larger than those expected from clusters composed of a few atoms. The mobility size shown in the size distributions is inherently larger than the volumetric size of a charged cluster due to the ion-induced dipole effect, which pose a stronger drag force on charged cluster. Recent studies (Wang et al. 2016; 2017) also indicates that the major peak (1.01 nm) in the negative ion size distributions is mainly composed of nitrate ions (NO_3^-), which has an ionic radii of 0.179 nm (Volkov et al. 1997). Hence, further study with a mass spectrometer is needed in order to determine the exact chemical composition of the measured ions and charged clusters. On the other hand, the relatively large mobility size might be caused by the limitation of the sampling system, where the rapid quenching not only stopped particle dynamics, but also altered the chemical equilibriums, introducing new species to the measurement (Carbone et al. 2016). During CH_4 combustion, the chemically produced positively and negatively charged species mainly come from two reactions:

$$CH + O \rightarrow CHO^+ + e^- \tag{6.12}$$

$$CH^* + C_2H_2 \rightarrow C_3H_3^+ + e^- \tag{6.13}$$

where the formed ions and electrons collide with other molecules to form more stable charged species. According to recent work by Jones and Hayhurst (2016), the reaction shown in Eq. (6.12) dominates in fuel-lean combustion of methane (C/O $\leq$ 0.4). A pool of positive ions is then formed rapidly, mainly through proton transfer from CHO^+ to other intermediates and final products of combustion. The average mobility of negative ions was higher than that of positive ions, possibly because the positive ions were composed of organic species, which had higher proton affinities. As the flame transited from fuel-lean to fuel-rich, the concentration of the detected ions first increased and then decreased. The increase in ion concentration was caused by the stronger chemical ionization processes in the flame, while the decrease was a result of depletion of free oxygen atoms in the reaction zone (Jones and Hayhurst 2016). It also shows that the number concentration of positive ions is higher than that of negative ions. According to charge neutrality, this result suggests that electrons may serve as a major species of negative charge carriers. The presence of highly mobile electrons can lead to a higher fraction of particles being negatively charged. The chemical species of these stable intermediates did not change as a function of ϕ (as indicated by the same peak location), except that the relative magnitude of these charged species differed. For example, at $\phi = 1.1$, the concentration of the larger positive ions (1.10 and 1.27 nm) was higher than that at $\phi = 0.6$, while the concentration of 1.04 nm positive ions was lower than that at $\phi = 0.6$, implying a conversion from smaller to larger ions as ϕ increased. However, as indicated in existing studies conducted with molecular beam mass spectrometry, these charged species may alter as ϕ further increases to sooting conditions (Jones and Hayhurst 2016). Based on the measurement results, the positive and negative ion mobilities used for calculating ion-particle combination coefficients were 1.54 cm^2/Vs and 1.97 cm^2/Vs, by averaging the mobility distributions measured at $\phi = 0.85$ and H_{AB}=5 mm.

6.3.2 Simultaneous particle charging and coagulation

Using the calculated ion-particle and particle-particle combination coefficients (Figures A2.2 and A2.3), particle and ion concentrations are analyzed with the population balance equations (Eqs. (6.5) to (6.8)). The results of simultaneous particle charging and coagulation in the unipolar and bipolar ion environments are shown as follows.

Unipolar ion environment

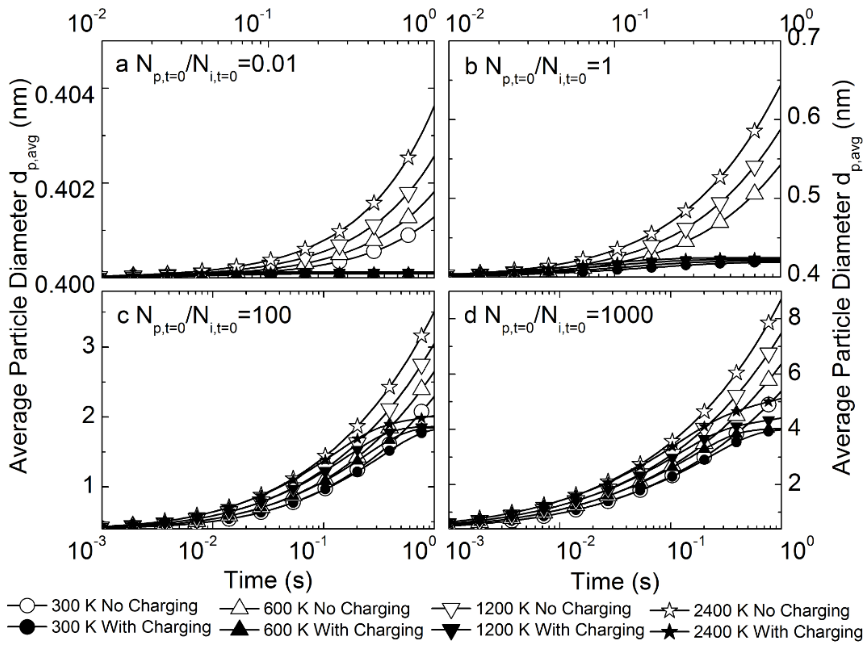

Figure 6.4 Evolution of average particle size as a function of time at different temperatures, with and without charging effects in a unipolar ion environment. Subplots represent initial particle-to-ion concentration ratios of a) 0.01, b) 1, c) 100, and d) 1000. Note the different scales of x-axes and y-axes.

Figures 6.4 and 6.5 show the change of particle average size and concentration as a function of time in a unipolar ion environment with different initial particle-to-ion ratios. The effect of the unipolar ion environment on particle growth is very prominent. Due to particle charging, the coagulation among unipolarly charged particles is significantly suppressed. In all the calculated cases, the average particle size first increases and then reaches a plateau where particle size stops increasing (Figure 6.4). Similar results were observed in existing experimental studies when unipolar ions were introduced into flames synthesizing nanoparticles: The electrostatic repulsion dispersed the synthesized particles, and a monodisperse product was obtained (Vemury and Pratsinis 1995). The point where particle size stopped increasing was determined by the relative concentrations of particles and ions, which is shown more directly in Figure 6.5. The particle concentration stops decreasing when it is comparable to the initial ion concentration (Figures 6.5c and 6.5d). Hence, creating unipolar ion environments during flame synthesis of nanoparticles can effectively suppress particle growth, and the size of the synthesized particles can be controlled by manipulating the relative concentrations of unipolar ions and particles.

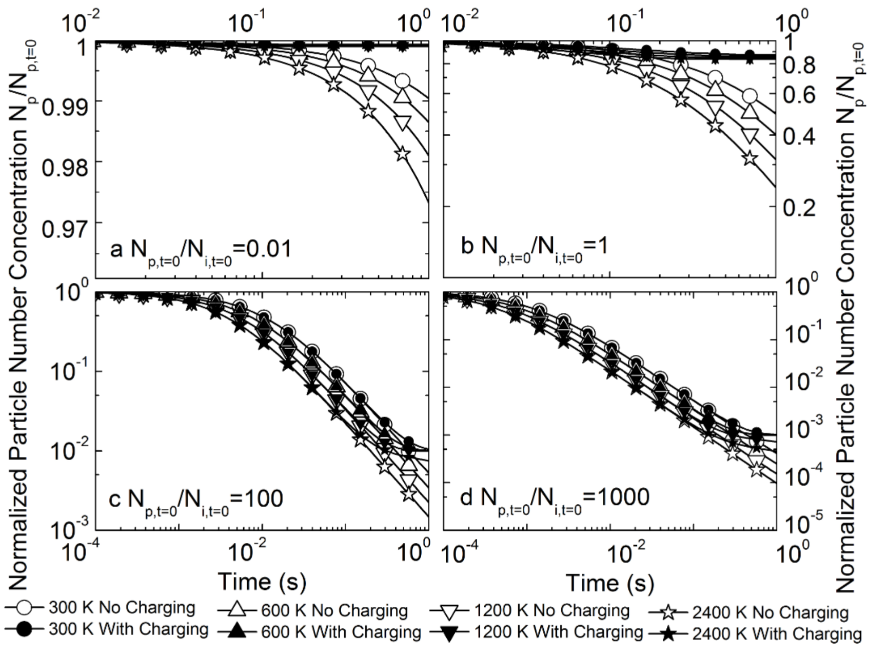

Figure 6.5 Evolution of normalized particle number concentration as a function of time at different temperatures, with and without charging effects in a unipolar ion environment. Subplots represent the cases with initial particle-to-ion concentration ratios of a) 0.01, b) 1, c) 100, and d) 1000. Note the different scales of x-axes and y-axes.

Bipolar ion environment

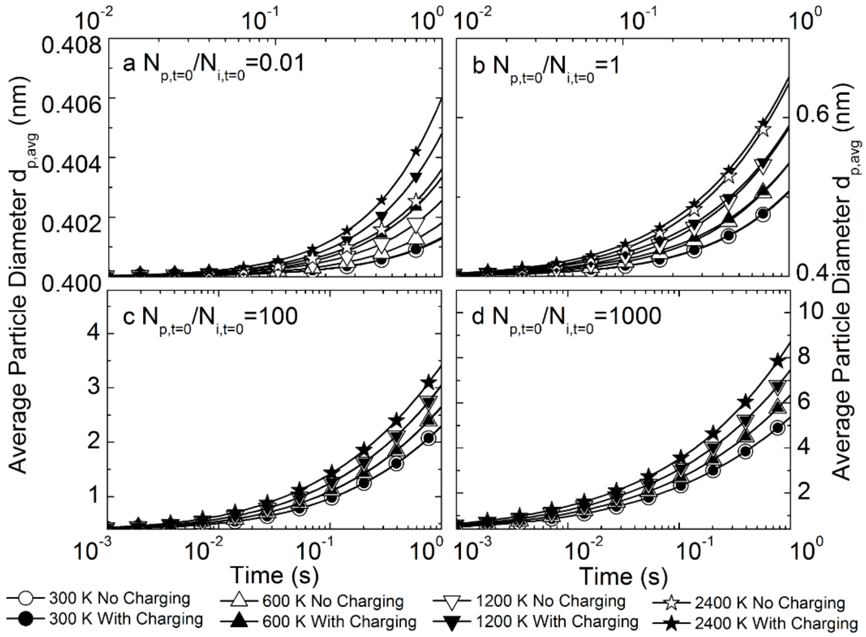

Figure 6.6 Evolution of average particle size as a function of time at different temperatures, with and without charging effects in a bipolar ion environment. Subplots represent initial particle-to-ion concentration ratios of a) 0.01, b) 1, c) 100, and d) 1000. Note the different scales of x-axes and y-axes.

Figure 6.6 shows the evolution of average particle size as a function of time in a bipolar ion environment. When the initial particle concentration is low ($N_{p,t=0} / N_{i,t=0} = 0.01$, Figure 6.6a), minimal particle growth is observed after a simulated time of 1 s. The bipolar ion environment is found to enhance particle growth, especially at higher temperatures. This finding also agrees with atmospheric studies on ion-induced nucleation, where the participation of ions plays a more significant role when the molecular cluster concentration is lower (Kangasluoma et al. 2016b; Laakso et al. 2002). The effect of a bipolar ion environment is less important or even negligible when the initial particle concentration is comparable to or higher than the initial ion concentration (Figures 6.6b, 6.6c, and 6.6d). The limited effect of bipolar ions is a result of ion recombination, which quickly consumes all the available ions. As the initial particle concentration increases, the grown particle size also becomes larger, reaching 9 nm at a temperature of 2400 K after 1 s. The evolution of normalized particle concentration as a function of time with different initial particle-to-ion concentration ratios is displayed in Figure A2.5, which corresponds well with the results on particle size, showing that the initial particle-to-ion concentration determines the influence of bipolar ion environment.

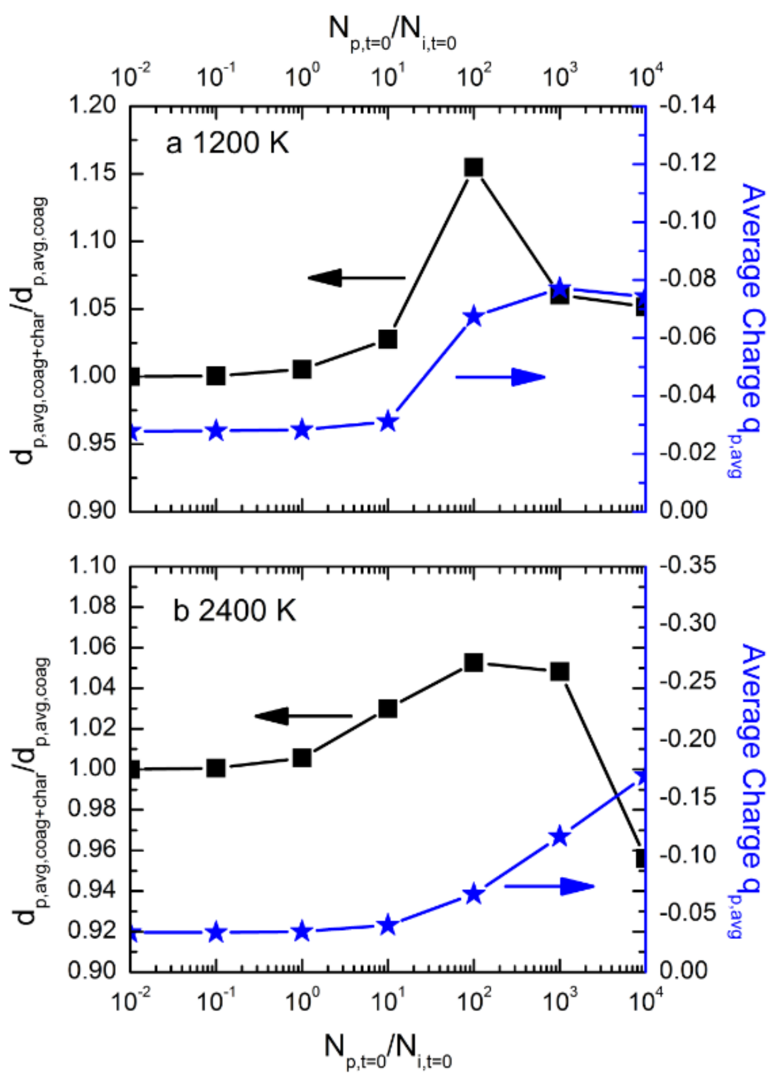

Figure 6.7 Evolution of normalized average particle size ($d_{p,avg,coag+chrg} / d_{p,avg,coag}$) and average charge as a function of initial particle-to-ion concentrations ratio at a) 1200 K and b) 2400 K. Here, ion concentration = 10^{10} /cm^3.

Due to the continuous chemical ionization in certain flames, the ion concentrations may remain relatively constant during a period of time before the quick consumption of ions through recombination. To simulate such a system, it was assumed that the ion concentrations stay constant (10^{10} /cm^3) during a period of 10 ms. Different initial particle concentrations in the flame were simulated to understand the effect of a constant ion presence on the particle dynamics. In Figure 6.7, the ratio of final particle sizes obtained with and without charging ($d_{p,avg,coag+chrg} / d_{p,avg,coag}$), and the average charge on each particle ($q_{p,avg}$) are plotted against the initial particle-to-ion concentration ratios. As particle concentration increases, initially, $d_{p,avg,coag+chrg} / d_{p,avg,coag}$ increases due to the similar concentrations of positively and negatively charged particles at small sizes, resulting in attractive forces among particles. Note that an average negative charge is developed, due to the higher negative ion-particle combination coefficients caused by the larger mobilities of negative ions. As the initial particle concentration further increases, the particle size becomes larger through coagulation, and the difference between negatively and positively charged particle concentrations also becomes larger. Hence, the average negative charge increases to a higher value, causing a decrease of $d_{p,avg,coag+chrg} / d_{p,avg,coag}$. This result indicates that, during simultaneous particle charging and coagulation with a constant ion concentration, initially, the attractive forces between oppositely charged particles play a more important role in influencing the particle size. Gradually, as the average charge increases, repulsive forces dominate, and therefore the average particle size drops compared to the coagulation-only case. This phenomenon is, to some extent, similar to the screening effect in aquatic environments. Similar results were obtained in a bipolar ion environment with higher ion concentrations, as shown in Figure A2.6, where a constant ion concentration of 10^{12} /cm^3 is applied.

6.3.3 Time scale analysis of particle charging and coagulation

The competition between particle charging and coagulation can be simplified by comparing the characteristic time scales for these two processes. According to Eq. (6.6), initially, since all particles are neutral and have the same size, the decrease in neutral particle concentration is mainly caused by ion collisions with particles and particle self-coagulation. Additionally, due to the similar magnitude of the positive and negative ion-particle combination coefficients, Eq. (6.6) can be simplified as

$$\frac{dN_{p,0}}{dt} = -2\eta_0^+ n^+ N_{p,0} - 1/2\beta_{coag}^{0,0} N_{p,0}^2 \tag{6.14}$$

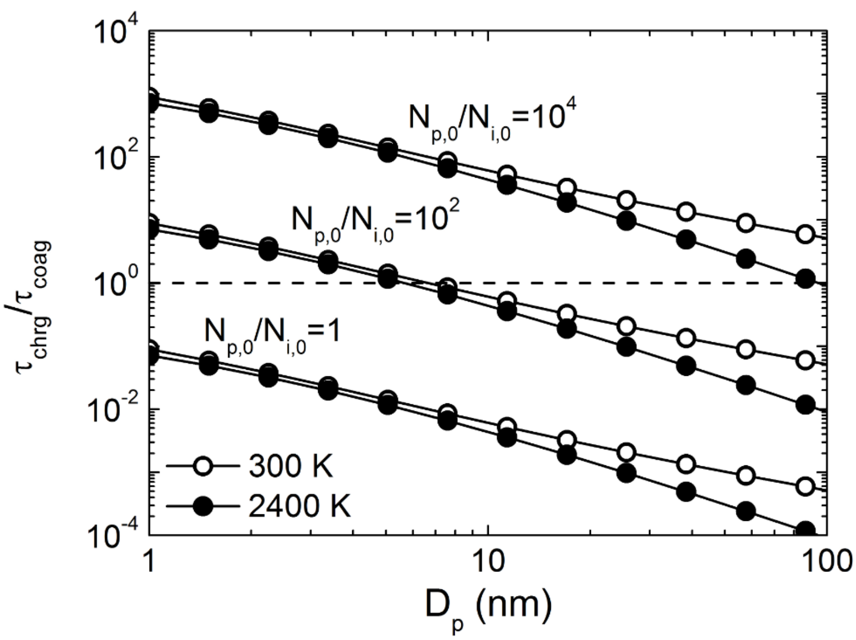

Figure 6.8 Ratio of characteristic charging time over coagulation time as a function of particle size at particle-to-ion concentration ratios of 1, 10^2, and 10^4. The ratio of the characteristic time determines the sequence of the two mechanisms. When $\tau_{chrg}/\tau_{coag} >> 1$, coagulation takes place much earlier than charging. When $\tau_{chrg}/\tau_{coag} << 1$, charging is faster than coagulation.

Hence, two characteristic time scales can be derived, where the characteristic charging time can be derived as $\tau_{chrg} = 1/2\eta_0^+ n^+$, and the characteristic coagulation time can be derived as $\tau_{coag} = 2/\beta_{coag}^{0,0} N_{p,0}$. The ratio of these two time scales (τ_{chrg}/τ_{coag}) further determines the relative sequence of the two physical processes. τ_{chrg}/τ_{coag} is plotted as a function of particle size with different initial particle-to-ion concentration ratios ($N_{p,t=0}/N_{i,t=0}$) in Figure 6.8. As particle size increases, the collision-cross section area of particles also increases, leading to a faster charging process, but the effect of the enlarged collision-cross section area on particle coagulation is counteracted by the smaller particle diffusion coefficient. Hence, introducing ions to particles with larger sizes can cause a stronger influence on particle growth dynamics. The particle-to-ion concentration ratio significantly affects the temporal sequence of charging and coagulation, especially when particle size is smaller than 10 nm, which has already been shown in Figures 6.4 to 6.6. When the particle-to-ion concentration ratio is 1, charging takes place significantly earlier than coagulation, which can induce or suppress particle growth, depending on the ion environment. When the particle-to-ion concentration ratio is 10^4, particle coagulation is much faster than particle charging, so particles can grow to a relatively larger size before the electrostatic potential begins to play a role. This effect is more evident in a unipolar ion environment, where particles grow until the concentration of ions and particles are comparable (Figure 6.5). No noticeable difference in τ_{chrg}/τ_{coag} is observed when system temperature increased from 300 K to 2400 K, since as temperature increases, both the ion-particle and particle-particle combination coefficients increase. By comparing the relative magnitudes of the characteristic charging and coagulation time, it can be concluded that particle size and the initial particle-to-ion concentration determine the influence of flame-generated ions on the simultaneous charging and coagulation of nanoparticles, and this influence becomes more significant when particle size or ion concentration is larger.

6.4 Conclusions

By coupling Fuchs' charging theory with a monodisperse particle dynamics model, the simultaneous charging and coagulation of nanoparticles was simulated at various temperatures. As input values for Fuchs' charging theory, the mobility distributions of flame-generated ions were measured with a high-resolution differential mobility analyzer (DMA). Measurements showed that positive ions had smaller mobilities than negative ions, which resulted in higher probabilities of nanoparticles carrying negative charges. Characteristic peaks at 1.04, 1.10, and 1.27 nm in positive ions and at 1.01 and 1.06 nm in negative ions were detected by the high-resolution DMA. The modeling of particle dynamics with simultaneous charging and coagulation showed that the effect of ion interaction was more prominent in unipolar ion environments, where particle coagulation is significantly suppressed. The presence of bipolar ions promoted particle growth only when the particle concentration was lower than the ion concentrations. A simplified model using time scale analysis was proposed, suggesting that the initial particle-to-ion concentration and particle size were two important factors that determine the relative importance of particle charging and coagulation.

6.5 References

Alonso, M., Hashimoto, T., Kousaka, Y., Higuchi, M., Nomura, T. (1998). Transient bipolar charging of a coagulating nanometer aerosol. J. Aerosol Sci. 29:263-270.

Alquaity, A. B., Han, J., Chahine, M., Selim, H., Belhi, M., Sarathy, S. M., Bisetti, F., Farooq, A. (2016). Measurements of positively charged ions in premixed methane-oxygen atmospheric flames. Combustion Science and Technology. just-accepted.

Biswas, P. and Wu, C.-Y. (2005). Nanoparticles and the environment. J. Air Waste Manage. Assoc. 55:708-746.

Carbone, F., Attoui, M., Gomez, A. (2016). Challenges of measuring nascent soot in flames as evidenced by high-resolution differential mobility analysis. Aerosol Sci. Technol. 50:740-757.

Fang, J., Wang, Y., Attoui, M., Chadha, T. S., Ray, J. R., Wang, W.-N., Jun, Y.-S., Biswas, P. (2014). Measurement of sub-2 nm clusters of pristine and composite metal oxides during nanomaterial synthesis in flame aerosol reactors. Anal. Chem. 86:7523-7529.

Fernández de la Mora, J. and Kozlowski, J. (2013). Hand-held differential mobility analyzers of high resolution for 1-30nm particles: Design and fabrication considerations. J. Aerosol Sci. 57:45-53.

Fialkov, A. B. (1997). Investigations on ions in flames. Prog. Energy Combust. Sci. 23:399-528.

Friedlander, S. K. (2000). Smoke, dust, and haze: fundamentals of aerosol behavior. Oxford University Press New York, USA.

Fuchs, N. (1963). On the stationary charge distribution on aerosol particles in a bipolar ionic atmosphere. Geofisica pura e applicata 56:185-193.

Fujimoto, T., Kuga, Y., Pratsinis, S. E., Okuyama, K. (2003). Unipolar ion charging and coagulation during aerosol formation by chemical reaction. Powder Technol. 135:321-335.

Gopalakrishnan, R., McMurry, P. H., Hogan Jr, C. J. (2015). The bipolar diffusion charging of nanoparticles: A review and development of approaches for non-spherical particles. Aerosol Sci. Technol. 49:1181-1194.

Hoppel, W. A. and Frick, G. M. (1986). Ion-aerosol attachment coefficients and the steady-state charge distribution on aerosols in a bipolar ion environment. Aerosol Sci. Technol. 5:1-21.

Hu, Y., Jiang, H., Li, Y., Wang, B., Zhang, L., Li, C., Wang, Y., Cohen, T., Jiang, Y., Biswas, P. (2016). Engineering the outermost layers of TiO_2 nanoparticles using in situ Mg doping in a flame aerosol reactor. AIChE J.

Jean, L., Swanson, J. J., Boies, A. M. (2015). Unsteady bipolar diffusion charging in aerosol neutralisers: A non-dimensional approach to predict charge distribution equilibrium behaviour. J. Aerosol Sci. 86:55-68.

Jiang, J., Hogan Jr, C. J., Chen, D.-R., Biswas, P. (2007a). Aerosol charging and capture in the nanoparticle size range (6–15nm) by direct photoionization and diffusion mechanisms. J. Appl. Phys. 102:034904.

Jiang, J., Lee, M.-H., Biswas, P. (2007b). Model for nanoparticle charging by diffusion, direct photoionization, and thermionization mechanisms. J. Electrostat. 65:209-220.

Jones, H. R. and Hayhurst, A. N. (2016). Measurements of the concentrations of positive and negative ions along premixed fuel-rich flames of methane and oxygen. Combust. Flame 166:86-97.

Kangasluoma, J., Attoui, M., Korhonen, F., Ahonen, L., Siivola, E., Petäjä, T. (2016a). Characterization of a Herrmann type high resolution differential mobility analyzer. Aerosol Sci. Technol. 50:222-229.

Kangasluoma, J., Samodurov, A., Attoui, M., Franchin, A., Junninen, H., Korhonen, F., Kurtén, T., Vehkamäki, H., Sipilä, M., Lehtipalo, K. (2016b). Heterogeneous Nucleation onto Ions and Neutralized Ions: Insights into Sign-Preference. J. Phys. Chem. C 120:7444-7450.

Karnani, S., Dunn-Rankin, D. (2016). Detailed characterization of DC electric field effects on small non-premixed flames. Combust. Flame 162(7): 2865-2872.

Kim, S. H., Woo, K. S., Liu, B. Y. H., Zachariah, M. R. (2005). Method of measuring charge distribution of nanosized aerosols. J. Colloid Interface Sci. 282:46-57.

Kim, Y.-h., Yiacoumi, S., Nenes, A., Tsouris, C. (2016). Charging and coagulation of radioactive and nonradioactive particles in the atmosphere. Atmos. Chem. Phys. 16:3449-3462.

Laakso, L., Mäkelä, J. M., Pirjola, L., Kulmala, M. (2002). Model studies on ion - induced nucleation in the atmosphere. J. Geophys. Res 107.

Landgrebe, J. D. and Pratsinis, S. E. (1990). A discrete-sectional model for particulate production by gas-phase chemical reaction and aerosol coagulation in the free-molecular regime. J. Colloid Interface Sci. 139:63-86.

Larriba, C., Hogan Jr, C. J., Attoui, M., Borrajo, R., Garcia, J. F., de la Mora, J. F. (2011). The mobility-volume relationship below 3.0 nm examined by tandem mobility-mass measurement. Aerosol Sci. Technol. 45:453-467.

Li, Q., Li, X., Jiang, J., Duan, L., Ge, S., Zhang, Q., Deng, J., Wang, S., Hao, J. (2016a). Semi-coke briquettes: towards reducing emissions of primary PM2. 5, particulate carbon, and carbon monoxide from household coal combustion in China. Sci. Rep. 6:19306.

Li, S., Ren, Y., Biswas, P., Stephen, D. T. (2016b). Flame aerosol synthesis of nanostructured materials and functional devices: Processing, modeling, and diagnostics. Progress in Energy and Combustion Science 55:1-59.

Liu, P., Arnold, I. J., Wang, Y., Yu, Y., Fang, J., Biswas, P., Chakrabarty, R. K. (2015). Synthesis of titanium dioxide aerosol gels in a buoyancy-opposed flame reactor. Aerosol Sci. Technol. 49:1232-1241.

López-Yglesias, X. and Flagan, R. C. (2013). Ion–aerosol flux coefficients and the steady-state charge distribution of aerosols in a bipolar ion environment. Aerosol Sci. Technol 47:688-704.

Maißer, A., Thomas, J. M., Larriba-Andaluz, C., He, S., Hogan, C. J. (2015). The mass-mobility distributions of ions produced by a Po-210 source in air. J. Aerosol Sci. 90:36-50.

Mäkelä, J. M., Jokinen, V., Mattila, T., Ukkonen, A., Keskinen, J. (1996). Mobility distribution of acetone cluster ions. J. Aerosol Sci. 27:175-190.

Reischl, G., Mäkelä, J., Karch, R., Necid, J. (1996). Bipolar charging of ultrafine particles in the size range below 10 nm. J. Aerosol Sci. 27:931-949.

Seinfeld, J. H. and Pandis, S. N. (2012). Atmospheric chemistry and physics: from air pollution to climate change. John Wiley & Sons.

Tigges, L., Jain, A., Schmid, H.-J. (2015). On the bipolar charge distribution used for mobility particle sizing: Theoretical considerations. J. Aerosol Sci. 88:119-134.

Tsantilis, S., Kammler, H., Pratsinis, S. (2002). Population balance modeling of flame synthesis of titania nanoparticles. Chem. Eng. Sci. 57:2139-2156.

Turns, S. R. (1996). An introduction to combustion. McGraw-hill New York.

Ude, S. and De la Mora, J. F. (2005). Molecular monodisperse mobility and mass standards from electrosprays of tetra-alkyl ammonium halides. J. Aerosol Sci. 36:1224-1237.

Vemury, S. and Pratsinis, S. E. (1995). Corona - assisted flame synthesis of ultrafine titania particles. Appl. Phys. Lett. 66:3275-3277.

Vemury, S. and Pratsinis, S. E. (1996). Charging and coagulation during flame synthesis of silica. J. Aerosol Sci. 27:951-966.

Vemury, S., Pratsinis, S. E., Kibbey, L. (1997). Electrically controlled flame synthesis of nanophase TiO_2, SiO_2, and SnO_2 powders. J. Mater. Res 12:1031-1042.

Volkov, A., Paula, S., Deamer, D. (1997). Two mechanisms of permeation of small neutral molecules and hydrated ions across phospholipid bilayers. Bioelectroch. Bioener. 42:153-160.

Wang, X., Williams, B., Tang, Y., Huang, Y., Kong, L., Yang, X., Biswas, P. (2013). Characterization of organic aerosol produced during pulverized coal combustion in a drop tube furnace. Atmos. Chem. Phys. 13:10919-10932.

Wang, Y., Fang, J., Attoui, M., Chadha, T. S., Wang, W.-N., Biswas, P. (2014). Application of Half Mini DMA for sub 2 nm particle size distribution measurement in an electrospray and a flame aerosol reactor. J. Aerosol Sci. 71:52-64.

Wang, Y., Kangasluoma, J., Attoui, M., Fang, J., Junninen, H., Kulmala, M., Petäjä, T., Biswas, P. (2017). The High Charge Fraction of Flame-generated Particles in the Size Range below 3 nm Measured by Enhanced Particle Detectors. Combust. Flame. 176: 72-80.

Wang, Y., Kangasluoma, J., Attoui, M., Fang, J., Junninen, H., Kulmala, M., Petäjä, T., Biswas, P. (2016). Observation of incipient particle formation during flame synthesis by tandem differential mobility analysis-mass spectrometry (DMA-MS). Proc. Combust. Inst. just accepted.

Wang, Y., Liu, P., Fang, J., Wang, W.-N., Biswas, P. (2015). Kinetics of sub-2 nm TiO2 particle formation in an aerosol reactor during thermal decomposition of titanium tetraisopropoxide. J. Nanopart. Res. 17:1-13.

Weinberg, F., Dunn-Rankin, D., Carleton, F., Karnani, S., Markides, C., Zhai, M. (2013). Electrical aspects of flame quenching. Proc. Combust. Inst., 34(2): 3295-3301.

Wu, J. J. and Flagan, R. C. (1988). A discrete-sectional solution to the aerosol dynamic equation. J. Colloid Interface Sci. 123:339-352.

Xiong, G., Kulkarni, A., Dong, Z., Li, S., Stephen, D. T. (2016). Electric-field-assisted stagnation-swirl-flame synthesis of porous nanostructured titanium-dioxide films. Proc. Combust. Inst.

Zhang, Y., Li, S., Yan, W., Stephen, D. T. (2012). Effect of size-dependent grain structures on the dynamics of nanoparticle coalescence. J. Appl. Phys. 111:124321.

Zhang, Y., Li, S., Yan, W., Yao, Q., Stephen, D. T. (2011). Role of dipole-dipole interaction on enhancing Brownian coagulation of charge-neutral nanoparticles in the free molecular regime. J. Chem. Phys. 134:084501.

Chapter 7: Conclusions and Suggestions for Future Work

The results of this chapter have been compiled in Wang, Y., Attoui, M., Biswas, P. (2017). Sub-2 nm Particle Measurement in High-temperature Aerosol Reactors: a Review. J. Aerosol Sci. In preparation.

7.1 Conclusions

This section summarizes the major findings of this dissertation.

7.1.1 Applicability of high-resolution DMAs in sub 2 nm particle characterization (Chapters 2 and 3)

While particle formation and growth above 2 nm have been well characterized with current microscopic, spectroscopic, and chromatographic techniques, the initial stages of particle formation are still not well understood. This is partly due to the limitations of instruments, which cannot characterize the highly diffusive and condensationally inactive particles. The first part of this dissertation studied the applicability of high-resolution DMAs in measuring sub 2 nm particles generated from aerosol reactors, i.e., a flame aerosol reactor and a furnace aerosol reactor. In the measurement of sub 2 nm ions and charged particles generated by electrospray and by a premixed flat flame reactor, the comparison between a half mini DMA (one type of high-resolution DMAs) and a Nano DMA showed that the half mini DMA withstood the diffusion effects better. This superior performance attributed to the significantly increased sheath flow rate, which enhanced the resolution and shortened the residence time of particles in the DMA.

The half mini DMA was first used to investigate the formation of TiO_2 clusters during flame synthesis (Chapter 1). When TTIP was introduced into the flame reactor, discrete TiO_2 ion peaks were observed, indicating a discrete size distribution in the initial stages of particle formation. The use of a radioactive neutralizer and different types of tube materials resulted in different size distributions of sub 2 nm particles, suggesting the challenges of sampling these incipient particles.

Further, the half mini DMA was used in a furnace aerosol reactor to investigate the initial stage kinetics of TiO_2 particle formation and growth during the thermal decomposition of TTIP (Chapter 2). For the first time, clusters below 2 nm were detected, during the thermal decomposition of TTIP. As the reaction temperature increased, a higher consumption of TTIP molecules was observed, and larger particles with characteristic sizes were detected, signifying the formation and growth of particles. The first order reaction rate derived from the decay of the TTIP signal as a function of the reaction temperature yielded a quantitative match with existing studies, implying that sub 2 nm particle size measurement can serve as a new method for monitoring reaction rates. These reaction rates are important information for engineering the structure of flame-synthesized nanomaterials (Appendix III). The obtained knowledge on incipient particle formation and growth can bridge the gap between chemical reactions on the molecular scale and particle growth beyond the nanometer scale, which is of interest in applications such as nanomaterial production and atmospheric pollutant control.

7.1.2 Analysis of the physical and chemical formation pathways aerosol during combustion (Chapters 4, 5, and 6)

In addition to the physical characterization of sub 2 nm particles with DMAs, the chemical analysis of sub 2 nm particles can complete the picture of particle formation and growth pathways at high temperatures. Furthermore, despite the limitations of instruments that measure charged particles only, the charging characteristics of these incipient particles are of great interest. Studies conducted with the combination of a high-resolution DMA, an atmospheric interface time-of-flight mass spectrometer (APi-TOF MS), and a particle size magnifier (PSM) facilitated our understanding of particle formation during combustion.

For the first time, incipient particle formation during flame synthesis was investigated using the tandem differential mobility analysis-mass spectrometry (DMA-MS) technique (Chapter 4). A high resolution DMA and an APi-TOF were used to measure the size and mass of the sub 3 nm particles simultaneously in the flames, without the addition of synthesis precursors and with the addition of TEOS or TTIP. Measurements in a blank flame detected a large number of sub 3 nm particles generated from chemical ionization reactions, and determined that nitrate ions dominated in the negative ions. The formation of nitrate ions may be related to the NO_x formation in flames. The blank flame-generated ions played an important role during particle synthesis, since the APi-TOF observed the appearance of nitrate ions in particles containing silicon or titanium. The effective densities of the incipient particles were calculated by assuming that the particles were spheres. These particles had lower densities than the bulk SiO_2 and TiO_2, because of the impurities in the particles and their amorphous structures. The commonly used Kilpatrick's mass-mobility relationship was also evaluated in this study, and the difference between the measured data and the Kilpatrick's relationship suggested that particle compositions largely determined particle mass and mobility.

With the help of three enhanced particle detectors (a high-resolution DMA, an APi-TOF, and a PSM), the charging characteristics of sub-3 nm flame-generated particles were studied for the first time (Chapter 5). The PSM-bCPC and high resolution DMA matched qualitatively well in measuring the sub-3 nm particle size distributions. Coupled with a CPR, the PSM-bCPC measured the neutral particle size distributions during combustion, and the neutral particle fraction in the flame was found to be significantly lower than predicted by classical theory. The formation of particles during combustion consumed the flame-generated ions, which further increased the neutral particle fraction in the flame. These results show that flame-generated ions play an important role during particle formation in the initial stages.

To elucidate the influence of ion environments on particle formation and growth during combustion, we numerically simulated simultaneous particle charging and coagulation at various temperatures. This was done by coupling Fuchs' charging theory with a monodisperse particle dynamics model. As input values for Fuchs' charging theory, the mobility distributions of flame-generated ions were measured with a high-resolution differential mobility analyzer (DMA). The modeling of particle dynamics showed that the effect of ion interaction was more prominent in unipolar ion environments, where particle coagulation was significantly suppressed. The presence of bipolar ions promoted particle growth only when the particle concentration was lower than the ion concentrations. A simplified model using time scale analysis was proposed, suggesting that the initial particle-to-ion concentration and particle size were two important factors that determine the relative importance of particle charging and coagulation. These findings provide new perspectives on the synthesis of functional nanomaterials by changing the ion characteristics in flame environments.

7.1.3 Relevance of this work to industrial synthesis of functional nanoparticles

Flame aerosol reactors have been shown to be one of the most stable, scalable, and economical methods for the synthesis of functional nanomaterials. Recently, flame aerosol reactors have also been demonstrated to be capable for the synthesis of quantum dots, whose sizes are typically below 5 nm. The size and chemical composition of quantum dots must be strictly controlled. Analyzing the incipient particle formation and growth with high-resolution DMAs and mass spectrometers can provide important insights to the flame synthesis of quantum dots. In this work, the high charge fraction and the strong influence of flame chemical ionization demonstrate that the synthesis of incipient particles cannot be solely predicted by precursor reaction and particle coagulation growth. Additional measurements are still needed to extend the measurement size, while new modeling methods are needed which are based on these observations. On the other hand, material doping in flame synthesis has become a routine method for synthesizing functional materials due to the exceptional properties of nanocomposites. In order to understand the doping mechanisms (molecular doping, surface doping, or doping segregated phases), characterizing incipient particles synthesized with multiple precursors is indispensable. Size analysis that can monitor the evolution of characteristic peaks could suggest the direct influence of adding different precursors to existing flame synthesis. Mass spectrometers that can measure the chemical composition of particles without fragmentation could show the mixing states of particles starting from molecular scales. Synthesis techniques can then be modified to control the doping of multicomponent nanomaterials.

7.2 Suggestions for Future Work

7.2.1 Incipient particle characterization in various combustion sources

As indicated in this dissertation, premixed flat flame aerosol reactors were used in most of the studies due to their high stability, uniformity, and broad usage. At the same time, the nanoparticle synthesis precursor, such as TTIP or TEOS, was fed to the flame in the vapor phase, ensuring the combustion mixture was homogeneous. A flame with a stable structure greatly facilitated the sampling of incipient particles with a dilution probe. However, in industries, for safety, diffusion flames are widely used. The natural and anthropogenic burning of biomass also take place heterogeneously most of the time. Hence, a series of experiments whose combustion conditions are systematically changed will greatly help us understand the particle formation in combustion sources. These conditions include, but are not limited to, the flame mode (premixed flame/diffusion flame), flame structure (flat/conical), precursor choice (organometallic/inorganic/none (sooting flame)), fuel species (H_2/CH_4/others), diluting gas species (N_2/Ar/none). As shown in the mass spectrometric measurement in this dissertation, nitrate species were found in fuel lean premixed flames, and these species played important roles in the formation of incipient particles. These nitrate species might come from the diluting N_2 gas in the combustible mixture. Hence, it will be interesting to study how incipient particle formation and growth may be affected by eliminating these species through the usage of another type of diluting gas. Studies on particle charging characteristics in these flame conditions can be conducted in a similar manner to that described in Chapter 5, which will elucidate the electrical properties of the flames.

7.2.2 Electric field-assisted combustion and flame synthesis

The high charge fraction of flame-generated sub 2 nm particles observed by the experiments in Chapter 5 suggests that combustion can be manipulated by external electric fields. Lately, plasma-assisted combustion and electric field-assisted combustion have become new research directions in the combustion field. As shown in recent research studies, flame properties, such as structure, temperature, and reactions, are strongly affected by external electric fields. As a result, flame-synthesized particles can be impacted by these techniques. Future work may focus on particle formation and growth during combustion under the influence of electric fields.

7.2.3 Improvement to current incipient particle sampling methods

Dilution sampling is commonly used in the online and offline characterization of aerosols, when the aerosol concentrations are higher than the detection limit of instruments. It is especially challenging when the dilution sampling is conducted for aerosols generated in high temperature environments, such as flames and furnace reactors, because the dilution should be operated not only to reduce the aerosols to a measurable concentration, but also to quench all the ongoing reactions and particle growth. The design of dilution sampling systems should satisfy the two requirements of: sampling as close to isokinetic conditions as possible, and choosing the dilution ratio to ensure minimal deposition loss due to thermophoresis and diffusion and minimal alteration of size distribution by nucleation, coagulation, and condensation. Existing dilution sampling systems has not been fully evaluated in the measurement of sub 3-nm particles generated at high temperature environments. Concerns may be raised regarding the validity of the measurement, especially in such a minuscule size range, where the particles may be very unstable. Dilution sampling involves the reduction of temperature, which inevitably alters the equilibrium of reactions in the sampled stream. This influence may be substantial for the incipient particles that are physically and chemically instable. Future work can focus on the design and evaluation of dilution sampling systems for incipient particle measurement at high temperatures to ensure the validity of incipient particle measurements. Some preliminary work on evaluating dilution samplers for incipient particle measurement is discussed in Appendix V.

7.2.4 Comprehensive characterization of high-resolution DMAs

The inversion of DMA measured particle size distributions needs DMA transfer function as an important parameter. The transfer function of a DMA is commonly characterized with tandem DMAs, where the first DMA size-classifies monodisperse particles, and the second DMA measures the size distribution. The transfer function of the second DMA can be obtained from the spread of size distribution being measured. Due to limited instrument resources, the transfer functions of the high-resolution DMAs used in this work were not characterized. Future work may focus on the comprehensive characterization of high-resolution DMAs, including DMA transfer function, particle transmission efficiency, and the influence of RH/temperature on the size classification of incipient particles. Simulation software, such as Fluent® and COMSOL® can be utilized to compare with experimental observations. Due to the short time scale of the experiments, the commonly used diffusion coefficient and other equations may not work for these studies in quasi-steady state. The ballistic collision may dominate the particle dynamics, while equilibrium and steady states are not reached. Regarding influences on data inversion should be considered. The error propagation of the measurements, from the inlet of the DMA to the outlet of particle counting devices, should also be considered to evaluate the uncertainties of the measurements.

Appendix I. Supporting materials for Chapter 5

Estimating ion concentration in the investigated flame

The estimation of ion concentration in the investigated flame was done by evaluating the I-V characteristics of the flame [1]. A ring-shaped stainless steel electrode with a diameter of 51 mm and a height of 3 mm was placed around the flame. A high voltage source (Bertan 205B, Spellman Inc.) was connected with the electrode, and the stainless steel burner was grounded. By increasing the voltage, the charged species will transport towards or against the electrode, forming an electric current. When the applied voltage exceeds certain value, all the charged species will become depleted and form a saturation current. As shown in the figure below, for a premixed flame at an equivalence ratio of 0.7, the saturation current was around 40 μA. As voltage further increases, corona effect appears, which further increases the ion current.

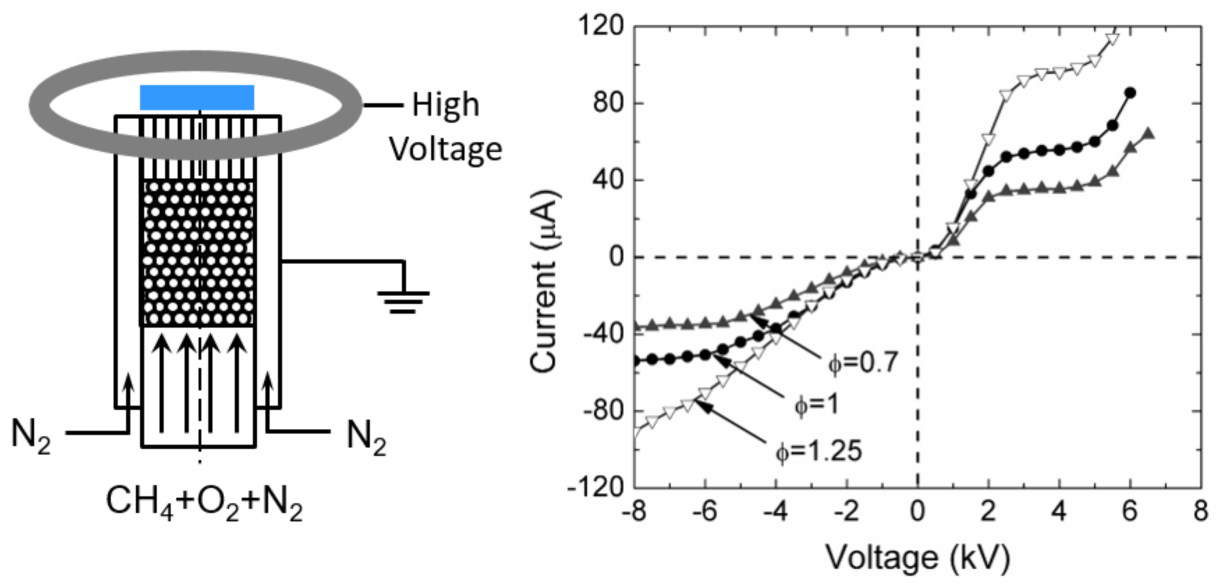

Figure A1.1 Setup for estimating the ion concentration in the investigated flame (left) and the I-V characteristics of the flame (right).

An estimation of the ion/charged species concentration can be done by following the Appendix A of Katzer et al. [1] The ion flux densities towards the electrode can be expressed as

$$\dot{n} = \frac{I / e}{A} = N_i v_i \,,$$

where I is the electric current, e is the elementary charge, A is the area of the ring electrode facing the flame, N_i is the ion/charged species concentration, and v_i is the velocity of the ions/charged species. v_i can be calculated based on the definition of electrical mobility,

$$Z_i = \frac{v_i}{E} \,,$$

where Z_i is the ion electrical mobility obtained from DMA measurements, and E is the electric field strength. In this experiment, the saturation voltage was determined as 4 kV and an averaged ion mobility of 1.6 cm^2/Vs was used (from Figure 5.3). By using a simple estimation of electric field strength with $E = V / d$, where d is the distance between the electrode and the burner, N_i can be calculated as 9.95×10^9 $\#/cm^3$. This value is similar to the one obtained by Jones and Hayhurst [2]. We should note that adding an electric field in the flame can change the flame chemistry by introducing ionic winds [3]. This effect may introduce errors in estimating the ion concentrations.

References

[1] M. Katzer, A. Weber, G. Kasper, The effects of electrical fields on growth of titania particles formed in a $CH_4 – O_2$ diffusion flame, Journal of Aerosol Science 32 (2001) 1045-1067.

[2] H.R. Jones, A.N. Hayhurst, Measurements of the concentrations of positive and negative ions along premixed fuel-rich flames of methane and oxygen, Combust. Flame 166 (2016) 86-97.

[3] S. Vemury, S.E. Pratsinis, L. Kibbey, Electrically controlled flame synthesis of nanophase TiO_2, SiO_2, and SnO_2 powders, journal of materials research 12 (1997) 1031-1042.

Appendix II. Supporting materials for Chapter 6

In this supplemental information, the following aspects will be discussed:

1. DMA setting and calibration method

2. Detailed explanations and calculation results of ion-particle and particle-particle combination coefficients

3. Size and mobility distribution of flame-generated ions at different sampling heights

4. Effect of bipolar ion environment on normalized particle concentration

5. Effect of bipolar ion environment on particle charging and coagulation with a different initial constant ion concentration

A2.1 DMA setting and calibration method

The recirculating sheath flow of the DMA was provided by a high-power brushless blower (Domel Inc.), and was cooled and cleaned inline by a homemade heat radiator and a HEPA filter (Ideal Vacuum Products, LLC). Since the DMA was operated in a closed loop, the sheath gas was gradually replaced by the sampling gas, whose major composition was N_2. The temperature of the sheath gas was 298 K as determined by a type-K thermocouple. The DMA electrodes were connected to a high voltage power supply (Bertan 205B, Spellman High Voltage Electronics Corp.), which was controlled by a Labview program. The program used a modest step voltage of 5 V and a relatively long step time of 2 s to ensure the repeatability of the measurement. A homemade electrometer measured the concentration of the classified particles at a flow rate of 10 lpm. Before measuring flame-generated ions, the DMA was calibrated using monodisperse ionic standards generated from the electrospray of tetraheptylammonium bromide-methanol solution (Ude and de la Mora 2005). During the calibration, the voltages (V) at which DMA detected these monodisperse ions with known mobilities (Z) were recorded. Furthermore, for a DMA operated at the same flow condition, the product of voltage and mobility ($V \cdot Z$) remains constant. Hence, mobility of ions detected at an arbitrary voltage can be calculated. The size distributions of charged clusters were obtained by relating the particle mobility size calculated from the applied DMA voltage, to the particle concentration monitored by the electrometer, via using the relationship of $I=ceQ$, where I is the electrometer current, c is the charged cluster concentration, e is the elementary charge, and Q is the flow rate through the electrometer. Note that the actual particle size distribution function ($dN/d\log D_p$) (Stolzenburg and McMurry 2008) was not calculated, due to the complexity in determining the transfer function and transmission efficiency of the high-resolution DMA (which will use two high-resolution DMAs arranged in tandem). A recent study shows that the transmission efficiency of sub 3 nm clusters in another type of high-resolution DMA (Herrmann DMA) was in the range of 1 to 22% (Kangasluoma et al. 2016).

A2.2 Detailed explanations and calculation results of ion-particle and particle-particle combination coefficients

The ion-particle combination coefficient $\eta_i^{\pm}$ of positive (+) and negative (–) ions with a particle carrying *i* elementary units of charge can be derived as

$$\eta_i^{\pm} = \frac{\beta_i^{\pm} \exp[-\phi_i(\delta^{\pm})/kT]}{1+\exp[-\phi_i(\delta^{\pm})/kT][\beta_i^{\pm}/4\pi D^{\pm}]\int_0^1 \exp[\phi_i(\delta^{\pm}/x)/kT]dx} \qquad \text{(A2.1)}$$

In this equation, $\beta_i^{\pm}$ is the proportionality between the ion flux onto a particle and the ion concentration, $\delta^{\pm}$ is the radius of the limiting sphere (inside which the movement of ions is guided by the electrostatic potential between the ion and the particle), k is the Boltzmann's constant, T is temperature, and $D^{\pm}$ is the diffusion coefficient of the ions. $\beta_i^{\pm}$ and $D^{\pm}$ are functions of ion mass and mobility respectively. The averaged mobilities measured by the high-resolution DMA were used as inputs for calculating the ion-particle combination coefficient. However, since the mobility values were measured at 298 K, which was the sheath flow temperature of the DMA, one needs to convert the measured mobility values to those at other temperatures. In this study, the mobility of the particle in the free molecular regime is set to be proportional to $T^{0.5}$ (Larriba et al. 2011). The effect of mobility-temperature dependence ($Z \propto T^0$, $T^{0.5}$, or T^1) on the ion attachment coefficient was further explored. Figure A2.1 shows the ion attachment coefficients between a positive ion and particles with different charging states as a function of particle size. A temperature of 2400 K was used, since the difference among mobilities was the largest based on different mobility-temperature relationships. It can be seen that the ion attachment coefficients do not differ significantly by using different mobility-temperature relationships. This result, on the other hand, matches with the study conducted by Tigges et al. (2015).

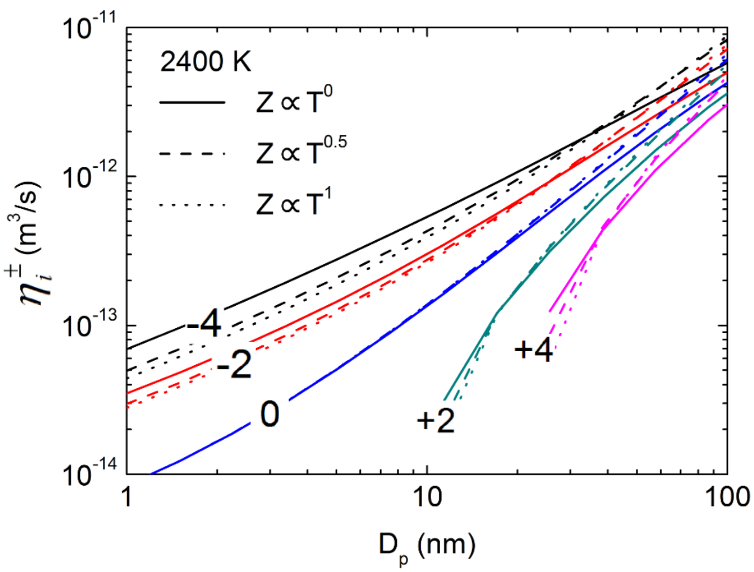

Figure A2.1 The effect of using different mobility-temperature relationships on calculating ion-particle combination coefficients.

A detailed derivation of the terms in Eq. (A2.1) can be found in Reischl et al. (1996) The three body trapping was not included in calculating the ion-particle combination coefficient, since it did not cause a significant change in simulation, as also indicated by previous studies (Hoppel and Frick, 1986; López-Yglesias and Flagan, 2013). It should be noted that Fuchs' charging theory assumes the ion attachment on particles is in steady state, which may not apply for environments with intense chemical reactions, such as combustion. Future studies comparing Fuchs' charging theory and charging mechanism predicted by Langevin equation will be conducted for conditions with high temperatures and high ion concentrations to evaluate the effect of nonsteady-state process on particle charging (Gopalakrishnan et al. 2015).

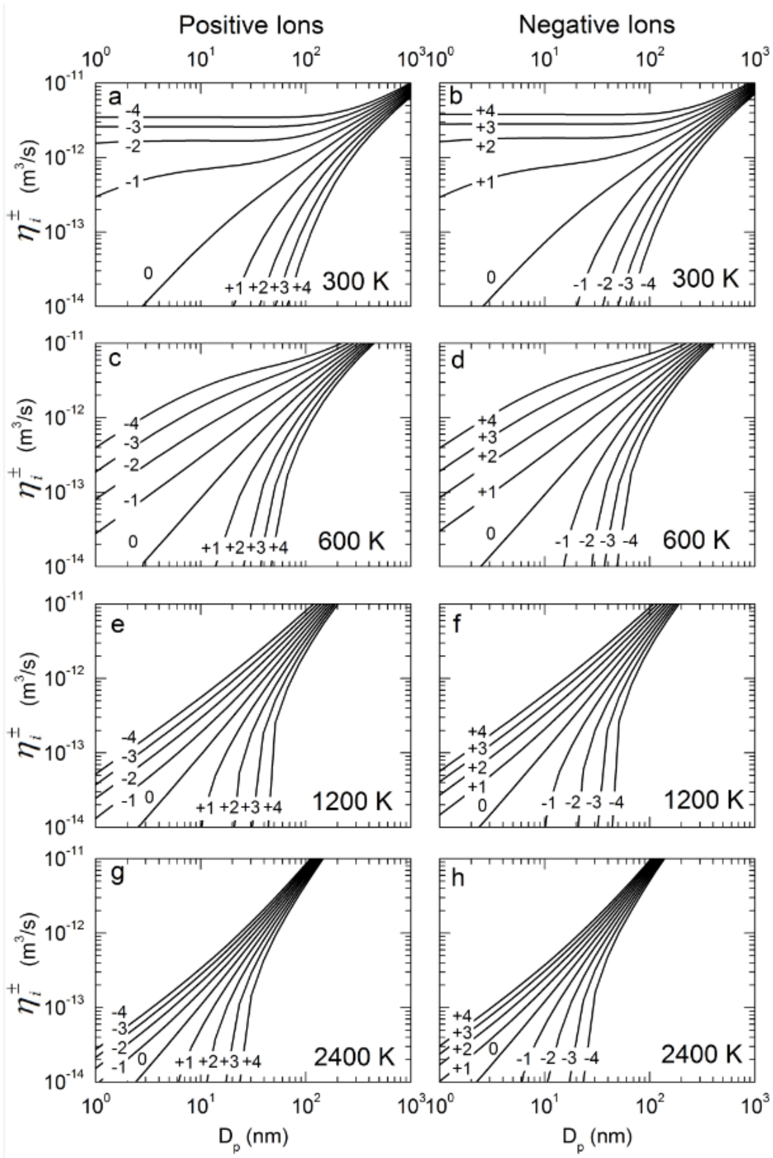

Figure A2.2 Ion-particle combination coefficients ($\eta_i^{\pm}$) as a function of particle size at different temperatures. Left column: positive ion-particle combination coefficient; Right column: negative ion-particle combination coefficient. The numbers labeled on each curve indicate the particle charging state.

Figure A2.2 displays the calculated ion-particle combination coefficients as a function of particle size at different temperatures. The positive and negative ion mobilities used in calculation were

1.54 cm^2/Vs and 1.97 cm^2/Vs by averaging the measured mobility distributions measured at $\phi = 0.85$ and H_{AB}=5 mm. As particle size increases, the combination coefficients increase due to the enlarged collision cross section. Because of the attractive electrostatic forces, the combination coefficients of ions and particles with opposite polarities are larger than those with the same polarity. However, this difference becomes smaller as temperature increases, which can be explained by the higher kinetic energy of ions at elevated temperatures. When an ion moves towards a particle with opposite polarity, the chance of the ion escaping from the particle becomes higher if the kinetic energy of the ion is large; similarly, when the ion moves towards a particle with the same polarity, the chance of the ion overcoming the repulsive potential and finally colliding with the particle is also higher. This behavior also suggests that at high temperatures, the charging process is dominated by ballistic collisions between the ions and particles, where the electrostatic potential becomes less important. The relatively higher mobility of negative ions did not result in a significant increase in the ion-particle combination coefficients which can be seen by comparing the left and right columns of Figure A2.2. The difference in the combination coefficients is observable with highly charged particles at low temperatures only (particles with ±4 charges in Figure A2.2a and Figure A2.2b). This difference is even smaller at higher temperatures, which shows that Fuchs' charging theory is not sensitive to small differences in ion properties, as pointed out by several other studies (Reischl et al. 1996; Tigges et al. 2015).

The particle-particle combination coefficient for the Brownian collision of spherical particles in the free molecular and continuum regime (Seinfeld and Pandis 2012) is given by

$$\beta_{brownian}(d_i,d_j)=2\pi(d_i+d_j)(D_i+D_j)\left\{\frac{d_i+d_j}{d_i+d_j+2(g_i^2+g_j^2)^{1/2}}+\frac{8(D_i+D_j)}{(d_i+d_j)(c_i^2+c_j^2)^{1/2}}\right\}^{-1} \quad \text{(A2.2)}$$

where d_i is the diameter of the colliding particle, and c_i is the mean particle velocity, where $c_i=(8k_BT/(\pi m_i))^{1/2}$. m_i is calculated by multiplying the particle volume by the density of the bulk material. In this study, the bulk density of TiO_2 (4230 kg/m^3) was used. D_i is the diffusion coefficient of the particle, where $D_i=\frac{k_BT}{3\pi\mu d_i}\left\{\frac{5+4Kn_i+6Kn_i^2+18Kn_i^3}{5-Kn_i+(8+\pi)Kn_i^2}\right\}$, and Kn_i is the particle Knudsen number. Furthermore, $g_i=\frac{1}{3d_il_i}\left\{(d_i+l_i)^3-(d_i^2+l_i^2)^{3/2}\right\}-d_i$ and $l_i=8D_i/(\pi c_i)$. Eq. (A2.2) calculates the coagulation coefficient for Brownian diffusion in the absence of any force field. In the presence of electrostatic interaction between charged particles, the combination coefficient is modified by a correction factor (W) (Friedlander 2000) which is given by

$$\beta_{coag}^{i,j}(d_i,d_j)=\frac{\beta_{brownian}(d_i,d_j)}{W(z_i,z_j)} \quad \text{(A2.3)}$$

where $W=\frac{1}{y}\left(e^y-1\right)$, and $y=\frac{z_iz_je^2}{2\pi\varepsilon_0\varepsilon(d_i+d_j)}$. In these equations, z_i is the number of elementary charge on the particle, d_i is the size of the particle with z_i elementary charges, ε is the relative permittivity of the medium, ε_0 is the dielectric constant of vacuum, and e is the elementary charge.

Figure A2.3 shows the particle-particle combination coefficients of two equally sized particles as a function of their diameters. The three lines in each subplot represent the particle charging states of no charge, same charge, and opposite charges. Similar to the ion-particle combination coefficients, as system temperature increases, the difference among the particle-particle combination coefficients with different charging states becomes smaller because of the higher kinetic energy of the particles. Due to the enhanced effect of the exponential term in Eq. (A2.3), the effect of electrostatic potential for smaller particles is much greater than that for larger particles. The fact that larger particles are less sensitive to the charging states indicates that particles can scavenge more particles and carry more charges as they grow.

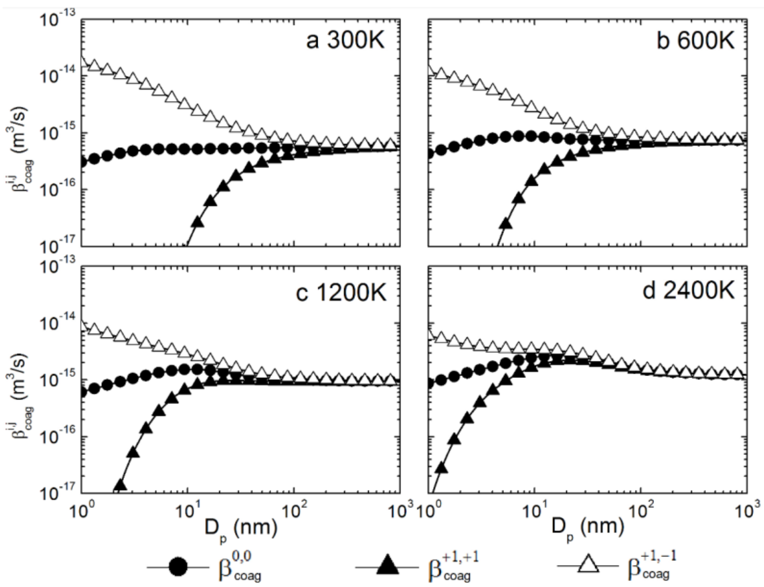

Figure A2.3 Particle-particle combination coefficients ($\beta^{i,j}_{coag}$) as a function of particle size at different temperatures. Conditions are plotted for two particles carrying no charge, opposite single charges, and the same single charge.

A2.3 Size and mobility distribution of flame-generated ions at different sampling heights

As the ion residence time increased, the positive and negative ions demonstrated different characteristics. Figure A2.4 shows the size distribution of flame-generated ions sampled at different heights above the flame. As sampling height increased, the first peak in the positive ions decreased, possibly caused by the chemical reactions that form larger clusters and diffusion loss. However, characteristic peaks at 1.04 and 1.27 nm were detectable repeatedly even at a sampling height of 20 mm, demonstrating the high stability and long age of these ions. The negative ions, however, displayed contrary properties in terms of ion stability. The size distributions were detectable at a sampling height between 5 and 6 mm only (note that the radius of the dilution probe was 5 mm). This rapid dissipation might be caused by the instability of these ions, since they may release electrons as they pass out of the flame reaction zone. The different properties of the measured ions will affect the particle coagulation and growth as time proceeds; for example, ion environments biased towards a certain polarity may be created at higher locations above the flame.

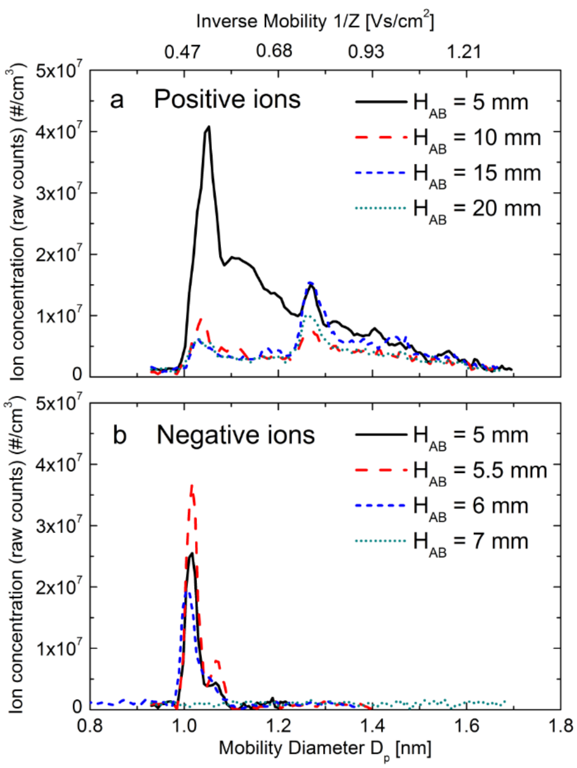

Figure A2.4 Positive and negative ion size distributions as a function of sampling height (H_{AB}). Flame equivalence ratio ϕ = 0.85. The corresponding ion inverse mobility is labeled in the upper x-axis. Note that the y-axis is the raw counts monitored by the electrometer.

A2.4 Effect of bipolar ion environment on normalized particle concentration

The bipolar ion environment is more influential on particle growth dynamics with a lower initial particle concentration, where the particle growth is also slower (Figure A2.5). When the initial particle concentration is comparable to or higher than the ion concentration, the particles speed up the coagulation process, and the normalized particle concentration can quickly drop to 10^{-4} after 1 s at 2400 K.

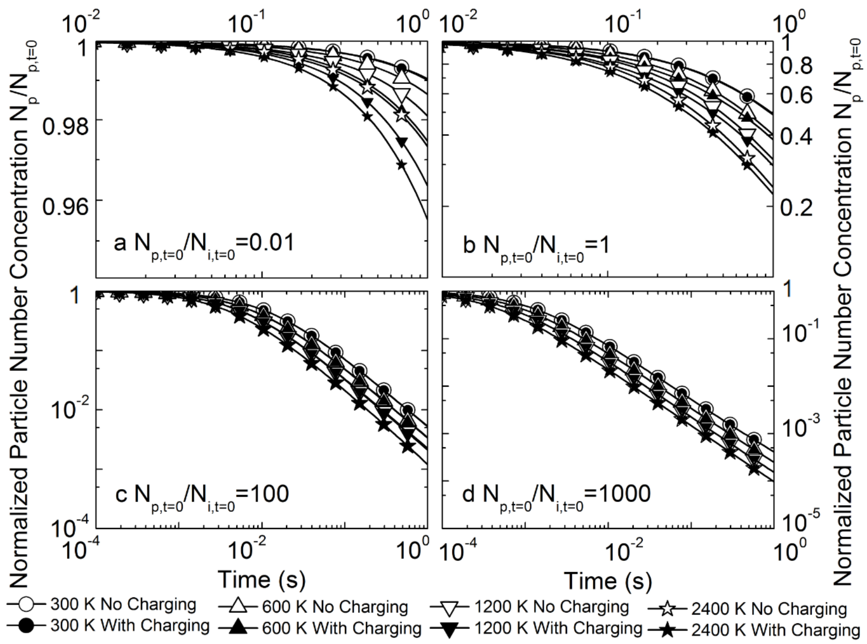

Figure A2.5 Evolution of normalized particle number concentrations as a function of time at different temperatures, with and without charging effects in a bipolar ion environment. Subplots represent the cases with initial particle-to-ion concentration ratios of a) 0.01, b) 1, c) 100, and d) 1000. Note the different scales of x-axes and y-axes.

A2.5 Effect of bipolar ion environment on particle charging and coagulation with a different initial constant ion concentration

Figure A2.6 shows the ratio of particle sizes obtained with and without charging ($d_{p,avg,coag+chrg} / d_{p,avg,coag}$), and the average charge on each particle ($q_{p,avg}$) as a function of initial particle-to-ion concentration ratio. A bipolar ion concentration of 10^{12} /cm^3 is kept constant for

10 ms. As the initial particle-to-ion concentration ratio increases, firstly, particle coagulation was enhanced by the bipolar ion environment. As this ratio further increases, the average negative charge also becomes higher, causing a suppress of particle growth. Similar results were observed with a lower initial ion concentration (10^{10} /cm^3) as shown in the main body of the manuscript.

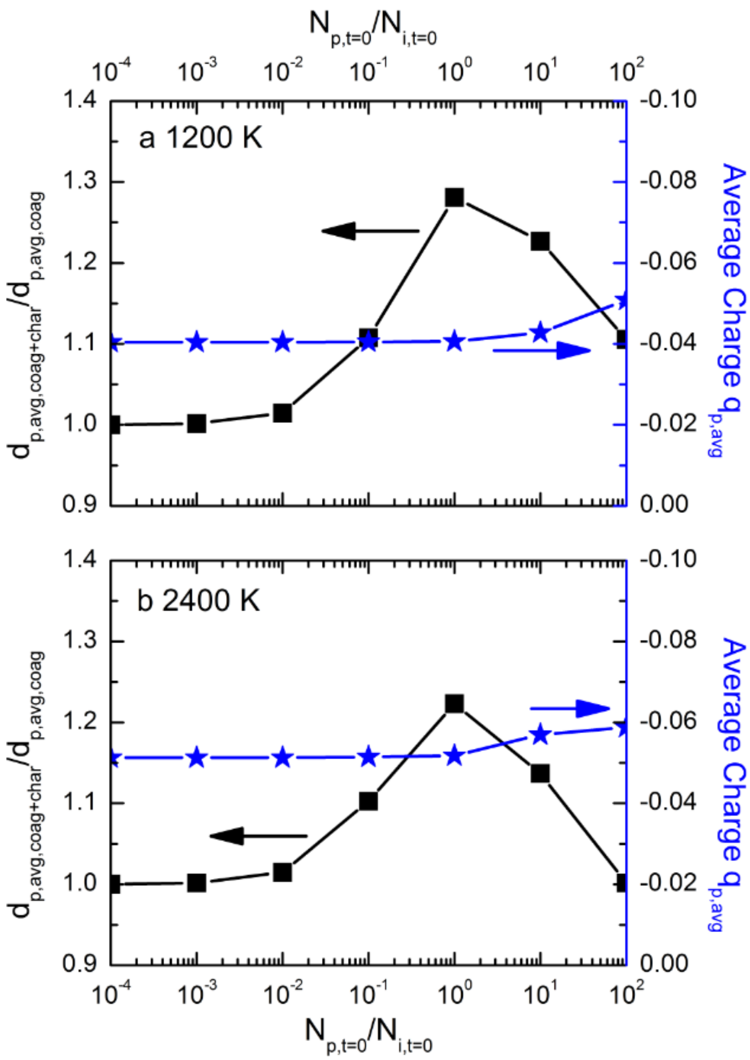

Figure A2.6 Evolution of normalized average particle size ($d_{p,avg,coag+chrg} / d_{p,avg,coag}$) and average charge as a function of initial particle-to-ion concentrations ratio at a) 1200 K and b) 2400 K. Here, ion concentration = 10^{12} #/cm^3.

References

Friedlander, S. K. (2000). Smoke, dust, and haze: fundamentals of aerosol behavior. Oxford University Press New York, USA.

Gopalakrishnan, R., McMurry, P. H., Hogan Jr, C. J. (2015). The bipolar diffusion charging of nanoparticles: A review and development of approaches for non-spherical particles. Aerosol Sci. Technol. 49:1181-1194.

Hoppel, W. A. and Frick, G. M. (1986). Ion-aerosol attachment coefficients and the steady-state charge distribution on aerosols in a bipolar ion environment. Aerosol Sci. Technol. 5:1-21.

Kangasluoma, J., Attoui, M., Korhonen, F., Ahonen, L., Siivola, E., Petäjä, T. (2016). Characterization of a Herrmann type high resolution differential mobility analyzer. Aerosol Sci. Technol. 50:222-229.

Larriba, C., Hogan Jr, C. J., Attoui, M., Borrajo, R., Garcia, J. F., de la Mora, J. F. (2011). The mobility-volume relationship below 3.0 nm examined by tandem mobility-mass measurement. Aerosol Sci. Technol. 45:453-467.

López-Yglesias, X. and Flagan, R. C. (2013). Ion–aerosol flux coefficients and the steady-state charge distribution of aerosols in a bipolar ion environment. Aerosol Sci. Technol 47:688-704.

Reischl, G., Mäkelä, J., Karch, R., Necid, J. (1996). Bipolar charging of ultrafine particles in the size range below 10 nm. J. Aerosol Sci. 27:931-949.

Stolzenburg, M. R. and McMurry, P. H. (2008). Equations governing single and tandem DMA configurations and a new lognormal approximation to the transfer function. Aerosol Sci. Technol. 42:421-432.

Tigges, L., Jain, A., Schmid, H.-J. (2015). On the bipolar charge distribution used for mobility particle sizing: Theoretical considerations. J. Aerosol Sci. 88:119-134.

Ude, S. and De la Mora, J. F. (2005). Molecular monodisperse mobility and mass standards from electrosprays of tetra-alkyl ammonium halides. J. Aerosol Sci. 36:1224-1237.

Appendix III: Engineering the Outermost Layers of TiO_2 Nanoparticles Using in situ Mg Doping in a Flame Aerosol Reactor

The results of this chapter have been compiled as a paper: Hu, Y., Wang, Y.*, Jiang, H., Li, Y., Cohen, T., Jiang, Y., Wang, B., Zhang, L., Biswas, P., Li, C. (2017). Engineering the outermost layers of TiO_2 nanoparticles using in situ Mg doping in a flame aerosol reactor. AIChE J. 63:870-880. * Equal contribution*

Abstract

Titanium dioxide nanoparticles with disordered outermost layer sturctures have significantly enhanced light absorption and photocatalytic properties and thus receiving enhanced attention in recent years. Engineering the outermost layers using in situ magnesium doping to tailor the band-edge of TiO_2 nanoparticles was achieved via a flame aerosol reactor (FLAR). We proposed that the distribution of doped elements in nanoparticles could be controlled in a high temperature flame process, and which could be predicted by the comparison of different characteristic time scales, such as reaction time, coagulation time, and sintering time. In situ magnesium doping on the outermost layers effectively tailored the conduction band and electron structure of the TiO_2 nanoparticles, and simultaneously improved the maximum photocurrent as well as the maximum photovoltage in dye-sensitized solar cells (DSSCs). These improvements were largely attributed to red-shifted light absorption, and rapid photoelectron injection into the conduction band.

Introduction

Sustainable and clean energy producing devices are urgently needed to meet the challenges of global environmental pollution and the energy crisis.[1,2] TiO_2 nanoparticles have attracted tremendous interest due to their applications in transforming solar energy into electric energy, in photocatalytic hydrogen generation, and in environmental pollution management.[3,4] More recently, it has been shown by Chen et al.[5] that solar energy conversion can be enhanced by introducing a controlled disorder in the surface layers of black TiO_2 nanoparticles through hydrogenation. These authors proposed that disorder-engineered TiO_2 nanocrystals exhibit substantial solar-driven photocatalytic activities, including the photo-oxidation of organic molecules in water and the production of hydrogen with the use of methanol as a sacrificial reagent. The improved performance caused by disordered layer structures in application such as photoelectric conversion and photocatalysis has triggered world-wide research interest.[6] Based on the high-pressure hydrogen thermal treatment process, a variety of methods have produced TiO_2 nanoparticles with disordered outermost layer structures. These methods include hydrogen plasma,[7] aluminium reduction,[8] X-doping (X= H, N, S, I),[9] and chemical oxidation. Dhumal et al.[10] have demonstrated the synthesis of oxygen deficient titanium dioxide with superior visible light activated photocatalytic properties. However, most existing techniques involve multiple steps and require a long synthesis time and high temperature to produce the outermost disordered layer on the surface of TiO_2 nanoparticles, making them unattractive for industrial scale up.[11,12]

Flame aerosol reactors (FLAR), which are an industrially successful route to synthesize nanoparticles, provide an alternate choice for designing and fabricating nanostructures in a one-step and scalable process.[13-21] Thimsen et al.[22] used a FLAR system to deposit a nanostructured photocatalytic film of titanium dioxide with well-controlled morphologies, and various aerosol phase characteristic times were estimated to confirm that the deposition of individual particles was important. Buesser et al.[13] elucidated the gas-phase coating in considerable details via computational fluid dynamics (CFD) and particle dynamics for core-shell TiO_2@SiO_2, and assessed the performance of a simpler coating model by comparison with the present detailed CFD model. Huo et al.[23] synthesized blue TiO_2 nanoparticles with disordered outermost layers by introducing H_2 via a quench ring in a FLAR system. The nanoparticles' visible light absorption and photocatalytic performance were enhanced significantly. Teleki and Pratsinis[24] achieved the synthesis of blue titania in diffusion flames by rapid quenching, and the oxygen deficiencies were found to be located in the bulk and not only on the surface of the particles. Using a flame spray pyrolysis (FSP) method, Fujikawa et al.[25] synthesized "black" titania which showed a strong photo-reduction of cationic species and photo-oxidation of organics. However, due to the complex interactions among different process parameters, such as the precursor concentration, time-dependent flame temperature profile, chemical reaction rate, particle growth rate, coagulation rate, and sintering rate, it is truly hard to relate process conditions to the nanoparticles' structures (such as shape, crystallinity, chemical composition, etc., except particle size) obtained from one-step FLARs.[26-31] Specifically, it should be remarked that the comprehensive effects of the modification at the surface structure by in situ doping in the rapid flame process have been scarcely considered to date. The surface disordered layers and surface bonded groups may play a noteworthy role in the yield of photoelectric conversion taking place at the surface, bearing in mind that the outermost layers can determine the surface density, band gap, and recombination kinetics of the photo-generated electrons.

The photoelectronic performance of dye-sensitized solar cells (DSSCs) can be effectively altered by tailoring the band-edge of TiO_2 nanoparticles in a photoanode, which determines the photo-induced voltage and current, and the efficiency of DSSCs. Up until now, many strategies have been developed to minimize the interfacial charge recombination in a TiO_2-based photoelectrode. Among them, impurity-doping has been proved to be a convenient way to promote the photoelectric performance by adjusting the band gap structure and the electrical conductivity of photoanode materials. With an ionic radius close to that of Ti^{4+}, Mg^{2+} ions are widely used as dopants to fine tune the band-edge and electron structure of TiO_2, since Mg^{2+} doping can usually lead to a negative shift in the energy level of the conduction band of TiO_2.

In this work, TiO_2 nanoparticles were engineered with disordered outermost layers, using in situ magnesium doping and a FLAR system. To the best of our knowledge, for the first time, we proposed that the distribution of doped elements in nanoparticles could be controlled in a high temperature flame process, and which could be predicted by the comparison of different characteristic time scales, such as reaction time, coagulation time, and sintering time. In situ magnesium doping on the outermost layers effectively tailored the conduction band and electron structure of TiO_2 nanoparticles, and simultaneously improved the maximum photocurrent as well as the maximum photovoltage in DSSCs. The proposed methodology is simple, single-step, and rapid, and thus has great potential for commercial-scale applications.

Experimental Methods

Material Synthesis

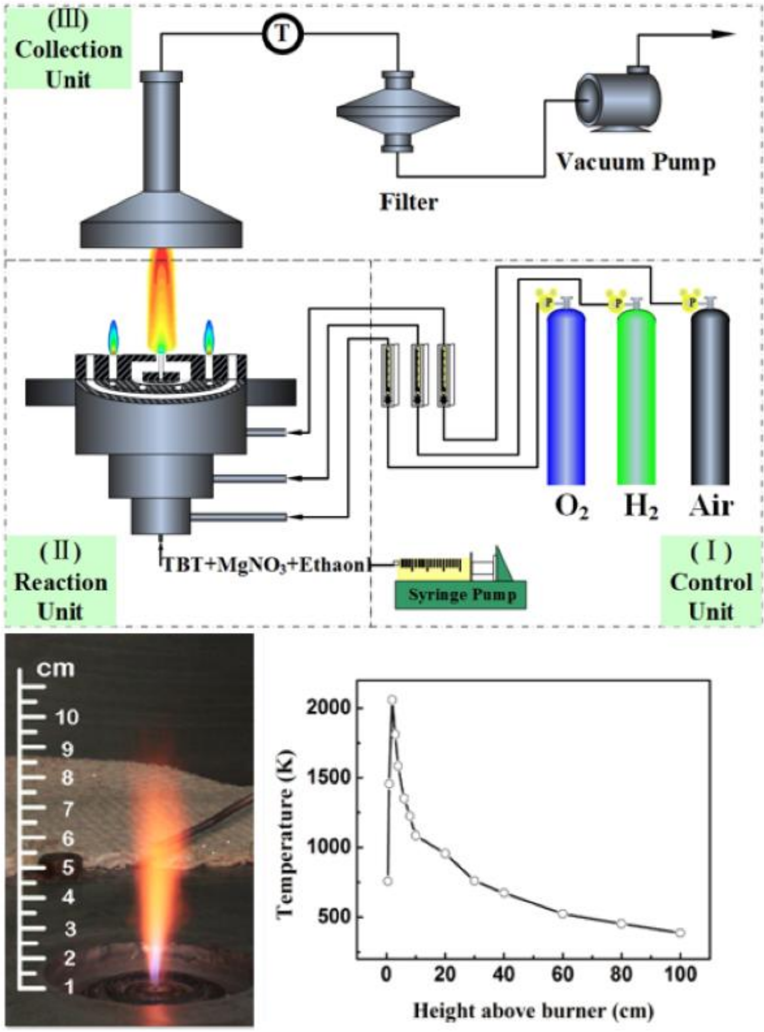

Figure A3.1 Schematic of flame aerosol reactor and measured temperature as a function of height above the burner (HAB).

Unless stated otherwise, all chemicals (magnesium nitrate hexhydrate (≥ 99 %, AR, SCRC), titanium butoxide (TBT) (≥ 98 %, CP, Yonghua), and alcohol (≥ 98 %, AR, Titan)) were reagent grade. TiO_2 and Mg^{2+}-doped TiO_2 nanoparticles each was synthesized via a fast and convenient liquid-feed flame spray pyrolysis (FSP) process. In brief, for synthesizing doped TiO_2 nanoparticles, a homogeneous precursor solution was prepared by dissolving TBT and magnesium nitrate hexahydrate in alcohol. The TBT concentration was controlled at 0.5 M. Then the precursor solution was injected with O_2 (5 L/min) at a flowrate of 5 mL/min through a spray nozzle while the pressure drop at the tip of nozzle was about 0.15 MPa. To support flame combustion, 1.5 L/min H_2 and 15 L/min air was fed through the nozzle. Schematic of flame aerosol reactor (FLAR) and the temperature profile as a function of the height above the burner (HAB) are shown in Figure A3.1. The temperatures were measured with a type B thermocouple (Pt/Rh 70%/30%-Pt/Rh 94%/6%) along the centerline of above the nozzle. It should be noted that measuring temperatures in FSP systems is very difficult and may not be accurate due to the harsh environment (high gas velocity and high temperature). This effect is much more significant at locations near to the outlet of the nozzle, where short-time measurements can be conducted only, since the high-velocity gas can easily break the thermocouple. With the precursor chemical reaction, nucleation, coagulation, and sintering process, the precursor was finally converted into Mg^{2+}-doped TiO_2 nanoparticles. Various experimental amounts of magnesium were added, in Mg/Ti atomic molar ratios of x %, where x=0, 0.5, 1.0, 1.5, and 2.0. The as-prepared samples were denoted as x Mg-TiO_2. To obtain pure TiO_2 nanoparticles, we followed the same procedure, but omitted magnesium nitrate hexahydrate from the precursor.

Materials Characterizations

A field emission scanning electron microscope (FE-SEM: HITACHI S-4800), transmission electron microscope (TEM: JEOL JEM-2100) and high resolution transmission electron microscope (HRTEM: JEOL JEM-2100) were utilized to study the morphological structures of the samples. X-ray diffraction (XRD: D/max 2550V) in a 2θ range from 10° to 80° measured the crystal phases of the products. The doping of Mg into the TiO_2 lattice was examined with an X−ray photoelectron spectroscope (ESCALAB MK II), using Mg Kα (hν = 1253.6 eV) as the standard. A Shimadzu UV3600 UV-vis-NIR spectrometer was utilized to plot the UV-vis reflectance spectra of the particle samples. To evaluated the amount of dye loaded on the TiO_2

films, A UV-vis-NIR spectrophotometer (UV-3150) was used to plot the absorption spectra of N719 dye-desorption solutions (dye-absorbed TiO_2 film was immersed into 0.05 M NaOH aqueous solution for 10 s).

Results and discussion

Characteristic times and particle formation mechanism in FLAR system

Droplet combustion Time

In a spray nozzle, the high kinetic energy of the gas flow breaks the liquid into droplets. In this study, the size of the sprayed droplets was determined by an Aerodynamic Particle Sizer (APS, TSI 3321) based on the time-of-flight technique. The sprayed droplets had a mode size of around 2 μm. On the other hand, sprayed droplet diameter is often estimated by[32]

$$D_d = \frac{585\sqrt{\sigma}}{u_{rel}\sqrt{\rho_l}} + 597\left(\frac{\mu_l}{\sqrt{\rho_l \sigma}}\right)^{0.45} \times \left(1000\frac{Q_l}{Q_a}\right)^{1.5}, \qquad \text{(A3.1)}$$

where D_d is average droplet diameter, σ is the surface tension of the precursor solution, ρ_l is the density of the precursor solution, μ_l is the viscosity of the precursor solution, u_{rel} is the relative speed of the gas and liquid, Q_l is the volume of the liquid flow, Q_a is the volume of the diffusion gas flow. The calculated droplet size is 42 μm, which is far larger than the measured droplet size. This huge difference indicates that semi-empirical equations predicting droplet sizes are dependent on the design of the spray nozzles, which may not accurately predict the size of the particles. Droplet combustion times were determined using the simplified differential energy balance model from Turns et al.[33] The model was developed assuming that droplets combust in a quiescent, infinite medium and that the droplets are pure ethanol. The energy balance yields a vaporization time of

$$\tau_d = \frac{D_d^2}{K_E}. \tag{A3.2}$$

$$K_E = \frac{8k_g}{\rho_l c_{pg}} \ln(B_q + 1), \tag{A3.3}$$

where k_g is the average specific heat capacity of the surrounding gas, ρ_l is the density of the liquid ethanol, and c_{pg} is the specific heat of the ethanol vapor. Furthermore, B_q is calculated as follows:

$$B_q = \frac{\Delta h_c / \nu + c_{pg}(T_\infty - T_{boil})}{h_{fg}}. \tag{A3.4}$$

In this expression, T_∞ is the temperature of the surrounding gas, T_{boil} is the boiling temperature of the ethanol droplet, h_{fg} is the enthalpy of vaporization of the droplet, Δh_c is the enthalpy of combustion of the droplet, and ν is the stoichiometric air-fuel ratio. All gas properties are assumed to be the values obtained at the average of T_{boil} and the adiabatic flame temperature (2200 K). It should be noted that the temperature and velocity gradients in the FSP process are very steep, affecting the validity of this assumption. However, due to its wide usage in studying single droplet combustions[29], this assumption is still used in this study to simplify the calculation of different time scales. Also, droplet combustion and precursor reaction were assumed to be taking place separately, since water molecules was produced at the flame sheet outside, instead of on the surface of the droplet. Furthermore, no hollow spherical structures were observed in the synthesized particles, and particle sizes measured in TEM images showed a unimodal shape, suggesting the precursor reaction on the surface of the droplet was unlikely. After droplet combustion completed, the precursor molecules were released from the droplet and went through further reactions.

TBT reaction time

In flames, the TBT could react through thermal decomposition and hydrolysis:

$$Ti(OC_4H_9)_4 \xrightarrow{Heat} TiO_2 + 4C_4H_8 + 2H_2O \text{, and} \tag{A3.5}$$

$$Ti(OC_4H_9)_4 + 2H_2O \longrightarrow TiO_2 + 4C_4H_9OH \,. \tag{A3.6}$$

However, it should be noted that the hydrolysis of TBT is significantly faster than its thermal decomposition.[34,35] Since combustion generates a high concentration of water vapour, it is reasonable to neglect the thermal decomposition of TBT and to assume that hydrolysis is the only reaction that produces TiO_2 nanoparticles. Further, by assuming that the hydrolysis of TBT is a first-order reaction, the time-dependent TBT concentration satisfies the differential equation of

$$dC_{TBT} / dt = -k_h C_{TBT} \,, \tag{A3.7}$$

where C_{TBT} is the concentration of TBT, t is the time, and k_h is the first-order hydrolysis reaction rate constant. Due to the lack of data on TBT' hydrolysis reaction rate and the similarity among titanium alkoxides,[36] we used the first-order reaction rate of titanium isopropoxide (TTIP) hydrolysis,[34]

$$k_h = 3\times10^{15}\exp(-\frac{1013.9}{T}), \quad \text{(A3.8)}$$

to calculate the characteristic reaction time of the precursor's hydrolysis, according to the equation

$$\tau_{rxn,TBT,h} = 1/k_h. \quad \text{(A3.9)}$$

On the other hand, it should be noted that precursor hydrolysis rates are often obtained from experiments conducted in liquid environments. By considering the fact that the precursor hydrolysis is a bimolecular reaction which involves the collision between a water molecule and a precursor molecule, the collision-limited pseudo-first order reaction rate which assumes each collision converts to a successful reaction can be calculated (supporting information) and shown as:

$$k_{coll} = \frac{3}{18.5}\frac{P}{RT}N_A\pi\sigma_{AB}^2(\frac{8k_BT}{\pi\mu})^{\frac{1}{2}} \quad \text{(A3.10)}$$

The characteristic time for this reaction is then

$$\tau_{rxn,TBT,c} = 1/k_{coll}. \quad \text{(A3.11)}$$

$Mg(NO_3)_2$ reaction time

At elevated temperatures (> 400 ^oC), *$Mg(NO_3)_2$* reacts through thermal decomposition producing MgO:

$$Mg(NO_3)_2 \xrightarrow{Heat} MgO + 2NO_2 + 1/2O_2. \quad \text{(A3.12)}$$

It should be noted that the thermal decomposition rate of $Mg(NO_3)_2$ in vapor form may be different than that obtained in its crystal form. Due to the difficulty in verifying the actual decomposition rate, the available data from literature was used. It is also possible that the crystal water attached in the $Mg(NO_3)_2$ might react with TBT before the precursors react in the flame. However, due to the low concentration of the $Mg(NO_3)_2$ precursor, this reaction is neglected. We obtained the first-order decomposition reaction rate by fitting data from the work of Stern[37] (ESI) and using the equation:

$$k_d = 5.67\times10^{22}\exp(-\frac{30304}{T}) . \tag{A3.13}$$

The thermal decomposition of $Mg(NO_3)_2$ has a high activation energy due to the high stability of the ionic bond. The high activation energy also result in a fast reaction rate at high temperatures. The characteristic time for $Mg(NO_3)_2$ decomposition is calculated by

$$\tau_{rxn,Mg(NO_3)_2} = 1/k_d . \tag{A3.14}$$

Coagulation time

The synthesis precursors react in the FLAR and generate highly concentrated metal oxide monomers which are the building blocks of nanoparticles. Typically, the saturation vapour pressures of metal oxides are extremely low, meaning that a single metal oxide molecule is stable enough to be a particle, and thus particle coagulation and growth become irreversible. A simplified model to evaluate monodisperse particle coagulation uses the coagulation coefficient β and total particle concentration N_0 to calculate the characteristic coagulation time[38], where

$$\tau_{coag} = \frac{2}{\beta N_0}. \quad \text{(A3.15)}$$

The coagulation coefficient is further given by

$$\beta = 8\pi D r_c \left[\frac{r_c}{2r_c + \sqrt{2}g} + \frac{\sqrt{2}D}{c r_c}\right]^{-1}, \quad \text{(A3.16)}$$

where D is the particle diffusion coefficient, r_c is the particle collision radius, c is the particle velocity, and g is the transition parameter. Detailed expressions of these parameters can be found in Seinfeld and Pandis.[39] For simplicity, the particle collision radius was considered to be the same as the primary particle radius. It should be noted that Eq. [16] covers the particle coagulation characteristics from free molecular regime to continuum regime. τ_{coag} was examined at several primary particle sizes. Mass balance gives the that $N_0 d_p^3$ remains a constant during the monodisperse particle coagulation. N_0 at d_p=0.4 nm can be calculated based on the flow rates of the gas species and TBT precursor, and has a value of. 7.0×10^{22} #/m^3.

Sintering time

The characteristic sintering time is calculated with the equation used in Tsantilis et al.[34]

$$\tau_{sinter} = 7.4\times10^{16} T d_p^4 \exp\left(\frac{31000}{T}\right), \quad \text{(A3.17)}$$

where d_p is the particle size in meters.

Residence time

The residence time (τ_{res}) of particles in high temperature zone significantly affect the characteristics of the synthesized.[40] However, determining the residence time is a difficult task, since it is strongly dependent on the temperature and flow field during the heterogeneous FSP process. Based on the temperature profile above the burner, and further by assuming the gas species transports and reacts similar to the ones in a tubular reactor (with a diameter of 5 cm) where the temperature and flow field can be seen as one-dimensional, the residence time of particles in the high temperature zone can be estimated. The residence time of particles in the region where temperature is higher than 2000, 1000 K, and 700 K are 0.008, 0.198 s, and 0.613 s, respectively. Note that in real situations, the heat expansion is not in one dimension. The three-dimensional expansion can result in a longer residence time in high temperature regions.

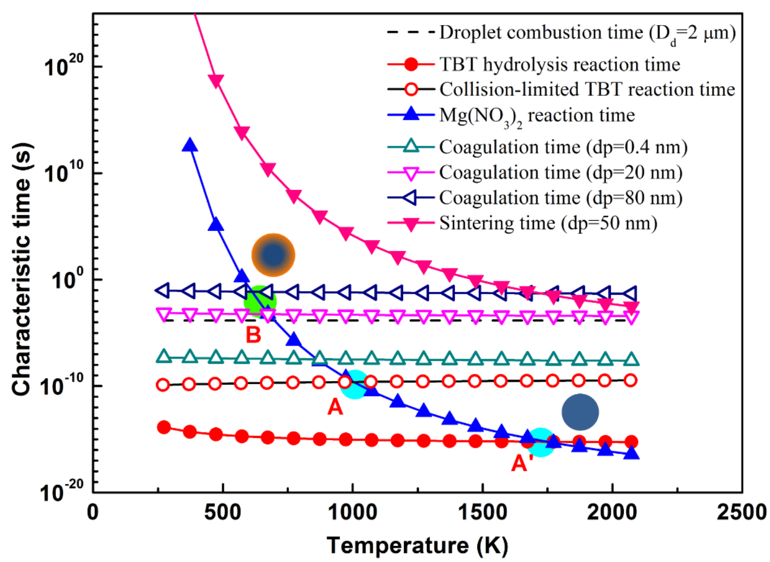

Figure A3.2 Various characteristic time scales in the flame synthesis process.

The characteristic time scales in the flame are shown in Figure A3.2. The relative magnitude of *$Mg(NO_3)_2$* and *TBT* reaction time is dependent on the system temperatures. At low temperatures, *TBT* reaction is faster than *$Mg(NO_3)_2$* thermal decomposition, while this trend is reversed at high temperatures. The collision-limited reaction rate of TBT is much lower than the hydrolysis rate predicted by Eq. [8]. We should note that the collision-limited reaction rate predicts the highest possible rate that is achievable in the gas-phase reaction of TBT (considering the fact that the hydrolysis of a TBT molecule needs two water molecules). This large difference between the reaction rates indicates that more caution is needed when reaction rate formulas determined from different experimental conditions are used. On the basis of these estimated characteristic time scales, one can first briefly analyse the doping characteristics of the synthesized materials by imagining an environment with a constant temperature and an infinitely long processing time (imaging drawing a vertical line corresponding to a specific temperature).

Point A (A') marks the crossover temperature of TBT reaction and $Mg(NO_3)_2$ reaction. At this temperature, TBT and $Mg(NO_3)_2$ converts to metal oxides with similar time scales, forming a homogeneous mixture. As time proceeds, TiO_2 molecules coagulates together with the available MgO molecules, leading to uniform Mg^{2+}-doping throughout the TiO_2 nanoparticles. The primary particle size at a specific time can be estimated by looking for the crossover point of sintering time and coagulation time (not shown in the figure), although residence time is another limiting factor in real situations, which is also discussed in the following section.

At low temperatures (e.g., point B), the TBT quickly reacts and coagulates, while $Mg(NO_3)_2$ is still in its precursor form. When the TiO_2 coagulation time is comparable to the thermal decomposition time of $Mg(NO_3)_2$, Mg ions can dope into TiO_2 nanoparticles at outermost layers, but not completely penetrate them. As particles further sinter, the highly concentrated Mg contents remain in the outer layers of the TiO_2 nanoparticles. At temperatures higher than Point A (A'), $Mg(NO_3)_2$ thermal decomposition is significantly faster than TBT reaction. However, the low concentration of MgO and high concentration of TiO_2 used in this study determines that

MgO molecules will dope uniformly in coagulated TiO_2 particles, similar to the situation taking place at point A (A').

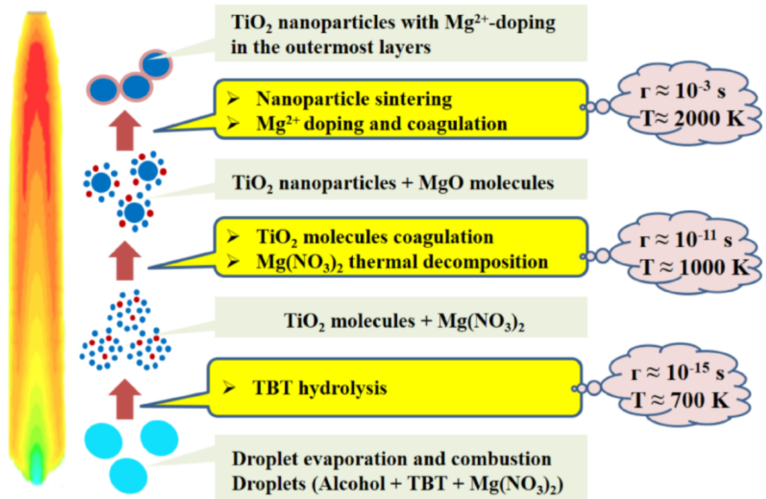

Figure A3.3 Formation mechanism of TiO_2 nanoparticles with Mg^{2+} doping in the outermost layers in the flame.

Note that in a FSP process, the particle residence time plays a critical role in determining the synthesized particle properties, where the assumption of infinitely long residence time is not valid. On the basis of these conclusions, we proposed a formation mechanism for TiO_2 nanoparticles with Mg^{2+}-doping in the outermost layers in a rapid flame process, as shown in Figure A3.3. First, precursor solution was dispersed into droplets, which began to evaporate and combust as the temperature rose. After the precursors were released from the droplets, TBT starts hydrolysing. Since the thermal decomposition rate of $Mg(NO_3)_2$ is far less than the hydrolysis rate of TBT, we got a mixture of TiO_2 molecules and $Mg(NO_3)_2$ in the gas phase. Second, TiO_2 molecules coagulated into nanoparticles, and at the same time, the $Mg(NO_3)_2$ thermal decomposition took place. The residence time of particles at high temperature regions in the flame determines the size of the particles. It was found that the residence time at the temperature above 2000 K was similar to the sintering and coagulation time of particles with diameters between 20 nm and 80 nm. Hence, we are more likely to obtain nanoparticles in this size range, and Mg^{2+} were doped on the outermost layers of these TiO_2 nanoparticles.

Structural characterization and outermost layer analysis

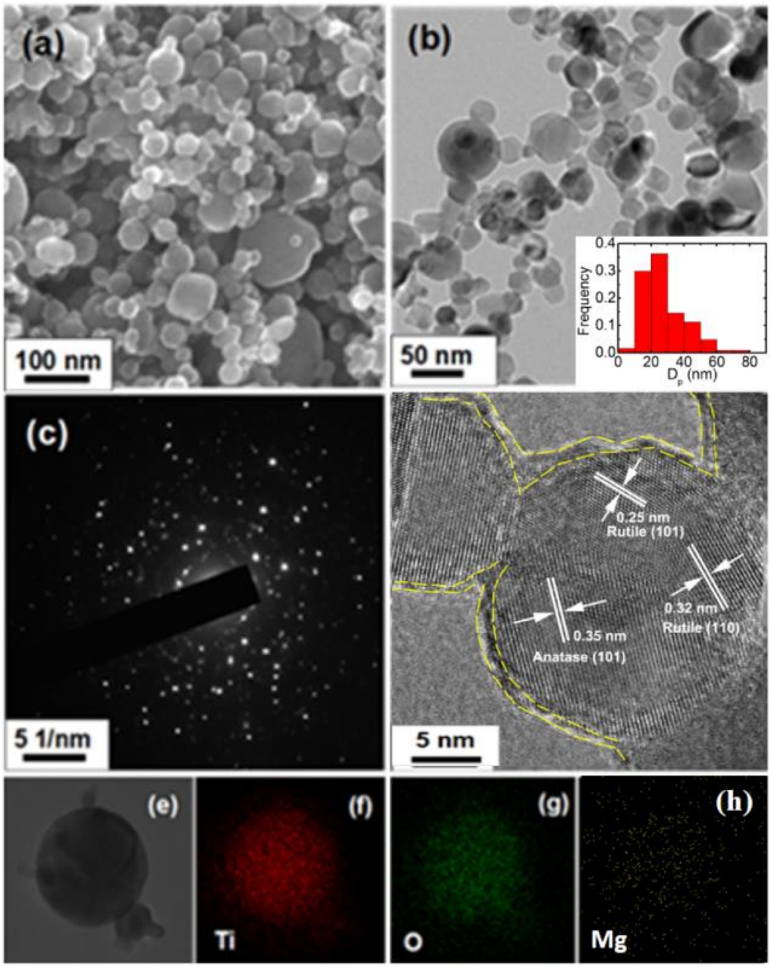

Figure A3.4 Images of 1.0 Mg-TiO_2 nanoparticles: (a) SEM image, (b) TEM image (inset figure shows the size distribution of the particles), (c) SAED pattern image, (d) HRTEM image, (e-h) TEM image of single particles and corresponding elemental mapping images.

The morphology and crystal structure of 1.0 Mg-TiO_2 produced by the FLAR system were observed by SEM and TEM. Figure A3.4a and Figure A3.4b show a wide size distribution, ranging from 20 - 50 nm. Figure A3.4d shows the SAED pattern, indicating that the 1.0 Mg-TiO_2 nanoparticles are polycrystalline, which is consistent with XRD. The disordered layer structure on the surface of the TiO_2 nanoparticles can clearly be seen in Figure A3.4d, the thickness of the disordered layer was about 1 - 2 nm. Clear lattice fringes in the HRTEM image (Figure A3.4d) demonstrate that the obtained doped TiO_2 nanoparticles have a high crystallinity and a polycrystalline nature. The crystal lattice distances were measured to be 0.35 nm, 0.33 nm and 0.25 nm, which respectively correspond with the (101) plane of anatase TiO_2 (JCPDF No.: 21-1272), the (110) plane of rutile (JCPDF No.: 65-0191), and the (101) plane of rutile TiO_2 (JCPDF No.: 65-0191). Further, the TEM elemental mapping of the spatial distribution of Ti, O, and Mg (as shown in Figure A3.4e-h) confirms that the Mg^{2+}-doping on the surface of TiO_2 nanoparticles is very homogeneous.

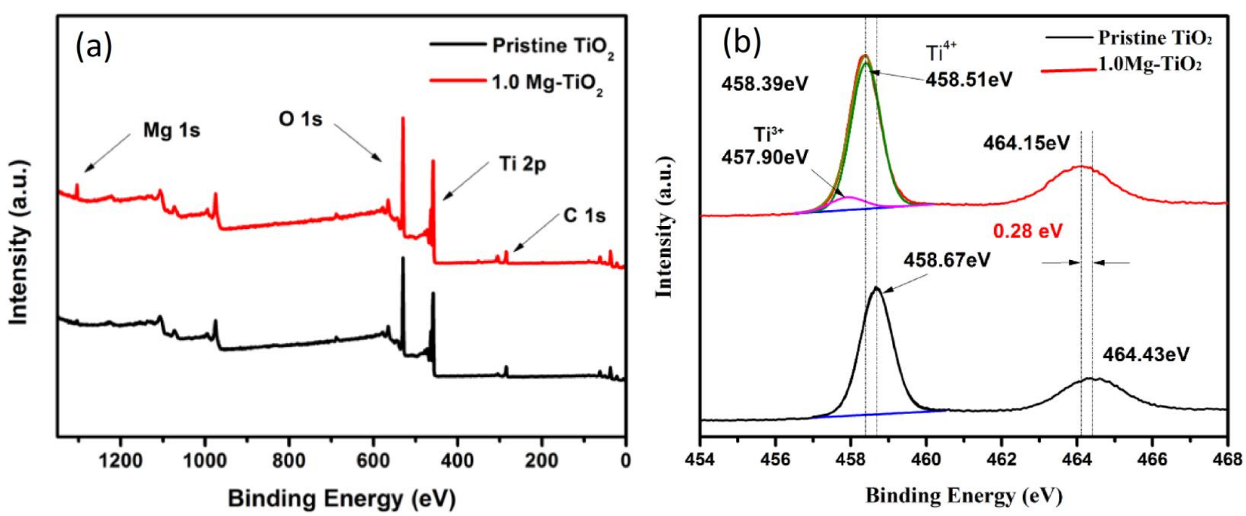

Figure A3.5 (a) XPS profile of pristine TiO_2 and 1.0 Mg-TiO_2 nanoparticles; (b) High resolution XPS spectra of Ti 2p of pristine TiO_2 and 1.0 Mg-TiO_2 nanoparticles.

To confirm the presence of Mg^{2+} ions and the chemical states of Ti ions in TiO_2, X-ray photoelectron spectroscopy was employed, as shown in Figure A3.5. The corresponding XPS depicts the elements and associated chemical bonds of the top atomic layers of the samples, because the escape-depth of electrons is several nanometers. Figure A3.5a shows the XPS curves of pristine TiO_2 and 1.0 Mg-TiO_2 nanoparticles. Compared with pristine TiO_2, the curve of 1.0 Mg-TiO_2 has an obvious peak of Mg^{2+} ions, which indicates the successful of Mg-doping. The ratio of Mg /Ti detected in the 1.0 Mg-TiO_2 is 13.9 %, which is much larger than 1.0 %. This ratio suggests that Mg^{2+} ions are enriched on the surface, in accordance with our conclusion obtained by estimate characteristics times, it can also be confirmed by disorder layers structures causing by Mg^{2+} in situ doping on the surface of TiO_2 nanoparticles that have be shown in TEM images.

High resolution XPS spectra of the Ti 2p molecular orbital of pristine TiO_2 and 1.0 Mg-TiO_2 are shown in Figure A3.5b. Two peaks, of Ti $2p_{3/2}$ (458.39 eV) and Ti $2p_{1/2}$ (464.15 eV), are shown in the high resolution Ti 2p XPS spectrum of 1.0 Mg-$TiO_{2,}$ while the peaks of pristine TiO_2 are Ti $2p_{3/2}$ (458.67 eV) and Ti $2p_{1/2}$ (464.43 eV).[41] The peak of 1.0 Mg-TiO_2 shows a shift towards the lower binding energy, indicating that the chemical environment of Ti atoms is different from that in pristine TiO_2 because of the Ti^{3+} ion produced by oxygen vacancies introduced via Mg^{2+}-doping. The Ti 2p peaks of Mg doped TiO_2 are well de-convoluted into two peaks: Ti^{3+} $2p_{3/2}$ at 457.90 eV, Ti^{4+} $2p_{3/2}$ at 458.51 eV. The abundance of Ti^{3+} ions on the surface of the 1.0 Mg-TiO_2 was calculated to be ~9.46%, and is related to the band-edge shift. Such a high content of Ti^{3+} ions is due to the enrichment of Mg^{2+} ions in situ doping on the surface of TiO_2 nanoparticles in flame process.

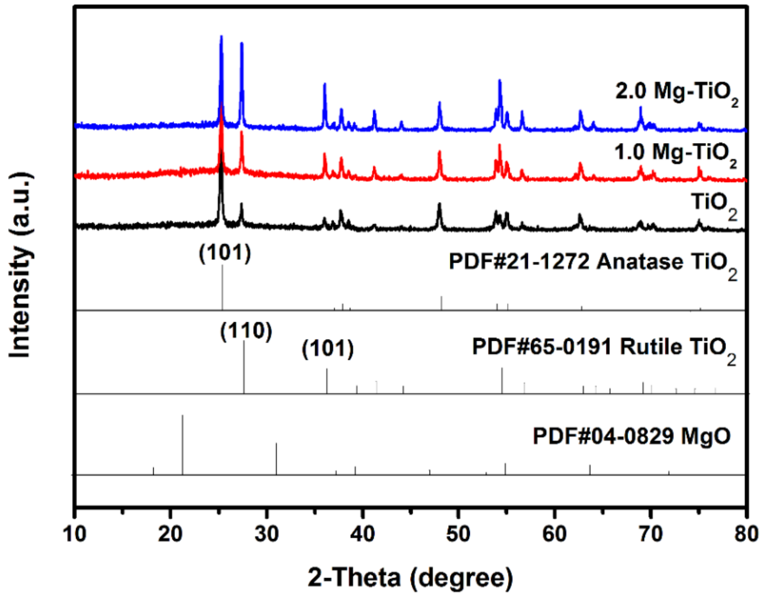

Figure A3.6 XRD spectra for flame spray produced TiO_2, 1.0 Mg-TiO_2, and 2.0 Mg-TiO_2 nanoparticles.

Table A3.1 Anatase and rutile contents of three samples with different Mg contents.

Sample	Phase content (%)		Crystal size (nm)		Anatase c (nm)
	Anatase	Rutile	Anatase	Rutile	
Pure TiO_2	74.84	25.16	31.7	48.7	0.9519
1.0 Mg-TiO_2	59.70	40.30	33.8	42.6	0.9515
2.0 Mg-TiO_2	46.08	53.92	35.6	40.7	0.9498

The phase compositions of TiO_2, 1.0 Mg-TiO_2, and 2.0 Mg-TiO_2 were characterized by XRD. As shown in Figure A3.6, all the diffraction peaks are consistent with those of standard XRD patterns of anatase TiO_2 (JCPDF No.: 21-1272) and rutile TiO_2 (JCPDF No.: 65-0191), which identifies the polycrystalline nature of the product, in agreement with the results from selected area electron diffraction (SAED). It is noted that no diffraction peak of impurities, such as MgO, was detected in XRD spectra, which means that doping did not change the critical form of TiO_2, and Mg^{2+} was doped into the lattice, which we attributed to rapid sintering in the high temperature process. The stronger three peaks of (101) anatase, (110) rutile, and (101) rutile are observed in both pure and doped TiO_2.[42] The rutile peaks from Mg^{2+}-doped TiO_2 are obviously stronger, which suggests that doping with Mg^{2+} can promote the generation of rutile (the anatase and rutile contents of three samples are shown in Table A3.1). Existing studies found that the phase transition temperatures of $Mg(NO_3)_2$-doped TiO_2 from amorphous to anatase and to rutile were significantly reduced.[43] Rutile generation can be attributed to the formation of oxygen vacancies induced by the doping of Mg^{2+} in the lattice of TiO_2, and every Mg^{2+} means two oxygen vacancies in theory. According to the Kroger-Vink notation, the defective reaction caused by Ti^{4+} substitution by Mg^{2+} can be expressed as follows[12]:

$$MgO \xrightarrow{TiO_2} Mg_{Ti}^{''} + O_O^X + V_{O^{\bullet\bullet}} \tag{A3.18}$$

Where $Mg_{Ti}^{''}$ indicates a Mg^{2+} in a Ti^{4+} lattice site; O_O^X represents a O^{2-} in a normal lattice site and $V_{O^{\bullet\bullet}}$ an ionized oxygen vacancy. In addition, the lattice cell parameter in the c-axis calculated for the pure TiO_2 sample was c = 0.9519 nm, while those for the Mg^{2+}-doped TiO_2 sample were c = 0.9515 and 0.9498 nm (1% and 2% Mg^{2+}-doping) indicating that Mg^{2+} insertion into the TiO_2 lattice could slightly contract the lattice. The average crystallite sizes calculated from the broadening of the (101) and (110) XRD peak of the anatase phase were about 31.7, 33.8 and 35.6 nm for TiO_2 and Mg^{2+}-doped TiO_2 samples, respectively. These sizes are relatively larger compared to a similar study which also conducted Mg^{2+}-doping in TiO_2 nanoparticles, which may be due to the difference in synthesis methods. Future work will be conducted to further tune the flame conditions to control the crystal characteristics.

Photovoltaic Performance, Optical Properties, and Charge Transfer Dynamics

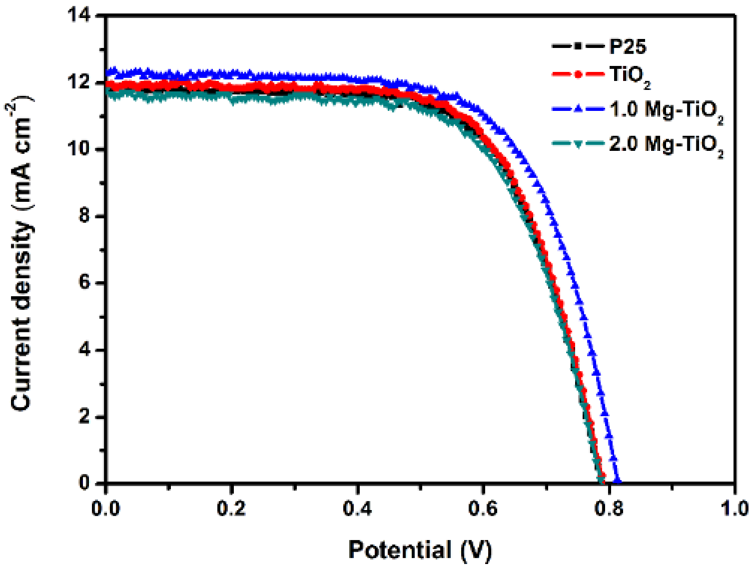

Figure A3.7 J-V curves of DSSCs based on TiO_2 and Mg doped TiO_2 nanopaticles, as well as the curve for commercially available P25 nanopaticles.

Table A3.2 Summary of DSSC performance parameters obtained from different 5 µm thick photoanodes: TiO_2, Mg^{2+}-doped TiO_2 nanopaticles, and P25 nanoparticles, all under one sun illumination (100 mW/cm^2).

Samples	V_{OC} (mV)	J_{SC} (mAcm^{-2})	Fill factor (FF)	Conversion Efficiency (η) (%)
P25	788	11.93	65.94	6.19
TiO_2	790	11.97	66.27	6.27
0.5 Mg-TiO_2	797	11.03	68.10	5.98
1.0 Mg-TiO_2	813	12.34	66.07	6.63
1.5 Mg-TiO_2	797	12.89	61.85	6.35
2.0 Mg-TiO_2	787	11.67	65.88	6.05

Using the measured characteristics of the photocurrent density - voltage (J-V) under simulated AM 1.5 G solar light illumination (100 mW/cm^2), photoanode electrodes were prepared to investigate the influence of Mg^{2+}-doping on the photovoltaic performance of TiO_2 as an anode material, as shown in Figure A3.7 and summarized in Table A3.2. With an approximately 5 µm thick film, the TiO_2 showed an efficiency of 6.27 % based on a V_{oc} of 790 mV and a J_{sc} of 11.03 mA/cm^2. As expected, Mg-TiO_2 showed significantly improved V_{oc} and J_{sc} compared with pristine TiO_2. With an increase in J_{sc} of up to 12.34 mA/cm^2 (3.1 % higher) and a V_{oc} of 813 mV (3.0 % higher), the 1.0 Mg-TiO_2 sample improved the efficiency from 6.27 % to 6.63 % (5.8 % higher).

Mg^{2+}-doping improved the J_{sc} for 1.0 Mg-TiO_2 in two ways: a red shift in light absorption and enhanced electron transfer and injection. The red shift results from a downward shift of the conduction band, and the enhanced electron transfer and injection result from narrowing of the energy gap. The reasons that the overall incident photon-to-current efficiency (IPCE) of 0.5 Mg-TiO_2 and 2.0 Mg-TiO_2 are lower than for pristine TiO_2 are different. If the amount of Mg doped into TiO_2 is too small, Mg^{2+} ions will become defects that impede electron injection and transfer, as shown (0.5 Mg-TiO_2) in Table A3.2. If the amount is too large, too many oxygen vacancies will be produced, which will capture more electrons, so that V_{oc} and J_{sc} will become lower together. In addition, for comparison, a sensitized photoanode film was also prepared with P25 TiO_2 nanoparticles, and its efficiency was 6.19 %.

Figure A3.8a displays the IPCE of DSSCs based on TiO_2, Mg-doped $TiO_{2,}$ and P25 nanoparticles. It is clear that TiO_2 1.0 is higher than the others, especially in the 400-580 nm range. As is known, the IPCE is connected with light-harvesting efficiency, charge collection efficiency, and electron injection efficiency. The data in Figure A3.8a suggest that the downward-shift in conduction caused by Mg^{2+}-doping narrows the energy gap and enlarges the D-value between the conduction band of the photoanode and the lowest unoccupied molecular orbital (LUMO) of dye, which would improve J_{sc}.

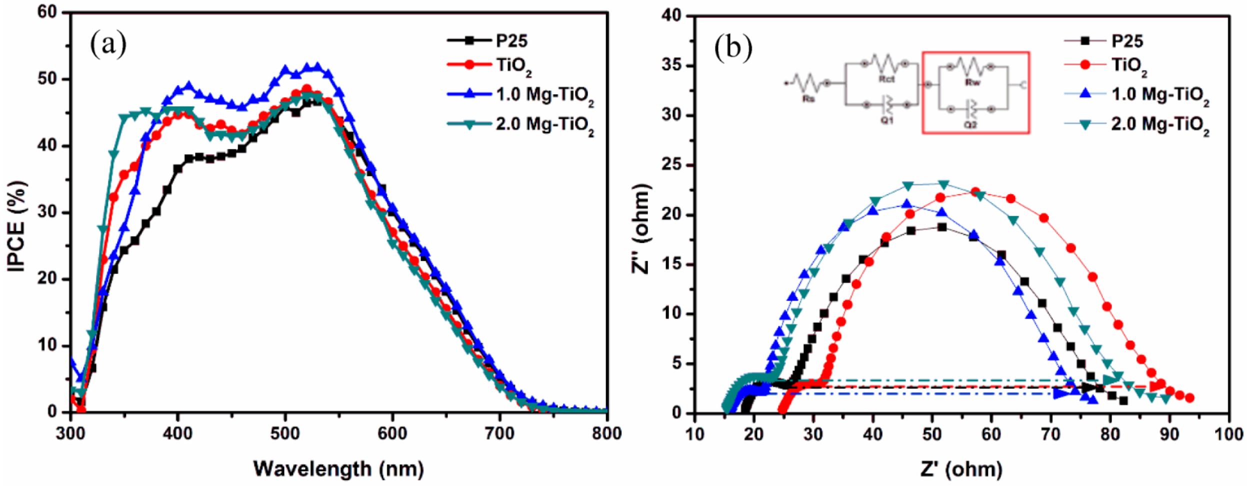

Figure A3.8 (a) IPCE and (b) Impedance spectra of DSSCs using TiO_2 and Mg-doped TiO_2 nanopaticles, as well as for P25 TiO_2 nanopaticles.

Table A3.3 R_{ct} for solar cells with different photoanodes.

Samples	P25	TiO_2	1.0 Mg-TiO_2	2.0 Mg-TiO_2
Rct, (ohm)	51.67	56.84	50.12	57.35

EIS is a powerful characterization method to research charge transport properties in the photoelectrode films of DSSCs. Figure A3.8b shows the Nyquist plots of EIS for DSSCs based on pristine TiO_2, 1.0 Mg-TiO_2, 2.0 Mg-TiO_2,a P25 nanoparticles, which are all similar in shape and size. The corresponding equivalent circuit is shown in the inset. Two general semicircles can be observed in the EIS Nyquist spectra, where the plot reflects the kinetic processes of electrons at the interfaces between the TiO_2, dye, and the electrolyte. The capability of electron-hole recombination can be calculated from the diameters of the semicircular Z_2 frequency current, which are representative of charge transfer resistance (R_{ct}). Table A3.3 shows the R_{ct} for different solar cells.

Owning to the electron concentration on the surface of the photoanode, a result of the oxygen vacancy produced by Mg doping, the R_{ct} of 1.0 Mg-TiO_2 is the minimum. In 1.0 Mg-TiO_2, electrons on the surface more easily recombine with holes because of the electron concentration. As the number of oxygen vacancies increases, the capacity of attracting electrons increases rapidly, so that R_{ct} becomes larger in 2.0 Mg-TiO_2. In conclusion, compared with the beneficial influence of Mg^{2+}-doping on current production, any detrimental influence can be ignored.

Conduction Band and Quasi-Fermi Level Movement

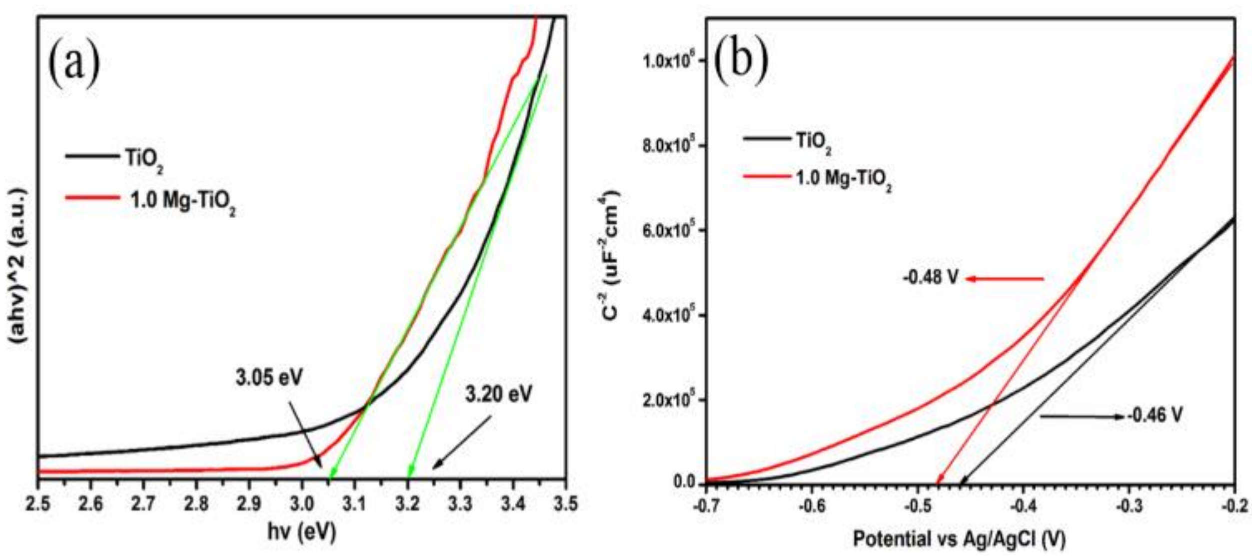

Figure A3.9 (a) Band gaps of TiO_2 and 1.0 Mg-TiO_2; (b) Mott-Schottky plots of TiO_2 and 1.0 Mg-TiO_2 electrodes in KCl and Na_2SO_4 electrolyte solutions (Ag/AgCl reference electrode).

The change in the band gap from doping with Mg^{2+} is shown in Figure A3.9a, calculated from the UV-vis absorption spectra of pure TiO_2 and 1.0 Mg-TiO_2. The energy band gap of TiO_2 is 3.20 eV, while the energy band gap of 1.0 Mg-TiO_2 is 3.05 eV. The obvious decrease in the energy gap means the shift of the conduction band moving negatively is less than that of the valence band moving negatively. The presence of Mg^{2+} ions can produce oxygen vacancies, leading to a negative shift of the original conduction band and a narrowing of the energy gap.[44] This change in the energy gap leads to a red shift in light absorption, which is beneficial to sunlight absorption, as the IPCE showed before. In addition, the movement of the conduction band can improve the electron injection efficiency because of the smaller energy difference between the LUMO of the dye and the CB of TiO_2. Compared with pure TiO_2, the potential maximum photocurrent (I_{max}) in DSSCs based on Mg^{2+}-doped TiO_2 is improved.

In the present work, the TiO_2 nanoparticles ranged from 20 nm to 50 nm in diameter, and this diameter range presented a band bending phenomenon which could not be ignored. The flat-band potentials (V_{fb}) of the TiO_2 and 1.0 Mg-TiO_2 photoanodes were tested by Mott-Schottky analysis, and the results are plotted in Figure A3.9b. An obvious negative shift of the potential could be observed for 1.0 Mg-TiO_2 photoanodes, corresponding to the upward movement of the quasi-Fermi level from Mg^{2+}-doping. The oxygen vacancies induced by doping play an important role in the movement of the quasi-Fermi level. Because oxygen vacancies in nanoparticles attract free electrons, the resulting higher density of free electrons causes an upward shift to appear in the quasi-Fermi levels. This upward shift improves the maximum photovoltage (V_{max}) obtained in the DSSCs, because V_{max} is governed by the energy difference between the quasi-Fermi level of the photoanode and the redox potential of the redox mediator in the electrolyte. Compared with pure TiO_2, the V_{max} in DSSCs based on Mg^{2+}-doped TiO_2 is improved.

Figure A3.10 schematically shows the band-edge and the quasi-Fermi level movements in Mg^{2+}-doped TiO_2. The conduction band moves negatively, which leads to a red shift in light absorption and higher electron injection efficiency, and thus improves the maximum photocurrent (I_{max}).

Although the quasi-Fermi level moves upward, the potential V_{max} increases because of the higher energy gap between the quasi-Fermi level of the photoanode and the redox potential of the redox mediator in the electrolyte. These phenomena both increase the efficiency of DSSCs.

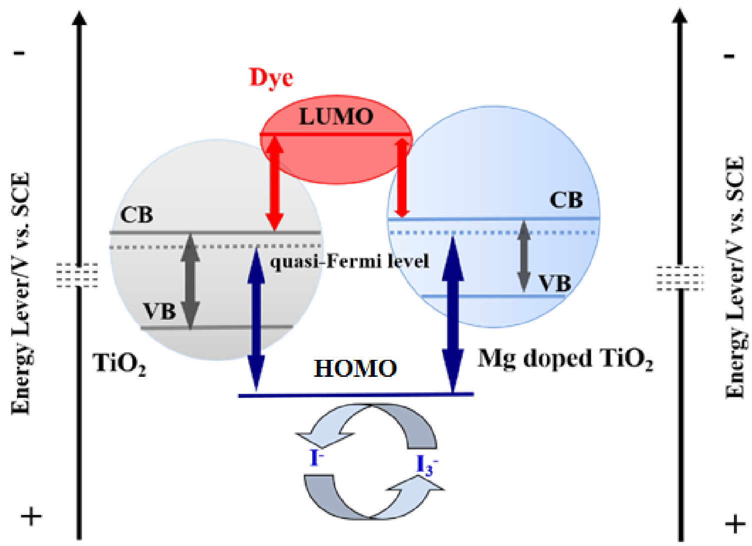

Figure A3.10 Schematic of conduction band and quasi-Fermi level movements in Mg^{2+}-doped TiO_2.

Conclusions

Using in situ magnesium doping in a flame aerosol reactor, we tailored the band-edge of TiO_2 nanoparticles by disordering their outmost layers. For the first time to our knowledge, the various characteristic times of precursor chemical reaction, coagulation, and sintering were estimated to explain the formation mechanism of TiO_2 nanoparticles' outermost layer in one-step high temperature flame process. In situ magnesium doping on the outermost layers effectively tailored the conduction band and electron structure of TiO_2 nanoparticles, and simultaneously improved the maximum photocurrent as well as the maximum photovoltage in dye-sensitized solar cells. The negatively shifted band-edge resulting from Mg-doping led to a red shift in light-absorption and enhanced electron injection in DSSCs, resulting in a 3.1 % improvement in the photocurrent. The upward shifted quasi-Fermi level led to a higher energy gap between the quasi-Fermi level of the photoanode and the redox potential of the redox mediator in the electrolyte, which resulted in a 3.0 % improvement of the photovoltage. As a result, the cell efficiency improved by about 5.8 %. More generally, the fast and convenient in situ doping method via flame spray pyrolysis can be used with most metal ions and oxides, and estimation of the various characteristic times can provide a reference for the design of nanoparticles with disordered outermost layers.

References

1. Hagfeldt A, Boschloo G, Sun L, Kloo L, Pettersson H. Dye-sensitized solar cells. *Chem. Rev.* 2010;110(11):6595-6663.

2. O'Regan B, Grätzel M. Photovoltaic and photochemical conversion of solar cell. Low cost and highly efficient solar cells based on the sensitization of colloidal titanium dioxide. *Nature.* 1991;335:7377-7385.

3. Yang HG, Sun CH, Qiao SZ, et al. Anatase TiO_2 single crystals with a large percentage of reactive facets. *Nature.* 2008;453(7195):638-641.

4. Yella A, Lee H-W, Tsao HN, et al. Porphyrin-sensitized solar cells with cobalt (II/III)–based redox electrolyte exceed 12 percent efficiency. *Science.* 2011;334(6056):629-634.

5. Chen X, Liu L, Huang F. Black titanium dioxide (TiO_2) nanomaterials. *Chem. Soc. Rev.* 2015;44(7):1861-1885.

6. Chen X, Liu L, Peter YY, Mao SS. Increasing solar absorption for photocatalysis with black hydrogenated titanium dioxide nanocrystals. *Science.* 2011;331(6018):746-750.

7. Wang Z, Yang C, Lin T, et al. H-doped black titania with very high solar absorption and excellent photocatalysis enhanced by localized surface plasmon resonance. *Adv. Funct. Mater.* 2013;23(43):5444-5450.

8. Wang Z, Yang C, Lin T, et al. Visible-light photocatalytic, solar thermal and photoelectrochemical properties of aluminium-reduced black titania. *Energy Environ. Sci.* 2013;6(10):3007-3014.

9. Lin T, Yang C, Wang Z, et al. Effective nonmetal incorporation in black titania with enhanced solar energy utilization. *Energy Environ. Sci.* 2014;7(3):967-972.

10. Dhumal SY, Daulton TL, Jiang J, Khomami B, Biswas P. Synthesis of visible light-active nanostructured TiO_x ($x<2$) photocatalysts in a flame aerosol reactor. *Appl. Catal. B.* 2009;86(3):145-151.

11. Lin Z-H, Xie Y, Yang Y, Wang S, Zhu G, Wang ZL. Enhanced triboelectric nanogenerators and triboelectric nanosensor using chemically modified TiO_2 nanomaterials. *ACS Nano.* 2013;7(5):4554-4560.

12. Manzanares M, Fàbrega C, Ossó JO, Vega LF, Andreu T, Morante JR. Engineering the TiO_2 outermost layers using magnesium for carbon dioxide photoreduction. *Appl. Catal. B.* 2014;150:57-62.

13. Buesser B, Pratsinis S. Design of gas-phase synthesis of core-shell particles by computational fluid-aerosol dynamics. *AIChE J.* 2011;57(11):3132-3142.

14. Hirai T, Sato H, Komasawa I. Mechanism of formation of titanium dioxide ultrafine particles in reverse micelles by hydrolysis of titanium tetrabutoxide. *Ind. Eng. Chem. Res.* 1993;32(12):3014-3019.

15. Li C, Hu Y, Yuan W. Nanomaterials synthesized by gas combustion flames: morphology and structure. *Particuology.* 2010;8(6):556-562.

16. Scharmach WJ, Sharma MK, Buchner RD, Papavassiliou V, Vajani GN, Swihart MT. Amorphous carbon encapsulation of metal aerosol nanoparticles for improved collection and prevention of oxidation. *AIChE J.* 2013;59(11):4116-4123.

17. Strobel R, Pratsinis SE. Flame aerosol synthesis of smart nanostructured materials. *J. Mater. Chem.* 2007;17(45):4743-4756.

18. Sunsap P, Kim D-J, Kim K-S. Characterization of TiO_2 particles synthesized in diffusion flame reactor. *Ind. Eng. Chem. Res.* 2008;47(7):2308-2313.

19. Widiyastuti W, Purwanto A, Wang WN, Iskandar F, Setyawan H, Okuyama K. Nanoparticle formation through solid-fed flame synthesis: Experiment and modeling. *AIChE J.* 2009;55(4):885-895.

20. Yang G, Zhuang H, Biswas P. Characterization and sinterability of nanophase titania particles processed in flame reactors. *Nanostruct. Mater.* 1996;7(6):675-689.

21. Wang Z-M, Yang G, Biswas P, Bresser W, Boolchand P. Processing of iron-doped titania powders in flame aerosol reactors. *Powder Technol.* 2001;114(1):197-204.

22. Thimsen E, Biswas P. Nanostructured photoactive films synthesized by a flame aerosol reactor. *AIChE J.* 2007;53(7):1727-1735.

23. Huo J, Hu Y, Jiang H, Li C. In situ surface hydrogenation synthesis of Ti^{3+} self-doped TiO_2 with enhanced visible light photoactivity. *Nanoscale.* 2014;6(15):9078-9084.

24. Teleki A, Pratsinis SE. Blue nano titania made in diffusion flames. *Phys. Chem. Chem. Phys.* 2009;11(19):3742-3747.

25. Fujiwara K, Deligiannakis Y, Skoutelis CG, Pratsinis SE. Visible-light active black TiO_2-Ag/TiOx particles. *Appl. Catal. B.* 2014;154:9-15.

26. Basak S, Tiwari V, Fan J, Achilefu S, Sethi V, Biswas P. Single step aerosol synthesis of nanocomposites by aerosol routes: γ-Fe_2O_3/SiO_2 and their functionalization. *J. Mater. Res.* 2011;26(10):1225-1233.

27. Cho K, Biswas P, Fraundorf P. Characterization of nanostructured pristine and Fe-and V-doped titania synthesized by atomization and bubbling. *J. Ind. Eng. Chem.* 2014;20(2):558-563.

28. Rosebrock CD, Riefler N, Wriedt T, Mädler L, Tse SD. Disruptive burning of precursor/solvent droplets in flame-spray synthesis of nanoparticles. *AIChE J.* 2013;59(12):4553-4566.

29. Rosebrock CD, Wriedt T, Mädler L, Wegner K. The role of microexplosions in flame spray synthesis for homogeneous nanopowders from low-cost metal precursors. *AIChE J.* 2015;62(2):381-391.

30. Sharma MK, Qi D, Buchner RD, Swihart MT, Scharmach WJ, Papavassiliou V. Flame synthesis of mixed tin-silver-copper nanopowders and conductive coatings. *AIChE J.* 2016;62(2):408-414.

31. Taleby M, Hossainpour S. Numerical investigation of high velocity suspension flame spraying. *J. Therm. Spray Technol.* . 2012;21(6):1163-1172.

32. Goldsmith H, Mason S, Eirich F. Rheology: Theory and applications. *New York.* 1967:85.

33. Turns SR. *An introduction to combustion.* Vol 287: McGraw-hill New York; 1996.

34. Tsantilis S, Kammler H, Pratsinis S. Population balance modeling of flame synthesis of titania nanoparticles. *Chemical Engineering Science.* 2002;57(12):2139-2156.

35. Zhang Y, Xiong G, Li S, Dong Z, Buckley SG, Tse SD. Novel low-intensity phase-selective laser-induced breakdown spectroscopy of TiO_2 nanoparticle aerosols during flame synthesis. *Combustion and Flame.* 2013;160(3):725-733.

36. Golubko N, Yanovskaya M, Romm I, Ozerin A. Hydrolysis of titanium alkoxides: thermochemical, electron microscopy, SAXS studies. *J. Sol-Gel Sci. Technol.* . 2001;20(3):245-262.

37. Stern KH. High temperature properties and decomposition of inorganic salts. Part 3. Nitrates and nitrites. *J. Phys. Chem. Ref. Data.* . 1972;1(3).

38. Friedlander SK. *Smoke, dust, and haze: fundamentals of aerosol behavior.* Vol 198. New York, USA: Oxford University Press 2000.

39. Seinfeld JH, Pandis SN. *Atmospheric chemistry and physics: from air pollution to climate change*: John Wiley & Sons; 2012.

40. Gröhn AJ, Pratsinis SE, Sánchez-Ferrer A, Mezzenga R, Wegner K. Scale-up of nanoparticle synthesis by flame spray pyrolysis: the high-temperature particle residence time. *Ind. Eng. Chem. Res.* 2014;53(26):10734-10742.

41. Liu Q. Photovoltaic performance improvement of dye-sensitized solar cells based on Mg-doped TiO_2 thin films. *Electrochim. Acta.* 2014;129:459-462.

42. Wang H, Hu Y, Zhang L, Li C. Self-cleaning films with high transparency based on TiO_2 nanoparticles synthesized via flame combustion. *Ind. Eng. Chem. Res.* 2010;49(8):3654-3662.

43. Mei LF, Liang KM. Crystallization Behavior of Mg-Doped Titania. Paper presented at: Key Engineering Materials2010.

44. Khan MM, Ansari SA, Pradhan D, Ansari MO, Lee J, Cho MH. Band gap engineered TiO_2 nanoparticles for visible light induced photoelectrochemical and photocatalytic studies. *J. Mater. Chem. A.* 2014;2(3):637-644.

Appendix IV: Ion Generation in a Radioactive and a Soft X-ray Neutralizer: Effects of Carrier Gas and Humidity

Introduction

This set of experiments was aimed at:

1. Compare the concentration and mobility of the ions generated through these two charge conditioning methods. Further numerical evaluation on charging efficiency can be made.

2. Study the effect of carrier gas species on ion generation to evaluate the change of charging efficiency when measuring aerosol size distribution under different conditions (e.g. flue gas of combustion have high concentration of H_2O, CO_2, N_2, but low O_2, charging efficiency may be different).

3. Existing studies indicate that the ions generated in charge conditioners are strongly influenced by humidity . Positive and negative ions may be composed of $H_3O^+(H_2O)_n$ and $X^-(H_2O)_n$. Experiment can be conducted to observe how ion mobility/species distribution evolve with humidity .

Methods

Half Mini DMA – Electrometer. Open loop setup.

Aerosol flow: 6 lpm; Sheath flow: 224 lpm (ambient lab air); Sheath to aerosol ratio: 1: 37.3

Reason for not using closed loop: aerosol flow recirculation in the DMA will change the property of the sheath flow. The change in collision cross section area between sheath air molecule and sample aerosol will cause a mobility drift . At the same time, the change in viscosity results in the instability of blower. PTFE and copper tubings are used to transport aerosols to minimize the contamination. 7 different carrier gases were used in experiments. Properties are listed in Table A4.1.

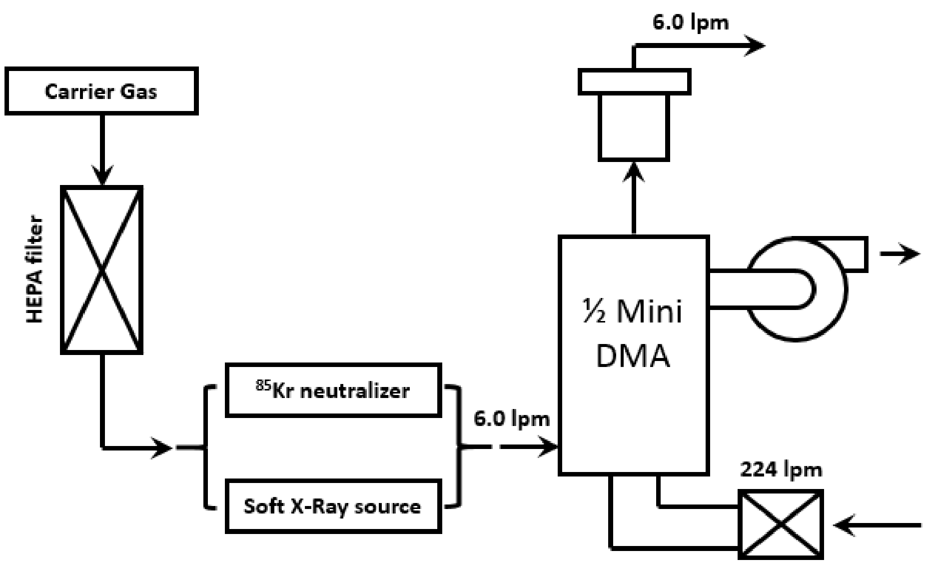

Figure A4.1 Experimental setup for measuring the mobility of ions generated from a radioactive and a soft X-ray neutralizer.

Table A4.1 Properties of the carrier gases.

Species	Air	N_2	O_2	CO_2	Ar	He	N_2 wet
Purity	Ambient	UHP (Ultra High Purity)	UHP	Lab grade	UHP	UHP	UHP pass through Milli-Q water (18.2 MΩ·cm)

Results

1. Ion generation in a radioactive neutralizer

Positive ions:

6 characteristic peaks can be detected when passing ambient air through a neutralizer (black line). Peak positions are marked with dashed lines. It could be seen that when passing different

species of carrier gases through the neutralizers, several peaks can be detected repeatedly (peak 1, 3, 4, 5, 6), meaning the generation of certain ions is not dependent on the carrier gas species. When passing wet N_2 through neutralizer, there is a significant increase in the position corresponding to peak 2, indicating humidity indeed influences ion generation. However, the influence on mean mobility is not very large. Therefore, we may classify the 6 peaks into two categories: inherent peaks (peak 1, 3, 4, 5, 6) and humidity influenced peak (peak 2).

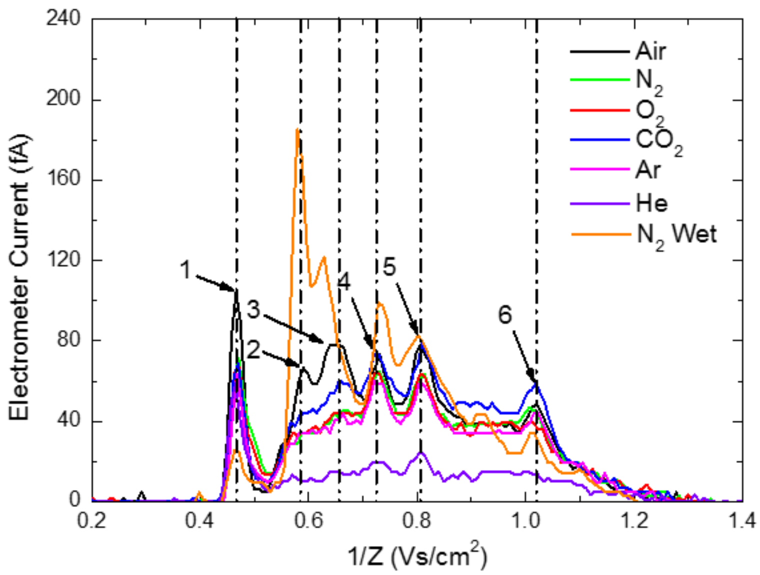

Figure A4.2 Mobility distribution of positive ions generated in a radioactive neutralizer.

Negative ions:

Similar phenomena can be observed in negative ions. There is an inherent peak (peak 1) with an inverse mobility of 2.17 Vs/cm^2 (0.986 nm, similar to size measured in previous works). Peak 2 was found to be humidity dependent as shown in the case of wet N_2.

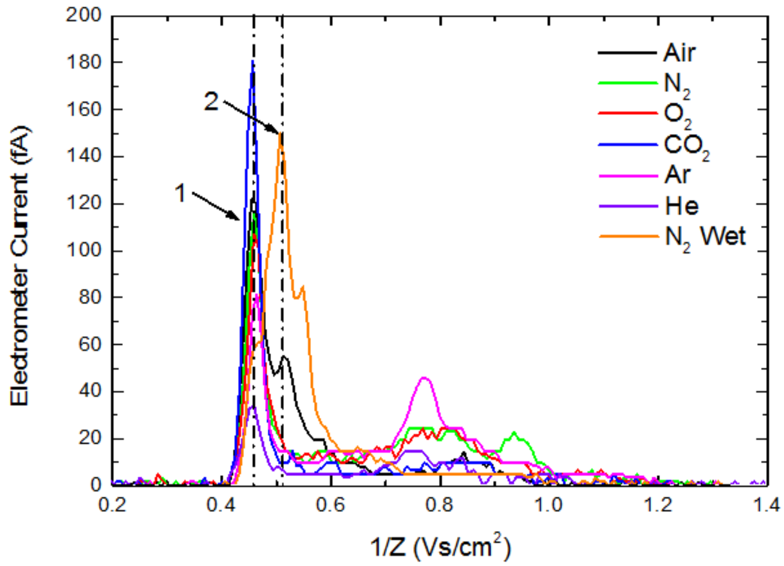

Figure A4.3 Mobility distribution of negative ions generated in a radioactive neutralizer.

2. Ion generation in a soft X-ray charger

Positive ions:

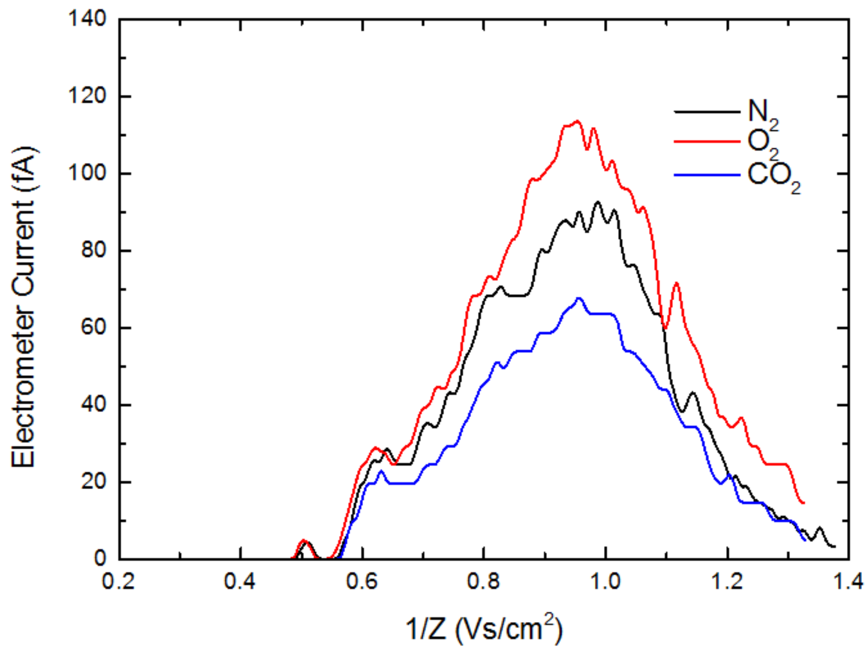

Figure A4.4 Mobility distribution of positive ions generated in a soft X-ray charger.

It could be seen that the change in carrier gas species do not have a significant effect on ion generation in the soft X-Ray charger. However, positive ions generated in soft X-Ray possess a continuous distribution. The mean ion mobility is smaller than the case using radioactive neutralizer. The negative ions generated in soft X-ray source have a similar distribution with that of a radioactive neutralizer. Both have a sharp peak at 1/Z of 0.46 Vs/cm^2 and a broad peak at around 0.8 Vs/cm^2. The similar distribution of negative ions implies that the ion generation mechanism may be the same in a radioactive and a soft X-ray neutralizer. The difference in positive ions may be explained by the difference of ion age. In the experiments, I used a larger chamber for soft X-ray neutralization. This may increase the residence time of the ions and form larger ion clusters having a reduced mobility. The negative ions might have higher stability to keep them from aging.

Negative ions:

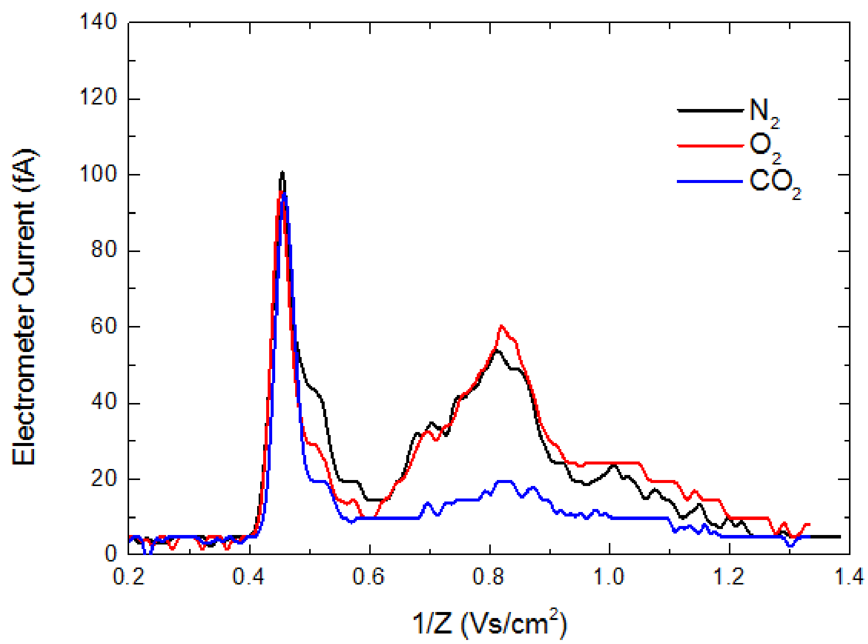

Figure A4.5 Mobility distribution of negative ions generated in a soft X-ray charger.

Appendix V: Effect of Dilution Sampler Designs on the Measurement of Sub 3-nm Particles Generated during Combustion

Introduction

The sampling of incipient particles from high temperatures is challenging, because the dilution probe should sufficiently quench all particle growth dynamics and gas-phase reactions during the particle transport in the sampling line. On the other hand, the perturbation to flames caused by the insertion of the dilution probe should also be minimized. Concerns may be raised regarding the validity of the measurement, especially in such a minuscule size range, where the particles may be very unstable. Two types of dilution samplers were assembled for the measurement of incipient particles generated from combustion. They are called a hole-in-a-tube (HiaT) sampler and a straight tube (ST) sampler. These two types of dilution samplers have been evaluated in previously on the sampling of agglomerates generated from flame synthesis. However, as the particle size reduces to sub nanometer range, the sampling of these particles becomes more difficult, as they may actively coagulate to form larger particles.

Methods

These two types of dilution samplers were evaluated with the following experimental setup. The gas analyzer was used to calculate the dilution ratio (DR) of the sampler. After the particles are sampled, they are introduced to the Half Mini DMA for size measurement. The size distributions measured at different dilution ratios will become "asymptotic" (has a same normalized shape) when the DR is high enough to stop all the chemical reaction and further particle growth.

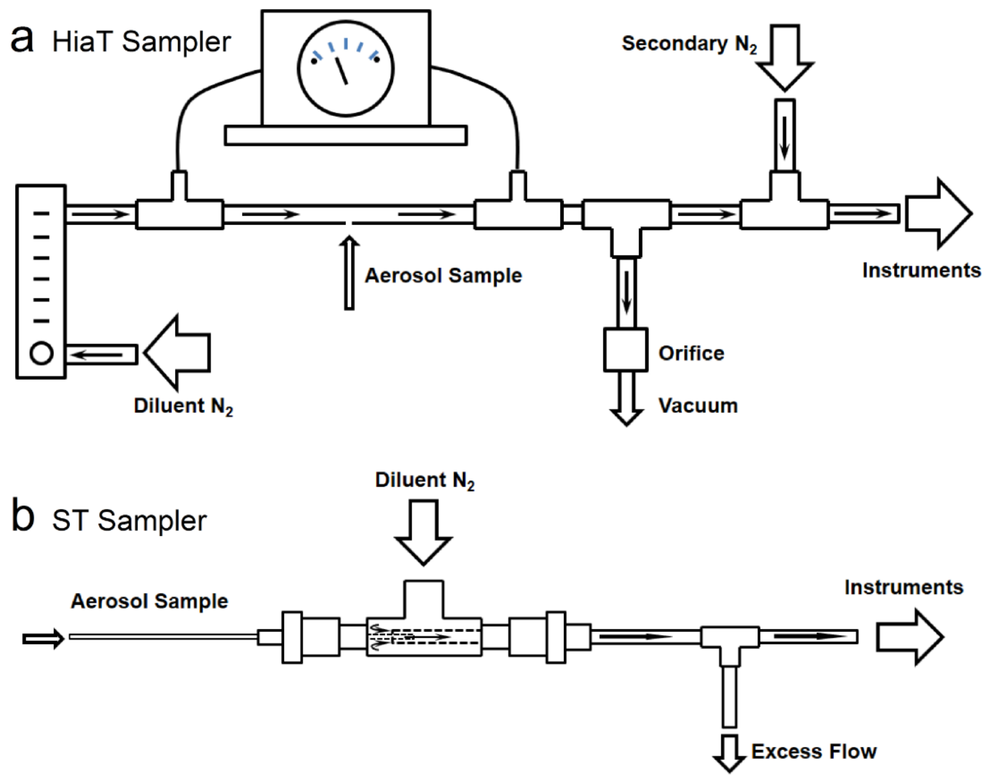

Figure A5.1 Designs of the dilution samplers (HiaT, ST)

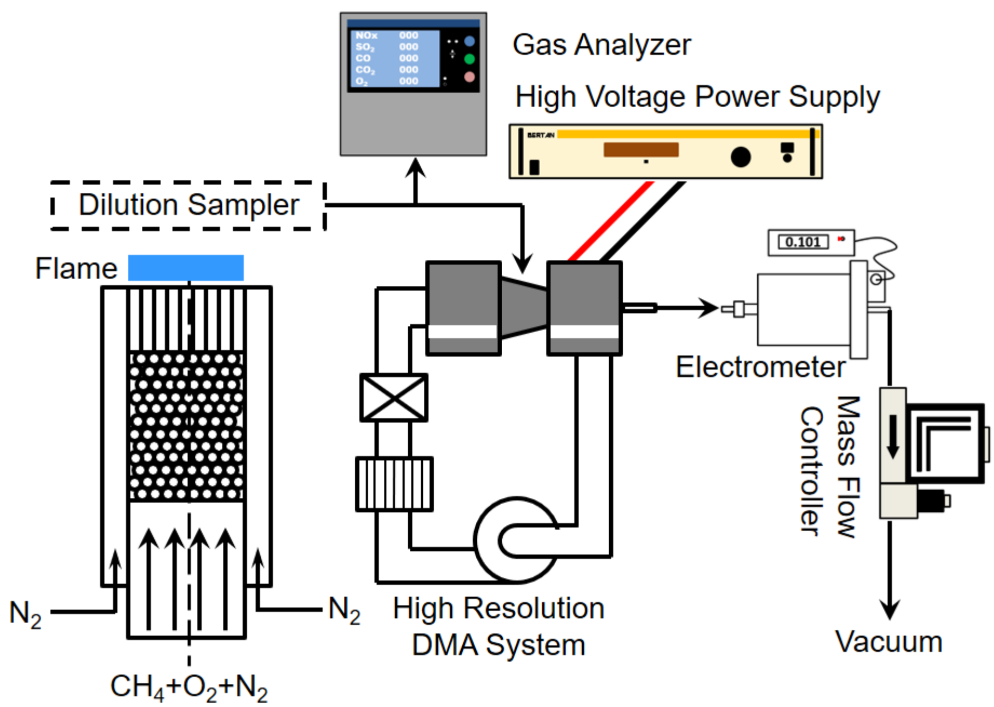

Figure A5.2 Experimental setup for evaluating the performance of the dilution samplers (HiaT, ST).

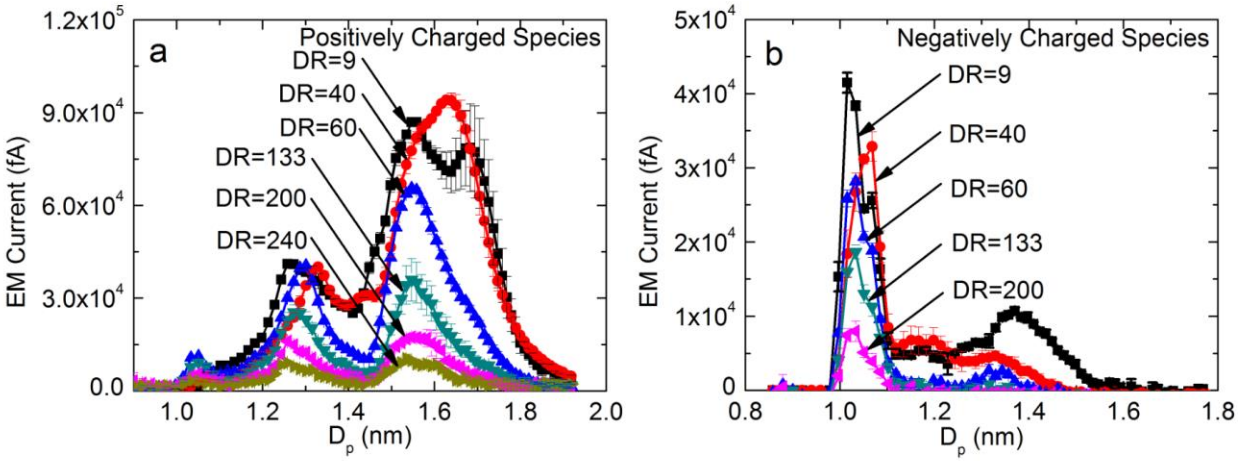

Figure A5.3 Size distributions of sub 2 nm particles generated in the premixed flat flame without precursor addition measured with the HiaT dilution sampler operated at various dilution ratios.

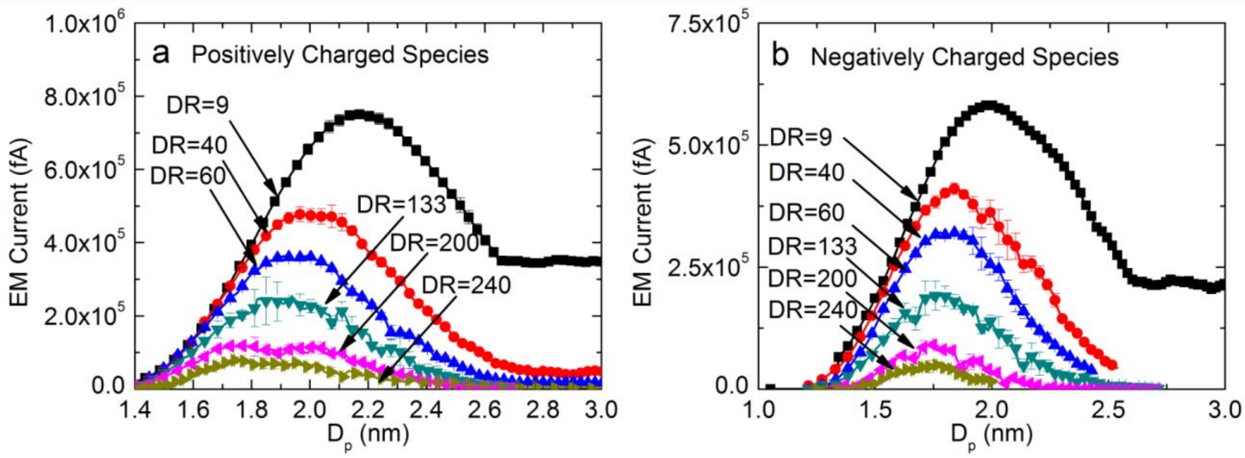

Figure A5.4 Size distributions of sub 2 nm particles generated in the premixed flat flame with precursor addition measured with the HiaT dilution sampler operated at various dilution ratios.

Results

Up until now, the HiaT sampler has been evaluated. The size distributions of particles generated in the flame without and with precursor addition at different dilution ratios (DR) are shown above. It is observed that when DR is higher than 133, the shape of the particle size distribution becomes identical, meaning that the DR is high enough to stop the particle growth dynamics.

This also indicates that the HiaT sampler can be used in measuring incipient particles generated during combustion.

The effect of precursor concentration and sampling height were also studied at a DR of 200, and the results are shown in Figures A5.5 and A5.6. As precursor concentration and sampling height increased, the particle size also increased, which can be simulated with a detailed discrete-sectional model.

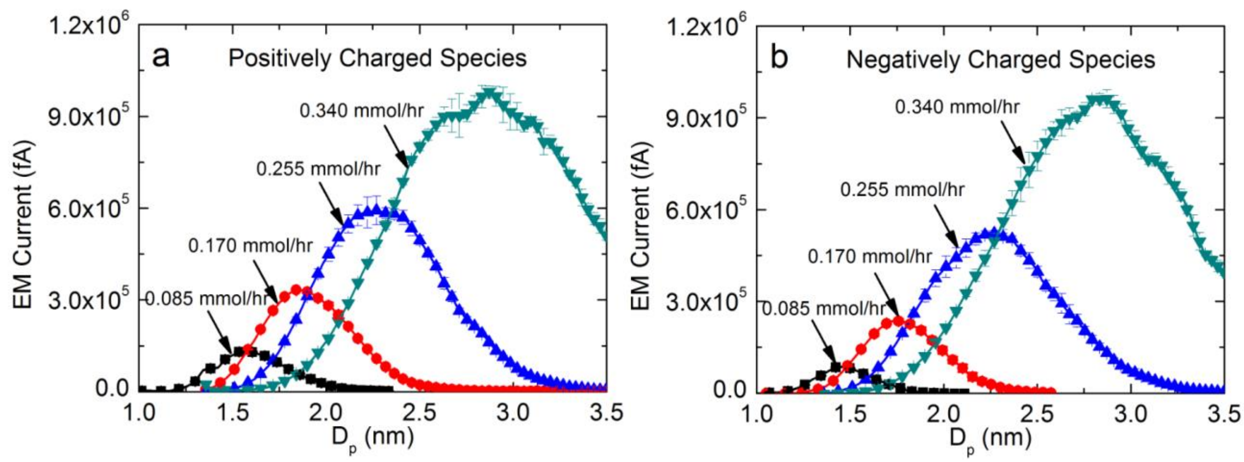

Figure A5.5 Size distributions of sub 2 nm particles generated in the premixed flat flame with precursor addition at different precursor concentrations. The HiaT dilution sampler was operated at a DR of 200.

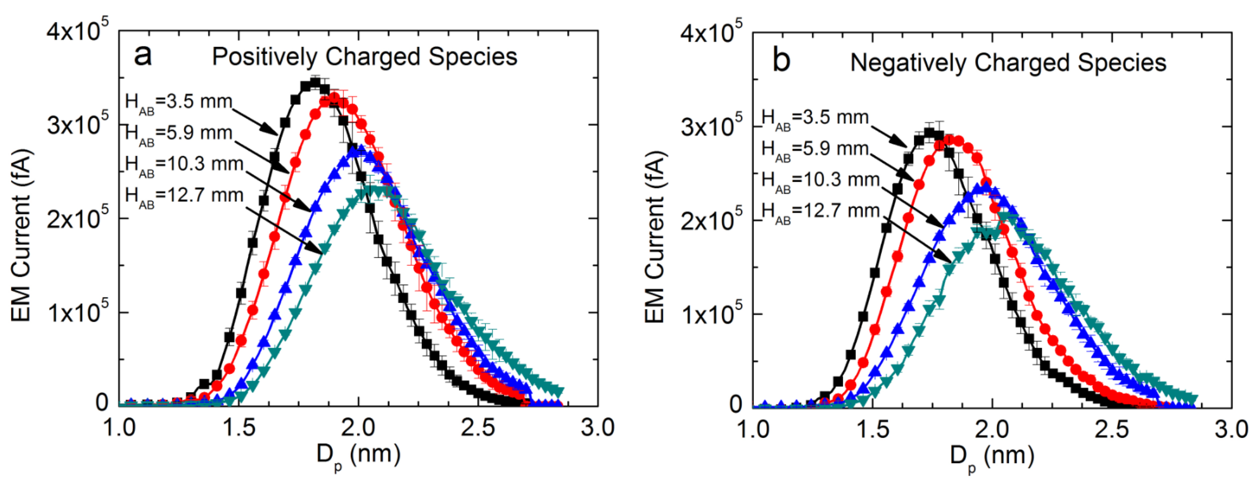

Figure A5.6 Size distributions of sub 2 nm particles generated in the premixed flat flame with precursor addition measured at different sampling heights. The HiaT dilution sampler was operated at a DR of 200.

The temperature at the sampling location (5 mm above the burner) was approximately 1800 K without the interference of the sampling probe. With the addition of the sampling probe, the local temperature will be inevitably reduced. Existing studies showed that a difference of 500 K was expected due to the perturbation of inserting the dilution probe (Zhao et al. 2003). Due to this temperature decrease, combustion and reaction of TTIP may be interfered. The characteristic reaction time of TTIP can be evaluated using the one-step reaction rates of TTIP. The first-order reaction rate of TTIP thermal decomposition is $k_g = 3.96\times10^5 \exp(-8480/T)$ (Tsantilis et al. 2003). The characteristic reaction time is then calculated by $\tau_{rxn} = 1/k_g$. Based on the calculation, the reaction time scale ranged from 0.3 to 1.7 ms, corresponding to a temperature range from 1800 K to1300 K (considering the effect of temperature reduction due to probe insertion). The particle residence time (1.5 ms) was comparable to TTIP reaction time, indicating the measured clusters could be not fully reacted precursor clusters. The comparable time scales also suggested that the insertion of the cold dilution probe may affect the reaction of precursor molecules in the high temperature zone.

The performance of the dilution sampling system in quenching the particle growth dynamics can be evaluated through comparing the characteristic time scales of particle transport and particle coagulation. The transport time of particles can be calculated through dividing the volume of the transport line (tube with 4.35 mm diameter and 0.2 m length) by the gas flow rate (25 lpm), yielding a value of 7 ms. The characteristic coagulation time is dependent on the coagulation coefficient β and total particle concentration N_0, where

$$\tau_{coag} = \frac{2}{\beta N_0}. \tag{A5.1}$$

The coagulation coefficient for neutral particles in the free molecular regime is given by

$$\beta = (\frac{3}{4\pi})^{1/6}(\frac{6k_b T}{\rho_p})^{1/2}(\frac{1}{v_i}+\frac{1}{v_j})^{1/2}(v_i^{1/3}+v_j^{1/3})^2, \quad \text{(A5.2)}$$

where k_b is the Boltzmann constant, ρ_p is the particle density, T is temperature, and v_i is the volume of the particle *i*. Based on this equation, the self-coagulation coefficient of 1 to 2 nm particles ranges from 1.0×10^{-16} to 1.4×10^{-16} m^3/s at a temperature of 298 K . Further by assuming each TTIP molecule converted to a particle, the highest particle concentration (N_0) in the dilution probe after dilution was 1.7×10^{17} /m^3 (in the case of 0.22 mmol/hr, 8.8 ppm). Based on these values, the minimum characteristic coagulation time of incipient particles (τ_{coag}) was 84 ms, which was longer than the transport time of 7 ms. This comparison of time scales demonstrates that particle growth dynamics was sufficiently quenched in the dilution sampling system.

However, the suppression of gas-phase reactions could not be verified through similar calculations or experimental techniques. Dilution sampling involves the reduction of temperature, which inevitably alters the equilibrium of reactions in the sampled stream. This influence may be substantial for the incipient particles that are physically and chemically instable. Due to the lower stability of nitrate species at elevated temperatures, the detected nitrate-bounded Ti-containing clusters might be formed through a post oxidation step during dilution, or between the sampling nozzle and the APi-TOF inlet. Furthermore, charged species typically observed in methane flames, for example, CH*, CHO^+, and $C_3H_3^+$, were not detected by the APi-TOF, implying the possible conversion of these species in the dilution system. It was possible that this conversion took place instantaneously, where increasing dilution ratio could not efficiently suppress the regarding chemical reactions. The chemical composition of the diluent gas (N_2) may also play a role in this rapid conversion of incipient particles. However, the research findings of this study can still be applied in quantum dot synthesis and material molecular doping, where rapid dilution is needed to control the small size and uniform composition of particles. This calculation also suggests that the synthesis of quantum dots requires a set of parameters, such as precursor concentration, dilution ratio, and sampling height, to accommodate the growth, quenching, and sampling of particles. In this study, a TTIP concentration of 8.8 ppm (0.22 mmol/hr), sampling height of 5 mm, and dilution ratio of 180 was suitable for the synthesis of quantum dots below 2 nm. The synthesis of quantum dots with larger sizes, needs a higher precursor concentration, a higher sampling height, and an adequate dilution ratio. Future work can focus on the design, testing, and evaluation of dilution sampling systems for incipient particle measurement at high temperatures with various diluent gas species to ensure the validity of incipient particle measurements.

References

Tsantilis, S., Kammler, H., Pratsinis, S. (2002). Population balance modeling of flame synthesis of titania nanoparticles. Chem. Eng. Sci. 57:2139-2156.

Zhao, B., Yang, Z., Wang, J., Johnston, M. V., Wang, H. (2003). Analysis of soot nanoparticles in a laminar premixed ethylene flame by scanning mobility particle sizer. Aerosol Sci. Technol. 37:611-620.

Appendix VI. Curriculum Vitae and Course Summary

Department of Energy, Environmental, and Chemical Engineering

Washington University in St. Louis | Email: yangwang@wustl.edu

St. Louis, MO 63130 | Url: http://yangwang-wustl.webs.com/

EDUCATION

Ph. D. Candidate, Washington University in St. Louis | Aug 2012 – May 2017

Energy, Environmental, and Chemical Engineering | Cumulative GPA: 4.0/4.0

Dissertation: Sub 2 nm particle characterization in systems with aerosol formation

Advisor and Chair of Committee: Pratim Biswas

B. S. Tsinghua University | Aug 2008 – July 2012

Thermal Engineering | Cumulative GPA: 90.0/100

RESEARCH EXPERIENCE

2012 – present **Graduate Research Assistant**

Supervisors: Professors Pratim Biswas, Brent Williams, Richard Axelbaum, Rajan Chakrabarty, Michel Attoui, and Jingkun Jiang

Sub 2 nm particle characterization in systems with aerosol formation

2010 – 2012 **Undergraduate Research Assistant**

Supervisor: Professor Shuiqing Li

Premixed stagnation swirl flame synthesis of nanostructured TiO_2 films for dye sensitized solar cells

PUBLICATIONS

Peer-Reviewed Publications

16. Jiayu Li, Anna Leavey, **Yang Wang**, Caroline O'Neil, Meghan A. Wallace, Carey-Ann D. Burnham, Adrianus CM Boon, Hilary Babcock, and Pratim Biswas (2017). "Comparing the Performance of 3 Airborne Virus Samplers for Influenza Virus." ***J. Aerosol Sci.*** *Under review*.

15. Caroline O'Neil, Jiayu Li, Anna Leavey, **Wang Yang**, Matthew Hink, Meghan Wallace, Pratim Biswas, Carey-Ann Burnham, and Hilary Babcock. "Aerosol Generation during Patient Care Activities." ***Clin. Infect. Dis.*** *Under review*.

14. Li Lu, Yanjie Hu, Hao Jiang, **Yang Wang**, Yi Jiang, Xiaofeng Niu, Pratim Biswas, and Chunzhong Li (2017). "Ultra-high Lithium Storage by Synergistic Effect of Doping of Mesoporous Structure for Multi-shell $LiMn_2O_4$ Cathode" ***Adv. Powder Technol.*** *Under review*.

13. Jiaxi Fang*, **Yang Wang***, Juha Kangasluoma, Michel Attoui, Jiaxi Fang, Heikki Junninen, Markku Kulmala, Tuukka Petäjä, and Pratim Biswas (2017). "Cluster Formation Mechanisms of Metal Oxides during Combustion Synthesis." ***Aerosol Sci. Technol.*** *Under review*. **(*equal contribution)**

12. Yao Nie, **Yang Wang**, and Pratim Biswas (2017). “Mobility and Bipolar Diffusion Charging Characteristics of Crumpled Reduced Graphene Oxide Nanoparticles Synthesized in a Furnace Aerosol Reactor.” ***J. Phys. Chem. C.*** *Accepted.*

11. **Yang Wang***, Girish Sharma*, Clement Koh, Vivek Kumar, Rajan Chakrabarty, and Pratim Biswas (2017). “Influence of Flame-Generated Ions on the Simultaneous Charging and Coagulation of Nanoparticles during Combustion.” ***Aerosol Sci. Technol*.** 10.1080/02786826.2017.1304635. **(*equal contribution)**

10. **Yang Wang**, Juha Kangasluoma, Michel Attoui, Jiaxi Fang, Heikki Junninen, Markku Kulmala, Tuukka Petäjä, and Pratim Biswas (2017). “The High Charge Fraction of Flame-generated Particles in the Size Range below 3 nm Measured by Enhanced Particle Detectors.” ***Combust. Flame*.** 176: 72-80.

9. Yanjie Hu*, **Yang Wang***, Hao Jiang, Yunfeng Li, Theodore Cohen, Yi Jiang, Binqi Wang, Ling Zhang, Pratim Biswas, and Chunzhong Li (2017). “Engineering the Outermost Layers of TiO_2 Nanoparticles Using in situ Mg Doping in a Flame Aerosol Reactor.” ***AIChE J.***, 63 (3) 870-880. **(*equal contribution)**

8. **Yang Wang**, Juha Kangasluoma, Michel Attoui, Jiaxi Fang, Heikki Junninen, Markku Kulmala, Tuukka Petäjä, and Pratim Biswas (2017). “Observation of Incipient Particle Formation during Flame Synthesis by Tandem Differential Mobility Analysis-Mass Spectrometry (DMA-MS).” ***Proc. Combust. Inst.*** 36(1), 745-752.

7. **Yang Wang**, Jiayu Li, Anna Leavey, Hilary Babcock, and Pratim Biswas (2016). “Comparative Study on the Size Distributions and Respiratory Deposition of

Particles Generated from Commonly Used Medical Nebulizers." ***J. Aerosol Med. Pulm. Drug Deliv.*** doi:10.1089/jamp.2016.1340.

6. Kelsey Haddad, Ahmed Abokifa, Shalinee Kavadiya, Tandeep S. Chadha, **Yang Wang**, John Fortner, Pratim Biswas (2016). "Growth of Oriented, Single Crystal SnO_2 Nanocolumn Arrays by Aerosol Chemical Vapor Deposition (ACVD)." ***CrystEngComm*****.** 18(39): 7544-7553.

5. Liu, Pai, Ian Arnold, **Yang Wang**, Yang Yu, Jiaxi Fang, Pratim Biswas, and Rajan K. Chakrabarty (2015). "Synthesis of Titanium Dioxide Aerosol Gels in a Buoyancy-opposed Flame Reactor." ***Aerosol Sci. Technol.***, 49(12), 1232-1241.

4. **Yang Wang**, Jiayu Li, He Jing, Qiang Zhang, Jingkun Jiang, and Pratim Biswas (2015). "Laboratory Evaluation of Three Low-Cost Particle Sensors for Particulate Matter Measurement." ***Aerosol Sci. Technol.*** 49(11), 1063-1077. (**Editor's selection of notable 2015 papers in *Aerosol Sci. Technol.*** Featured in AAAR 2015 Winter Newsletter)

3. **Yang Wang**, Pai Liu, Jiaxi Fang, Wei-Ning Wang, and Pratim Biswas (2015). "Kinetics of Sub 2 nm TiO_2 Particle Formation in an Aerosol Reactor during Thermal Decomposition of Titanium Tetraisopropoxide." ***J. Nanopart. Res.*** 17 (3): 1-13.

2. Fang, Jiaxi, **Yang Wang**, Michel Attoui, Tandeep S. Chadha, Jessica R. Ray, Wei-Ning Wang, Young-Shin Jun, and Pratim Biswas (2014). "Measurement of Sub-2 nm Clusters of Pristine and Composite Metal Oxides during Nanomaterial Synthesis in Flame Aerosol Reactors." ***Anal. Chem.*** 86 (15): 7523-7529.

1. **<u>Yang Wang</u>**, Jiaxi Fang, Michel Attoui, Tandeep S. Chadha, Wei-Ning Wang, and Pratim Biswas (2014). “Application of Half Mini DMA for Sub 2nm Particle Size Distribution Measurement in an Electrospray and a Flame Aerosol Reactor.” ***J. Aerosol Sci.*** 71: 52-64.

Manuscripts in Preparation

6. Miguel Vazquez-Pufleau*, **<u>Yang Wang</u>***, Elijah Thimsen, and Pratim Biswas. “Measurement of Critical Nucleus Size Distributions during Silane Pyrolysis.” In preparation for *AIChE J*. **(*equal contribution)**

5. Jiaxi Fang*, **<u>Yang Wang</u>***, Juha Kangasluoma, Michel Attoui, Jiaxi Fang, Heikki Junninen, Markku Kulmala, Tuukka Petäjä, and Pratim Biswas. “The Initial Stages of Multicomponent Particle Formation during the Combustion Synthesis of Mixed SiO_2/TiO_2.” In preparation for *Anal. Chem*. **(*equal contribution)**

4. Yanjie Hu, Nan Xu, **<u>Yang Wang</u>**, Yao Nie, Yi Jiang, Pratim Biswas, and Chunzhong Li. “Anatase Porous TiO_2 Microspheres: Aerosol Spray Pyrolysis Synthesis and Tailored Photocatalytic Activity.” In preparation for *Chem. Eng. J*.

3. Wang, Y., Attoui, M., Biswas, P. (2017). “Sub-2 nm Particle Measurement in High-temperature Aerosol Reactors: a Review.” In preparation for *J. Aerosol Sci*.

2. Jiayu Li, Haoran Li, Yehan Ma, **<u>Yang Wang</u>**, Chenyang Lu, and Pratim Biswas. “Spatiotemporal 3D Measurements of Particle Mass Concentrations with a Distributed Sensor Network Platform.” In preparation for *Sensor Actuat. A-Phys*.

1. Fei Xie, Yanjie Hu, Hao Jiang, Yi, Jiang, Su Huang, **<u>Yang Wang</u>**, Wenge Li, Li Lu, Sanmathi Chavalmane, Pratim Biswas, and Chunzhong Li. “Constructing Li_3VO_4 Nanoparticles

Anchored on Crumple Reduced Graphene Oxide for High-Power Lithium-ion Batteries." In preparation for *J. Mater. Chem. A.*

SELECTED PRESENTATIONS (Presenter with *)

9. **Yang Wang***, Sherrie Elzey, and Pratim Biswas. October 2016. "Measurement of flame-generated sub 3 nm particles with a TSI 1-nm SMPS." Portland, Oregon. AAAR 35th Annual Conference.

8. **Yang Wang***, Juha Kangasluoma, Michel Attoui, Jiaxi Fang, Heikki Junninen, Markku Kulmala, Tuukka Petäjä, and Pratim Biswas. August 2016. "Observation of Incipient Particle Formation during Flame Synthesis by Tandem Differential Mobility Analysis-Mass Spectrometry (DMA-MS)." Seoul, Korea. 36th International Symposium on Combustion.

7. Jiayu Li, **Yang Wang**, and Pratim Biswas*. August 2016. "Optical Characterization and Deployment of a Distributed Low-Cost Wireless Particle Sensor Network." Tours, France. 22nd European Aerosol Conference.

6. **Yang Wang***, Juha Kangasluoma, Michel Attoui, Jiaxi Fang, Heikki Junninen, Tuukka Petäjä, Markku Kulmala, and Pratim Biswas. October 2015. "Studying the Charging Characteristics of Flame Generated Particles below 3 nm with Enhanced Condensation Particle Counters." Minneapolis, MN. AAAR 34th Annual Conference.

5. **Yang Wang**, Jiayu Li*, He Jing, Qiang Zhang, Jingkun Jiang, and Pratim Biswas. October 2015. "Laboratory Evaluation of Three Low-cost Particle Sensors for Particulate Matter Measurement." Minneapolis, MN. AAAR 34th Annual Conference.

4. Christopher Oxford*, **Yang Wang**, Steven Dhawan, David Hagan, Dhruv Mitroo, Pratim Biswas, Brent Williams. October 2014. “Initial Field Deployment of a Custom Multi-channel Tandem Differential Mobility Analyzer (mc-TDMA).” Orlando, FL. AAAR 33rd Annual Conference.

3. **Yang Wang***, Pai Liu, Tandeep S. Chadha, Jiaxi Fang, and Pratim Biswas. October 2014. “Kinetics of sub 3 nm Titanium Dioxide Particle Formation in an Aerosol Reactor during the Thermal Decomposition of Titanium Isopropoxide (TTIP).” Orlando, FL. AAAR 33rd Annual Conference.

2. **Yang Wang**, Jiaxi Fang, Tandeep S. Chadha, Pai Liu, Michel Attoui and Pratim Biswas*.August 2014. “Sub 2 nm Particle Size Distribution Measurements in Aerosol Reactors: Bridging the Gap between Chemical Reactions and Particle Formation.” Busan, Korea. International Aerosol Conference.

1. **Yang Wang***, Jiaxi Fang, Michel Attoui, Tandeep S. Chadha, Wei-Ning Wang, Pratim Biswas. October 2013. “Application of Half Mini DMA for Sub 2 nm Particle Size Distribution Measurement in an Electrospray and a Flame Aerosol Reactor.” Portland, OR. AAAR 32nd Annual Conference.

FELLOWSHIPS AND AWARDS

- ✧ Editor’s selection of notable 2015 papers in Aerosol Sci. Technol. — 2016
- ✧ Outstanding and recognized reviewer of J. Aerosol Sci. — 2015
- ✧ Doctoral Student Teaching Assistant Award, Washington University — 2014

- ✧ The Otis, Dorothy and Bryce Sproul Family Fellowship 2012-2013
- ✧ Outstanding Graduates of Tsinghua University (top 5 %) 2012
- ✧ National Comprehensive Scholarship Recipient, Tsinghua Univ. 2009, 2011

SELECTED RESEARCH ACTIVITIES

2015-2016 Session Chair: American Association for Aerosol Research Annual Conference.

2015 Secretary of the Center of Aerosol Science and Engineering at Washington University

2015 September-October: Visiting scholar at the Division of Atmospheric Science, University of Helsinki.

2014-2016: Treasurer: Association of Graduate Engineering Students at Washington University.

2013-2014: Student Assistant: American Association for Aerosol Research Annual Conference.

2010 Student Assistant: 33rd International Symposium on Combustion, Beijing, China.

TEACHING EXPERIENCES

Teaching Assistant (Awarded with Doctoral Student Teaching Assistant Award, 2014)

- ✧ Aerosol Science and Technology (EECE 504, Fall 2013)
- ✧ Transport Phenomena (EECE 368, Spring 2014)

Guest Lectures

- ✧ Aerosol Science and Technology (EECE 504, Fall 2013, 2015, 2016)

JOURNAL REVIEW ACTIVITY

Journal of Aerosol Science, Aerosol Science and Technology, Aerosol and Air Quality Research, Journal of the Air and Waste Management Association

COURSEWORK SUMMARY

E63 ChE600	Doctoral Research	30 units	A
E63 ChE518	Aerosol Science and Technology	3 units	A^+
E63 ChE502	Mathematical Methods in Engineering	3 units	A^+
E63 ChE501	Transport Phenomena	3 units	A^+
E63 ChE503	Kinetics and Reaction Engineering	3 units	A^+
E63 ChE534	Environmental Nanochemistry	3 units	A
E63 ChE591	Computational Chemistry of Molecular Systems	3 units	A^+
L07 Chem465	Solid-State and Materials Chemistry	3 units	A
E33 EECE547	Atmospheric Science and Climate	3 units	A
E33 EECE5404	Combustion Phenomena	3 units	A^+
E33 EECE510	Advanced Topics in Aerosol Science & Engineering	3 units	A^+